Search for supersymmetric particles in final states with leptons, jets and missing transverse energy with the ATLAS detector.

Dissertation

zur Erlangung des Doktorgrades der
Fakultät für Mathematik und Physik der

ALBERT LUDWIGS UNIVERSITÄT FREIBURG

Author:
PETER TORNAMBÈ

Supervisor:
PROF. DR. GREGOR HERTEN

Peter Tornambè: *Search for supersymmetric particles in final states with leptons, jets and missing transverse energy with the ATLAS detector*

Datum der mündlichen Prüfung: January 10, 2019

DEKAN:	Prof. Dr. Gregor Herten
BETREUER DER ARBEIT:	Prof. Dr. Gregor Herten
KOREFERENT:	Prof. Dr. Markus Schumacher
PRÜFER:	Dr. Christian Weiser
	Prof. Dr. Gregor Herten
	Prof. Dr. Harald Ita

"*Always look at the world with eyes full of wonder.*"

My grandmother

Declaration of Authorship

- Ich erkläre hiermit, dass ich die vorliegende Arbeit **ohne** unzulässige Hilfe Dritter und **ohne** Benutzung anderer als der angegebenen Hilfsmittel angefertigt habe. Die aus anderen Quellen direkt oder indirekt übernommenen Daten und Konzepte sind unter Angabe der Quelle gekennzeichnet. Insbesondere habe ich hierfür **nicht** die entgeltiche Hilfe von Vermittlungs-beziehungsweise Beratungsdiensten (Promotionsberater/-beraterinnen oder anderer Personen) in Anspruch genommen. Die Arbeit wurde bisher weder im In-noch im Ausland in gleicher oder ähnlicher Form einer Prüfungsbehörde vorgelegt.

- Ich habe mich **nicht** bereits an einer in- oder ausländischen Hochschule um die Promotion beworben.

- Die Bestimmungen der Promotionsordnung der Universität Freiburg für die Fakultät für Mathematik und Physik sind mir bekannt; insbesondere weiß ich, dass ich vor der Aushändigung der Doktorkunde zur Führung des Doktorgrades **nicht** berechtigt bin.

Unterschrift:

Date: 22-10-2018

Abstract

Supersymmetry (SUSY) is one of the most studied models to extend the Standard Model (SM) of Particle Physics beyond the electroweak scale. In many supersymmetric models, the lightest supersymmetric particle is stable and can be a suitable candidate for dark matter.

This dissertation summarises a search for supersymmetric phenomena produced via the strong or the electroweak interaction leading to final states with two leptons (electrons or muons) of the same electric charge, or three leptons, jets and missing transverse momentum. While the same-sign or three leptons signature is present in many SUSY scenarios, SM processes leading to such events have very small production rates. Therefore, this analysis benefits from a small SM background in the signal regions leading to a good sensitivity especially in SUSY scenarios with compressed mass spectra or in which the R-parity is not conserved. The search was performed with cut-and-count analyses exploiting the full dataset recorded with the ATLAS detector at the Large Hadron Collider during the years 2015 and 2016, corresponding to a total integrated luminosity of 36.1 fb^{-1}. No significant excess above the Standard Model expectations is observed. The results are interpreted in several simplified supersymmetric models featuring R-parity conservation or R-parity violation, extending the exclusion limits from previous searches.

Since no sign of SUSY particles has been observed, this dissertation presents prospects for a search for compressed electroweakino production. This supersymmetric scenario is particularly challenging for LHC experiments since the products of the decay chain have low energies and are therefore difficult to detect. Results are obtained with a parameterised simulation of the ATLAS detector performances at a centre-of-mass energy of 14 TeV and for an integrated luminosity of 3000 fb^{-1}.

Zusammenfassung

Supersymmetry (SUSY) gehört zu den am besten untersuchten Erweiterungen des Standard Models (SM) der Teilchenphysik jenseits der elektroschwachen Skala. In vielen dieser supersymmetrischen Modelle ist das leichteste supersymmetrische Teilchen stabil und bietet sich daher als geeigneter Dunkle-Materie-Kandidat an.

Diese Dissertation fasst eine Suche nach supersymmetrischen Phänomenen zusammen, die auf der starken und elektroschwachen Wechselwirkung basieren und zu Endzuständen mit zwei Leptonen (Elektronen oder Myonen) der selben elektrischen Ladung oder drei Leptonen, Jets und fehlendem transversalem Impuls führen. Während Signaturen mit zwei gleichgeladenen oder drei Leptonen in vielen supersymmetrischen Szenarios auftreten, werden derartige Ereignisse im SM nur mit geringer Wahrscheinlichkeit produziert. Somit profitiert diese Analyse von sehr niedrigem SM Untergrund in den Signalregionen und ist dementsprechend äußerst sensitiv gegenüber spezifischen supersymmetrischen Szenarios die ein komprimiertes Massenspektrum aufweisen oder jenen in denen die R-Parität nicht erhalten ist. Diese Suche wurde mittels “cut-and-count” Analysen durchgeführt und nutzt den gesamten Datensatz, der mit dem ATLAS Detektor am Large Hadron Collider in den Jahren 2015 und 2016 aufgenommen wurde und einer integrierten Luminosität von 36.1 fb^{-1} entspricht. Es konnte keine signifikante Abweichung von den Vorhersagen des Standard Modells beobachtet werden. Ergebnisse wurde im Rahmen verschiedener vereinfachter supersymmetrischer Modelle, basierend auf Erhaltung oder Verletzung der R-Parität, interpretiert und somit die oberen Grenzwerte aus früheren Suchen verbessert.

Nachdem bis jetzt noch keine Anzeichen für SUSY Teilchen beobachtet wurden, wird in dieser Dissertation auch eine Studie über eine Suche nach einer komprimierten Electroweakinos-Produktion präsentiert. Dieses spezielle supersymmetrische Szenario ist eine besondere Herausforderung für die Experimente am LHC, da die Zerfallsprodukte lediglich niedrige Energien aufweisen und somit sehr schwierig zu detektieren sind. Die präsentierten Ergebnisse wurden mittels einer parametrisierten Simulation der Leistung des ATLAS Detektor bei einer Schwerpunktenergie von 14 TeV und bei einer integrierten Luminosität von 3000 fb^{-1} erzielt.

Contents

Chapter 1

Introduction

The Standard Model (SM) of Particle Physics is a quantum field theory which successfully describes the majority of the known particle physics phenomena with high precision. The discovery of the Higgs boson at the Large Hadron Collider (LHC) in 2012 set the last missing piece to the Standard Model theory. Nevertheless, this theory leaves open unaddressed questions and does not provide a description of the particle physics interaction beyond the electroweak energy scale. The fact that it does not describe the gravitational interaction, a missing candidate for dark matter and the fine-tuning required to ensure the stability of the Higgs mass under radiative corrections (mass hierarchy problem) are examples of the limitations of the Standard Model. Therefore, many models which provide an extension to the SM have been postulated.

Supersymmetry (SUSY) is one of the most studied models that provide an extension of the SM beyond the electroweak scale. It solves some of the limitations of the SM such as the mass hierarchy problem and also provides suitable dark matter candidates. SUSY theory predicts the existence of supersymmetric partners of the known SM particles. If R-parity (a newly introduced symmetry) is conserved, SUSY particles are produced in pairs and the lightest supersymmetric particle (LSP), which is typically the lightest neutralino $\tilde{\chi}_1^0$, is stable. In many models, the LSP can be a dark-matter candidate and is produced with leptons, jets and large missing transverse momentum. If R-parity is violated (RPV), the LSP can decay and therefore generate events with high jet and lepton multiplicities.

The LHC performances were upgraded after the end of the first data taking period (Run-I). In particular, the increase of luminosity and energy at the centre-of-mass allows to perform significative searches of Beyond SM theories (BSM) with the data recorded by the general-purpose particle detectors such as ATLAS and CMS.

A search for supersymmetric phenomena in final states with two leptons (electrons or muons) of the same electric charge, referred to as same-sign (SS) leptons, or three leptons (3L), jets and in some cases also missing transverse momentum $E_{\mathrm{T}}^{\mathrm{miss}}$ is presented in this dissertation. The analysed data-sample corresponds to an integrated luminosity of 36.1 fb^{-1} and has been collected in 2015 and 2016. While the same-sign leptons signature is present in many supersymmetric scenarios, SM processes leading to such events have very small production rates. Therefore, this analysis benefits from a small SM background in the signal regions leading to a good sensitivity in particular regions of the SUSY phase-space and in R-parity violated scenarios. Except for the prompt production of same-sign lepton pairs, the main sources of background are fake/non-prompt leptons and leptons with a charge mis-identification. This allows to use relatively loose kinematic requirements on $E_{\mathrm{T}}^{\mathrm{miss}}$ increasing the sensitivity to several different signal models.

In case the results of the SUSY searches until the end of Run-III of the LHC data taking program do not show any sign of new physics, it is important to start designing the future searches for SUSY with

leptons in the final state. During the long shutdown, until 2023, the LHC will be upgraded to increase the instantaneous luminosity by a factor three (High Luminosity LHC).
The naturalness condition in the MSSM (Minimal Supersymmetric Model) suggests that the absolute value of the higgsino mass parameter μ is at the weak energy scale. A prospect study of the exclusion power at High Luminosity LHC for the natural mass range of a pure higgsino scenario with leptons, jets and $E_{\mathrm{T}}^{\mathrm{miss}}$ in the final state is presented in this thesis.
Chapter 2 introduces the SM theory with the description of the electroweak interactions, quantum chromodynamics and the symmetry breaking mechanism which introduces the Higgs boson. Chapter 3 summarises the Supersymmetry theory, one of the most important theories beyond SM theories which inspired the searches discussed in this thesis. Chapter 4 reviews the characteristics of the LHC facilities and of the ATLAS detector, while chapter 5 shows the techniques used in ATLAS to identify and reconstruct the particles produced in the collision. The search for strongly produced SUSY particles with 2015 and 2016 data (36.1 fb^{-1}) is described in chapter 6, from the targeted signal models to the background estimation and final results. Chapter 7 is dedicated to the electroweak produced SUSY particles describing the main differences with the equivalent strong analysis of the previous chapter. In chapter 8, the prospect studies of the exclusion power for the natural mass range of a pure higgsino scenario at High Luminosity LHC are presented. Finally, in chapter 9, a summary of the results of the two analyses and the future prospects of the search of SUSY particles with leptons in final state is given. All auxiliary material is included in the Appendices A-C, while a brief summary of publications and details about the personal contributions from the author of this thesis can be found in the list of publications.

Chapter 2

Standard Model

2.1 Fundamental particles and forces

The Standard Model of particle physics (SM) includes several particles classified as matter interacting particles fermions, force mediators vector bosons, plus an additional Higgs scalar boson. Moreover, the SM theory describes three of the four main fundamental forces: electromagnetic, weak and strong. Fermions are further subdivided into leptons, which interact only via electroweak forces, and quarks, which are additionally interacting via the strong force. The fermions have three different generations, where corresponding fermions between generations differ only by the mass. The leptons in SM come in doublets and include electron (e), muon (μ) and tau (τ), with the corresponding neutrinos (ν). Also quarks come in doublets (up-type and down-type) and are called up, down, charm, strange, top and bottom. Each fermion has an anti-particle partner with the same mass and opposite charge. Gauge bosons are grouped depending on the force they mediate. The photon (γ) is the electromagnetic mediator, the $W^{\pm}$ and Z^0 bosons are the weak interaction mediators and the gluons are the mediators of the strong force. The last fundamental particle discovered in the SM is the Higgs boson, observed first in 2012 by ATLAS and CMS experiments [1, 2]. As it will be explained in section 2.5, the Higgs boson is responsible for the spontaneous symmetry breaking mechanism which provides mass to the SM particles.
All particles in the SM are summarised in Figure 2.1.

2.2 Quantum Electrodynamics

Quantum Electrodynamics (QED) is a relativistic quantum field theory (QFT) developed in the 1940s to describe the electromagnetic interactions of the particles (see e.g. [4] for pedagogical introduction). In analogy with the classical mechanics, the Lagrangian function L may be used to derive the equation of motion and expressed in terms of Lagrangian density $\mathscr{L}$ ($L = \int \mathscr{L} d^4x$). The equation of motions can then be calculated using the *Euler-Lagrange equation* for fields:

$$\frac{\partial \mathscr{L}}{\partial \phi} - \partial_\mu \frac{\partial \mathscr{L}}{\partial(\partial_\mu \phi)} = 0, \tag{2.1}$$

where, in the QFT case, ϕ is a quantum field which represents a particle and $\partial_\mu = \frac{\partial}{\partial x^\mu}$ is the partial derivative with respect to the four-vector x^μ.
The Dirac equation describes the propagation of a free massive fermion (spin-1/2) and it can be derived

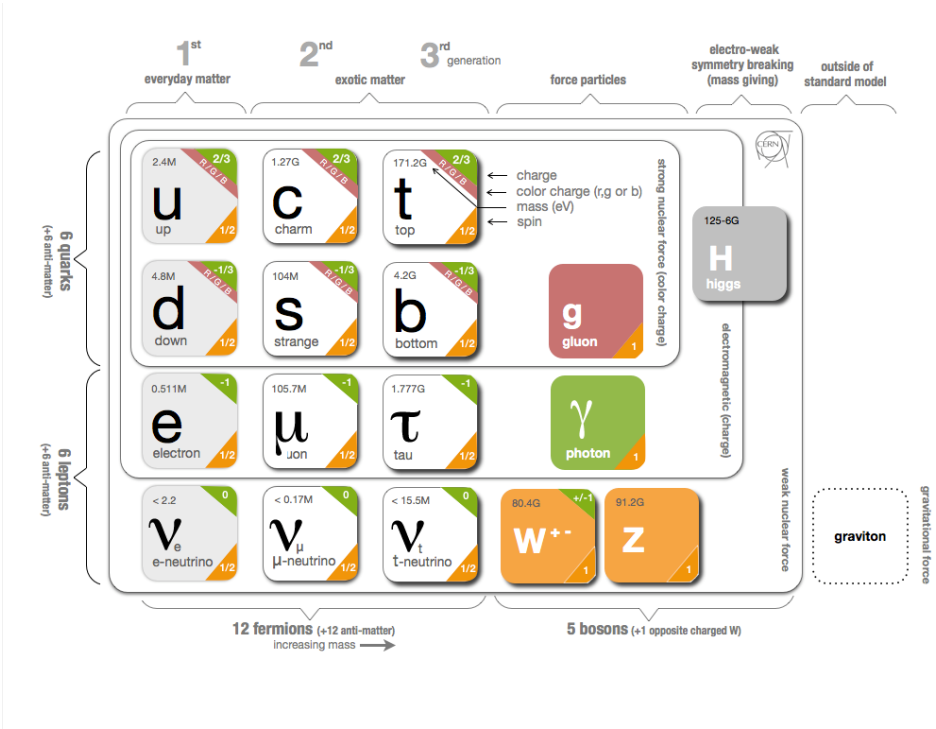

Figure 2.1: An overview of the Standard Model with the three generations of fermions and the gauge bosons which are the mediators of the fundamental forces [3].

from the following Lagrangian[1]:

$$\mathscr{L}_{\text{Dirac}} = \bar{\psi}(i\gamma^{\mu}\partial_{\mu} - m)\psi, \tag{2.2}$$

where ψ is the fermionic field (Dirac spinor), m is the mass of the fermion and γ^{μ} are the Dirac matrices. The Dirac Lagrangian, and thus the Dirac equation, is invariant under global gauge transformations, but when applying a local transformation of the abelian unitary group $U_Y(1)$:

$$\psi(x) \rightarrow \psi' = e^{iqf(x)}\psi(x), \tag{2.3}$$

where f(x) is the function defining the transformation in each point of the phase space and q represents the strength of the interaction, the Lagrangian loses its invariance:

$$\mathscr{L}_0 \rightarrow \mathscr{L}_0 - \partial_{\mu} f(x)(\bar{\psi}\gamma^{\mu}\psi). \tag{2.4}$$

To mantain a gauge invariant description of the dynamics of the particles, a new vector field A_{μ} needs to be added to the Lagrangian description in Equation 2.2. The electromagnetic field A_{μ} needs to transform under the same local phase transformations by:

$$A_{\mu}(x) \rightarrow A'_{\mu}(x) = A_{\mu}(x) + \partial_{\mu} f(x). \tag{2.5}$$

The interaction between the field ψ and the field A_{μ} guarantees the gauge invariance of the model. In QED, A_{μ} represents the electromagnetic field with its quantum photon. The intensity of the interaction is determined by the coupling constant q.

[1]The parametrisation in natural units ($\hbar = 1, c = 1$) is used throughout all the dissertation. In SI units, the values are $\hbar = 1.055 \cdot 10^{-34}$ Js and $c = 2.99 \cdot 10^{8}$ m/s [5].

When adding a new vector field, two extra terms need to be added: a kinetic term and a mass term. The mass term ($m_A^2 A_\mu A^\mu$) would violate once again the gauge invariance. Therefore the mass needs to be $m_A = 0$, leading to the massless photon observed in nature. The kinetic term for the gauge field A_μ is:

$$\mathscr{L}_{\text{Kin}} = -\frac{1}{4} F^{\mu\nu} F_{\mu\nu}, \tag{2.6}$$

where $F_{\mu\nu} = \partial_\mu A_\nu - \partial_\nu A_\mu$ is the electromagnetic field tensor.
The combined Lagrangian is invariant under local gauge transformation and it describes the electromagnetic interactions of a single spin 1/2 fermion:

$$\mathscr{L}_{\text{QED}} = \bar{\psi}[i\gamma^\mu(\partial_\mu - iqA_\mu) - m]\psi - \frac{1}{4} F_{\mu\nu} F^{\mu\nu}. \tag{2.7}$$

In conclusion, QED is able to describe the interactions between charged particles and photons by requiring the invariance of the Lagrangian with respect to the $\mathrm{U_Y}(1)$ symmetry group. It was able to predict many experimental results with high precision, among which the anomalous electron magnetic moment [6] is particularly impressive.

2.3 Electroweak interactions

The weak interaction was firstly described by Fermi [7] with its famous description of the β decay as a four fermion contact interaction with the Fermi constant G_F as the coupling strength. This theory was able to describe several processes such as the muon decay into electron, however, being an effective field theory, it is valid only for processes at low energies. At higher energies it violates unitarity and becomes non-renormalisable, losing its descriptive power.
Glashow, Salam and Weinberg [8, 9, 10] proposed another model, that solves the shortcomings of the Fermi model, where QED and weak interactions are not independent and can be described as the same interaction. As it was done in QED and following the development of the Yang-Mills theory [11], a symmetry group is needed to describe the chiral nature of fermions.
The $SU(2)_L \otimes U(1)_Y$ symmetry group is an example of a gauge group leading to a chiral theory. The group generators are the weak isospin $\vec{\tau} = \frac{1}{2}\vec{\sigma}$ (where $\vec{\sigma}$ are the Pauli matrices) and Y the hypercharge. Two new quantum numbers can be assigned to fermions: the third component of the weak isospin (I_3) and the weak hypercharge (Y). The isospin doublets χ_L ($I_3 = \pm\frac{1}{2}$) form *left-handed* chiral states, while the isospin singlets χ_R ($I_3 = 0$) form the *right-handed* chiral states.
A local gauge transformation can be applied to the *left-handed* and *right-handed* components:

$$\chi(x)_L \to e^{i\alpha(x)\vec{\tau} + i\beta(x)Y} \chi_L(x),$$
$$\chi(x)_R \to e^{i\beta(x)Y} \chi_R(x).$$

where $\alpha(x)$ and $\beta(x)$ are the phases of the local gauge transformations.
The condition of local gauge invariance leads to the addition of four vector fields, three for $SU(2)_L$ and one for $U(1)_Y$ symmetry group: $\vec{W}_\mu = (W_\mu^1, W_\mu^2, W_\mu^3)$ couples to weak isospin currents and B_μ couples to weak hypercharge currents. The fields W_μ^1 and W_μ^2 are electrically charged. while W_μ^3 and B_μ are neutral fields.

The electroweak Lagrangian becomes:

$$\mathscr{L}_{\text{EWK}} = \sum_{l=e,\mu,\tau} i\bar{\chi}_L^l \gamma^\mu D_\mu \chi_L^l + \sum_{k=e,\mu,\tau} i\bar{\chi}_R^k \gamma^\mu D_\mu \chi_R^k - \frac{1}{4} W_{\mu\nu}^a \cdot W_a^{\mu\nu} - \frac{1}{4} B_{\mu\nu} \cdot B^{\mu\nu},$$
$$D_\mu = \partial_\mu + ig\vec{\tau} \cdot \vec{W}_\mu + g' B_\mu,$$

where g and g' are the coupling strength constants. While $B_{\mu\nu} = \partial_\mu B_\nu - \partial_\nu B_\mu$ and $W_{\mu\nu}^a = \partial_\mu W_\nu^a - \partial_\nu W_\mu^a - g\varepsilon_{ijk} W_\mu^j W_\nu^k$ with a=(1,2,3).
The physical observed bosons, $W^\pm$, Z^0 and γ, are obtained with a combination of the gauge fields:

$$A_\mu = W_\mu^3 \sin\theta_W + B_\mu \cos\theta_W, \tag{2.8}$$
$$Z_\mu = W_\mu^3 \cos\theta_W - B_\mu \sin\theta_W, \tag{2.9}$$
$$W_\mu^\pm = \frac{1}{\sqrt{2}}(W_\mu^1 \mp W_\mu^2). \tag{2.10}$$

where θ_W is the Weinberg angle and is defined in terms of the coupling constants:

$$\sin\theta_W = \frac{g'}{\sqrt{g^2 + g'^2}}, \tag{2.11}$$
$$\cos\theta_W = \frac{g}{\sqrt{g^2 + g'^2}}. \tag{2.12}$$

It is important to notice that the $W^\pm$ bosons can interact only with *left-handed* particles, while the neutral bosons can couple also to *right-handed* states due to the presence of B_μ.
As in the QED case, the mass terms ($m^2 W_\mu W^\mu, m^2 B_\mu B^\mu$ and $m\psi\bar{\psi}$) should be set to zero to preserve the gauge invariance. Experimental evidence however show that W and Z bosons and fermions have masses. These are introduced via spontaneous breaking of the electroweak symmetry described in Section 2.5.

2.4 Quantum Chromodynamics

The strong interaction between quarks and gluons is described by the Quantum Chromodynamics (QCD). Spectroscopy experiments revealed that partons can exist in three different states expressed by the colour charge (as analogon of electric charge): red, blue and green. The QCD is a non-abelian Yang-Mills theory based on the symmetry group $SU(3)_C$ which explains the three colour states. Therefore, quark fields may be described as colour triplets and are required to follow the Dirac equation as equation of motion. A local gauge transformation is implied:

$$\psi_q \to e^{i\alpha^n \lambda_n} \psi_q, \quad \alpha \in \mathbb{R}, \quad n \in 1, ...8, \tag{2.13}$$

where λ_n are the eight Gell-Mann matrices [12] (SU(3) group generators) and α_n represent the phases of the local gauge transformation.
To ensure the gauge invariance, gauge fields and covariant derivative ($D_\mu = \partial_\mu - igA_\mu^\alpha \lambda_\alpha$) are added

to the Lagrangian. The QCD Lagrangian becomes:

$$\begin{aligned}\mathscr{L}_{\mathrm{QCD}} &= \sum_q \bar{\psi}_q(i\gamma^\mu D_\mu - m_q)\psi_q - \frac{1}{4}G^n_{\mu\nu}G^{\mu\nu}_n \\ &= \sum_q \bar{\psi}_q(i\gamma^\mu \partial_\mu - m_q)\psi_q - \frac{1}{2}g_s(\bar{\psi}_q\gamma^\mu\lambda_n\psi_q)G^n_\mu - \frac{1}{2}G^l_\mu G^l_\nu,\end{aligned}$$

where G_μ are the massless gauge fields, g_s is the strong coupling constant and the q index runs over the different quark flavours. The gluon field tensor is $G^n_{\mu\nu} = \partial_\mu G^n_\nu - \partial_\nu G^n_\mu + g_s f^n_{kl} G^k_\mu G^l_\nu$ and includes self-interactions terms of gluons, since they also carry colour charge (in opposition to photon which do not carry electric charge). The structure constant f^{nkl} of $SU(3)$ is related to the Gell-Mann matrices with the relation $[\lambda_n, \lambda_k] = if^{nkl}\lambda_l$.

The QCD theory has a couple of interesting differences from the QED theory. As a consequence of the gluon self-interaction, the potential energy of particles with colour includes also a linear term ($V = \frac{a}{r} + br$ where $a < 0$, $b > 0$), which means that quark and gluons are confined and cannot exist isolated, so called colour confinement.

Another effect is the asymptotic freedom. In QED, the bare electron charge is screened by a cloud of virtual e^+e^- pairs, similarly in QCD the quark-antiquark pairs around a quark screen the colour charge. But, the self-interaction of gluon generates a cloud of gluons which contributes to the effective colour charge of the quark. The anti-screening effects of gluon is stronger, causing an increase of the colour charge with the distance. Therefore, the strong coupling constant α_s increases for low energies (higher distances). Consequently, energetic quarks are almost free particles and perturbative calculations may be performed at high energies.

2.5 Brout-Englert-Higgs mechanism

Preservation of local gauge invariance leads to massless fermions and bosons, but experimental evidence shows that these particles are massive. The Brout-Engler-Higgs mechanism (BEH) [13, 14], proposed in 1964, solves this apparent problem.

The mechanism introduces an additional isospin doublet of complex scalar fields to break the symmetry:

$$\Phi = \begin{pmatrix}\phi^+ \\ \phi^0\end{pmatrix} = \frac{1}{\sqrt{2}}\begin{pmatrix}\phi_1 + i\phi_2 \\ \phi_3 + i\phi_4\end{pmatrix}, \tag{2.14}$$

where ϕ^+, ϕ^0 are complex fields and $\phi_{1,2,3,4}$ are real fields.

A Lagrangian of the complex scalar Higgs field invariant under $U(1)$ symmetry can be written as:

$$\mathscr{L}_{\mathrm{Higgs}} = (D_\mu\Phi)^\dagger D^\mu\Phi - \mu^2\Phi^\dagger\Phi - \lambda(\Phi^\dagger\Phi)^2, \tag{2.15}$$

where μ and λ are free parameters and $V_{\mathrm{Higgs}} = \mu^2\Phi^\dagger\Phi + \lambda(\Phi^\dagger\Phi)^2$ is the Higgs potential, where the first term is the mass term. The vacuum stability requires $\lambda > 0$, where λ is the quartic self-coupling of the Higgs boson, while the sign of μ^2 leads to two different shape of the potential. If μ^2>0, the potential has the form of a parabola with a global minimum at zero. If $\mu^2 < 0$, there is a set of degenerate minimum lying on a ring in the complex plane which do not coincide with the origin, as shown in Figure 2.2, with $(\phi^\dagger\phi) = 2\mu^2/\lambda$. Consequently, the gauge symmetry is broken in the vacuum state.

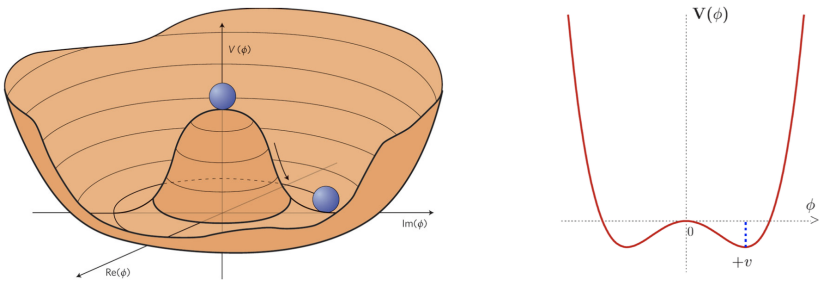

Figure 2.2: Left: Shape of the two-dimensional Higgs potential V(Φ). Right: One-dimensional projection of the potential for the case $\lambda > 0$ and $\mu^2 < 0$ [15].

Setting the derivative of the potential to zero allows to obtain the values of the ground states, a particular vacuum expectation value may be chosen:

$$\Phi_0 = \frac{1}{\sqrt{2}}\begin{pmatrix}0\\ v\end{pmatrix}, \quad v = \sqrt{\frac{-\mu^2}{2\lambda}}, \tag{2.16}$$

where v is called "vacuum expectation value" and it defines the set of minimum of the potential.
A perturbation expansion around the ground state is necessary to analyse the dynamic of the field around the minimum:

$$\Phi(x) = \frac{1}{\sqrt{2}}\begin{pmatrix}0\\ v+h(x)\end{pmatrix}\exp\{i\chi(x)\}. \tag{2.17}$$

Where $h(x)$ and $\chi(x)$ are real fields and $h(x)$ will be interpreted as the visible scalar Higgs field. The perturbation is expressed with this formula to have a constant part that represents the non-zero value of the ground state. In addition a variable field is added for small perturbations around the ground state.
The new field $\chi(x)$ is a massless scalar field and is a consequence of the spontaneous symmetry breaking, as postulated by the Goldstone theorem [16]. The Lagrangian is locally gauge invariant for $SU(2)$ and with a particular choice of the gauge ("unitary gauge") the new scalar field can be set to zero. When the perturbed field is replaced in the Lagrangian, one obtains:

$$\mathscr{L}_{\text{Higgs}} = \frac{1}{2}(\partial_\mu h)(\partial^\mu h) + \frac{g}{4}(v+h)^2 W_\mu W^\mu + \frac{g^2}{8\cos^2\theta_W}(v+h)^2 Z_\mu Z^\mu + \tag{2.18}$$

$$+\frac{\mu^2}{2}(v+h)^2 - \frac{\lambda}{16}(v+h)^4. \tag{2.19}$$

The Lagrangian includes mass terms, in the form of $m_\mu A_\mu A^\mu$, for the gauge fields. The fields corresponding to the physical Z^0 and $W^\pm$ bosons rise from the covariant derivative in the kinetic term of the new field. Moreover, the self interaction of the Higgs field leads to an additional mass term: the Higgs boson. The masses can be expressed in terms of coupling constants, vacuum expectation value and μ parameter:

$$m_W = \frac{gv}{2}, \quad m_Z = \frac{m_W}{\cos\theta_W}, \quad m_H = \sqrt{2}\mu. \tag{2.20}$$

The Higgs boson mass m_H is not predicted by theory, since μ is a free parameter. Nevertheless, the Higgs boson mass has been measured at LHC by the ATLAS and CMS experiments and is $\simeq$ 125 GeV [17, 18]. The BEH mechanism allows to include also the quark and leptons masses in the SM framework without violating the gauge symmetry. A new term, invariant under $SU(2)_L \otimes U(1)_Y$,

is add to the electroweak Lagrangian:

$$\mathscr{L}_{\text{Leptons}} = \lambda_l[(\bar{\nu},\bar{l})_L \begin{pmatrix}\phi^+\\ \phi^0\end{pmatrix} l_R + h.c.], \tag{2.21}$$

where λ_l defines the coupling of interaction between fermions and the Higgs field and is called the Yukawa coupling. When introducing the Higgs field $h(x)$ in the additional term, a lepton mass term and an interaction term are obtained:

$$\mathscr{L}_{\text{Leptons}} = -m_l\bar{l}l - \frac{m_l}{v}\bar{l}lh. \tag{2.22}$$

In the case of the quarks the procedure is similar, but all components of the doublets become massive. Therefore a different parametrisation is used:

$$\begin{pmatrix}-\Phi^0\\ \Phi^-\end{pmatrix} = \Phi_C = -i\sigma_2\Phi^* = \sqrt{\frac{1}{2}}\begin{pmatrix}v+h\\ 0\end{pmatrix}, \tag{2.23}$$

at the minimum.
The Lagrangian density of the quark Yukawa interaction is:

$$\mathscr{L}_{\text{Quarks}} = \lambda_d^{ij}(\bar{u}_i,\bar{d}_i')_L \begin{pmatrix}\phi^+\\ \phi^0\end{pmatrix} d_{jR} - \lambda_u^{ij}(\bar{u}_i,\bar{d}_i')_L \begin{pmatrix}-\bar{\phi}^0\\ \phi^-\end{pmatrix} u_{jR} + h.c., \tag{2.24}$$

where $d' = \sum_{n=1}^{3} \mathrm{V}_{in} d_n$, where V_{in} is the CKM matrix[2] and d_n denotes the d, s, and b quarks fields.
In conclusion, the BEH mechanism is able to include bosons and fermions masses in the SM framework without losing the gauge invariance of the Lagrangian.

2.6 Limits of the Standard Model

The SM theory provides a good description of the interaction of the particles found so far and it does not predict any new particle. Precise experimental measurements have confirmed the predicted results and did not show any significant deviation from the SM expectation. Standard Model is able to describe the interaction of particles up to the Planck scale, the energy scale where quantum effects of gravity should start to be significant ($\sim 10^{19}$ GeV). Unfortunately, gravity is a non-renormalisable theory and it cannot be described by QFT.
Despite the success, some experimental evidences suggest that the Standard Model is not describing all observed phenomena, such as the neutrino oscillations, the presence of non-baryonic, cold dark matter and the observed abundance of matter over anti-matter in our Universe.
In the following section an overview of the main problems in the SM is given.

Grand Unification Theory

If the SM is considered to be valid only at low energies (below the Planck scale), it should be derived from a more general description of the particle interactions in a wider energy scale. In the past years theorists proposed many models where the coupling constants of the SM unify at a high energy scale. Models of this type are called *Grand Unification Theory* (GUTs).

[2]The *Cabibbo-Kobayashi-Maskawa* matrix (CKM matrix) is a unitary 3x3 matrix that describes mixing of quarks and CP violation in flavour-changing processes in the SM. The CKM matrix can be parametrised by three mixing angles and one phase.

The main problem with high-energy completion of the SM is how to include the gravitational interaction in the GUT, since gravity is non-renormalisable and cannot be easily described with a Quantum Field Theory.

Hierarchy problem

One of the main questions is why the weak scale ($\sim 10^2$ GeV) is much smaller than other relevant scales such as the Planck scale ($\sim 10^{19}$ GeV): this is the so called *hierarchy problem*.
This "problem" is closely related to the un-naturalness of the Higgs boson mass. As a feature of the QFT, in the BEH mechanism scalar particles acquire large masses through large radiative corrections. As a consequence, the Higgs boson receives huge quantum corrections to the mass from every particle which couples to its field.
The radiative corrections can be expressed as function of the Yukawa couplings (λ_f) and the fermions masses (m_f). Moreover, they are dependent on a energy cutoff (Λ) which defines the upper limit of the theory in the energy scale:

$$\Delta m_h^2 = -\frac{\lambda_f^2}{16\pi^2}(2\Lambda^2 + \mathscr{O}[m_f^2 \ln\frac{\Lambda}{m_f}]). \tag{2.25}$$

If the SM would be the only theory valid up to the Planck scale, the radiative corrections would be much bigger than the experimental Higgs boson mass. Therefore, a strong *fine-tuning* would be needed to obtain the observed value. Many Beyond Standard Model theories (BSM) address the hierarchy problem.

Neutrino oscillations

An additional problem arises from the experimental results obtained with the study of neutrino oscillations. In the SM, neutrinos are described as massless, chargeless particles which have three different flavours. Experimental observations shows that neutrinos propagating in space can be observed with a different flavour from the initial one. That indicates that neutrinos are not massless and a mixing of neutrino eigen-states, which can be explained introducing three different mass eigen-states not corresponding to the flavour eigen-states [19]. The relations between mass and flavour eigenstates for the three neutrino generations are described by the *Pontecorvo-Maki-Nakagawa-Sakata matrix* (PMNS matrix) [20] containing the oscillation probabilities between the neutrino flavours.
Unfortunately the experimental results did not allow yet to have a precise measurement of the masses, which would shed a light on a possible New Physics.

Dark Matter and Dark Energy

In 1933, Fritz Zwicky observed a discrepancy in the mass of the Coma cluster measured with two different methods: doppler shift and visible light. In the first case a mass 400 bigger was measured. It was the beginning of several experimental indications of the presence of an invisible mass called *dark matter* (DM) [21].
A first example is the measurement of the radial velocity of rotating galaxies. Vera Rubin and collaborators observed an unexpected trend in the rotational velocity of galaxies which represents a hint for additional undetectable mass.
Another example is given by the micro-lensing effect predicted by Einstein's theory of general relativity. Light rays from a luminous source are deflected by a large amount of matter between the source and the observer due to the deformation of the space-time curvature. In some cases, the effect is so strong that is not justified by the observed baryonic matter [22].

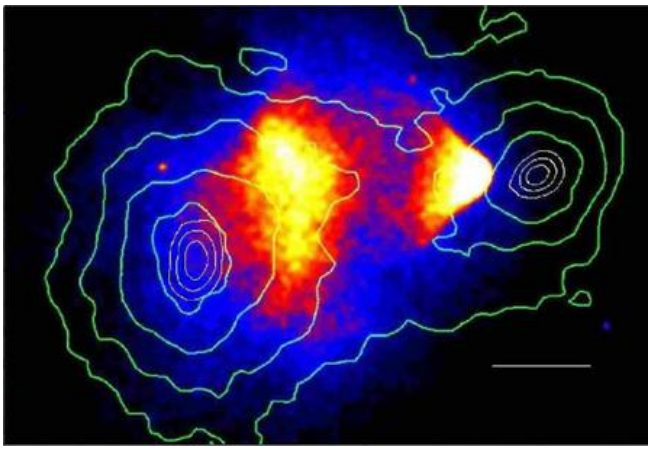

Figure 2.3: The merging cluster 1E0657-558. On the right is the smaller Bullet cluster which is passing through a larger cluster. The invisible mass distribution is indicated by the green lines [23].

Another DM evidence comes from the Bullet Cluster, where a collision between two galaxy clusters can be observed. Figure 2.3 shows the mass distribution of the underlying galaxies measured through gravitational lensing (green lines) and the X-ray emission from the hot gas (coloured) in a collision. The coloured halo is spread out because of electromagnetic effect, while the green lines passed through each other without any inelastic interactions and the only visible effect is a reduction of velocity of the stellar matter. This is a hint of dark matter particles interacting only gravitationally. From experimental results one can conclude that the mass-energy of the universe is composed of 4.9% of the known ordinary matter and 26.8% by dark matter. The remaining 68.3% is composed by *dark energy*, a form of energy which is not possible to detect with the current technology and which is responsible of the accelerating expansion of the universe [24].
After the discovery of the Higgs boson in 2012, one of the goals of the Large Hadron Collider is to find hints of New Physics which would allow to solve the problems of the SM. One of the most important theories beyond the SM which inspired many searches is the so-called *Supersymmetry*.

Chapter 3

Beyond the Standard Model

3.1 Introduction to Supersymmetry

In 1970s, several publications proposed a new theory which would solve some of the limitations of the SM such as the hierarchy problem and provide a suitable dark matter candidate: Supersymmetry (SUSY) [25, 26, 27, 28]. It is an extension of the SM which introduces a new symmetry between fermions and bosons. It has been considered a feasible Beyond Standard Model (BSM) candidate due to:

- the introduction of new supersymmetric particles that naturally solves the hierarchy problem without any "fine-tuning" of the Higgs boson mass;
- unification of the gauge coupling constants of the known interactions at high energies;
- additional particles that are possible candidates for dark matter;
- SUSY is characterised by a rich phenomenology with many different models leading to a wide range of final states, being an ideal benchmark for many analyses.

As mentioned in the previous chapter, the hierarchy problem is an important open question in the context of the SM. When introducing SUSY particles in the computation of the Higgs boson mass, their contribution is opposite to the SM particles and it reduces the radiative corrections. Since supersymmetric partners need to have different masses[1], the radiative corrections are reduced to a logarithmic divergent corrections and not a complete cancellation; which, if the mass splitting between the SM particles and their superpartners is not too huge, should be an acceptable solution to the hierarchy problem.
SUSY is an interesting theory since it also provides the unification of the gauge coupling constants. Figure 3.1 shows a schematic evolution of the inverse of the intensity of coupling constants at high energies. In the SM (left), the forces do not meet in a common point. Several SUSY models affects the effective couplings in such manner that the gauge couplings lead to a unique coupling value at high energy scale (right). The conserved quantities in the SM are a direct product of space-time symmetries (mass, momentum, spin) and internal gauge symmetries $SU_{\mathrm{C}}(3) \times SU_{\mathrm{L}}(2) \times U_{\mathrm{Y}}(1)$ (colour, weak isospin, electric charge). The SM symmetries commute with space-time symmetries, meaning that any transformation will not affect the space-time conserved quantities, such as electric charge or

[1] There was no observation of any non-SM particle in the SM mass range.

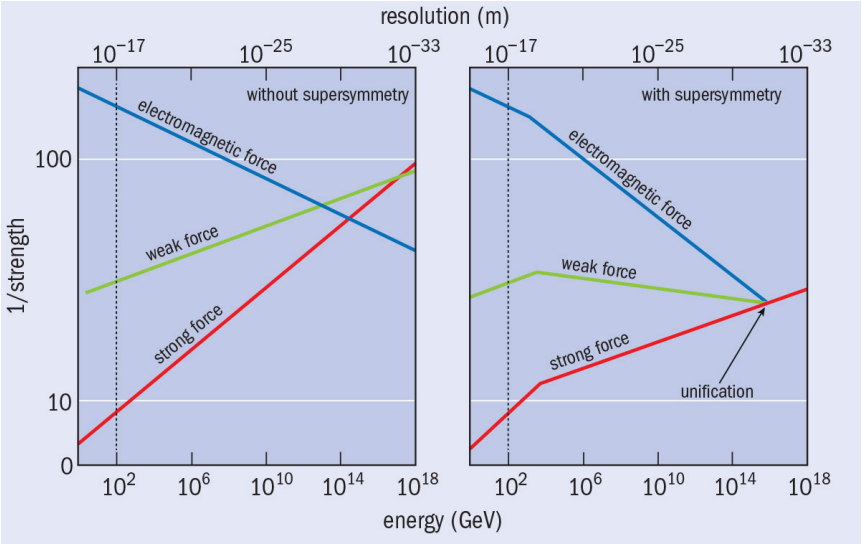

Figure 3.1: Energy dependent evolution of the inverse of the strength of the coupling of the three forces in the SM (left) and with the introduction of supersymmetry (right) [29].

the spin. Supersymmetry transformations considered in SUSY directly associate fermions and bosons, affecting the spin of the particles.

These kind of transformation would represent an exception to the Coleman and Mandula theorem [6], which states that space-time and internal symmetries need to commute with each other. Haag, Lopuszanski and Sohnius extended the possible symmetry to include anticommutating generators [30]. In this way SUSY provides a unique extension of the possible symmetries realised in nature.

In order to construct a supersymmetric extension of the SM, transformations that connect bosons and fermions are added via a super-Poincarè group. The SUSY group is represented by a fermionic operator Q and its hermitian conjugate $Q^{\dagger}$ which satisfy:

$$Q|\psi_{\text{boson}}>=|\psi_{\text{fermion}}> \quad Q^{\dagger}|\psi_{\text{fermion}}>=|\psi_{\text{boson}}>. \tag{3.1}$$

Supersymmetric particles and their SM partners are grouped in two different types of supermultiplets. The chiral multiplets contain SM fermions with their scalar superpartners (sleptons, squarks) or scalar Higgs boson with the corresponding SUSY partners with spin-1/2 (Higgsinos). In the second case, vector-supermultiplets are formed by the SM gauge bosons and their fermionic superpartners (gauginos). Due to commutation properties, the particles contained in the same supermultiplet share the same charges originated by the gauge symmetries. It follows that there always are two supersymmetric partners, a boson and a fermion, with the same quantum numbers except the spin.

3.1.1 Supersymmetry breaking

As mentioned previously, experimental observations have not shown any observation of SUSY particles in the SM particle mass range. Supersymmetry has to be a broken symmetry otherwise the supersymmetric partners would have the same masses as the SM particles and they would have been already observed.

The way to include the breaking mechanism in the SUSY framework, without losing the cancellation of the quadratic corrections to the Higgs mass, is to add a soft-breaking term to the effective Lagrangian density:

$$\mathscr{L} = \mathscr{L}_{\text{SUSY}} + \mathscr{L}_{\text{Soft}}. \tag{3.2}$$

where $\mathscr{L}_{\text{Soft}}$ includes many new terms and it allows squarks, sleptons and gauginos to acquire masses higher than SM particles. The term "soft" suggests that supersymmetry breaking is "soft" enough to avoid to introduce again quadratic divergent terms in the Higgs mass.
In fact, the corrections to the Higgs mass, with soft terms included, may be written as:

$$\Delta m_H^2 = [\frac{\lambda}{16\pi^2}\log(\frac{\Lambda}{m_{\text{Soft}}}) + ...], \tag{3.3}$$

where m_{Soft} is the largest mass scale associated to the additional Lagrangian term, while Λ is the SUSY breaking scale. In order to avoid the hierarchy problem, the mass splitting between SM particles and their superpartners should be in the order of 100 GeV - 1 TeV.

3.1.2 Minimal Supersymmetric Standard Model

The simplest supersymmetric extension of the SM is the Minimal Supersymmetric Standard Model (MSSM). It is called minimal since it predicts the smallest number of new particles and provides a natural solution for the hierarchy problem, if the masses of the predicted superpartners are in the range 100 GeV - 1 TeV. The particles are organised in supermultiplets containing SM particles and their superpartners. Moreover, the MSSM keeps the $SU_{\text{C}}(3) \times SU_{\text{L}}(2) \times U_{\text{Y}}(1)$ gauge symmetry of the SM. The chiral doublet supermultiplets are formed by the left-handed quarks (Q) and leptons (L) and the bosonic superpartners (sleptons and squarks). While the right-handed fermions form singlets: U^c and D^c for u-type and d-type antiquarks, and E^c for antileptons. The vector superfields include the SM bosons ($B^0, W^0, W^{\pm}$) and their fermionic superpartners (gluinos, winos and binos). Finally, the Higgs sector is described by 2 left-handed chiral supermultiplets:

$$H_u = \begin{pmatrix} H_u^+ \\ H_u^0 \end{pmatrix}, \quad H_d = \begin{pmatrix} H_d^0 \\ H_d^- \end{pmatrix}. \tag{3.4}$$

The two doublets are required since each of them give mass only to u-like and d-like quarks respectively.
The interaction of the superfields may be parametrized with the superpotential W:

$$W_{\text{MSSM}} = y_u U^c Q H_u - y_d D^c Q H_d - y_e E^c L H_d - \mu H_u H_d, \tag{3.5}$$

where y_u, y_d and y_e are 3×3 matrices which describe the Yukawa coupling parameters, while μ is the Higgsino mass.
The superpotential is written in order not to violate the R-parity[2], which suppresses possible lepton or baryon number violating terms not observed in nature. Terms may be added to consider a potential

[2]The R-parity is defined as $P_R = (-1)^{3B+L+2s}$ where s is the spin quantum number, B is the baryon number and L is the lepton number.

R-parity violation:

$$W_{\Delta L=1} = \frac{1}{2}\lambda^{ijk} L_i L_j L_k E_k^c + \lambda'^{ijk} L_i Q_j L_k D_k^c + \mu'^i L_i H_u, \quad i,j,k \in 1,2,3$$
$$W_{\Delta B=1} = \frac{1}{2}\lambda''^{ijk} U_i^c D_j^c D_k^c.$$

where i,j,k are the generation indices, λ, λ', μ' violate the leptonic number and λ'' the baryonic number.

If R-parity is conserved (RPC), all coefficients are set to zero. In a scenario of R-parity violation (RPV), the terms will contribute to the superpotential and lead to a scenario where all SUSY particles are unstable and decay to SM particles., thereforethe missing transverse momentum is lower compared to RPC scenarios. The analysis presented in this dissertation will also cover searches for RPV models.

As in the SM, the gauge eigenstates of SUSY multiplets do not necessary correspond to the mass eigenstates. The Higgs doublets mix to 5 different physical Higgs bosons: two charged scalars ($H^{\pm}$), two neutral scalar (h^0, H^0) and a psuedo-scalar state (A^0). The neutral gauginos (higgsinos, winos and binos) mix to form four neutralinos: $\tilde{\chi}_i^0$ with $i \in 1,2,3,4$, while the charged gauginos form the two chargino states $\tilde{\chi}_{1,2}^{\pm}$. The third generation sfermions are a mixing of left-handed and right-handed gauge eigenstates into mass eigenstates for stop and sbottom quarks ($\tilde{t}_{1,2}, \tilde{b}_{1,2}$) and tau slepton ($\tilde{\tau}_{1,2}$) and sneutrino ($\tilde{\nu}_\tau$). Table 3.1 resumes all supersymmetric particles of the MSSM.

Particles	Spin	Gauge eigenstates	Mass eigenstates
Higgs bosons	0	$H_u^0\ H_d^0\ H_u^+\ H_d^-$	$h^0\ H^0\ A^0\ H^{\pm}$
Squarks	0	$\tilde{u}_L\ \tilde{u}_R\ \tilde{d}_L\ \tilde{d}_R$	(same)
		$\tilde{s}_L\ \tilde{s}_R\ \tilde{c}_L\ \tilde{c}_R$	(same)
		$\tilde{t}_L\ \tilde{t}_R\ \tilde{b}_L\ \tilde{b}_R$	$\tilde{t}_1\ \tilde{t}_2\ \tilde{b}_1\ \tilde{b}_2$
Sleptons	0	$\tilde{e}_L\ \tilde{e}_R\ \tilde{\nu}_e$	(same)
		$\tilde{\mu}_L\ \tilde{\mu}_R\ \tilde{\nu}_\mu$	(same)
		$\tilde{\tau}_L\ \tilde{\tau}_R\ \tilde{\nu}_\tau$	$\tilde{\tau}_1\ \tilde{\tau}_2\ \tilde{\nu}_\tau$
Neutralinos	1/2	$\tilde{B}^0\ \tilde{W}^0\ \tilde{H}_u^0\ \tilde{H}_d^0$	$\tilde{\chi}_1^0\ \tilde{\chi}_2^0\ \tilde{\chi}_3^0\ \tilde{\chi}_4^0$
Charginos	1/2	$\tilde{W}^{\pm}\ \tilde{H}_u^+\ \tilde{H}_d^-$	$\tilde{\chi}_1^{\pm}\ \tilde{\chi}_2^{\pm}$
Gluinos	1/2	$\tilde{g}$	(same)
Gravitino	3/2	$\tilde{G}$	(same)

Table 3.1: Summary of the SUSY particles predicted by the MSSM.

The weak-scale R-parity conserving MSSM [31] has 120 free parameters. Most of these parameters are related to CP-violation and flavour changing neutral currents, which are constrained by experimental results. Therefore, introducing few reasonable assumptions on the flavour and CP structure, it is possible to strongly reduce the number of free parameters. A version of the MSSM with 19 free parameters can be introduced: the phenomenological MSSM (pMSSM).

The pMSSM includes all the SM parameters as well as additional free parameters such as three independent gaugino mass parameters (M_1, M_2, M_3), the ratio of the Higgs vacuum expectation values ($\tan\beta = v_2/v_1$), the higgsino mass parameter μ and the pseudoscalar Higgs boson mass m_A.

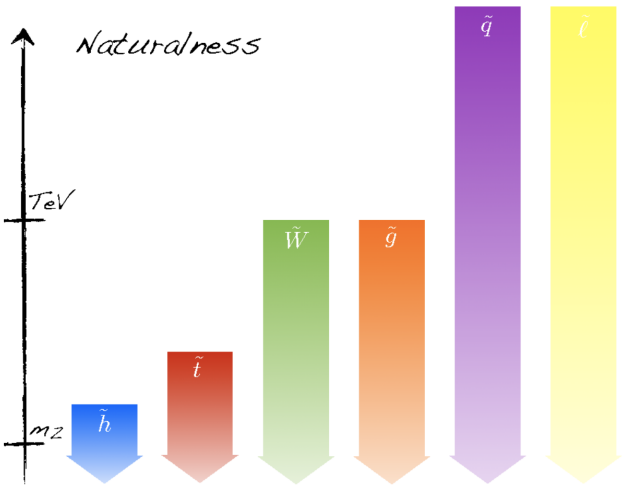

Figure 3.2: Sketch of a possible spectrum of a Natural SUSY model [32].

3.1.3 Natural SUSY spectrum

The mass spectrum of SUSY particles is expected to range from the electroweak mass scale (100-200 GeV) up to many TeV in order to not have a high level of fine-tuning to stabilise the mass scale of the electroweak symmetry breaking. In case of a high mass SUSY spectrum, a 'fine-tuning' would be needed to stabilise the Higgs mass.
The Higgs mass scale sets many constraints in SUSY scenarios. Also in the case of the MSSM, large radiative correction from top and stop quarks are needed to obtain m_H=125 GeV. This can be solved by adjusting the mixing of left-handed and right-handed mass eigenstates of the stop, subsequently the observed Higgs boson is set as h_0, the lightest neutral Higgs mass eigenstate.
Finally, the logarithmic terms from the divergent diagrams exactly cancel the top corrections if the top and both stops ($\tilde{t}_1$,$\tilde{t}_2$) are degenerate. Since it is known that SUSY particles and SM partners are not degenerate, the mass of the lightest stop is expected to be close to the top quark mass to keep a high cancellation of the radiative corrections. Due to this, the searches for direct production of top squark are considered to be crucial in the ATLAS SUSY program since the stop is expected to be the lightest squark. In Chapter 8, another important search for Natural SUSY scenarios is introduced.
A Natural SUSY model has different constraints on the SUSY particle masses. The Higgs boson mass should be related to the h_0, as mentioned above, while the sleptons and third-generation squarks should lie at the sub-TeV scale and be accessible to the LHC. Figure 3.2 shows a scheme of a Natural SUSY spectrum.

Chapter 4

LHC and the ATLAS detector

4.1 Large Hadron Collider

The Large Hadron Collider (LHC) [33] is currently the largest and most high energy proton-proton collider in the world. It is a synchrotron with a circumference of 27 km and it is located on the border between France and Switzerland. Inside the tunnel, which previously hosted the Large Electron Positron (LEP) collider, bunches of protons are accelerated and collided in the four main interaction points where the experiments (ATLAS, CMS, LHCb and ALICE) are situated. The bunches are accelerated by superconducting magnets and LHC is designed to have a centre-of-mass collision energy of $\sqrt{s} = 14$ TeV with a bunch spacing of 25 ns. Each bunch contains approximately 10^{11} protons.
The protons are accelerated by a group of pre-accelerators, before being injected in the LHC ring. In the linear accelerator LINAC2, the protons are generated and introduced in the Proton Synchrotron Booster (PSB), where they are accelerated up to 1.4 GeV. The Proton Synchroton (PS), cumulates and compress the protons to form the bunches and raise the energy to 25 GeV. The final boost, before entering the LHC ring, is given by the Super Proton Synchroton (SPS) which accelerate the bunches to 450 GeV.
Two long periods of data taking occurred up to now: 2010-2011 at 7 TeV and 2012 at 8 TeV form the Run-I, while the 2015-2018 at 13 TeV form the on-going Run-II.

4.1.1 Parameters and performances

The frequency of bunch collisions at LHC reached up to 40 MHz in Run-II. This was one of the main goals of the accelerator, in order to provide a high number of collisions. The instantaneous luminosity $\mathscr{L}$ is used to determine how many events are produced:

$$N_{\text{events}} = \sigma L_{\text{int}} = \sigma \times \int \mathscr{L} \cdot dt \tag{4.1}$$

where σ is the cross-section for the production of the studied events, L_{int} is the integrated luminosity and $\mathscr{L}$ is the instantaneous machine luminosity. The latter can be defined with a set of beam parameters:

$$\mathscr{L} = \frac{N_p^2 n_b f \gamma}{4\pi\varepsilon\beta^*} F \tag{4.2}$$

where, at the numerator, N_p is the number of particles per bunch, n_b the number of bunches in a single beam, f the beam revolution frequency and γ the relativistic γ-factor. In the denominator, ε is the

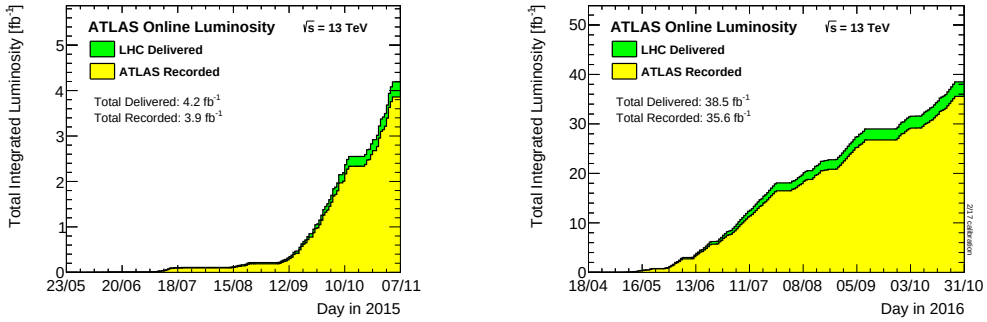

Figure 4.1: Cumulative luminosity versus time delivered to (green) and recorded by ATLAS (yellow) during stable beams for pp collisions at 13 TeV centre-of-mass energy in 2015 (left) and 2016 (right) [34].

normalized transverse beam emittance and β^* is the beta function which describes the transverse size of the particle beam at the interaction point. The numerator is related to the rate of interactions, while the denominator term is a measure of the area of the beam spot at the interaction point. The geometrical correction F takes into account the crossing angle at which the beams are colliding.
The integrated luminosity is the interesting quantity for physics analysis. In this thesis the data collected in 2015 and 2016 is considered. In Figure 4.1 the integrated luminosity delivered by LHC and recorded by the ATLAS experiment in 2015 and 2016 are shown. The luminosity peak reached in this period by LHC is $13.8\times10^{33}\text{cm}^{-2}\text{s}^{-1}$.

4.2 ATLAS detector

ATLAS (A Toroidal LHC ApparatuS) [35] is one of the four main experiments placed along the Large Hadron Collider. ATLAS played a crucial role in the discovery of the Higgs boson and in the study of its properties. In addition to high precision measurements of SM particles, it is involved in the search for hints of New Physics, such as Supersymmetry (SUSY), beyond SM models, Dark Matter and extra dimensions.
With its 46 meters of length, 25 meters of width, 25 meters of height and 7000 tons of weight, it is the largest high energy particle detector ever built.
The ATLAS detector (Figure 4.2) was initially designed to observe the Higgs boson in a large mass range and considering all the possible decay channels. The search for the Higgs boson was the reference to set the performance of the detectors which form the ATLAS experiment. Looking at the theoretical dependency of the branching ratio by the mass of the Higgs boson and at the characteristics of the final states, one can observe that the ideal and cleanest channels to study the Higgs boson are: at low masses H$\rightarrow$ZZ*, where the Z decays leptonically, and H$\rightarrow\gamma\gamma$; while at high masses the dominant are the WW and ZZ channels, where they produce leptons, jets and neutrinos in the final state. Furthermore, the expected decay width was of few MeV, consequently to observe the signal it was required a high resolution in the measurement of photons, leptons, jets and neutrinos.
To acquire a good sensitivity to the Higgs boson and New Physics, the ATLAS detector needed to fulfil a list of requirements:

- high acceptance, close to the solid angle;

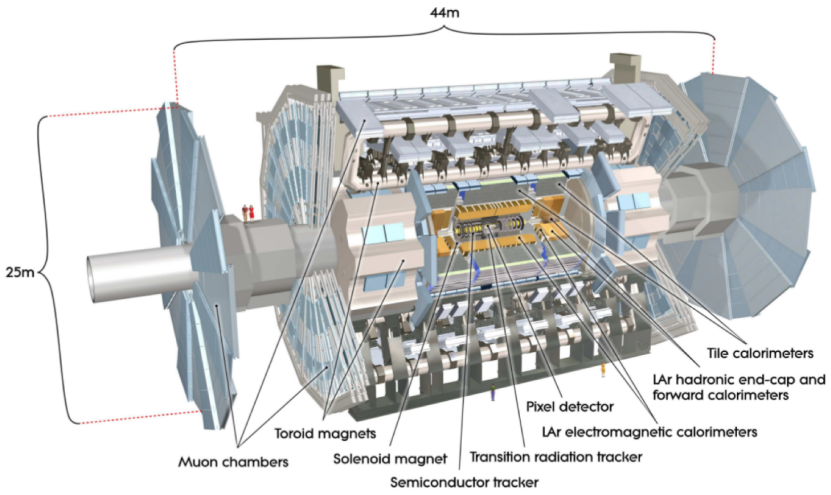

Figure 4.2: Scheme of the ATLAS detector [35].

- good momenta resolution of charged particles and good efficiency reconstruction with the inner tracker (from hundreds of MeV to few TeV);
- hermetic calorimeters to properly measure the missing transverse momentum and fine segmentation to distinguish photons, electrons and jets;
- good identification and momenta resolution of muons in a wide range of momenta, along with the capacity to determine the charge of high p_{T} muons;
- quick and efficient trigger system on low transverse momenta objects, rejecting most of the background is a crucial requirement to have an ideal rate to study events of interest;
- resistance to high flow of particles keeping high performances and avoid ageing effects.

4.2.1 Coordinate system

The experiment has a cylindrical symmetry around the axis of the beam collision. A scheme of the coordinates system and naming conventions used to describe the ATLAS detector is shown in Figure 4.3. The point of the nominal interaction of the beams defines the origin of the reference system. The z-axis is orientated along the beam lines, while the x-y plane is perpendicular to it with the positive x-semi-axis pointing towards the center of the ring, while the y-axis points upwards. The points on the x-y plane are given in polar coordinates (R, ϕ), where ϕ is the azimuthal angle and is set to 0 on the x-axis. The polar angle θ, measured with respect to the z-axis, is not a boost invariant quantity; therefore is preferable to use the rapidity, since the difference between the rapidities of two particles is invariant under the boost along the z-axis. The rapidity is defined as:

$$y = \frac{1}{2}\ln\left(\frac{E+p_z}{E-p_z}\right) \tag{4.3}$$

Since most of the particles observed in ATLAS are highly relativistic, the mass becomes negligible and the pseudorapidity can be used:

$$\eta = -\ln(\tan(\theta/2)). \tag{4.4}$$

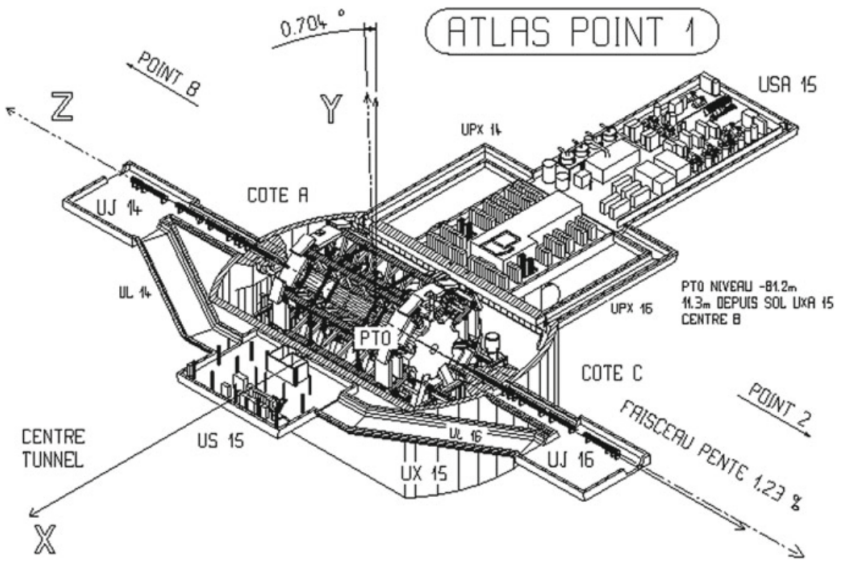

Figure 4.3: Scheme of the reference system of ATLAS [36].

Since both ϕ and η are Lorentz invariant, it is convenient to define the angular separation between two objects with

$$\Delta R = \sqrt{\Delta\eta^2 + \Delta\phi^2}. \tag{4.5}$$

On the x-y plane energy and momenta are conserved; therefore, important quantities used in the context of ATLAS analysis are the transverse momentum:

$$p_{\mathrm{T}} = \sqrt{p_x^2 + p_y^2} \tag{4.6}$$

and the transverse energy:

$$E_{\mathrm{T}} = \sqrt{E_x^2 + E_y^2}. \tag{4.7}$$

4.2.2 Magnet system

The ATLAS magnetic system [37], shown in Figure 4.4, is formed by three superconducting magnets sub-systems providing a strong magnetic field, which is crucial to measure the charged particle momenta in the TeV range.

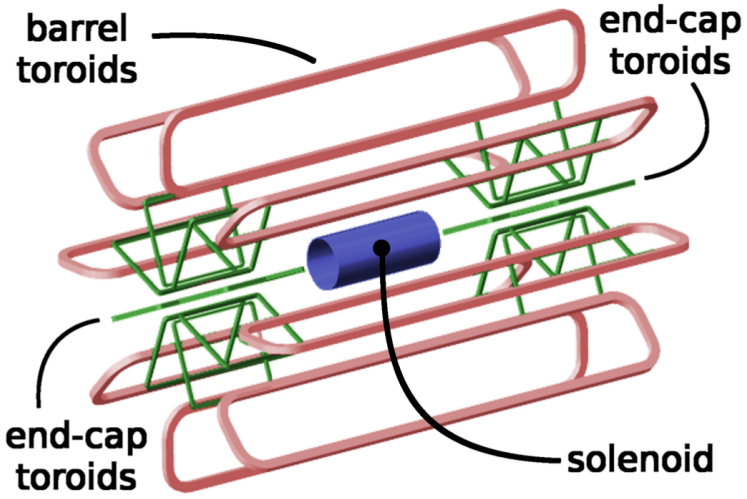

Figure 4.4: A schematic view of the ATLAS magnet systems [37].

The magnets forming the system are:

- Central Solenoid: its 2 T axial magnetic field is parallel to the beam and is exploited to reconstruct the transverse momenta of the charged particles from the primary vertex inside the inner part of the detector.
- Barrel Toroid: it is a cylindrical symmetrical toroid and it generates a 0.5 T and 1 T magnetic field for the muon detectors in the central and end-cap regions, respectively; the direction is tangential to the circumference with the z-axis as center.
- End-Caps Toroids: two toroid magnets which provide a 1.0 T field in the forward areas of the muon spectrometer.

4.2.3 Inner detector

The Inner Detector (ID) [38, 39] is the closest system to the interaction point. It is composed by silicon pixel and silicon strip SCT (Semi Conductor Tracker) detectors in the inner part and by the TRT (Transition Radiation Tracker) detector in the outer part, as shown in Figure 4.5. The system is immersed in a 2T axial magnetic field and it provides precise measurement of momentum, direction and impact parameter of charged particles. It also allows to reconstruct efficiently primary and secondary vertices. The ID is 6.2 m long and 2.1 m in diameter, and it covers a pseudorapidity range up to $|\eta| < 2.5$. By design the ID provides a combined track momentum resolution of

$$\frac{\sigma_{p_T}}{p_T} = 0.05\% p_T \oplus 1\% \tag{4.8}$$

where p_T should be expressed in GeV.

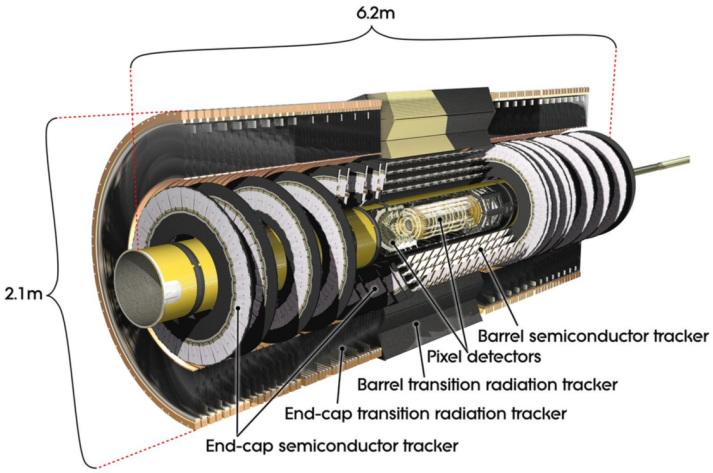

Figure 4.5: A schematic view of the ATLAS Inner Detector [40].

Pixel detector

The pixel detector is the closest sub-system to the beamline. It extends in the region with $|\eta| < 2.5$ and it consists of four cylindrical barrel layers and three forward disks layers on either end-caps. The layers are segmented in R - ϕ and z with typically three hits per track and all pixels have a minimum dimension of $50 \times 400\ \mu m^2$ (in R-$\phi \times$z). The resolution in the barrel is 10 μm (R-ϕ) and 115 μm (z), as in the end-cap. Each module has 40,080 pixel electronic channels for a total number of channels in the Pixel Detector of approximately 80.4 Millions.

During the last LHC long shutdown, the Insertable B-Layer (IBL) [41], a new tracking layer, was added at a distance of 33.3 mm adding other 12 million pixel read-out channels to the system.

Semi-Conductor Tracker

The SCT sits just outside the pixel detector and is based on silicon microstrip technology. In the barrel region, the detector has strips at small angles (40 mrad), with a group of strips axially placed with respect to the beam axis which provide a one-dimensional measurement. While in the endcap region, a group of strips is placed radially and a second one has a 40 mrad angle displacement to measure the second coordinate. The resolution in the barrel (end-caps) region is 17 μm in R-ϕ and 580 μm in R (z). The total amount of readout channels in the SCT is about 6.3 million.

Transition Radiation Tracker

The TRT is the most external detector in the inner detector and can provide up to 36 hits per track. The detector is composed of more than 300 000 4-mm diameter tubes, filled with a gaseous mixture of 70% Xe, 20% CO_2 and 10% CF_4. When the traversing particle excites the gas, the charge is collected by a thin wire of tungsten (anode), placed at the center of the tube and connected with the read-out electronics.

In the barrel (end-caps), the tubes are 144 cm (37 cm) long and parallel (radial) to the beamline. It only provides information on the coordinate R-ϕ in the barrel and z-ϕ in the end-caps with a nominal resolution of 130 μm per tube.

Another important characteristic of the TRT is the ability to distinguish electrons and charged pions. Transition radiation photons are produced in the polymer fibers (barrel) and foils (end-caps) interspersed with the tubes and then absorbed by the Xe atoms in the gas, amplifying the ionisation signal.

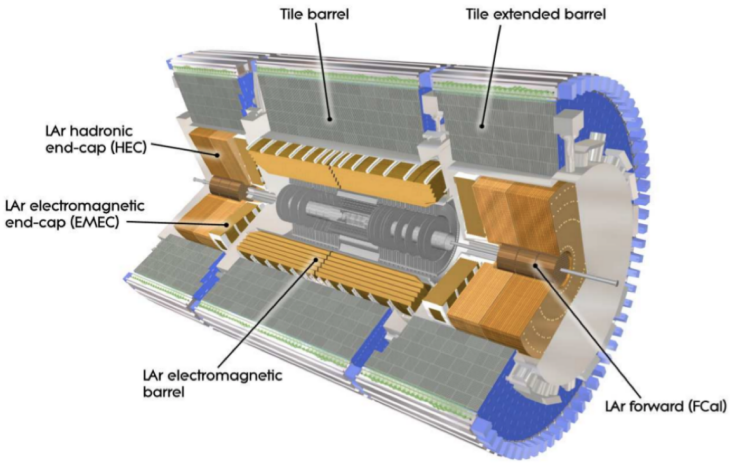

Figure 4.6: Schematic view of the ATLAS calorimeter system [35].

In the case of an electron the average number of photons produced is much higher than for charged pions, which allows to discriminate between the different type of particles.
The ID system provides tracking information which can be combined with the precision measurements from the electromagnetic calorimeter, in order to identify the electrons, and from the muon spectrometer, in order to measure more precisely the muon momenta.

4.2.4 Calorimeter system

The calorimeter system (Figure 4.6) is sub-divided into two parts. The inner part is the electromagnetic calorimeter (ECal) [42]; the outer part is the hadronic calorimeter (HCal). Both ECal and HCal are sampling calorimeters, consisting of alternating layers of absorbing material, to reduce the energy of the incident particle, and active medium to detect the signal.
The calorimeters are designed to contain electromagnetic showers up to a few TeV and absorb most of the energy of a typical hadronic shower. In the EM calorimeter the total thickness is expressed in radiation length (X_0)[1], while the Had calorimeter is expressed in interaction lengths (λ[2]). Additionally the calorimeters can limit the contamination of jets ('punch-through') which could deposit part of their energy in the muon calorimeter.

Electromagnetic calorimeter
The EM calorimeter is a liquid argon (LAr) sampling calorimeter, with lead plates as absorbers. It is formed by the barrel calorimeter (EMB), covering the region with $|\eta| < 1.475$, and two end-caps (EMEC), coaxially placed in the forward areas, where the internal one covers $1.375 < |\eta| < 2.5$ and the outer $2.5 < |\eta| < 3.2$. An additional calorimeter is placed in the inner position to the beamline ($|\eta| < 1.8$). At the transition region of the barrel and end-cap components, there exists a region of degraded performances called 'crack region' ($1.37 < |\eta| < 1.52$). Many analysis involving photons and electrons exclude this region to maintain a high quality of identification and measurement.

[1] radiation length (X_0): corresponds to the mean distance over which an electron loses 1/e of its energy via bremstrahlung.
[2] analogue of X_0 for hadronically interacting particles and $\lambda = \frac{a}{N_A \sigma_{tot}}$ where a is the atomic weight of the material crossed, N_A the Avogadro's number and σ_{tot} the total cross section.

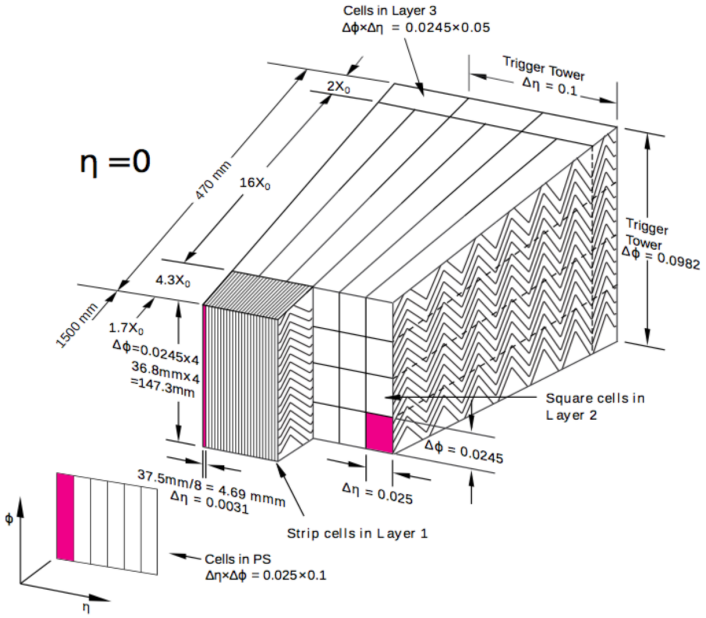

Figure 4.7: Structure of the EM calorimeter in the barrel [35].

Figure 4.7 shows a section of the EM calorimeter. The electrodes are built with an accordion geometry to ensure that particles pass through both the active and passive material. This design also allows to avoid the presence of dead-zones and a signal extraction at either end of the electrode, which means optimal tightness and which reduces electronic dead-time. The calorimeter is divided into three layers with decreasing granularity and it allows to distinguish prompt photons from $\pi^0 \to \gamma\gamma$ and electrons from charged pions.
EMB and EMEC share the same geometry, in the end-caps everything is rotated into the radial direction along with the accordion geometry.
The energy resolution of this calorimeter is:

$$\frac{\Delta E}{E} = \frac{10\%}{\sqrt{E/\mathrm{GeV}}} \oplus 0.3\%$$
$$\sigma_\eta = \frac{40}{\sqrt{E/\mathrm{GeV}}}$$

Hadronic calorimeter

The hadronic calorimeter (HCal) measures the energy and direction of the hadronic jets produced by the hadronization of quarks and gluons. It is placed outside the EM, as the hadronic showers are typically wider and longer than electromagnetic ones.

The system is composed by three parts:
Tile calorimeter: a sampling calorimeter [43] composed of steel as the absorber material and scintillating plates as the active medium. It is placed right after the EM and it covers $|\eta| < 1.0$ in the barrel and two additional extensions in $0.8 < |\eta| < 1.7$.
Hadronic LAr end-caps Calorimeter (HEC): It is formed by two independent wheels per end-cap. These are placed outside the EMEC and share the same cryostat system. HEC is a sampling calorimeter using LAr as active material and copper plates as absorbers, due to the higher radiation in the forward region. The coverage overlaps slightly with the Tile Calorimeter ($1.5 < |\eta| < 3.2$).
LAr forward calorimeter (FCal): It is integrated in the cryostats of the end-caps to have a more homogenous coverage of the calorimeter and to reduce the background in the muon spectrometer. The FCal covers the forward region of $3.1 < |\eta| < 4.9$, is 10 X_0 thick and is formed by three modules per end-cap. The inner is a Cu/LAr calorimeter, optimised for electromagnetic showers, while the other two are hadronic W/LAr calorimeters. A passive layer of brass is added at the end to absorb the remaining hadron shower.

4.2.5 Muon spectrometer

The muon spectrometer [44] constitutes the outer part of the ATLAS detector. It was designed to detect charged particles coming out of the calorimeters in the barrel and end-caps region, and to measure their momenta up to $|\eta| < 2.7$ with a resolution better than 10% for 1 TeV tracks. Moreover, trigger chambers are present in $|\eta| < 2.4$.
The momentum is calculated with the sagitta measurement, with a resolution of:

$$\frac{\Delta p}{p} = \frac{8}{0.3BL^2}\Delta s, \tag{4.9}$$

where B[T] is the magnetic field intensity, L[m] is the distance between the first and last hit in the spectrometer and Δs is the sagitta. This formula is valid only for constant B-field, which is not the case in the muon spectrometer.
Figure 4.8 shows a schematic view of the muon spectrometer. The precision chambers are placed inside the eight coils of the toroidal magnet in the barrel as well as on the two sides of the toroidal magnets in the end-caps. The structure of the system is composed by eight octants, reflecting the symmetry in ϕ of the toroids. Each octant is subdivided in two sectors in the azimuthal direction: the large sector and the small sector. Several lateral extensions cause an overlap which minimises the holes in ϕ of the coverage of the detector.
In the barrel, the chambers are arranged in three cylindrical shells around the beam axis, often called 'stations', with a radius of 5m, 7.5m and 10m. The end-caps form three wheels perpendicular to the beam axis and 7.4m (Small Wheel), 14m and are 21.5m (Big Wheel) away from the interaction point (along the z-axis). Figure 4.9 shows the transversal and longitudinal projection of the system.
The momenta measurement is performed by Monitored Drift Tube (MDT) chambers ($|\eta| < 2.7$) which have a high momenta resolution and are easy to construct. In the forward region ($2 < |\eta| < 2.7$), Cathode Strip Chambers (CSC) are used to complete the inner part of the tracker due to the low dead-time and good time resolution.
Since the muon spectrometer needs to act also as trigger for muons, a system of trigger chambers is integrated in between the precision chambers. The trigger chambers need to store information on the tracks, few nanoseconds after the muon has traversed the detector. For this purpose Resistive Plate

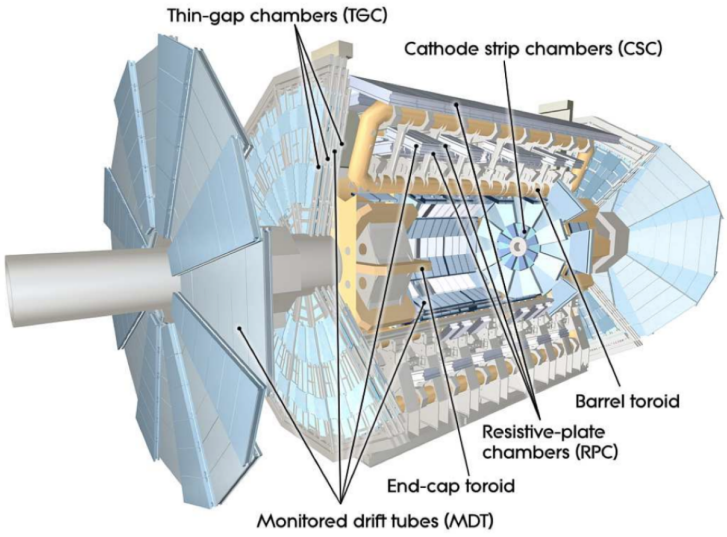

Figure 4.8: Overview of the different components of the muon system in ATLAS [35].

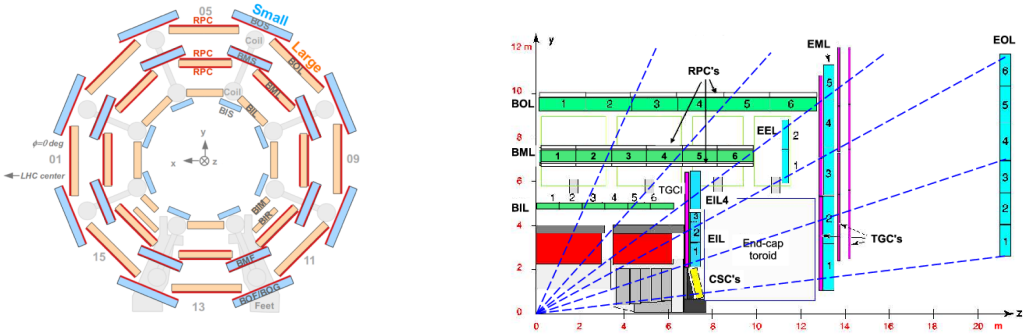

Figure 4.9: Scheme of the transversal (left) and longitudinal projection of the muon spectrometer [45].

Chambers (RPC) are placed in the barrel region ($|\eta| < 1.05$) and Thin Gap Chambers (TGC) in the end-caps ($1.05 < |\eta| < 2.4$). These chambers also measure coordinates of the tracks: one in the direction of the curvature of the track (η) and the other in the transverse plane of the curvature (ϕ).
The aim of the precision chambers is to measure the η coordinate, which is useful for the momenta extrapolation. In addition, the combination of the hits on the MDTs and of the trigger chambers provides the ϕ coordinates of the tracks. This method assumes that for each MDT-trigger chamber pair only one track per event is detected, since two or more η and ϕ tracks cannot be combined univocally. If this happens (rarely), the ambiguity is solved combining the tracks of the muon candidate with the information from the ID. Muon reconstruction efficiency is well above 95% in almost all p_{T} and η region.

Monitored drift-tube Chambers (MDTs)

MDTs are aluminum tubes with a 30 mm diameter and a 400 μm thickness, filled with a gas mixture of 93% Ar - 7% CO_2 which provides an excellent resistance against ageing. When a muon crosses the tubes, it ionises the gas and the electron avalanches are collected by a tungsten wire placed in the center of the tube. Each chamber is formed by two multi-layers of drift tubes, separated by aluminium spacer bars. Each of them consists of three (middle and outer) or four (inner) layers of tubes. The resolution achieved by a single tube is about 80 μm, while the total chamber resolution is about 35 μm.

Cathode strip chambers (CSCs)
In the forward region, the rate of particle is higher (> 150 Hz/cm^2) and MDTs performance strongly decreases, such that Cathode Strip Chambers are used. These are multiwire proportional chambers with multiple anodes wires in a mixture gas of 80% Ar and 20% CO_2. They are characterised by a fast response time and high spatial resolution. The orthogonal layout allows to measure the charge distribution in both radial and ϕ coordinate with a resolution of 40 μm and 5 mm respectively.

Resistive Plate Chambers (RPCs)
RPCs are used mainly as trigger chambers, but also provide a measure of the second coordinate in the barrel. The chambers are filled with a gas mixture of $C_2H_2F_4$ and a small fraction of resistive component SF_6 contained in two resistive parallel plates of bakelite, kept at a 2mm distance. Similarly to the MDTs, the muon ionises the gas and the signal is amplified by the electric field of about 4.5 kV/mm between the plates. The signal is then readout by metallic reading strips.
The two detector layers which form the chamber are placed orthogonally to read both the η and ϕ coordinates. Two layers of chambers (middle station) provide the trigger for low-p_T muons, while a third one (outer station) is used for high p_T trigger thresholds.

Thin Gap Chambers (TGCs)
As mentioned above, the end-cap region suffers from a higher particle rate. TGCs are multi-wire proportional chambers, filled with a mixture of CO_2 and n-pentane (n-C_5H_{12}), and have a similar structure as the CSCs but a higher granularity. They are used as trigger chambers for muon tracks and, in addition to the MDTs, they provide a second measurement of the azimuthal coordinate. Both TGC and RPC chambers are designed to provide a signal over a time shorter than 25 ns. This allows to identify the bunch crossing responsible for firing the trigger with an efficiency higher than 99%.

4.2.6 Trigger system

When the LHC is running at the designed performances, 40 million bunch crossings per second are expected inside the ATLAS detector. Considering the average number of collisions expected in one bunch crossing ($\sim$20), the total rate of events expected is 1 GHz. Clearly it is difficult and inefficient to store such a large amount of data, also due to the fact that many of these are soft physics events which are not of high interest for most analyses. To reduce this rate, the ATLAS detector is equipped with a two-level trigger system [46] based on hardware and software information. Figure 4.10 shows a scheme of the ATLAS trigger system.
The first level (L1) is hardware-based; it exploits the MS and calorimeter information to take a decision within 2.5 μs and reduce the rate down to 100 kHz. The second level (HLT) is software-based; it consists of fast algorithms accessing to data from a region of interest within the event that may contain objects such as leptons or jets. The final rate of data is reduced to 1 kHz.

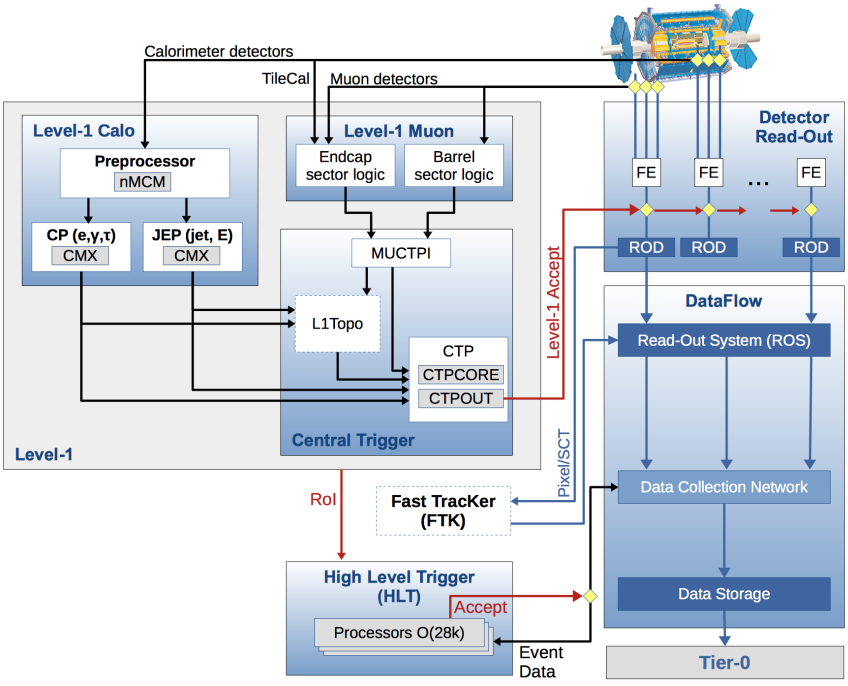

Figure 4.10: Schematic view of the ATLAS trigger system [47].

4.3 Phenomenology of pp collisions

The description and simulation of the proton-proton collisions at the LHC is of crucial importance to predict expected events detected by the ATLAS experiment, which allows to design the analyses and compare data and theoretical calculations.

The nature of strong coupling α_S allows to do perturbative calculations only at high energy scales (hard processes), but proton-proton collisions are composed by a hard scattering process and lots of soft (underlying) processes. The *factorisation theorem* [48] states that the hard part and soft part of the collision can be factorised: the hard process is calculated with perturbative calculations, while the soft processes are measured experimentally (for example parton distribution functions) and cannot be calculated from first principles. In the following section, the parton distribution functions, event simulation with Monte Carlo generators and detector simulation are introduced.

4.3.1 Parton distribution functions

The measurement of the parton distribution function (PDF) is essential to describe the proton-proton interactions with high precision.

Protons are composed of valence quarks (two up quarks and one down quark), gluons and the so-called sea quarks (quark-antiquark pairs generated by vacuum fluctuations). All the components of the colliding protons (partons) are involved in the interaction, therefore it is very challenging to describe it properly. The PDF is defined as the probability density function to find, at a specific energy scale, a parton with a defined momentum fraction inside a hadron. The dynamics of the hadronic substructure can be completely described by the PDF, not depending on the type of underlying scattering process, as stated in the *factorisation theorem*.

The parton densities cannot be calculated perturbatively, but they can be measured at fixed energy

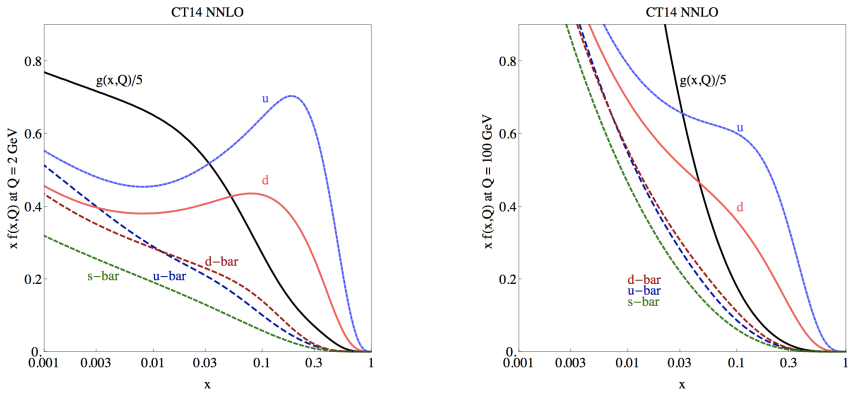

Figure 4.11: Parton distribution functions (PDFs) as a function of the momentum fraction for gluons and different quark flavours. The CT14 PDFs are calculated at NNLO for Q = 2 GeV (left) and Q = 100 GeV (right) [51].

scale, typically with deep inelastic $e^{\pm}p$ scattering experiments or at the LHC. The dependency of the PDF from the energy scale is then extrapolated with the *Dokshitzer-Gribov-Lipatov-Altarelli-Parisi equation* (DGLAP equation) [48, 49, 50].
Figure 6.12 shows two examples of PDFs for gluons and quarks at different energy scales Q (2 GeV and 100 GeV). Many collaborations perform these important measurements and provide PDF sets: CT, MSTW, NNPDF and LHAPDF [51, 52, 53, 54].
The PDFs are used for cross-section calculations and simulation of SM and BSM processes.

4.3.2 Event simulation and Monte Carlo generators

The simulation of signal and background processes for particle physics analyses is crucial for the development of the analysis strategy and prediction of the experimental results. These simulations are done with the so-called Monte Carlo (MC) event generators.
The proton-proton interactions are complex processes that MC are able to simulate, up to a certain order in perturbative QCD, from the hard scattering to the final stable particles observed in a detector. The simulation goes through several steps explained in the following section and outlined in Figure 4.12: parton shower evolution, hadronisation and interaction with the detector.
After all steps mentioned above, the simulated pp collision events are undergoing full detector simulation as discussed in 4.3.3.

Hard scattering process

The cross-section of the hard scattering processes can be calculated perturbatively as a series of expansion in powers of α_S. The leading order (LO) computation gives a qualitative prediction, but it does not describe all data well. The next-to-leading order (NLO) calculation, which includes diagrams with one extra power of α_S, also accounts for extra radiation and provides a prediction of the normalisation and shape of the kinematic distributions.

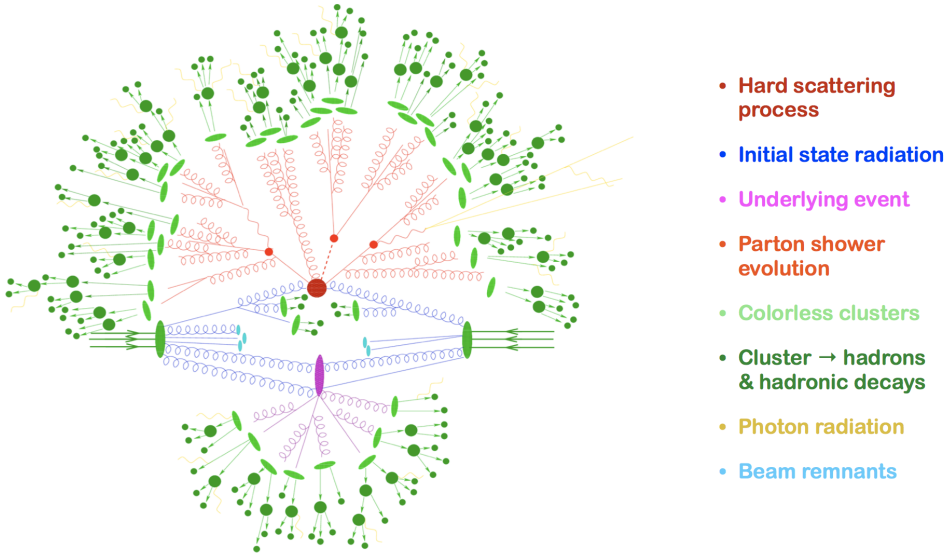

Figure 4.12: Scheme of a hadron-hadron collision as simulated by a Monte Carlo event generator: hard collision (red circle), Bremsstrahlung as simulated by parton showers (light red), secondary hard scattering event (purple), parton-to-hadron transitions (light green ovals), hadron decays (dark green) and soft photon radiation (yellow). [55].

Parton shower and hadronisation

The partons involved in the hard scattering induce a cascades of radiation called parton shower (PS). There are two types of parton showers: electromagnetic showers and hadron showers.

The first ones are generated by charged particles which can radiate photons that subsequently may decay in lepton-antilepton pairs. The second ones are formed by quarks and gluons producing quark-antiquark pairs or additional gluons. The hadronic shower shape has a more complicated structure due to gluon self-interaction and low-energy gluons inside the shower.

The PS algorithm proceeds with a backward evolution, starting from the hard scatter and then simulating the evolution down to lower momentum scales corresponding to earlier points in the cascade. The algorithm stops when the factorisation scale is reached and the resolution of the perturbative calculation is too low. The splitting of partons are estimated with a parton splitting probability function (i.e. quark emitting gluon) and can also include the radiation emitted by an incoming parton (so-called initial state radiation).

Three hadronisation process consists of colourless hadrons formed from quarks and gluons.

Three different types of algorithms are used, such as SHERPA, HERWIG (*cluster hadronisation* method [56]) and PYTHIA (*Lund string* model [57]) [58, 59, 60]. The results obtained with the different algorithms can be used to estimate theoretical uncertainties on the parton shower and hadronisation model.

Unstable particle decays

Finally, the decay of the unstable hadron particles is simulated. The lifetime and branching ratio decay of the considered particles are estimated from the matrix element of the processes, later adjusted with experimental results. These values are documented in the PDG [5]. Except for SHERPA samples, EVTGEN [61] is used to simulate the unstable hadron decays.

Underlying event

In hadron-hadron scattering, the underlying event (UE) is defined as all the hadronic activity in the collision, except the hard scattering part and its ISR and FSR emissions [62]. The contribution to UE

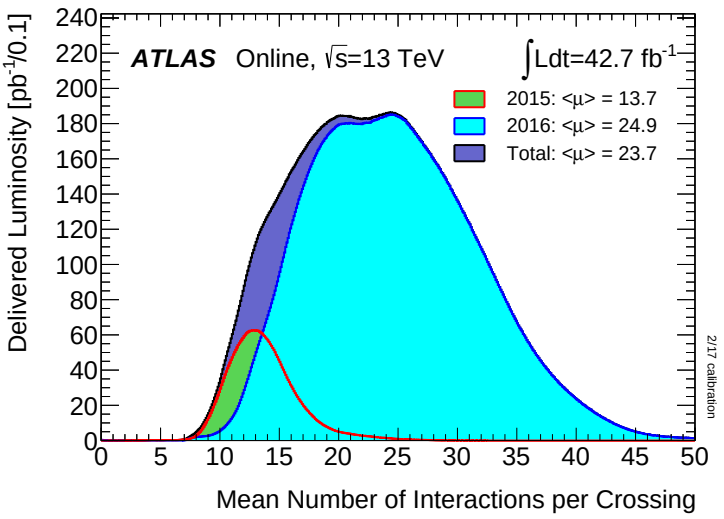

Figure 4.13: Distribution of the average number of pp interactions per bunch-crossing for the combined 13 TeV data from 2015 and 2016 [34].

comes from multiple parton interaction (MPI) between the partons, or from beam-beam remnants, which are left-overs of initial hadrons after the parton hard scattering.
These events populate mainly the forward region, but occasionally an additional energetic jet can be produced. Since non-perturbative QCD processes in the UE cannot be calculated, many generators tune the simulation parameters with collected pp data.

Pile-up

Another significant effect is the multiple interaction of particles in the same bunch-crossing, *in-time pile-up*, or from previous or subsequent bunch-crossings, *out-of-time pile-up*.
The amount of pile-up depends strongly on the instantaneous luminosity and is usually characterised via the number of reconstructed primary vertices N_{PV} (for in-time interactions) and the average number of interactions per bunch-crossing $< \mu >$. Figure 4.13 shows the average number of pp interactions per bunch-crossing for the data collected in 2015 and 2016.

The pile-up effect is simulated and added to the hard scattering process in the MC generation. The MC samples are further reweighted such that the pile-up profile in the simulation matches the one in data.

4.3.3 Detector simulation

The simulation of the interaction of the particle level objects with the detector is done with the GEANT4 framework [63], which includes a full reconstruction of the detector geometry and of the response of the tracking and calorimetry system. It takes into account also possible inactivity of read-out modules and changes of the detector and of the trigger. The ATLAS collaboration developed a similar framework which is able to simulate the detector with significantly lower computational time. It is called ATLASFASTII framework [64] and fully simulates the inner detector and muon spectrometer with GEANT4, while the calorimeter response is parametrised for different type of particles.
All the SUSY signal samples used in the analyses discussed in this dissertation are simulated with ATLASFASTII, while the SM background samples are simulated by GEANT4.

Chapter 5

Physics Objects

The following chapter describes the techniques used in ATLAS experiment to reconstruct and identify final state particles like electrons, muons and jets. Isolation requirements are applied to separate the signal particles from the background. Significant systematic uncertainties on particle reconstruction, identification and isolation are explained. Only the physics objects relevant for the same-sign and three leptons (SS3L) analysis are considered; therefore, photons and hadronically decaying taus are not taken into account.

5.1 Electrons

Reconstruction

A combination of calorimeter signals (clusters) in the EM calorimeter and the tracks in the ID ($|\eta| < 2.47$) is used to reconstruct the electron candidate. In the Run-II analyses, the track associated with the electron is required to be compatible with the primary interaction vertex of the hard collision. This requirement helps reduce the background from photon conversions and secondary particles.

The cuts applied to the *signal* on the track parameters are: $|d_0|/\sigma_{d_0} < 5$ and $|\Delta z_0 \sin\theta| < 0.5$ mm, where the impact parameter d_0 is the distance of closest approach of the track to the measured beam-line, z_0 is the distance along the beam-line between the point where d_0 is measured and the beam-spot position, and θ is the polar angle of the track.

The transition region between the barrel part of the electromagnetic calorimeter and the EM end-caps, called *crack region*, in the range $1.37 < |\eta| < 1.52$ is characterised by a 5-10% drop in the efficiency reconstruction and is excluded in some analyses.

Identification

Electron identification is crucial to discriminate prompt electrons from hadronic jets or converted photons. It is based on an algorithm which uses electron cluster information and track related quantities. In Run-II, the IBL provides the number of hits in the innermost pixel layer to help discriminating electrons from converted photons.

The baseline ID algorithm used for Run-II data analyses is a likelihood-based (LH) method. It is a multivariate analysis (MVA) technique which uses signal and background probability density functions (PDFs) of the discriminating variables to make decisions on the candidate electrons. Three different operating points are provided: *Loose*, *Medium* and *Tight*. They are ordered according to the increasing background rejection power.

The variables used by the different working points are the same; only the selection differs.

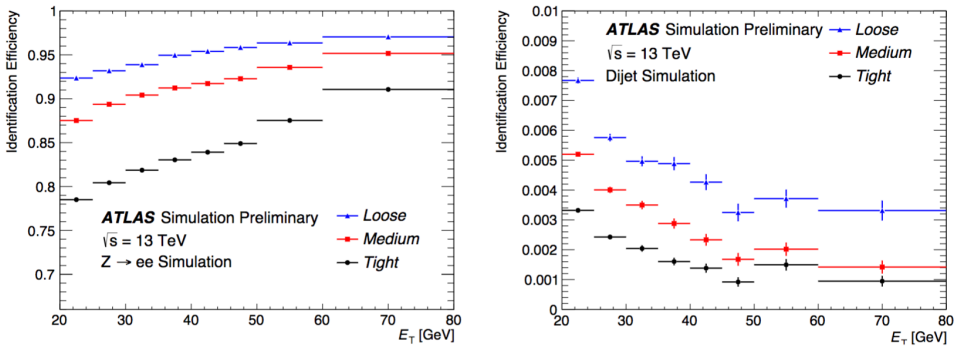

Figure 5.1: The identification efficiency of electrons from Z→ee decays (left) and of hadrons as electrons (background rejection, right) estimated using simulated dijet samples. The efficiencies are obtained using Monte Carlo simulation, and are measured with respect to reconstructed electrons [65].

The distribution of the variables used in the algorithm depend on the quantity of material with which the candidate electron interacts. Moreover, higher energetic electrons are expected to deposit more in the outer layers of the EM calorimeter or in the Hadronic calorimeter. Therefore, the ID operating points are binned and optimised in $|\eta|$ and E_{T}.
Figure 5.1 shows the efficiency to identify electrons and hadrons as electrons in Monte Carlo simulations. The efficiencies of the electron identification increase (decrease) for signal (background) from 78% (0.8%) to 90% (0.3%) with increasing E_{T}.
At higher E_{T} values (above 125 GeV), the shower shape is varying. The inner layer of the EM calorimeter collects smaller fractions of energy, while more is collected in the outer layers and in the hadronic calorimeter. The efficiencies of *Loose* and *Medium* are not affected, while the *Tight* isolation point is inefficient at high E_{T}. To avoid this effect, for electron candidates with E_{T} above 125 GeV, rectangular cuts on shower width w_{stot}[1] and E/p are added to the *Medium* selection.

Isolation

Analyses with leptons in the final state are typically affected by non-prompt electrons originated from heavy flavour decays and photon conversion or misidentified light hadrons. The isolation requirement increases the discrimination between signal and background electrons. The isolation requirements are applied on variables quantifying the energy of particles produced around the electron candidate. Two discriminating variables have been designed:

- $E_{\mathrm{T}}^{\mathrm{cone0.2}}$: it is a *calorimeter* isolation, defined as the sum of transverse energies of topological clusters [66] within a cone of $\Delta R = 0.2$ built around the candidate electron cluster. The sum is based only on clusters with positive reconstructed energy and the E_{T} of the electron candidate is subtracted. A correction is applied to take into account the effects of pile-up and underlying events.

- $p_{\mathrm{T}}^{\mathrm{cone0.2}}$: it is a *track* isolation, defined as the sum of transverse momenta of all tracks within a cone of $\Delta R = \min(0.2, 10\ \mathrm{GeV}/E_{\mathrm{T}})$ around the candidate electron track, apart from the electron candidate track itself. The tracks must be associated with reconstructed primary vertex of the hard collision and satisfy track quality requirements.

[1] Lateral shower width, $\sqrt{(\Sigma E_i \eta_i^2)/(\Sigma E_i) - ((\Sigma E_i \eta_i)/(\Sigma E_i))^2}$, where E_i is the energy and η_i is the pseudorapidity of the cell i. The sum is calculated within a window of 3 x 5 cells.

Different sets of cuts on the quantities $E_{\mathrm{T}}^{\mathrm{cone0.2}}/E_{\mathrm{T}}$ and $p_{\mathrm{T}}^{\mathrm{cone0.2}}/E_{\mathrm{T}}$ define the isolation working points used in the physics analysis. The operating points are divided into two classes:

- Efficiency targeted operating points: the requirements on quantities are set in order to obtain a defined isolation efficiency ε_{iso}, which may be either constant or a function of E_{T}. These operating points are shown in Table 5.1.
- Fixed requirement operating points: the upper cuts on the quantities are fixed and have been optimised for H$\rightarrow 4\ell$ and multilepton supersymmetry searches. These operating points are usually preferred in physics analyses with *soft* (low E_{T}) electrons which require a high background rejection. They are shown in Table 5.2.

	Efficiency		
Operating point	calorimeter isolation	track isolation	total efficiency
LooseTrackOnly	-	99%	99%
Loose	99%	99%	∼98%
Tight	96%	99%	∼95%
Gradient	$0.1143\% \times E_{\mathrm{T}} + 92.14\%$	$0.1143\% \times E_{\mathrm{T}} + 92.14\%$	90/99% at 25/60 GeV
GradientLoose	$0.057\% \times E_{\mathrm{T}} + 95.57\%$	$0.057\% \times E_{\mathrm{T}} + 95.57\%$	95/99% at 25/60 GeV

Table 5.1: The table illustrates the efficiency targeted operating points. The numbers expressed as a percentage represent the target efficiencies used in the operating point optimisation procedure. For the Gradient and GradientLoose operating points, E_{T} is in GeV [67].

	Cut value	
Operating point	calorimeter isolation	track isolation
FixedCutLoose	0.20	0.15
FixedCutTightTrackOnly	-	0.06
FixedCutTight	0.06	0.06

Table 5.2: The table illustrates the fixed requirement operating points. Calorimeter and track isolation values refer to the selection based on $E_{\mathrm{T}}^{\mathrm{cone0.2}}/E_{\mathrm{T}}$ and $p_{\mathrm{T}}^{\mathrm{cone0.2}}/E_{\mathrm{T}}$ [67].

5.2 Muons

Muons are reconstructed using information collected by the Muon Spectrometer, the ID and the calorimeters.

Reconstruction

Muon candidates are initially reconstructed separately in the MS and in the ID. Subsequently the information is combined to form the tracks used in the physics analysis. The method used for the ID reconstruction is described in [68, 69].

In the MS case, the track segments are reconstructed in the MDT chambers with a straight-line fit of the hits in the layers. The coordinates in the plane orthogonal to the bending plane are given by the RPC or TGC chambers.

The tracks reconstructed in the different layers are combined with a segment-seeded algorithm. The middle layer segments are used as seeds due to the higher number of trigger hits available. The search

is then extended to the inner and outer layers.
The reconstructed muon track candidate must have at least two matching segments, except for the barrel-endcap transition regions where one segment with $|\eta|$ and ϕ is sufficient.
Since the same segment can be shared by several tracks, an Overlap Removal procedure assigns the segment to one or two tracks. This ensures a high efficiency for close-by muons events.
After reconstructing the tracks in the ID and the MS, the information is combined with different methods. In ATLAS, four different types of combined reconstruction are used:

- Combined (CB) muon: the tracks are reconstructed independently in the ID and in the MS, after which a global fit is applied to reconstruct the combined track. Most muon track candidates follow an outside-in pattern recognition; the muon is first reconstructed in the MS and then extrapolated and matched to the ID. The inside-out pattern is used as complementary.
- Segment-tagged (ST) muons: the track reconstructed in the ID is extended to the MS. At least one local track in the MDT or CSC chambers must match the extrapolation. This method is typically used for low p_{T} muons or in the region where the MS acceptance is lower.
- Calorimeter-tagged (CT) muon: the ID track is extrapolated to the calorimeter and matched with an energy deposit compatible with a minimum ionising particle. The purity is lower compared with CB and ST methods, but the CT reconstruction increases the acceptance in the partially instrumented MS region ($|\eta| < 0.1$). The CT criterion is optimised for the aforementioned pseudorapidity region and for $15 < p_{\mathrm{T}} < 100$ GeV muons.
- Extrapolated (ME) muons: the acceptance in the $2.5 < |\eta| < 2.7$ region, where ID coverage is missing, is extended by considering only MS tracks with a loose requirement on the compatibility on the extrapolation to the IP.

The ID track can be shared by different reconstructed candidate. When the overlap removal procedure is applied, the CB muons are picked first, followed by the ST muons and then CT muons. The overlap removal on ME muons is done by comparing the fit quality and the number of hits in the layers.

Identification
The aim of the identification selection is to reject the pion and kaon decays and to select the prompt muons with high efficiency and high momentum resolution.
A study on simulated $t\bar{t}$ events has been carried out to select the optimal variable to discriminate signal and background. The muons originated from a W boson are considered as signal, while the muons arising from light-hadron decays are considered as background.

For CB tracks, three parameters are used:

- q/p *significance*: absolute value of the difference between the ratio of the charge and momentum of the muons measured in the ID and MS divided by the sum in quadrature of the corresponding uncertainties;
- ρ': absolute value of the difference between the transverse momentum measurements in the ID and MS divided by the p_{T} of the combined track;
- normalised χ^2 of the combined track fit.

In order to ensure a solid momentum measurement, requirements are applied to the number of hits in the ID and in the MS.
The identification selection is divided into four inclusive categories: *Loose*, *Medium*, *Tight* and *High* p_{T} [69].

- *Medium*: the default ATLAS identification selection. It minimises the systematic uncertainties on reconstruction and calibration. The light hadrons are suppressed by requiring a loose compatibility between the p_{T} measured in the ID and in the MS. Only CB and ME muons are considered.
- *Loose*: all kind of reconstructed muons are used, however CB and ST muons are restricted to $|\eta| < 0.1$ region. This looser selection is designed to maximise the reconstruction efficiency.
- *Tight*: purity is strongly increased, counterbalanced by a significant loss in efficiency. This selection is useful to maximise the fake muon rejection. Only CB muons are considered.
- *High* p_{T} muons: only takes into account CB muons passing the *Medium* selection. An extra reqeuirement of at least three hits in the MS stations gives a high momentum resolution for tracks with transverse momentum above 100 GeV.

Both *Medium* and *Tight* muons are used in the analyses presented in this dissertation.
Figure 5.2 shows the reconstruction efficiency as a function of η for different muon identification selections. The efficiency is measured from $Z \to \mu\mu$ events.
The efficiency for *Medium* muons is constantly above 99% for $p_{\mathrm{T}} > 6$ GeV, as shown in Figure 5.3.
The efficiency is measured using Z$\to \mu\mu$ and $J/\psi \to \mu\mu$ events in the $0.1 < |\eta| < 2.5$ region.
The muons selected for the analysis described in this thesis have a $p_{\mathrm{T}} > 10$ GeV.

Isolation

The muons originating from the decay of W, Z and Higgs bosons are typically isolated from other particles. In many SUSY analyses it is crucial to look for isolated muons, coming from the signal decay chain. A good rejection between the signal muons and the non-isolated one (originating from semi-leptonic decays from hadrons) can be obtained measuring the detector activity around the candidate.

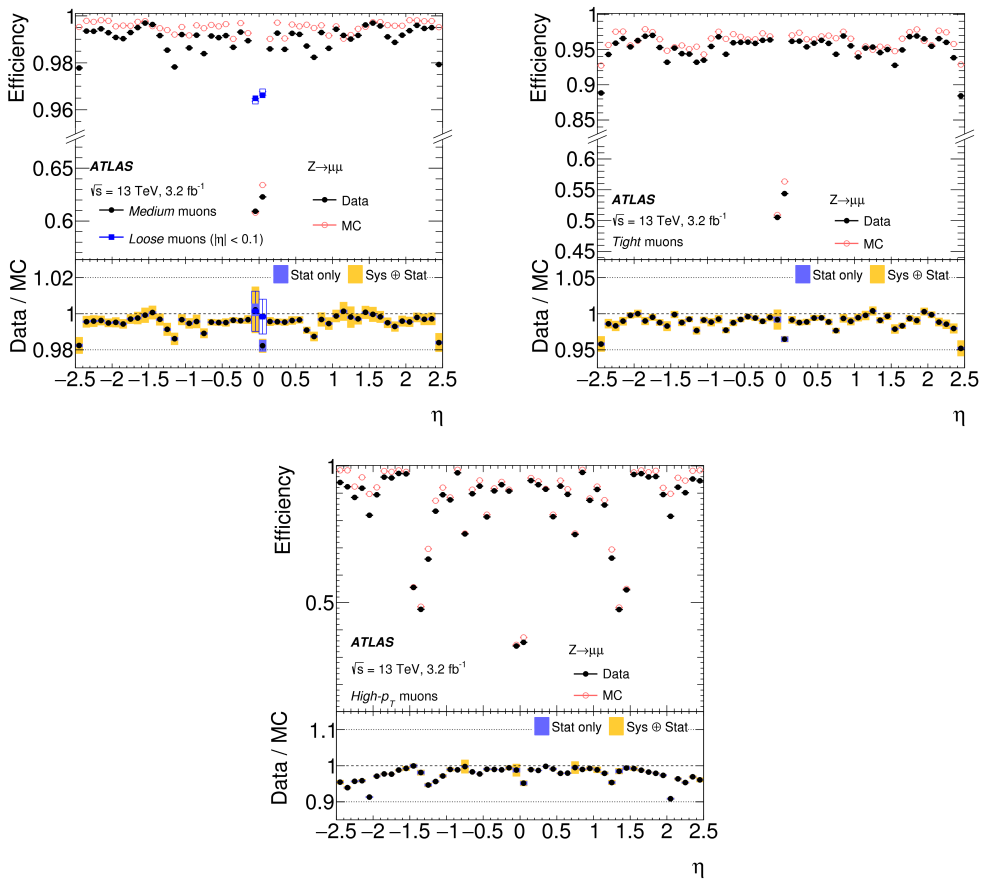

Figure 5.2: Muon reconstruction efficiency as a function of η measured in $Z \to \mu\mu$ events for muons with $p_{\mathrm{T}} > 10$ GeV shown for Medium (top left), Tight (top right), and High-p_{T} (bottom) muon selections. In addition, the top left plot also shows the efficiency of the Loose selection (squares) in the region $|\eta| < 0.1$ where the Loose and Medium selections differ significantly. The error bars on efficiencies indicate the statistical uncertainty. The panels at the bottom show the ratio of the measured to predicted efficiencies, with statistical and systematic uncertainties [69].

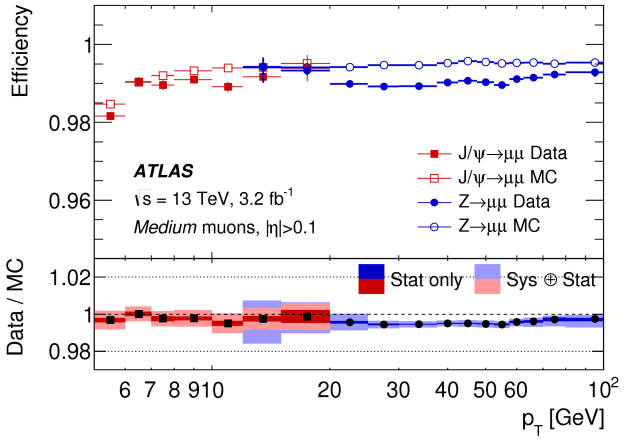

Figure 5.3: Reconstruction efficiency for the Medium muon selection as a function of the p_{T} of the muon, in the region $0.1 < |\eta| < 2.5$ as obtained with Z$\to \mu\mu$ and $J/\psi \to \mu\mu$ events. The error bars on the efficiencies indicate the statistical uncertainty. The panel at the bottom shows the ratio of the measured to predicted efficiencies, with statistical and systematic uncertainties [69].

As it was the case for electrons, track-based and calorimeter-based variables are used:

- $p_{\mathrm{T}}^{\mathrm{varcone30}}$: scalar sum of the transverse momenta of the tracks with $p_{\mathrm{T}} > 1$ GeV in a cone of size $\Delta R = \min(10\ \mathrm{GeV}/p_{\mathrm{T}}^{\mu}, 0.3)$ around the muon of transverse momentum p_{T}^{μ} excluding the muon track itself;
- $E_{\mathrm{T}}^{\mathrm{topcone20}}$: sum of the transverse energy of topological clusters in a cone of size $\Delta R = 0.2$ around the muon, after subtracting the contribution from the energy deposit of the muon itself and correcting for pile-up effects.

Isolation WP	Discriminating variable(s)	Definition
LooseTrackOnly	$p_{\mathrm{T}}^{\mathrm{varcone30}}/p_{\mathrm{T}}^{\mu}$	99% efficiency costant in η and p_{T}
Loose	$p_{\mathrm{T}}^{\mathrm{varcone30}}/p_{\mathrm{T}}^{\mu}$,$E_{\mathrm{T}}^{\mathrm{topcone20}}/p_{\mathrm{T}}^{\mu}$	99% efficiency costant in η and p_{T}
Tight	$p_{\mathrm{T}}^{\mathrm{varcone30}}/p_{\mathrm{T}}^{\mu}$,$E_{\mathrm{T}}^{\mathrm{topcone20}}/p_{\mathrm{T}}^{\mu}$	96% efficiency costant in η and p_{T}
Gradient	$p_{\mathrm{T}}^{\mathrm{varcone30}}/p_{\mathrm{T}}^{\mu}$,$E_{\mathrm{T}}^{\mathrm{topcone20}}/p_{\mathrm{T}}^{\mu}$	90(99)% efficiency at 25(60) GeV
GradientLoose	$p_{\mathrm{T}}^{\mathrm{varcone30}}/p_{\mathrm{T}}^{\mu}$,$E_{\mathrm{T}}^{\mathrm{topcone20}}/p_{\mathrm{T}}^{\mu}$	95(99)% efficiency at 25(60) GeV
FixedCutTightTrackOnly	$p_{\mathrm{T}}^{\mathrm{varcone30}}/p_{\mathrm{T}}^{\mu}$	$p_{\mathrm{T}}^{\mathrm{varcone30}}/p_{\mathrm{T}}^{\mu}$<0.06
FixedCutLoose	$p_{\mathrm{T}}^{\mathrm{varcone30}}/p_{\mathrm{T}}^{\mu}$,$E_{\mathrm{T}}^{\mathrm{topcone20}}/p_{\mathrm{T}}^{\mu}$	$p_{\mathrm{T}}^{\mathrm{varcone30}}/p_{\mathrm{T}}^{\mu}$<0.15, $E_{\mathrm{T}}^{\mathrm{topcone20}}/p_{\mathrm{T}}^{\mu}$<0.30

Table 5.3: Definition of the seven isolation working points. The discriminating variables are listed in the second column and the criteria used in the definition are reported in the third column [69].

These variables are divided by the transverse momentum of the muon and used to define seven different working points.
The isolation selections, shown in Table 5.3, are optimised for different physics analyses.
The analysis described in this thesis proposed the *FixedCutTightTrackOnly* selection criterion.
Figure 5.4 shows the isolation efficiency measured for *Medium* muons in data and simulation as a function of the muon p_{T} for the *LooseTrackOnly*, *Loose*, *GradientLoose*, and *FixedCutLoose* working points.

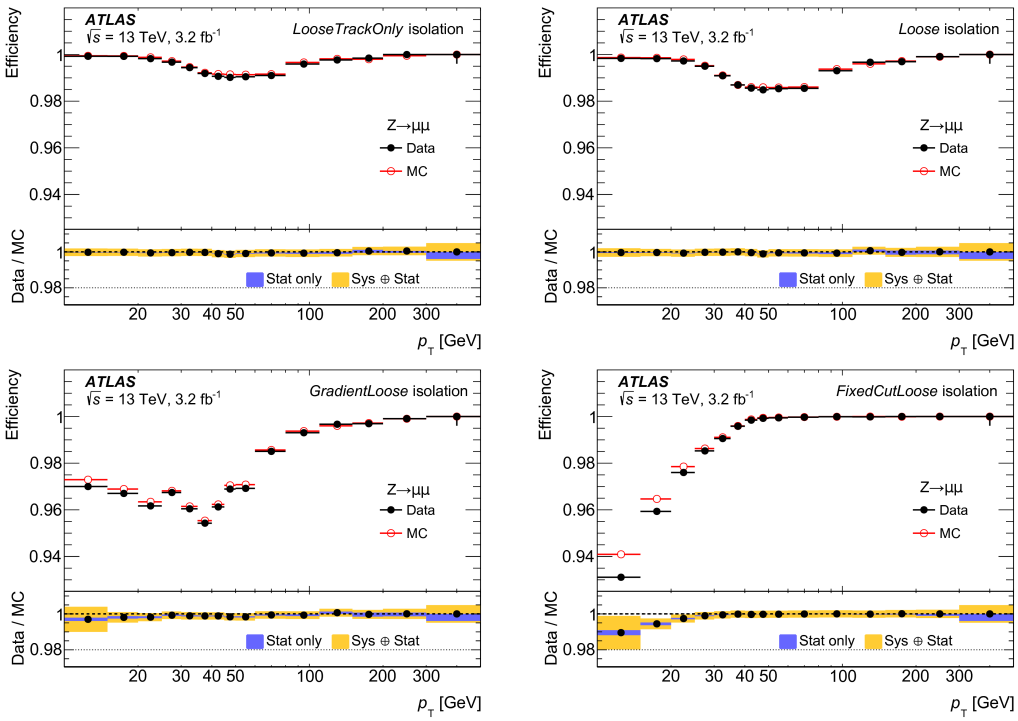

Figure 5.4: Isolation efficiency for the *LooseTrackOnly* (top left), *Loose* (top right), *GradientLoose* (bottom left), and *FixedCutLoose* (bottom right) muon isolation working points. The efficiency is shown as a function of the muon transverse momentum p_{T} and is measured in $Z \to \mu\mu$ events. The full (empty) markers indicate the efficiency measured in data (MC) samples. The errors shown on the efficiency are statistical only. The bottom panel shows the ratio of the efficiency measured in data and simulation, as well as the statistical uncertainties and combination of statistical and systematic uncertainties [69].

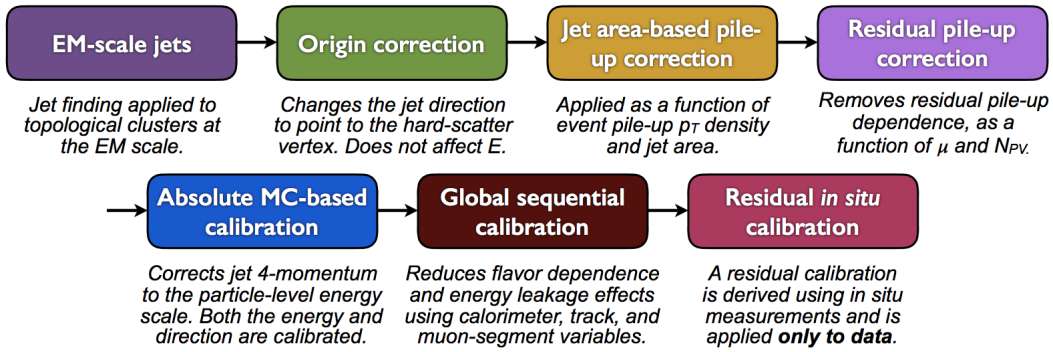

Figure 5.5: Overview of the jet calibration scheme [71].

5.3 Jets

Jets consist of particle bundles that originate from gluons and quarks and which deposit energy in the electromagnetic and hadronic calorimeters. In the ATLAS detector, they typically deposit most of the energy in the hadronic calorimeter and are characterised by a high multiplicity of tracks in the ID.
Many methods of jets reconstruction have been developed, and it is essential to choose one which is infrared and collinear safe. One method which fulfills these requirements is the anti-k_T algorithm [70]. In the SS3L analysis, it is used with an input distance parameter of R = 0.4 and three-dimensional topological energy clusters are used as inputs for the jet algorithm. Moreover, applying the anti-k_T algorithm results in jets with rather small circular area, thus less sensitive to pileup events.
Jets are calibrated to truth-particle level using a factorised and sequential scheme as shown in Figure 5.5.
The first step is the origin correction that corrects the calorimeter jet direction pointing back to the primary vertex position rather than to the nominal centre of the detector.
The second step consists of adding an offset to the pileup correction to remove the effect of additional energy from pileup particles inside the jet and to make the jet response independent of the number of primary vertices in the event. The correction is performed event-by-event pileup to reduce pileup fluctuations.
Then a multiplicative jet energy scale correction is derived from MC events to restore the jet response to that of truth-particle jets in QCD dijet events.
Subsequently, a Global Sequential Calibration(GSC) is applied with additional JES corrections using tracking and jet shape information to reduce the flavour dependence of the response and improve the jet energy resolution.
The last step is a residual in-situ correction that is only applied to jets in data and is computed as the ratio of MC to data jet energy response. It brings the energy response of jets in data and MC to agreement, reducing the jet energy scale systematic uncertainty.
The ratio between the jet's reconstructed energy and truth energy ($E_{\text{reco}}/E_{\text{truth}}$[2]) is the jet response distribution. It is of interest because the presence of dead material in the detector, the reconstruction inefficiency, and the structure of the sampling calorimeter cause a loss of energy associated with the jet shower. As it follows, the momentum of the reconstructed jet is lower than in the original process.
The Jet Energy Scale (JES) takes care of the calibration of the mean value of the jet response distribution. The method is composed of several steps described in detail in [72] and it provides a correction in bins of p_T and η. The width of the jet response, which quantifies the residual spread, is known as

[2] E_{truth} is the energy at particle level, without any contamination from pile-up.

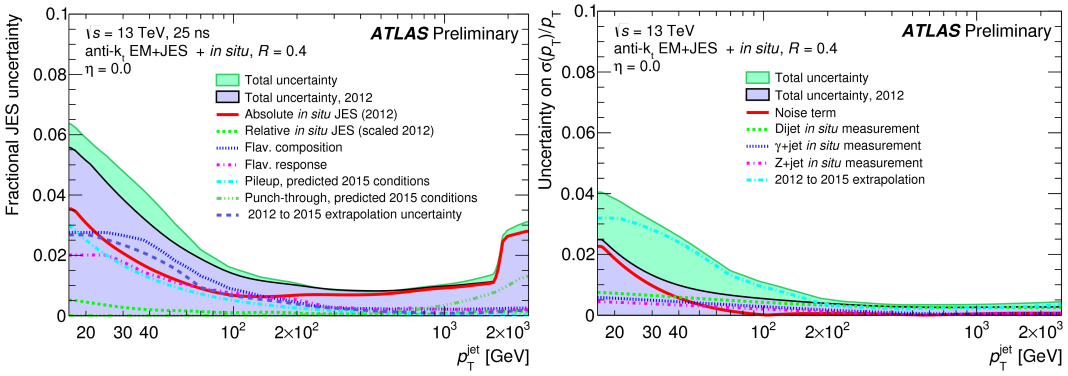

Figure 5.6: Left: final jet energy scale uncertainties estimated for 2015 data as a function of jet p_{T} for jets of $\eta = 0$. Right: final jet energy resolution uncertainties estimated for 2015 data with 25 ns bunch spacing as a function of jet p_{T} for jets of $\eta = 0$ [72].

Jet Energy Resolution (JER). The deviation in jet response may be caused by the stochastic nature of the hadronic shower, by detector noise or by improper detector simulation.
Figure 5.6 shows the JES and JER uncertainties estimated for 2015 data, which play an important role in the SS3L analysis.
Many extra jets are produced by pileup effects. In order to reduce this contribution, a Jet Vertex Tagging technique is used [73]. This technique uses a multivariate combination of two variables:

- Jet Vertex Fraction (JVF): sum of the scalar transverse momenta of the tracks which are associated with the jet and originate from the hard-scatter vertex, divided by the scalar sum of the p_{T} of all the tracks;
- $R_{p_{\mathrm{T}}}$: scalar sum of the p_{T} of the tracks that are associated with a jet and originate from the hard-scatter vertex divided by the fully calibrated jet p_{T}.

The jets originating from pileup are expected to have low values of JVF and $R_{p_{\mathrm{T}}}$, while the jets coming from hard scattering process tend to have higher values. In the SS3L analysis, a cut of JVT> 0.59 is applied to all jets with $20 < p_{\mathrm{T}} < 60$ GeV and $|\eta| < 2.4$.
Figure 5.7 (left) shows the jet selection efficiency as a function of the jet p_{T} for this standard selection. The JVT method is also stable against the increase of pileup.
Figure 5.7 (right) shows that the average number of jets with $p_{\mathrm{T}} > 20$ GeV does not change with the increase of average interactions per bunch crossing, when applying the JVT cut.

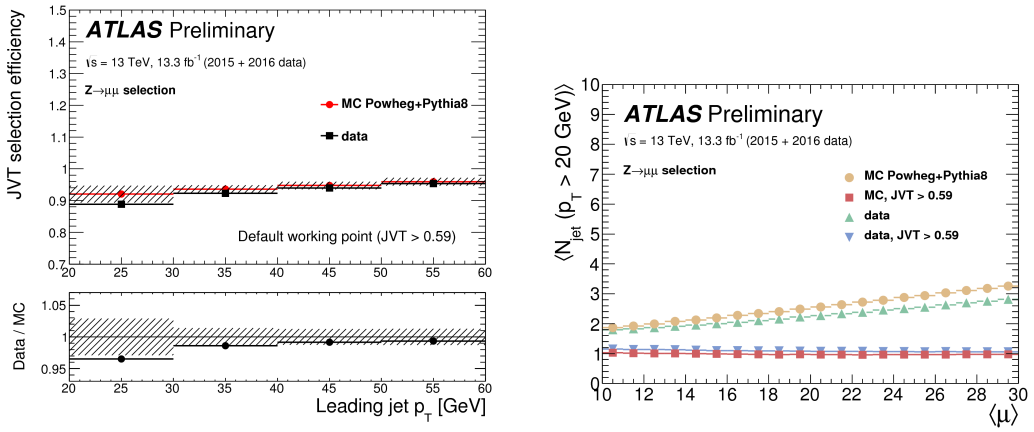

Figure 5.7: Left: The hard-scatter jet selection efficiency, in POWHEG+PYTHIA8 MC and in 2015+2016 data, of a JVT > 0.59 cut on a jet balanced against a Z boson decaying to muons. Right: The uncertainties shown are the statistical uncertainty summed in quadrature with the systematic uncertainty, evaluated varying the residual contamination from pileup jets by 20%. The average number of jets with $p_{\mathrm{T}} > 20$ GeV in POWHEG+PYTHIA8 MC and in 2015+2016 data before and after a cut of JVT > 0.59 [74].

The b-tagging technique:

As it will be explained in the description of the analysis, different b-jet multiplicities in the final state are expected for the different considered signal models. Therefore, the identification of jets containing b-hadrons is useful to define sensitive signal regions.

The b-hadrons are characterised by a longer life time ($c\tau \sim 450\ \mu$m) than other jets and they therefore decay at a longer distance (3-5 mm) away from the primary vertex compared to other type of particles. As shown in Figure 5.8 (left), a secondary vertex can be reconstructed and used to identify the b-jet. To further improve the b-jet identification, many variables are combined using a Boosted Decision Tree (BDT), called MV2 in the following [75].

The technique uses track impact parameters, reconstructed secondary vertices and multi-vertex reconstruction algorithm as discriminant variables. The algorithm has been optimised using different amounts of c-jets in the training of the BDT: MV2c00 (0%), MV2c10 (10%) and MV2c20 (20%).

The performances of these algorithms are shown in Figure 5.8 (right) as the c-jet rejection as a function of the b-jet efficiency. For a given b-jet efficiency, the MV2c20 performs the best: it has consequently been used in the SS3L analysis.

5.4 Missing transverse momentum

As discussed in Section 3.1, the typical decay chain of a SUSY process where the R-parity is conserved (RPC) features the LSP particle in the final state. Since it does not interact with the detector material, it can only be identified as missing momentum in the transverse plane.

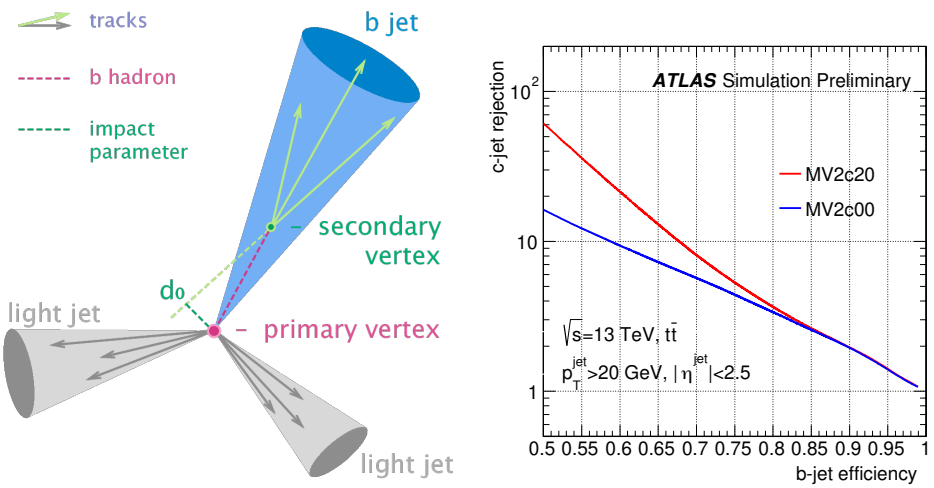

Figure 5.8: Left: Illustration showing the principle of b-jet identification. Right: The c-jet rejection versus b-jet efficiency for the MV2c20 (red) and MV2c00 (blue) b-tagging algorithms in $t\bar{t}$ events [75].

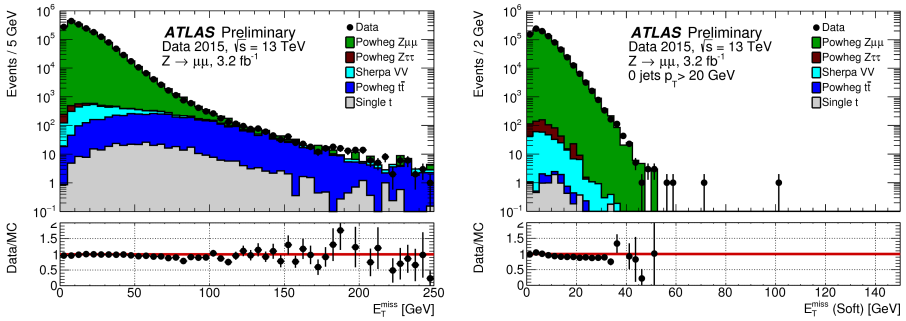

Figure 5.9: Left: $E_{\mathrm{T}}^{\mathrm{miss}}$ distribution for a Z decay to a pair of muons. The expectation from MC simulation is superimposed after each MC sample is weighted with its corresponding cross-section. Jets are selected requiring $p_{\mathrm{T}} > 20$ GeV. For central jets with $p_{\mathrm{T}} < 50$ GeV and $|\eta| < 2.4$, the Jet Vertex Tagger value is required to be greater than 0.64 [76].

The missing transverse momentum is defined as the negative vector sum of the transverse momenta of the visible reconstructed physics objects in the event, where the magnitude is:

$$E_{\mathrm{T}}^{\mathrm{miss}} = -\sum_{\text{visible}} p_{\mathrm{T}} = \sqrt{(E_x^{\mathrm{miss}})^2 + (E_y^{\mathrm{miss}})^2},$$
$$\phi^{\mathrm{miss}} = \arctan(E_y^{\mathrm{miss}}/E_x^{\mathrm{miss}})$$

where all the energies associated to electrons, muons, photons, jets and taus are considered. An extra term, called soft term, takes into account all the tracks (Track Soft Term) or calorimeter clusters (Calorimeter Soft Term) not associated with any specific physics object. Since the TST term is more robust to pile-up variations, it is used in the SS3L analysis.

The capacity of reconstructing correctly the $E_{\mathrm{T}}^{\mathrm{miss}}$ depends on the characteristics of the studied event. It is possible to distinguish between processes with and without genuine $E_{\mathrm{T}}^{\mathrm{miss}}$.

In the first case, $W \to e\nu$ and $W \to \mu\nu$ with additional jets are used to study the reconstruction performance, while $Z \to ee$ and $Z \to \mu\mu$ are well suited to provide events with zero true $E_{\mathrm{T}}^{\mathrm{miss}}$ [76]. Figure 5.9 shows the good agreement between data and MC for $E_{\mathrm{T}}^{\mathrm{miss}}$ and the track-based soft term (TST) for events with Z decaying into a muon pair.

Chapter 6

Strong SUSY production

Searches for different SUSY production modes were performed in the scope of this thesis. In the following chapter, the focus lies on the strong production mode. The author of this thesis contributed to the analysis in the statistical interpretation. The same search has been performed by the author with a smaller dataset (13.2 fb^{-1}) [77], the following analysis is an improvement of the previously obtained results.

6.1 Analysis strategy

A typical SUSY search analysis has a well defined structure. The initial goal is to define a region of the phase space, called Signal Region (SR), where the targeted signal model is enhanced, while at the same time the contribution from SM process should be small. A final state with either two leptons having the same electric-charge or at least three leptons meets these criteria.
The target of the search are SUSY particles produced via strong interaction: gluinos ($\tilde{g}$) and squarks ($\tilde{q}$). In a decay chain of SUSY particles, leptons can be produced. Since gluinos and squarks are Majorana fermions, the lepton can be equally produced with a positive or negative electric charge. While two leptons with opposite electric charges often originate from SM processes, a final state with leptons with same electric charge (SS) is rare.
For the same reason, final states with three or more leptons are considered: electroweak production of W and Z bosons has a low cross-section and the small branching ratio of leptonic decay reduces even more the chance to produce multi-lepton final states.
Considering a soft third lepton allows also to include SUSY signal models with a longer decay chain and to explore the so-called *compressed scenarios* (where the mass difference between SUSY particles is small).
For these reasons a search for supersymmetric particles in final state with either two same-sign leptons or three leptons (in the following abbreviated with SS3L) is sensitive to a wide range of RPC (R-Parity Conserving) and RPV (R-Parity Violating) models.
The background sources for this analysis can be divided into irreducible and reducible.
The irreducible background is composed of SM processes with exactly the same final state as the considered signal models. Either the production of a top-anti-top pair ($t\bar{t}$) in association with a vector boson (W,Z) or the production of diboson and triboson (VV and VVV with $V = W,Z$) processes are the main SM background processes; depending on the lepton and b-jet multiplicity requirements of the signal regions.
The reducible background comes mainly from $t\bar{t}$ pair production. When the decay is fully leptonic

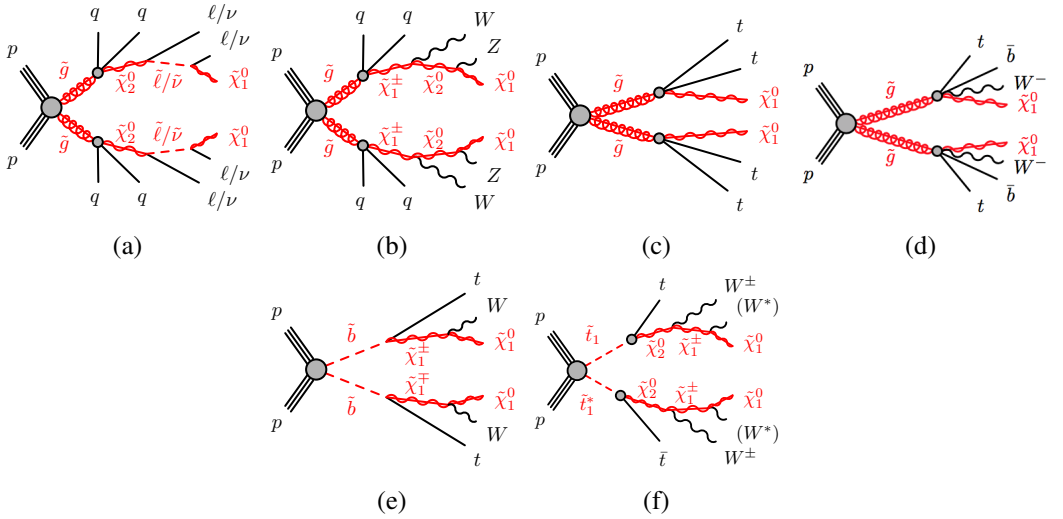

Figure 6.1: RPC SUSY processes featuring gluino ((a), (b), (c), (d)) or third-generation squark ((e), (f)) pair production studied in this analysis. In Figure 6.1a, $\tilde{\ell} \equiv \tilde{e}, \tilde{\mu}, \tilde{\tau}$ and $\tilde{\nu} \equiv \tilde{\nu}_e, \tilde{\nu}_\mu, \tilde{\nu}_\tau$. In Figure 6.1f, the W^* labels indicate largely off-shell W bosons, as the mass difference between $\tilde{\chi}_1^0$ and $\tilde{\chi}_1^\pm$ is around 1 GeV.

$(t\bar{t} \to (b\ell^+\bar{\nu})(\bar{b}\ell^-\nu))$, one of the two lepton charges can be mis-measured and contribute to the SS signal region, while in a semi-leptonic decay $((t\bar{t} \to (b\ell^+\bar{\nu})(\bar{b}q\bar{q}^{'}))$, the hadronic decay may be mis-identified as a lepton.

The fake/non-prompt lepton background is dominant in some of the considered signal regions and its estimation is crucial for the presented analysis. The techniques used to estimate the background contribution in the signal regions are based on Monte Carlo simulations and data-driven methods. The background is then estimated in dedicated region called Validation Region (VR). Finally the agreement with data is evaluated in the defined signal regions.

If data exceeds the background expectation, the excess is evaluated with statistical methods to check if the background-only hypothesis is rejected; and the data disagreement may be described with a new signal model. If this is not the case, both model-dependent and model-independent limits are set.

6.1.1 Targeted signal models

As mentioned above, the SS3L analysis is designed to be sensitive to a wide range of SUSY scenarios involving decays of heavy superpartners like massive gauge bosons, sleptons or stop quarks. Since SUSY is a complex theory with more than 100 free parameters, models with only one production process and a given decay chain (branching ratio of 100%), so called "simplified models", are assumed. The targeted signal models are used as a benchmark to optimise the signal regions defined for the analysis. Moreover, keeping a orthogonality with other SUSY searches is important.

The different kinematic characteristics of the targeted models, such as jet and b-jet multiplicity, are used to define the ideal set of signal regions. Six RPC SUSY scenarios are considered: gluino ($\tilde{g}$), bottom squark ($\tilde{b}$) and top squark ($\tilde{t}$) pair production with $\tilde{\chi}_1^0$ as lightest and stable super-partner (Figure 6.1).

In addition, eight RPV SUSY scenarios are considered with gluino ($\tilde{g}$) and down squark ($\tilde{d}$) pair production (Figure 6.2). Since the R-Parity is violated, $\tilde{\chi}_1^0$ and the SUSY particles decay to SM particles

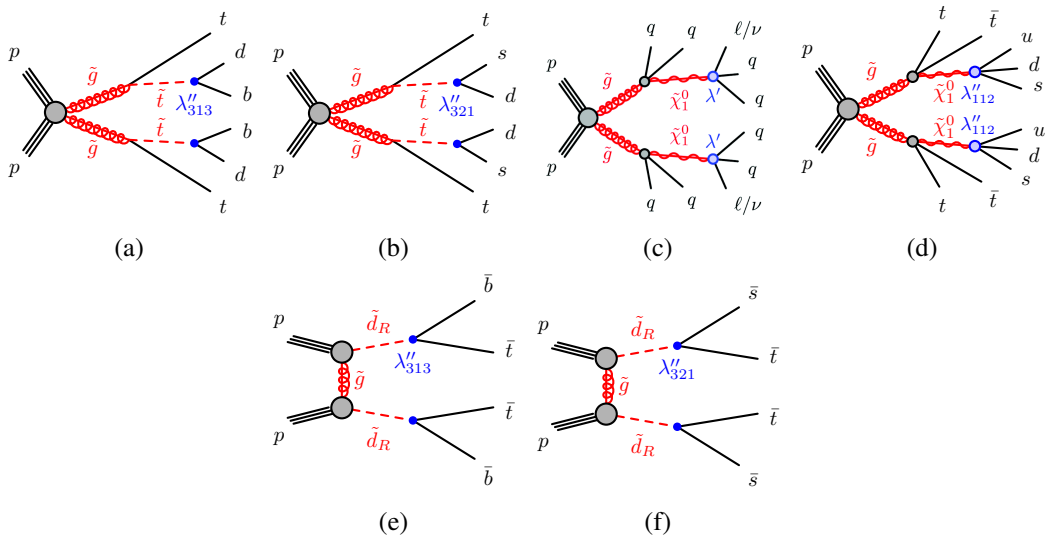

Figure 6.2: RPV SUSY processes featuring gluino production (a, b, c, d) and t-channel production of right-handed down squark (e, f) which decay via baryon or lepton-number violating couplings $\lambda^{''}$ and $\lambda^{'}$ respectively.

via violating λ'' and λ' terms, as introduced in Section 3.1.2.

Gluino pair production with slepton-mediated two-step decay $\tilde{g} \to q\bar{q}\ell\bar{\ell}\tilde{\chi}_1^0$

Figure 6.1a shows gluino pair production with two-step decays via neutralinos $\tilde{\chi}_2^0$ and sleptons , $\tilde{g} \to q\bar{q}^{'}\tilde{\chi}_2^0 \to q\bar{q}^{'}(\tilde{\ell}\ell/\tilde{\nu}\nu) \to q\bar{q}^{'}(\ell\ell,\nu\nu)\tilde{\chi}_1^0$. The decays are mediated by heavy squarks leading to a low b-jet multiplicity. Moreover, several leptons are produced while in other scenarios the leptonic branching ratios of W and Z bosons reduce strongly the acceptance. The final state is composed of several charged leptons, four or more jets, no b-tagged jets and invisible particles (neutrinos and neutralinos). Therefore, the signal regions targeting this model require at least three leptons and the application of a b-jet veto.

Signal samples are generated assuming variable gluino and $\tilde{\chi}_1^0$ masses; sleptons and $\tilde{\chi}_2^0$ masses are set equal and at half-way between gluino and neutralino masses. The $\tilde{\chi}_2^0$ may decay to any of the six "left-handed" sleptons ($\tilde{\ell}, \tilde{\nu}$) with equal probability. "Right-handed" sleptons are assumed to be heavy and do not contribute to the decay.

Figure 6.3a shows that same-sign leptons with additional jets search is able to exclude gluino masses up to 1.7 TeV and relatively heavy neutralinos with 13.2 fb^{-1} [77].

Gluino pair production with gaugino-mediated two-step decay $\tilde{g} \to q\bar{q}^{'}WZ\tilde{\chi}_1^0$

The second considered scenario assumes gluino pair-production with a two-step decay via gauginos and W and Z bosons, as shown in Figure 6.1b. The decay is mediated by heavy squarks of the first and second generation: $\tilde{g} \to q\bar{q}^{'}\tilde{\chi}^{\pm} \to q\bar{q}^{'}W\tilde{\chi}_2^0 \to q\bar{q}^{'}WZ\tilde{\chi}_1^0$. The final state is composed of two W and two Z bosons (possibly off-shell) with four additional jets and invisible particles. Despite a low SM BR leptonic decay of the W and Z bosons, the high number of bosons in the final state leads to a good signal acceptance.

Signal regions targeting this model require many jets and zero b-tagged jets. The analysis is powerful in the heavy-$\tilde{\chi}_1^0$ region of the phase space as shown in Figure 6.3b.

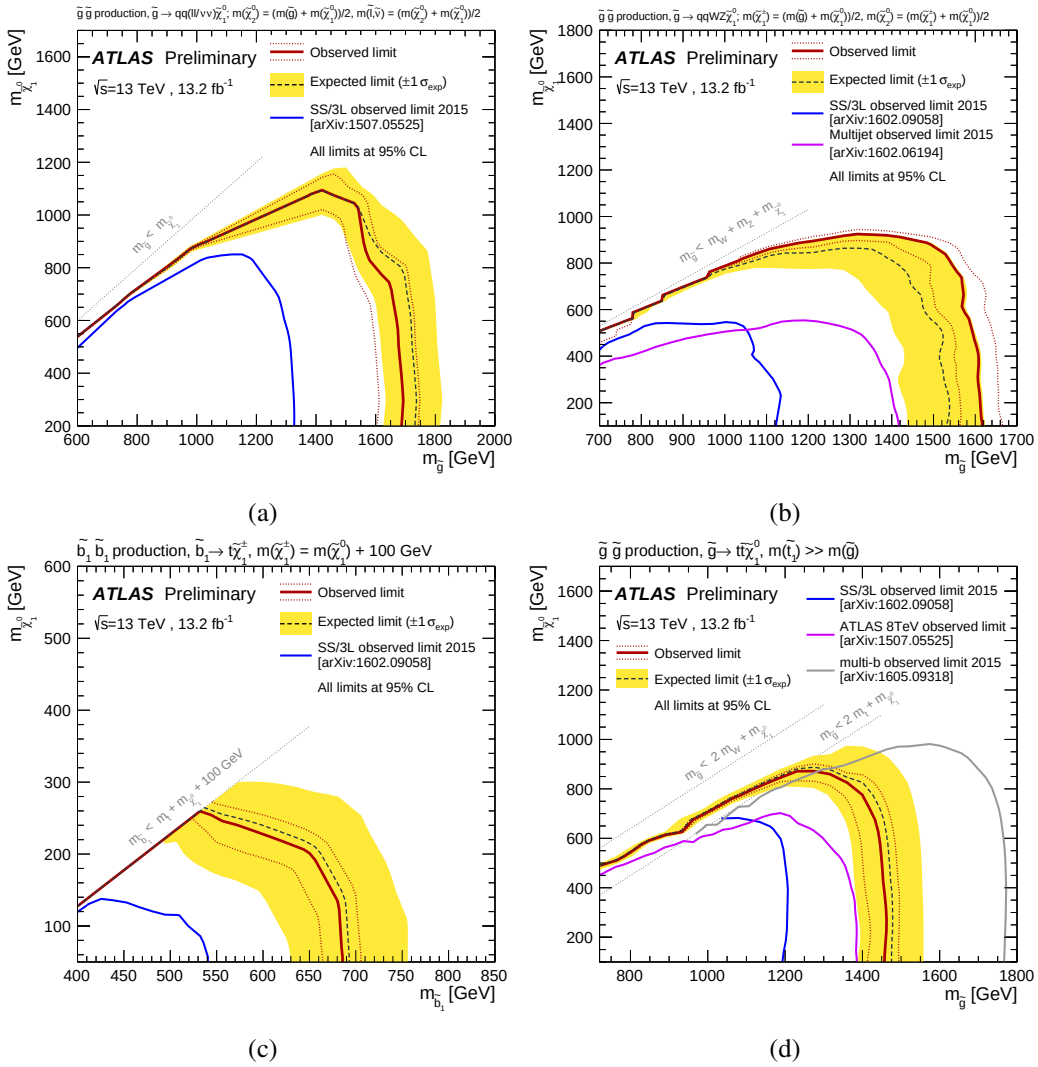

Figure 6.3: Exclusion limits on superpartner masses in different R-parity-conserving SUSY scenarios, for 13.2 fb^{-1} [77].

Signal samples are generated with variable gluino and LSP masses, while the $\tilde{\chi}_1^\pm$ mass is set half way between the two. Finally, the $\tilde{\chi}_2^0$ mass is half-way between $\tilde{\chi}_1^\pm$ and $\tilde{\chi}_1^0$.

Gluino pair production with stop-mediated decay $\tilde{g} \to t\bar{t}\tilde{\chi}_1^0$

In the scenario of gluino pair-production with stop-mediated decay, gluinos couple preferentially to top squarks, the lightest squarks. However gluinos are considered lighter than stops and decay to a $t\bar{t}\tilde{\chi}_1^0$ triplet via a virtual stop as shown in Fig. 6.1c. The final state is composed of four top quarks and two neutralinos, which can be targeted by several searches.

Figure 6.3d shows that this analysis is competitive only at large neutralino masses, reaching $m_{\tilde{\chi}_1^0} \simeq 800$ GeV of exclusion. Also in the phase space region with $\Delta m(\tilde{g}, \tilde{\chi}_1^0) < 2m_t$, where gluinos decay via one or two off-shell top quarks (Figure 6.1d), the search with same-sign leptons is very sensitive.

The larger number of top quarks in the event lead to several b-quarks in the final state, consequently signal regions with at least two b-tagged jets are considered.

Sbottom pair production with one-step decay $\tilde{b}_1 \to t\tilde{\chi}_1^{\pm}$

In this benchmark scenario (Figure 6.1e), light bottom squarks decaying to a top quark and a chargino are considered. Where the chargino decays: $\tilde{\chi}_1^{\pm} \to W\tilde{\chi}_1^0$. The decay products of the sbottom pair contain two top quarks, two W bosons and two neutralinos. Therefore, at least one or two b-jets are expected, leading to a signal region with at least one b-tagged jet. In [77] a mass of 690 GeV for $\tilde{b}_1$ is excluded for a light $\tilde{\chi}_1^0$ as shown in Figure 6.3c.

The model assumes a mass difference between the chargino and the neutralino of 100 GeV, allowing a decay via an on-shell W boson.

$\tilde{t}_1\tilde{t}_1^*$ with "three same sign leptons" signature

A pMSSM signal model with stop pair production with two step decays via a neutralino $\tilde{\chi}_2^0$ and a chargino $\tilde{\chi}_1^{\pm}$ is suggested in [78] and shown in Figure 6.1f. The lightest stop ($\tilde{t}^*$) is right-handed and the $\tilde{\chi}_2^0$ is bino-like causing an enhancement of the branching ratio for the decay $\tilde{t}_1 \to t\tilde{\chi}_2^0$. Moreover, the $\tilde{\chi}_1^{\pm}$ is wino-like which leads to a large branching ratio $\tilde{\chi}_2^0 \to \tilde{\chi}_1^{\pm}W^{\mp}$ if chargino and LSP are nearly mass degenerate and $m_{\tilde{\chi}_2^0} - m_{\tilde{\chi}_1^0} < m_H$ to suppress the decay $\tilde{\chi}_2^0 \to \tilde{\chi}_1^0 + H$.

In the signal generation, only $\tilde{t}_1$ is varied between 550 GeV and 800 GeV, while a two-body decay to an on-shell top quark is considered. In addition, $m_{\tilde{\chi}_2^0} - m_{\tilde{\chi}_1^0} = 100$ GeV and $m_{\tilde{\chi}_1^{\pm}} - m_{\tilde{\chi}_1^0} = 500$ Mev are set to satisfy the described conditions. Stop pair production has a decay chain similar to the sbottom pair production, the difference is in the extra W^* which can lead to three leptons with same electric charge in the final state. This kind of final state is even more suppressed in the SM and allows to loosen further the kinematic cuts (without losing signal acceptance) and explore highly compressed SUSY scenarios.

Non-Universal Higgs Model

The non-Universal Higgs model (NUHM2) ([79, 80, 81]) solves the hierarchy problem with a relatively low level of fine tuning. Several parameters are free: the scalar mass m_0, the soft SUSY breaking gaugino mass $m_{1/2}$, the pseudoscalar Higgs boson mass m_A, the trilinear SUSY breaking parameter A_0, the weak scale ratio of Higgs field vacuum expectation value $\tan\beta$ and the superpotential Higgs mass μ. Simulated samples are generated fixing $m_0 = 5$ TeV, $A_0 = -1.6m_0$, $\tan\beta = 15$, $m_A = 1$ TeV, sign(μ)>0, μ=150 GeV and varying $m_{1/2}$ between 300 GeV and 800 GeV.

R-parity violating decays of gluinos and down squarks with top quarks

As mentioned before, searches for a final state with same-sign leptons may be sensitive to R-parity violating decays SUSY scenarios. Proton lifetime measurement do not provide any constraint to the baryonic sector (λ''_{ijk} couplings). Therefore signal models predicted by Minimal Flavor Violation scenarios ([82, 83]) where couplings may lead to top quarks in decay products of gluinos and squarks and to same-sign leptons in the final state ([84, 85]) are considered.

Benchmark scenarios with gluino pair production followed by stop-mediated decays (Fig. 6.2a and 6.2b) and with pair production of right-handed[1] like-sign sdown quarks (Fig. 6.2e and 6.2f) are considered. Two like-sign top quarks are produced together with two to four hadronic jets, two of which may originate from bottom quarks in specific scenarios. Heavy $\tilde{\chi}_1^0$ are absent, so no compressed scenario can occur; leading to rather energetic particles in the final state. Moreover, due to the absence of an LSP particle, missing transverse momentum is only caused by neutrinos originating from top quark decays.

[1] Considered RPV baryon-number-violating couplings only couple to $SU(2)$ singlets.

In conclusion, final states originating from these signal scenarios contain same-sign leptons, several jets and generally energetic objects. The region of the phase space is orthogonal to the ones optimised for RPC searches, which require a high $E_{\mathrm{T}}^{\mathrm{miss}}$ due to the LSP particle at the end of the decay chain. The following signal models are considered:

- $pp \to \tilde{g}\tilde{g}, \tilde{g} \to tdb$ with off-shell stop mediation (Fig. 6.2a);
- $pp \to \tilde{g}\tilde{g}, \tilde{g} \to tdb$ with on-shell stop mediation (Fig. 6.2a);
- $pp \to \tilde{g}\tilde{g}, \tilde{g} \to tds$ with off-shell stop mediation (Fig. 6.2b);
- $pp \to \tilde{g}\tilde{g}, \tilde{g} \to tds$ with on-shell stop mediation (Fig. 6.2b);
- $pp \to \tilde{d}_R\tilde{d}_R/\tilde{d}_R^*\tilde{d}_R^*, \tilde{d}_R \to \bar{t}\bar{b}$ (Fig. 6.2e);
- $pp \to \tilde{d}_R\tilde{d}_R/\tilde{d}_R^*\tilde{d}_R^*, \tilde{d}_R \to \bar{t}\bar{s}$ (Fig. 6.2f);

Samples of gluino pair production with off-shell stop mediation were produced with a heavy stop mass of 2.0 TeV (to have a consistent 3-body decay from PYTHIA) and gluino mass between 0.6 and 1.8 TeV. For on-shell mediation stop and gluino masses are generated in ranges [0.4-1.8] TeV and [0.6-2.0] TeV, respectively. Regions where top squarks are lighter than gluinos are considered.
In like-sign d squark production, the gluino mass affects only the cross-section and not the signal acceptance. Therefore, samples with $m_{\tilde{g}} = 2.0$ TeV are produced and then re-scaled to the cross-section for the other gluino masses. The branching ratios of $\tilde{d}_R \to \bar{t}\bar{d}$ and $\tilde{d}_R \to \bar{t}\bar{b}$ decays are assumed to be 100%. The d-squark masses are set between 0.4 TeV and 1.8 TeV, keeping the d-squark lighter than gluino. Figure 6.4 shows exclusion limits placed by the same analysis with 13.1 fb^{-1} of data.

R parity-violating decays of neutralinos
R-parity violating scenarios, where the LSP is a neutralino and decays to SM particles via λ' and λ'', can lead to like-sign leptons in the final state. The following models are considered:

- $pp \to \tilde{g}\tilde{g}, \tilde{g} \to q\bar{q}\tilde{\chi}_1^0$ with $\tilde{\chi}_1^0 \to lq\bar{q}$ (Fig. 6.2c);
- $pp \to \tilde{g}\tilde{g}, \tilde{g} \to tt\tilde{\chi}_1^0$ with $\tilde{\chi}_1^0 \to uds$ (Fig. 6.2d).

Many jets are produced in these signal models, with only light jets being present in the first case and many b-tagged jets in the second case due to the top quarks in the topology. Finally, $\tilde{\chi}_1^0 \to lq\bar{q}$ does not contain any intrinsic $E_{\mathrm{T}}^{\mathrm{miss}}$.

6.1.2 Analysis inputs and event selection

This section describes the data and simulated samples used in this analysis; followed by a discussion of the event selection.

Data samples
The data used for the search presented here was recorded in 2015 and 2016 by the ATLAS experiment in pp collisions at $\sqrt{s} = 13$ TeV. The integrated luminosity of these datasets correspond to 3.21 fb^{-1}

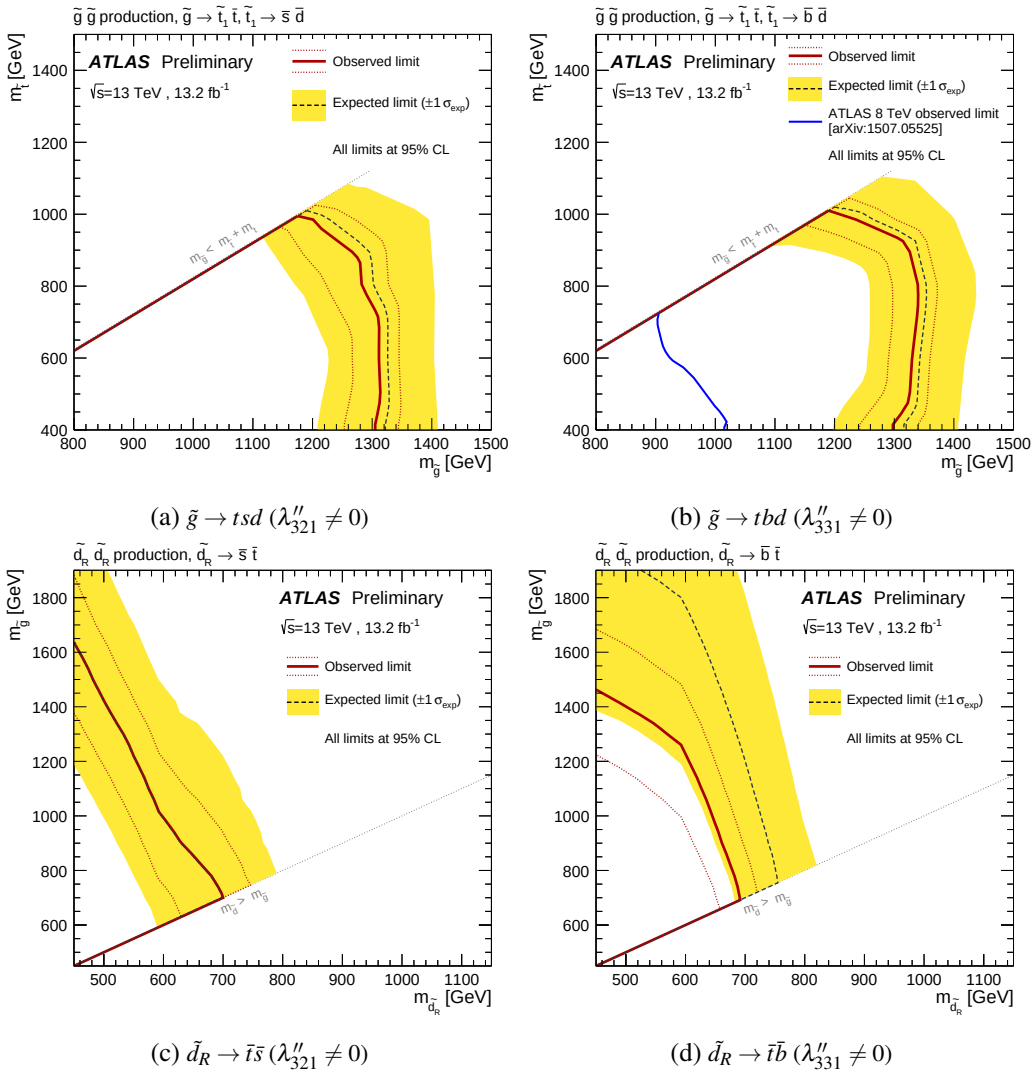

(a) $\tilde{g} \to tsd$ ($\lambda''_{321} \neq 0$)

(b) $\tilde{g} \to tbd$ ($\lambda''_{331} \neq 0$)

(c) $\tilde{d}_R \to t\bar{s}$ ($\lambda''_{321} \neq 0$)

(d) $\tilde{d}_R \to t\bar{b}$ ($\lambda''_{331} \neq 0$)

Figure 6.4: Exclusion limits on superpartner masses in different R-parity-violating SUSY scenarios, for 13.2 fb^{-1} [77].

and 32.86 fb^{-1}, respectively. The combined luminosity uncertainty is 3.2%, assuming partially uncorrelated uncertainties for 2015 and 2016. The integrated luminosity is measured with the method described in [86]. Only events where the ATLAS detector was fully operational are considered.

Simulated background and signal samples

Monte Carlo (MC) generators are used to simulate proton-proton collisions at $\sqrt{s}$=13 TeV with 25 ns of bunch-spacing of both SUSY signal and SM backgrounds processes (see Section 4.3.2 for more details). They allow to determine signal and background contribution in defined regions of the phase-space, systematic uncertainties and analysis acceptance and efficiency. Special sets of parameter tunes (i.e. A14, Perugia, etc.) are used for parton shower, fragmentation and underlying events modelling. Table 6.1 summarises the settings used for the different samples. Modelling of bottom and charm hadron decays is done by EvtGen v1.2.0 in all samples, apart from those generated with Sherpa [60]. The full simulation of ATLAS detector response is fully handled by Geant4 [63]; while part of the samples are using a fast detector simulation (AtlFastII) which parametrises the calorimeter response, while inner detector and muon spectrometer are still simulated by Geant4.

Physics process	Event Generator	Parton shower	Cross section normalization	PDF set	Set of tuned parameters
Signal					
RPC	MG5_aMC@NLO 2.2.3 [87]	Pythia 8.186	NLO+NLL	NNPDF2.3LO [88]	A14 [89]
RPV except Fig. 6.2d	MG5_aMC@NLO 2.2.3	Pythia 8.210	or	NNPDF2.3LO	A14
RPV Fig. 6.2d	Herwig++ 2.7.1 [90]	Herwig++ 2.7.1	NLO-Prospino [91, 92, 93, 94, 95]	CTEQ6L1[96]	UEEE5[97]
$t\bar{t}+X$					
$t\bar{t}W, t\bar{t}Z/\gamma^*$	MG5_aMC@NLO 2.2.2	Pythia 8.186	NLO	NNPDF2.3LO	A14
$t\bar{t}H$	MG5_aMC@NLO 2.3.2	Pythia 8.186	NLO	NNPDF2.3LO	A14
4t	MG5_aMC@NLO 2.2.2	Pythia 8.186	NLO	NNPDF2.3LO	A14
Diboson					
ZZ, WZ	Sherpa 2.2.1	Sherpa 2.2.1	NLO	NNPDF2.3LO	SHERPA default
inc. $W^{\pm}W^{\pm}$	Sherpa 2.1.1	Sherpa 2.1.1	NLO	CT10 [98]	SHERPA default
Rare					
$t\bar{t}WW, t\bar{t}WZ$	MG5_aMC@NLO 2.2.2 [87]	Pythia 8.186	NLO	NNPDF2.3LO	A14
$tZ, tWZ, tt\bar{t}$	MG5_aMC@NLO 2.2.2 [87]	Pythia 8.186	LO	NNPDF2.3LO	A14
WH, ZH	MG5_aMC@NLO 2.2.2 [87]	Pythia 8.186	NLO	NNPDF2.3LO	A14
Triboson	Sherpa 2.1.1	Sherpa 2.1.1	NLO	CT10	Sherpa default

Table 6.1: List of event generator, parton shower, cross-section order, PDF set and set of tuned parameters for all MC samples.

Simulation of the irreducible background processes

The irreducible background is the group of SM processes which produce a final state identical to the signal. In the SS3L analysis this background is dominated by $t\bar{t}V$ (where V=$W, Z/\gamma^*$) production in signal regions with multiple b-jets and by diboson in signal regions with a b-jet veto. Diboson processes have final states with either four charged leptons, three leptons and one neutrino or two same-sign leptons plus two neutrinos. Other considered processes are labeled as *Rare* since they give only small contributions to the signal regions.

An additional source of background can originate from two partons interacting simultaneously in the same collision: two hard scattering process are then overlapping in the detector. These scattering processes may lead to a $W^{\pm}W^{\pm}$ final state via double-parton-scattering (DPS). The contribution in the signal regions was estimated and was found to be negligible.

Signal simulation and cross-section

Signal processes are generated from leading order (LO) matrix elements with up to two extra partons (apart from slepton-mediated gluino decays with one extra parton), using the MG5_aMC@NLO 2.2.3 generator [87] interfaced to Pythia 8 for parton shower and hadronisation, using the ATLAS14 set of tuned parameters [89] with the NNPDF2.3LO and CTEQ6L1 PDF for RPC and RPV models respectively. The signal samples are normalised to the NLO cross-section calculation [99]. The cross-section uncertainties [99] have values between 15 and 25% and include contributions from varied renormalisation and factorisation scales and PDF uncertainties. Uncertainties on the signal acceptance are smaller than the uncertainties on the inclusive production cross-section, therefore they are not considered.

6.1.3 Object definitions

The definitions of the objects used in the analysis are described in Chapter 5. Additional analysis specific details are given below.

Jets: The jets selected in the analysis must satisfy, in addition to the definition given in Chapter 5, $p_T > 20$ GeV and $|\eta| < 2.8$. The MV2c10 b-tagging algorithm at 70% efficiency working point is used for jets with $|\eta| < 2.5$. Optimisation studies on signal and background samples have been performed to select the optimal efficiency working point. High rejection factors were measured in simulated $t\bar{t}$ events for light/gluon jets (380), c-jets (12) and hadronically decaying τ (54) [75, 100]

for the 70% efficiency working point.
Correction factors and uncertainties on *b*-tagging efficiencies and mis-tag rates are extracted from data and applied on the simulated events [75].
Table 6.2 summarises the selection criteria for jets and *b*-tagged jets.

	Jets
Collection	AntiKt4EMTopo
Acceptance	$p_{\mathrm{T}} > 20$ GeV, $\lvert\eta\rvert < 2.8$
Jet vertex tagger	JVT>0.64 for jets with
	$p_{\mathrm{T}} < 60$ GeV, $\lvert\eta\rvert < 2.4$ (applied after overlap-removal)
	***b*-jets**
Acceptance	$p_{\mathrm{T}} > 20$ GeV, $\lvert\eta\rvert < 2.5$
Identification	MV2c10 at 70% WP
	(85% WP for overlap-removal)

Table 6.2: Summary of the selection criteria for jets (top) and *b*-tagged jets (bottom).

Electrons: Electrons with $p_T > 10$ GeV and $|\eta| < 2.47$ and satisfying *Loose* likelihood based electron identification are considered as "baseline". The region between barrel and end-cap EM calorimeters ($1.37 < |\eta| < 1.52$) is vetoed to reduce contributions from fake/non-prompt electrons.
Electrons with wrongly measured charge (charge-flipped) represent a significant percentage of the same-sign lepton final state. A requirement on the transverse impact parameter d_0 with respect to the reconstructed primary vertex reduces the contribution from charge-flipped electrons: $|d_0/\sigma_{d_0}| < 5$. This requirement is applied also for baseline electrons to reduce the charge-flip contamination in the fake/non-prompt lepton estimation.
Electrons defined as "signal" must satisfy the *Medium* likelihood based electron identification and have $p_T > 20$ GeV and $|\eta| < 2.0$ to further reduce charge-flip contributions. Moreover, the *FixedCutTight* isolation working point and longitudinal impact parameters requirements ($|z_0 \cdot \sin(\theta)| < 0.5$ mm) are applied.
In addition, a Boosted Decision Tree (BDT) combines in a single classifier electron p_{T} and η with electron track and cluster properties (track impact parameter, track curvature significance, cluster width and quality of matching between cluster and its associated track). A cut on the BDT output allows to reach a rejection factor of almost 8 for electrons with wrongly assigned charge and 97% efficiency for properly measured electrons in $Z \to ee$ simulated events. Differences in efficiency between data and simulation are corrected with scale factors applied to electrons in the simulated samples [101].

Muons: Muons with $p_{\mathrm{T}} > 10$ GeV and $|\eta| < 2.4$ and satisfying *Medium* identification requirement are considered as "baseline". "Signal" muons are required in addition to pass the *FixedCutTightTrackOnly* isolation requirements and the cuts on the impact parameters ($|d_0/\sigma_{d_0}| < 3$ and $|z_0 \cdot \sin(\theta)| < 0.5$ mm). Differences in efficiency between data and simulation are corrected with event weights applied to muons in the simulated samples.
Table 6.3 summarise the selection criteria for electrons and muons.

	Baseline electrons	**Baseline muons**
Acceptance	$p_{\mathrm{T}} > 10$ GeV, $\lvert\eta^{\mathrm{clust}}\rvert < 2.47$ except $1.37 < \lvert\eta^{\mathrm{clust}}\rvert < 1.52$	$p_{\mathrm{T}} > 10$ GeV, $\lvert\eta\rvert < 2.4$
Quality WP	*LooseLH*	*Medium*
l-jet isolation	see Overlap Removal description	
Impact parameter	$\lvert d_0/\sigma(d_0)\rvert < 5.0$	
	Signal electrons	**Signal muons**
Quality WP	*TightLH* $\lvert\eta\rvert < 2.0$	*Medium*
Isolation WP	*FixedCutTight*	*FixedCutTightTrackOnly*
Impact parameter	$\lvert z_0 \cdot \sin(\theta)\rvert < 0.5$ mm	$\lvert z_0 \cdot \sin(\theta)\rvert < 0.5$ mm $\lvert d_0/\sigma(d_0)\rvert < 3.0$

Table 6.3: Summary of the selection criteria for electron (left) and muons (right).

Overlap removal: The overlap removal procedure used in this analysis is composed of four steps:

- Jets with a distance $\Delta R = \sqrt{(\Delta y)^2 + (\Delta\phi)^2}$ from a candidate lepton lower than 0.2 are discarded as they mostly originate from calorimeter energy deposits from electron shower or muon bremstrahlung, unless the jet is b-tagged (using 85% working point). In the latter case, the leptons are discarded since they may originate from a semi-leptonic b-hadron decay.
- The remaining leptons within a p_{T}-dependent cone of radius $\Delta R = \min(0.4, 0.1 + 0.96\mathrm{GeV}/p_{\mathrm{T}}(\ell))$ are discarded. If the lepton is a muon and the jet has fewer than 3 associated tracks, the jet is discarded to reduce inefficiencies for energetic muons suffering significant energy losses in the calorimeter.
- If an electron and a muon are identified with $\Delta R_y < 0.01$, the electron is most likely originated by muon bremsstrahlung. Since the electron is not prompt and the muon momentum is alterated, both objects are discarded.
- If two (or more) electrons are identified with $\Delta R_y < 0.05$, they are probably originated by the same EM shower. Therefore, only the most energetic electron is not discarded.

This procedure avoids any possible double-counting of the objects included in the analysis.

Missing transverse momentum: The missing transverse momentum ($E_{\mathrm{T}}^{\mathrm{miss}}$) is computed as the negative vector sum of the transverse momenta of all identified candidate objects (electrons, photons, muons and jets). The soft term is computed as the sum of all the tracks associated to the primary vertex but not to any physics object.
This configuration ensures the best calibration of all considered physics objects and general pile-up independency, due to the additional soft term [102, 103].

6.1.4 Event selection

Event cleaning

The collected data contain many events with calorimeter noise or non-collision background which need to be rejected. Further pre-selection of events is done by applying lepton requirements and kinematic cuts to suppress the SM background. A pre-selection of two same-sign or three lepton events is used. Furthermore, events are selected by applying kinematic criteria to reduce background contribution:

- **Jet cleaning**: quality requirements are applied on pre selected jets to remove events where significant energy was deposited in the calorimeters due to instrumental effects: cosmic rays, non-collision background and noise.
- **Primary vertex**: a reconstructed vertex, which needs to have at least two associated tracks with $p_{\mathrm{T}} > 400$ Mev, is required. The vertex with the largest $\sum p_{\mathrm{T}}^2$ of associated tracks is considered as the primary vertex.
- **Bad muon veto**: events containing at least one pre-selected muon satisfying $\sigma(q/p)/|q/p| > 0.2$ before the overlap removal are rejected, where q is the charge of the muon and p is the momentum of the muon.
- **Cosmic muon veto**: cosmic muon candidates may be rejected if pre selected muons fail the requirements longitudinal and transverse impact parameters calculated with respect to the primary vertex: $|z_0| < 1.0$ mm and $|d_0| < 0.2$ mm.
- **At least two leptons**: events with at least two or three leptons are selected. Signal leptons are required to have $p_{\mathrm{T}} > 20$ GeV for the two leading leptons; if a third signal lepton with $p_{\mathrm{T}} > 10$ GeV is present, the event is categorised as three-leptons (including also events with more than three leptons).
- **Same sign**: if only two leptons are present, they have to have identical charge, while events with three leptons do not have any requirement on the charge.

Trigger strategy

The optimal trigger configuration is a combination of dilepton triggers and $E_{\mathrm{T}}^{\mathrm{miss}}$ triggers. The triggers are combined in the following way:

- if $E_{\mathrm{T}}^{\mathrm{miss}} < 250$ GeV: logical *OR* of all dilepton triggers;
- if $E_{\mathrm{T}}^{\mathrm{miss}} > 250$ GeV: logical *OR* of all dilepton triggers and $E_{\mathrm{T}}^{\mathrm{miss}}$ trigger;

The increase of instantaneous luminosity between 2015 and 2016 required to raise the trigger thresholds. The $E_{\mathrm{T}}^{\mathrm{miss}}$ trigger was raised from 70 GeV (2015 data) to 100 GeV (2016 data). When an event is selected by a dilepton trigger, a matching between the signal leptons of the event and the lepton which fired the trigger is required. Trigger matching is applied to signal leptons. Final differences in the trigger efficiency between data and MC are corrected by trigger scale factors. No correlation is assumed between dilepton and $E_{\mathrm{T}}^{\mathrm{miss}}$ trigger. Scale factors are computed for each event selected by the dilepton trigger, considering combination of fired triggers, the number and flavors of the leptons.

6.2 Signal regions

A set of 19 inclusive signal regions (SR) have been defined to target all considered signal models and reach the best sensitivity. Table 6.4 shows the complete set of cuts which define the signal regions. The name assigned to SRs depends on the number of leptons (N), number of b-jets (M) and harshness

Signal region	$N_{\text{leptons}}^{\text{signal}}$	$N_{\text{b-jets}}$	N_{jets}	$p_{\text{T}}^{\text{jet}}$ [GeV]	$E_{\text{T}}^{\text{miss}}$ [GeV]	m_{eff} [GeV]	$E_{\text{T}}^{\text{miss}}$ / m_{eff}	Other	Targeted Signal
Rpc2L2bS	$\geq$ 2SS	$\geq$2	$\geq$6	>25	>200	>600	>0.25	-	Fig. 6.1c
Rpc2L2bH	$\geq$ 2SS	$\geq$2	$\geq$6	>25	-	>1800	>0.15	-	Fig. 6.1c, NUHM2
Rpc2Lsoft1b	$\geq$ 2SS	$\geq$1	$\geq$6	>25	>100	-	>0.3	20,10 <$p_T^{\ell_1}$,$p_T^{\ell_2}$< 100 GeV	Fig. 6.1d
Rpc2Lsoft1b	$\geq$ 2SS	$\geq$1	$\geq$6	>25	>200	600	>0.25	20,10 <$p_T^{\ell_1}$,$p_T^{\ell_2}$< 100 GeV	Figure Fig. 6.1d
Rpc2L0bS	$\geq$ 2SS	= 0	$\geq$6	>25	>150	-	>0.25	-	Fig. 6.1b
Rpc2L0bH	$\geq$ 2SS	= 0	$\geq$6	>40	>250	>900	-	-	Figure 6.1b
Rpc3L0bS	$\geq$ 3	= 0	$\geq$4	>40	>200	>600	-	-	Fig. 6.1a
Rpc3L0bH	$\geq$ 3	= 0	$\geq$4	>40	>200	>1600	-	-	Fig. 6.1a
Rpc3L1bS	$\geq$ 3	$\geq$1	$\geq$4	>40	>200	>600	-	-	
Rpc3L1bH	$\geq$ 3	$\geq$1	$\geq$4	>40	>200	>1600	-	-	
Rpc2L1bS	$\geq$ 2SS	$\geq$1	$\geq$6	>25	>150	>600	>0.25	-	Fig. 6.1e
Rpc2L1bH	$\geq$ 2SS	$\geq$1	$\geq$6	>25	>250	-	>0.2	-	Fig. 6.1e
Rpc3LSS1b	$\geq \ell^{\pm}\ell^{\pm}\ell^{\pm}$	$\geq$1	-	-	-	-	-	veto 81<$m_{e^{\pm}e^{\pm}}$<101 GeV	Fig. 6.1f
Rpv2L1bH	$\geq$ 2SS	$\geq$1	$\geq$6	>50	-	>2200	-	-	Fig. 6.2a, Fig. 6.2b
Rpv2L0b	= 2SS	= 0	$\geq$6	>40	-	>1800	-	veto 81<$m_{e^{\pm}e^{\pm}}$<101 GeV	Fig. 6.2c
Rpv2L2bH	$\geq$ 2SS	$\geq$2	$\geq$6	>40	-	>2000	-	veto 81<$m_{e^{\pm}e^{\pm}}$<101 GeV	Fig. 6.2d
Rpv2L2bS	$\geq l^-l^-$	$\geq$2	$\geq$3	>50	-	>1200	-	-	Fig. 6.2e
Rpv2L1bS	$\geq l^-l^-$	$\geq$1	$\geq$4	>50	-	>1200	-	-	Fig. 6.2f
Rpv2L1bM	$\geq l^-l^-$	$\geq$1	$\geq$4	>50	-	>1800	-	-	Fig. 6.2f

Table 6.4: Summary of the signal region definitions. Unless explicitly stated in the table, at least two signal leptons with p_{T} >20 GeV and same charge (SS) are required in each signal region. Requirements are placed on the number of signal leptons (N_{signal}), the number of b-jets with $p_{\text{T}} > 20$ GeV ($N_{\text{b-jets}}$), the number of jets (N_{jets}) above a certain p_{T} threshold ($p_{\text{T}}^{\text{jet}}$), $E_{\text{T}}^{\text{miss}}$, m_{eff} and/or $E_{\text{T}}^{\text{miss}}/m_{\text{eff}}$. The last column indicates the targeted signal model. The Rpc3L1bS and Rpc3L1bH SRs are not motivated by a particular signal model and can be seen as a natural extension of the Rpc3L0b SRs with the same kinematic selections but requiring at least one b-jet.

of $E_{\text{T}}^{\text{miss}}$ and m_{eff}[2] requirements (X=Soft, Medium and Hard): RpcNLMbX. All $\ell^{\pm}\ell^{\pm}$ ($\ell = e, \mu$) pairs are selected, any additional number of leptons is allowed (except in Rpv2L0b). For each lepton and b-jet multiplicity two SRs are optimised to target compressed or large mass splitting regions.

The optimisation is performed starting from a set of requirements on number of b-jets and leptons, depending on the signal scenario favoured by the corresponding final state. Subsequently, a brute-force scan of other main discriminant variables (number of jets, $E_{\text{T}}^{\text{miss}}$, m_{eff}, $E_{\text{T}}^{\text{miss}}/m_{\text{eff}}$) is performed to determine the best selection for each region of the parameter space. The figure of merit used to rank configurations is the discovery significance (Z_0) defined in Eq. 6.1 which represents a statistical test based on a ratio of two Poisson means [104]:

$$Z_0 = \sqrt{2(\text{s}+\text{b})\ln(1+\frac{\text{s}}{\text{b}}) - \text{s}} \tag{6.1}$$

where s and b represent the expected number of signal and background events. In the statistical test, a realistic estimation of the systematic uncertainty of 30% on the expected background is included.

Since MC samples of $t\bar{t}$ and Z+jets do not provide a good estimate of fake leptons and charge-flip background (determined from data in the analysis); scale factors are obtained from the MC Template Method (see Sec. 6.4.3)and applied to give a more reliable estimation in the optimisation procedure. Factors vary depending on the generator or showering of the sample (PYTHIA or SHERPA) and on the source of the fake leptons (heavy flavour or light flavour).

Finally for each signal scenario, model dependent exclusion limits are computed for each signal point using the signal region with the best expected sensitivity.

[2]The effective mass is defined as the sum of H_{T} and $E_{\text{T}}^{\text{miss}}$, where H_{T} is the scalar sum of the transverse momenta of all considered particles in the final state: $m_{\text{eff}} = E_{\text{T}}^{\text{miss}} + \Sigma_i |p_{\text{T}}|^i$.

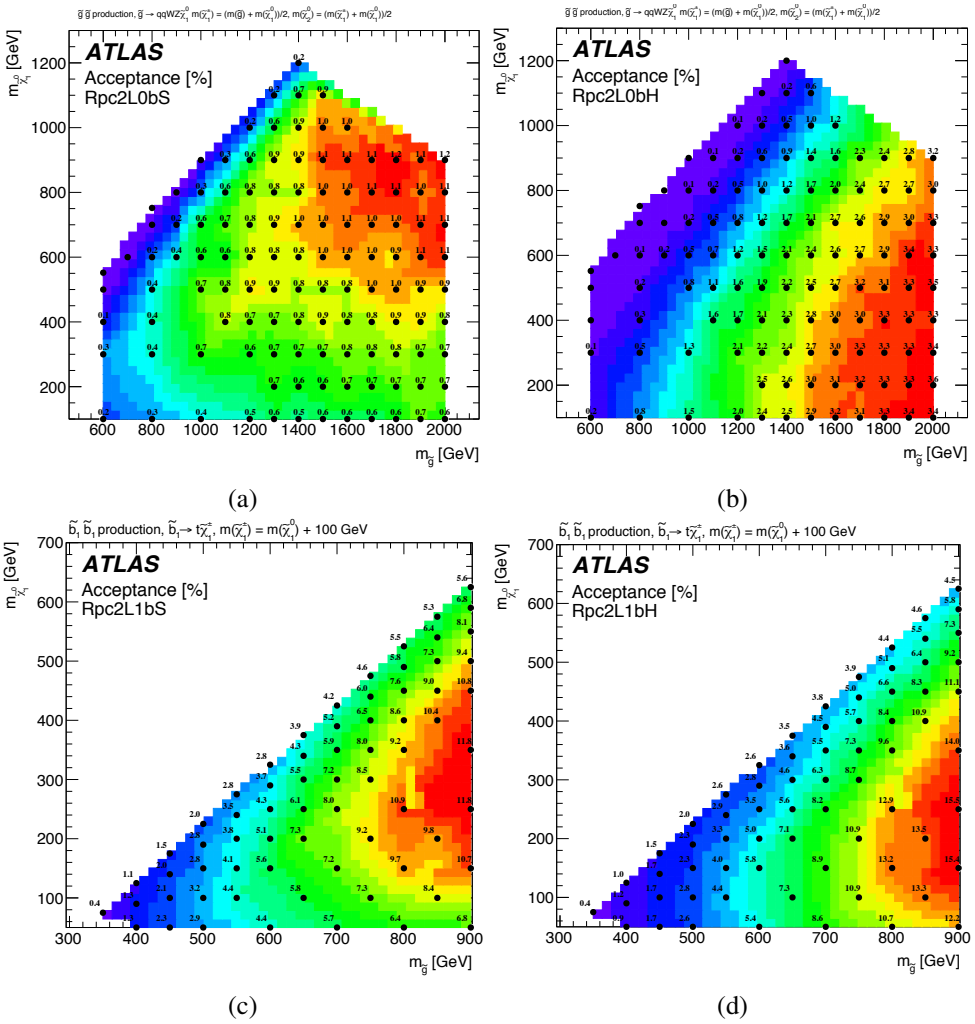

Figure 6.5: Signal acceptance for various simplified models in the signal regions Rpc2L0bS (a), Rpc2L0bH (b), Rpc2L1bS (c) and Rpc2L1bH (d) [105].

6.3 Analysis acceptance and efficiency

Important information is provided with the study of the signal acceptance and efficiency using particle-level MC simulation. The author of the thesis computed the signal acceptance and efficiency of the SS3L analysis.

The considered events are taken at generator-level including parton-level activity, showering, hadronisation and particle decays. The simulation of the interaction with the detector is not included. The particle selection (isolation, identification, overlap removal) is the same used in the analysis, except for the BDT cut to reduce the charge-flip electrons. Also, the complete set of kinematic cuts of the SRs defined is included in the computation, along with the branching ratio of all decaying particles considered. The signal acceptance, shown in Figure 6.5, gives an overview of the sensitivity power of the analysis and is defined as the percentage of generated events passing the signal region selection. Moreover, it can be used to interpret and compare signal models which have not been included in the analysis. Similarly, efficiency maps are computed where the efficiency is defined as the ratio between the number of reconstructed events and the number of generated events. The reconstructed events include also the detector simulation and it contains reconstruction and identification efficiency of the different particles considered in the analysis.

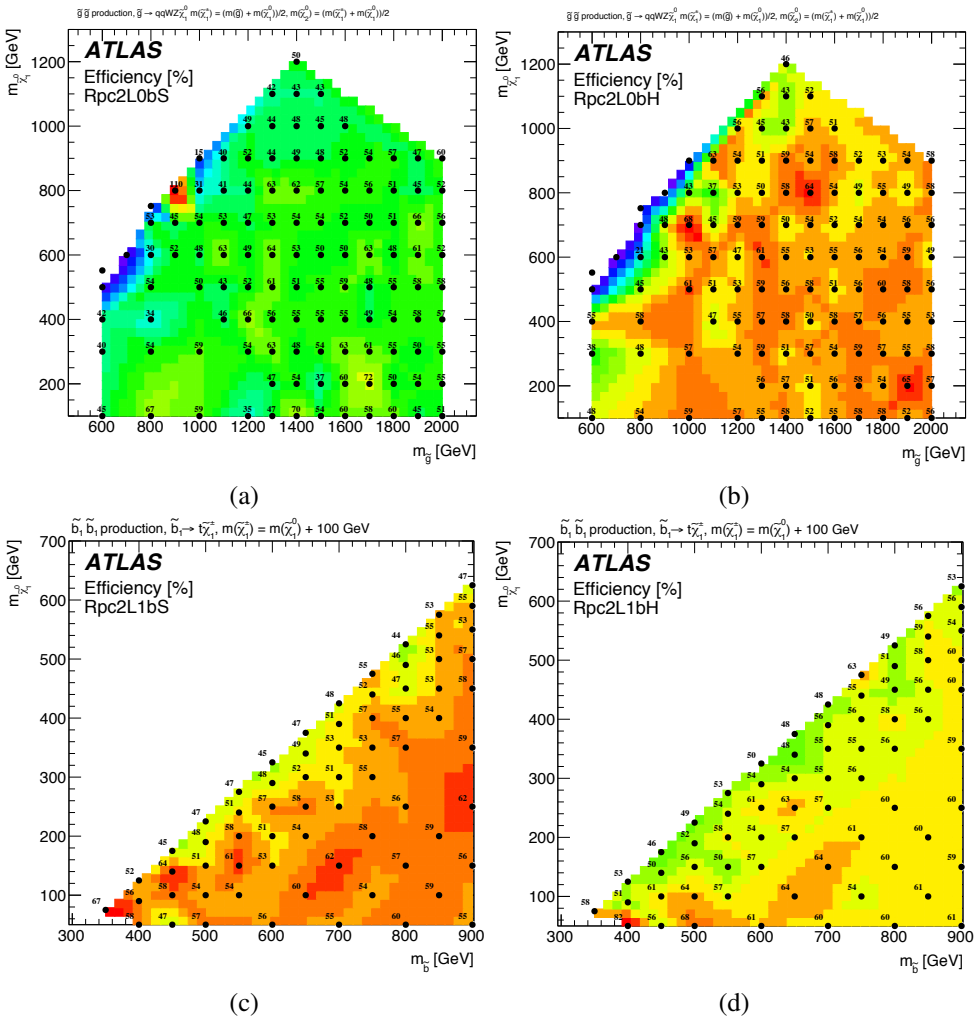

Figure 6.6: Signal efficiency for various simplified models in the signal regions Rpc2L0bS (a), Rpc2L0bH (b), Rpc2L1bS (c) and Rpc2L1bH (d) [105].

The efficiency can be used to estimate the number of expected events S:

$$S = \mathrm{L_{int}} \cdot \sigma_{\mathrm{prod}} \cdot A \cdot \varepsilon, \tag{6.2}$$

where σ_{prod} is the production cross section of the signal process, $\mathrm{L_{int}}$ is the integrated luminosity, and A is the acceptance. Figure 6.6 shows the efficiency map for the same SRs as shown in Figure 6.5.

6.4 Background estimation

Few Standard Model processes lead to same-sign (SS) or three leptons (3L) final states, and in addition they have relatively low cross-sections. Therefore, signal regions are characterised by low contamination from irreducible background processes. Additionally, two sources of reducible background have a significant contributions: fake/non-prompt leptons and charge-flip electrons:

- **Prompt SS/3L background:** the main sources are top-quark pair production in association with a vector boson ($t\bar{t}V$) and diboson processes (depending on the b-jet multiplicity in the signal region definition). All SM background processes have been introduced previously in paragraph 6.1.2, along with the list of MC samples (Table 6.1).
- **Fake or non-prompt lepton background:** caused by objects misidentified as leptons. The background can originate from light flavour jets or heavy flavour hadron decays, as well as electrons from photon conversion. If produced in a process with a prompt lepton, they can lead to a final state with same-sign leptons.
- **Charge-flip background:** it denotes events where the electron charge is wrongly measured, commonly referred to as "charge-flip". This is due to electrons having emitted a hard bremsstrahlung photon which is subsequently converted to an electron pair; or a bad electron track reconstruction. It is negligible for muons. In this case events with opposite-sign (OS) lepton pairs are wrongly identified as SS events.

A precise and reliable estimation of these background sources is crucial. The estimation of prompt background relies on Monte Carlo simulations, while fake (FNP) leptons and "charge-flip" leptons are estimated with data-driven methods.

6.4.1 Fake lepton background

Background arising from fake objects is a common problem in many analyses in ATLAS, from SM precision measurements to New Physics searches. When reconstructing an object the expectation is to associate it to the 'real' corresponding particle which caused the track in the detector. Unfortunately, a significant number of times an object is mistakenly reconstructed as different from the 'real' particle: these are called fake objects.
The processes leading to fake/non-prompt leptons (will be referred as FNP for the rest of the thesis) change depending on the considered final state. In the SS/3L analysis, the main contribution comes from top-quark pair production ($t\bar{t}$) and associated production of a vector boson and jets (V+jets). These SM processes are not leading to two leptons with the same-charge, unless there is a charge-flip electron or a FNP lepton produced.
A common example is a hadronic jet which may leave a narrow deposit in the calorimeter, inducing the reconstruction algorithms to treat it as an electron. Fake lepton background has a significant role in the search described in this dissertation; therefore a reliable estimation of the contribution in the SRs is needed. A first option is to rely on MC simulation, with two downsides: a not perfect reproduction of the behaviour of fake objects and a high statistical uncertainty in the interesting regions of the phase space.

Therefore, data is exploited to provide a better prediction of fake background with *data-driven methods* such as matrix method [106], fake factor method and MC template method (supported by measurements on MC).
Fake leptons are caused by instrumental effects which lead to inability to identify objects from the measured properties. The processes causing this effect are different for electrons and muons.

Fake electrons
As explained in section 5.1, candidate electrons are reconstructed with a charged track in the ID aligned with a deposit in the EM calorimeter, additionally the extrapolated mass must be consistent with electron mass. A photon deposit in the EM calorimeter can look similar to the one produced by an electron, therefore any process with one or more photons and an aligned charged track may be reconstructed as a 'real' electron.
Hadronic jets with a charged and a neutral pion can be reconstructed as electrons. Charged pions can leave a charged track in the ID similar to an electron, and in case of a high-momentum particle the extrapolation of the mass is less precise. Neutral pions often decay to photons, resulting in a a deposit in the EM calorimeter. Charged track and calorimeter deposit will be matched since the pions are coming from the same jet, causing an electron-like signature in the detector.
Heavy-flavour hadron decay is another important source of non-prompt electrons (and muons). The heavy flavour hadron decay may contain a $W^{\pm}$ or Z^0 which decays leptonically. High energy muons may also fake electrons with photons emitted via bremstrahlung. Energetic muons and electrons cause similar tracks in the ID, while the emitted photon will again leave a calorimeter deposit compatible with the charged track. If the muon is reconstructed, fake electrons are removed with the Overlap Removal procedure, however cases where the muon is not subsequently reconstructed cannot be removed.

Fake muons
Candidate muons are reconstructed when a track in the muon spectrometer (MS) is matched to a track in the ID. Charged hadrons with sufficient lifetime go through the calorimeter and leave a track only in the MS. The activity inside the detector is high enough to produce random tracks. These can be associated to the hits in the MS and cause the reconstruction of a fake muon. Another case is originated by pions and kaons decaying in-flight to muons in the MS and aligning to the primary vertex.

6.4.2 Dynamic matrix method

The estimation of FNP lepton background is performed with a purely data-driven procedure called *matrix method* [106]. It is based on the relation between the number of real and FNP leptons (physical quantities) and the number of baseline[3] and signal leptons (measurable quantities). A matrix defines this relation taking into account the different response to identification and isolation for prompt and FNP leptons.

[3]For consistency with the acceptance used for signal electrons, only baseline electrons with $|\eta| < 2.0$ are considered.

In the case of events with one lepton, a matrix Λ is defined as:

$$\begin{pmatrix} N_S \\ N_B \end{pmatrix} = \Lambda \times \begin{pmatrix} N_P \\ N_F \end{pmatrix}, \quad \Lambda = \begin{pmatrix} \varepsilon_P & \varepsilon_F \\ (1-\varepsilon_P) & (1-\varepsilon_F) \end{pmatrix} \tag{6.3}$$

where N_S and N_B denote the numbers of leptons passing the baseline or signal requirements. N_P and N_F denote the numbers of prompt and FNP leptons. The parameters ε_P and ε_F are the probabilities for real and FNP leptons to be selected as signal leptons in the considered analysis. Since we are interested in the number of FNP leptons entering the signal regions selection, the efficiency matrix has to be inverted:

$$\begin{pmatrix} N_P \\ N_F \end{pmatrix} = \Lambda^{-1} \times \begin{pmatrix} N_S \\ N_B \end{pmatrix}, \quad \Lambda^{-1} = \frac{1}{\varepsilon_P - \varepsilon_F} \begin{pmatrix} (1-\varepsilon_F) & -\varepsilon_F \\ (\varepsilon_P - 1) & \varepsilon_P \end{pmatrix} \tag{6.4}$$

The number of FNP leptons passing the signal selection $N_{\{F|S\}}$ is given by the total number of FNP leptons times the baseline to signal efficiency:

$$N_{\{F|S\}} = N_F \cdot \varepsilon_F = \frac{\varepsilon_F}{\varepsilon_P - \varepsilon_F}(N_S(\varepsilon_P - 1) + \varepsilon_P N_B). \tag{6.5}$$

This equation provides the number of FNP leptons passing the signal requirements. The linearity of the method allows to calculate the total yields by assigning a weight to each event: $w = \frac{\varepsilon_F}{\varepsilon_P - \varepsilon_F}(\varepsilon_P - \mathbb{I}_\ell)$. The weight value changes depending if lepton passes ($\mathbb{I}_\ell = 1$) or fails ($\mathbb{I}_\ell = 0$) the signal requirements. The sum of weights assigned to each event gives the total yields from fake lepton background. Therefore both the shape and normalisation of the background are estimated.
In the SS3L analysis, the starting point is the two-lepton event case, therefore the efficiency matrix is extended to a 4x4 matrix which includes real and fake rates of both leptons:

$$\begin{pmatrix} N_{SS} \\ N_{SB} \\ N_{BS} \\ N_{BB} \end{pmatrix} = \Lambda \times \begin{pmatrix} N_{PP} \\ N_{PF} \\ N_{FP} \\ N_{FF} \end{pmatrix},$$

$$\Lambda = \begin{pmatrix} \varepsilon_{P,1}\varepsilon_{P,2} & \varepsilon_{P,1}\varepsilon_{F,2} & \varepsilon_{F,1}\varepsilon_{P,2} & \varepsilon_{F,1}\varepsilon_{F,2} \\ \varepsilon_{P,1}(1-\varepsilon_{P,2}) & \varepsilon_{F,1}(1-\varepsilon_{F,2}) & \varepsilon_{F,1}(1-\varepsilon_{P,2}) & \varepsilon_{F,1}(1-\varepsilon_{F,2}) \\ (1-\varepsilon_{P,1})\varepsilon_{P,2} & (1-\varepsilon_{P,1})\varepsilon_{F,2} & (1-\varepsilon_{F,1})\varepsilon_{P,2} & (1-\varepsilon_{F,1})\varepsilon_{F,2} \\ (1-\varepsilon_{P,1})(1-\varepsilon_{P,2}) & (1-\varepsilon_{P,1})(1-\varepsilon_{F,2}) & (1-\varepsilon_{F,1})(1-\varepsilon_{P,2}) & (1-\varepsilon_{F,1})(1-\varepsilon_{F,2}) \end{pmatrix}.$$

The procedure is the same as in one lepton case. Since in the analysis events with more than two leptons are selected, the method may be extended to an arbitrary number of leptons: called *dynamic matrix method*. However events with three leptons or more have a negligible contribution. Real and fake efficiencies are measured in different p_{T} and η bins, to take into account different rates in all the regions of the phase space, and for electrons and muons separately.

Real lepton efficiency

The baseline-to-signal efficiency for the leptons is calculated with the so-called *Z tag-and-probe* method in a pure $Z \to \ell\ell$ data sample. Events with at least two baseline lepton candidates with an invariant mass falling into the Z mass window ($80 < m_{\ell\ell} < 100$ GeV) are selected. One of the two lepton candidates, the *tag* lepton, is required to have a transverse momentum $p_{\mathrm{T}} > 25\,\mathrm{GeV}$ and pass the signal lepton requirements. The *probe* lepton, which is used to measure the real lepton efficiency, is required to pass the baseline lepton requirements and have to carry opposite charge and same flavour with respect to the corresponding tag lepton. All possible tag-and-probe combinations are considered in an event (including permutation of the tag and probe leptons), to avoid any bias and increase the statistic.

The real lepton efficiency is obtained by computing the ratio between the number of probe leptons passing the signal requirements (N_{signal}) and the number of probe leptons passing the baseline requirements (N_{baseline}) as shown in Equation 6.6:

$$\varepsilon_R = \frac{N_{\mathrm{signal}}}{N_{\mathrm{baseline}}}. \tag{6.6}$$

Fake lepton efficiency

The fake rate is measured in a data control region enriched in fake leptons from heavy flavour decays. Same-sign events with at least one b-jet, one signal muon with $p_{\mathrm{T}} > 40$ GeV and an additional baseline lepton are selected. The control region is enriched in $t\bar{t}$ events, which do not lead to a same-sign final state. Therefore, the signal muon is assumed to be prompt and be originated from a semi-leptonic decay of the W boson, while the additional lepton has to be produced from a heavy flavour decay. Consequently the measurement of the fake rate is performed on the additional lepton with the formula:

$$\varepsilon = \frac{N_{\mathrm{tight}}^{\mathrm{data}} - N_{\mathrm{tight}}^{\mathrm{prompt\ bkg}}}{N_{\mathrm{loose}}^{\mathrm{data}} - N_{\mathrm{loose}}^{\mathrm{prompt\ bkg}}}, \tag{6.7}$$

where ‘loose‘ leptons are satisfying baseline lepton requirements and ‘tight‘ leptons are satisfying signal lepton requirements.

A caveat of this measurement is that different sources of FNP cannot be disentangled: a systematic uncertainty is assigned to cover differences in fake composition between control region and signal regions. Additionally in the electron case, the charge-flip background can affect the fake rate measurement, therefore this contribution is subtracted for both signal and baseline electrons. The fake rates are strongly dependent on the lepton flavour and kinematic characteristics.

6.4.3 MC template method

In the SS3L analysis, an alternative method is used to estimate the fake lepton background. The processes which lead to FNP leptons can be simulated with Monte Carlo event generators and then processed through GEANT4 to estimate the detector response. This estimation is usually not reliable due to a not-perfect simulation of the ATLAS detector. In addition, the stringent requirements in the signal region definitions cause a significantly high statistical uncertainty from Monte Carlo events. The latter issue is solved with an increase of generated Monte Carlo events, while the MC Template Method [106] is able to address the former.

The MC template method relies on the correct modelling of FNP leptons kinematics in MC simulation to extrapolate background predictions from control regions to the signal regions. The basic assumption

is that kinematic shapes of each FNP source is modelled correctly. For each process which contains FNP leptons, control regions enriched with those processes are defined and normalisation factors are extracted from a combined fit to data.
In the SS/3L analysis, five categories are defined to classify the sources of FNP leptons: prompt electrons or muons decaying from on-shell W and Z bosons, non-prompt leptons from heavy flavour b decays (HF) and fakes arising from light flavour jet or photon-conversion (LF). Prompt electrons are further split into electrons with correctly assigned charge or mis-measured charge.
Control regions are defined in a low jet-multiplicity and low $E_{\mathrm{T}}^{\mathrm{miss}}$ region of the phase space, and the b-jet multiplicity is varied to target the different categories. A likelihood fit is defined as the product of the Poisson probabilities describing the observed events in the binned distributions from the expected number of events rescaled by the five multipliers which are left free to float in the fit. At last, the charge-flip and FNP backgrounds are estimated applying the extracted multipliers (which vary from 1.2 to 2.9) to the Monte Carlo prediction in signal regions. The dominant uncertainty of the method ($\simeq 80\%$) originates from different MC predictions, comparing the simulations from POWHEG-BOX+PYTHIA and SHERPA.

6.4.4 Expected fake/non-prompt background yields in signal regions

The expected yield for processes with fake leptons, estimated with the dynamic matrix method as well as MC Template Method are presented in Table 6.5 for the signal regions. The estimated yields are in good agreement in all SRs, except for Rpv2L1bS which is however affected by a high statistical error. The final numbers obtained for the fake lepton background estimate (also shown in this table) are taken as the weighted average of the predictions from the matrix method and the MC template method. The weights are based on the statistical component, and the systematic uncertainties are propagated assuming conservatively a full correlation between the two methods.
When the estimated yield is too small (below 0.15), the expected values is set to 0.15 ± 0.15 (e.g. RPV2L2bH), to cover for possibilities of an under-fluctuation of the number of baseline-not-signal leptons when applying the matrix method, as well as lack of statistics in the MC samples for the other method.

6.4.5 Charge-flip background

The main process leading to a misidentification of electric charge of a lepton is denoted as "trident event": an electron emits a hard photon via bremstrahlung which consequently decays into a e^+e^- pair. The charge-flip occurs when the main fraction of the original momentum is transferred to the electron with an electric charge opposite to the prompt electron (positron). A small contribution is also given by wrong track reconstruction of energetic leptons. These two processes are shown in Figure 6.7.
Figure 6.8 shows distributions of the invariant mass of opposite-sign and same-sign lepton pairs for electrons (left) and muons (right) at the Z resonance peak. The electron channel shows clearly a peak in the same-sign case, originated by the charge-flip, while the effect is negligible for muons. In addition, the same-sign invariant mass peak is shifted to lower values due to the loss of energy caused by the bremstrahlung.
A data-driven method is used to estimate the charge-flip rate in a defined control region and then

Region	Matrix method	MC template method	Final estimate
Rpc2L0bH	$0.83 \pm 0.56 \pm 0.74$	$1.00 \pm 0.96 \pm 0.81$	$0.87 \pm 0.48 \pm 0.76$
Rpc2L0bS	$1.51 \pm 0.60 \pm 0.66$	$1.68 \pm 1.02 \pm 1.26$	$1.55 \pm 0.52 \pm 0.81$
Rpc2L1bH	$3.54 \pm 1.62 \pm 3.12$	$2.07 \pm 0.63 \pm 1.56$	$2.26 \pm 0.59 \pm 1.76$
Rpc2L1bS	$2.69 \pm 1.25 \pm 2.07$	$2.48 \pm 1.32 \pm 1.86$	$2.59 \pm 0.91 \pm 1.97$
Rpc2L2bH	$-0.11 \pm 0.11 \pm 0.18$	< 0.5	$0.15 \pm 0.15 \pm 0.00$
Rpc2L2bS	$1.31 \pm 1.07 \pm 1.65$	$0.41 \pm 0.33 \pm 0.45$	$0.49 \pm 0.32 \pm 0.55$
Rpc2Lsoft1b	$4.75 \pm 1.42 \pm 2.64$	$2.48 \pm 1.32 \pm 1.86$	$3.53 \pm 0.97 \pm 2.22$
Rpc2Lsoft2b	$1.91 \pm 1.18 \pm 1.63$	$1.66 \pm 0.66 \pm 1.28$	$1.72 \pm 0.58 \pm 1.36$
Rpc3L0bH	$-0.01 \pm 0.11 \pm 0.10$	< 0.5	$0.15 \pm 0.15 \pm 0.00$
Rpc3L0bS	$2.31 \pm 1.50 \pm 2.63$	$0.21 \pm 0.15 \pm 0.16$	$0.23 \pm 0.15 \pm 0.18$
Rpc3L1bH	$0.57 \pm 0.43 \pm 0.50$	$0.42 \pm 0.29 \pm 0.32$	$0.47 \pm 0.24 \pm 0.38$
Rpc3L1bS	$4.94 \pm 1.83 \pm 2.96$	$3.55 \pm 1.80 \pm 2.76$	$4.23 \pm 1.28 \pm 2.86$
Rpc3LSS1b	$-0.18 \pm 1.24 \pm 2.85$	$0.90 \pm 0.14 \pm 0.69$	$0.89 \pm 0.14 \pm 0.72$
Rpv2L0b	$0.14 \pm 0.22 \pm 0.27$	$1.02 \pm 0.96 \pm 0.76$	$0.18 \pm 0.21 \pm 0.29$
Rpv2L1bH	$-0.06 \pm 0.03 \pm 0.09$	$0.60 \pm 0.35 \pm 0.48$	$0.15 \pm 0.15 \pm 0.00$
Rpv2L1bM	$1.70 \pm 2.07 \pm 1.68$	$1.20 \pm 0.69 \pm 0.95$	$1.25 \pm 0.65 \pm 1.02$
Rpv2L1bS	$16.49 \pm 4.04 \pm 18.70$	$4.46 \pm 1.67 \pm 3.45$	$6.22 \pm 1.54 \pm 5.68$
Rpv2L2bH	$-0.04 \pm 0.02 \pm 0.04$	< 0.5	$0.15 \pm 0.15 \pm 0.00$
Rpv2L2bS	$9.67 \pm 3.29 \pm 9.04$	$7.24 \pm 2.36 \pm 5.43$	$8.07 \pm 1.92 \pm 6.66$

Table 6.5: Expected yields for background processes with fake leptons, in the signal regions proposed. Uncertainties include all statistical and systematic sources for the nominal estimate. Values are presented in a *nominal*$\pm$*syst. err.*$\pm$*stat. err.* format.

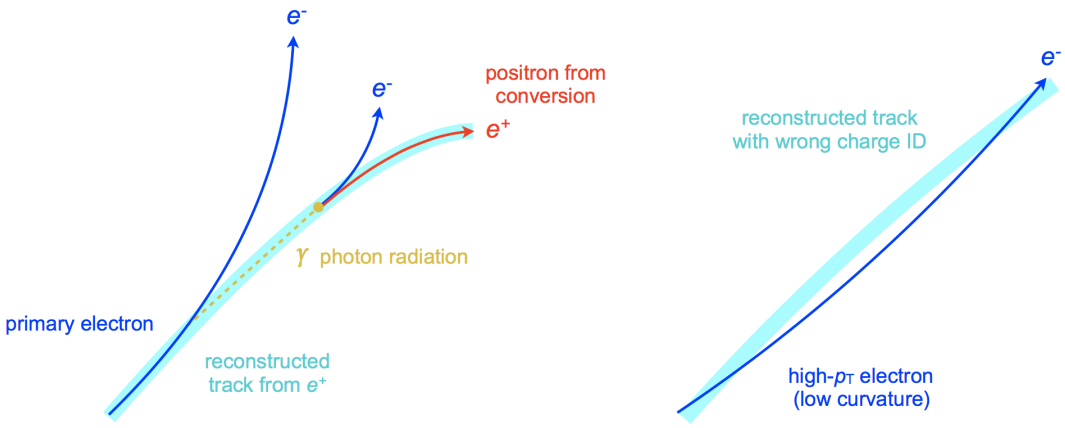

Figure 6.7: Processes leading to a charge mismeasurement: emittance of a bremsstrahlung photon with subsequent e^+e^- conversion (left). Wrong track reconstruction of an energetic lepton (right).

extrapolate the expected yields to the signal regions. Event yields are predicted considering pairs of opposite sign leptons (OS) in data with a weight w_{CF} assigned. Weights depend on the probability of a lepton charge to be mis-measured ($\xi_{1,2}$).

Rates are measured as a function of p_{T} and η, since the processes described have a significant dependency on the momentum and position of the particles in the detector:

$$w_{CF} = \xi_1 \cdot (1-\xi_2) + (1-\xi_1) \cdot \xi_2, \quad \xi_{1(2)} = \xi(p_{T,1(2)}, \eta_{1(2)}). \tag{6.8}$$

The sum of the weights assigned to the OS events passing signal region selection estimates the charge-flip contribution. The electron charge-flip probability ξ is extracted from a $Z \to e^+e^-$ data sample selecting SS and OS electron pairs in the Z mass window ($75 < m_{\ell\ell} < 100$ GeV). Subsequently, a

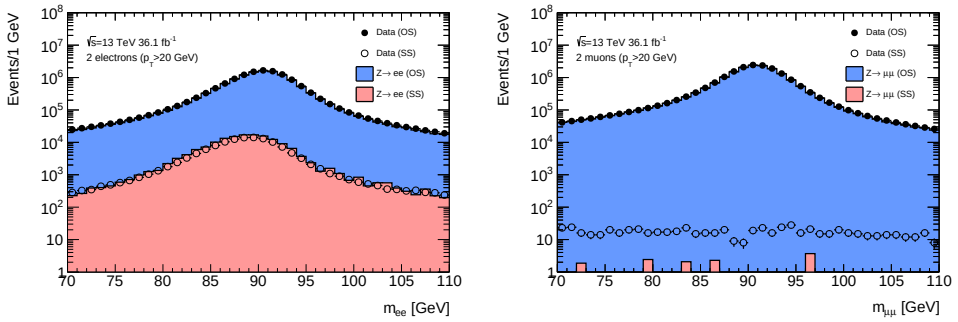

(a) (b)

Figure 6.8: Invariant mass distributions of opposite-sign and same-sign electron (left) and muon (right) pairs: the data is compared to simulated $Z_0 \to \ell\ell$ OS (blue) and SS (red) events.

likelihood fit is performed with $\xi_{1(2)}$ as free parameters and the number of SS and OS electron pairs as input variables. The charge-flip rate is extracted as a function of p_{T} and η and compared with values obtained from $Z \to e^+e^-$ Monte Carlo samples to validate the estimation.
The high number of OS events leads to a low statistical error in the estimation; additionally, systematic uncertainties related to simulation are not affecting this method. The measured charge-flip rates vary from 0.1 to 0.5%, for electrons reconstructed in the barrel part of the EM calorimeter ($|\eta| < 1.37$). However, electrons with higher pseudorapidity have significantly larger rates, up to 3% for energetic electrons.

6.5 Uncertainties on the background estimation

The SS/3L final state is rarely produced in SM processes. Therefore, the analysis is affected by a high relative statistical error. In addition, the methods used to estimate the background of the analysis are affected by several systematic uncertainties. In the following paragraph, the estimation of uncertainties for the prompt and FNP backgrounds is explained.

6.5.1 Theoretical uncertainties

The sources of theoretical uncertainties on prompt SM background processes can affect normalisation and shape of the MC simulation. Uncertainties on the cross-section affect the normalisation of MC samples, while an imperfect simulation will lead to imprecise shape of kinematic variables.
The uncertainty on the normalisation is originated by the uncertainty on the cross-section calculations: 6% for diboson processes [107] and 12-13% for $t\bar{t}V$ [108]. Modelling uncertainties are estimated by comparing different MC generators for $t\bar{t}V$ (MG5_AMC@NLO and SHERPA) in the signal regions; and varying renormalization, factorisation and resummation scales used in the diboson simulation computation.
The choice of PDF sets affects the results of MC simulations. Therefore, PDF parameters are varied by $\pm 1\sigma$ and propagated to the MC event weights with LHAPDF6 framework [109]. The different sources of theoretical uncertainties are added up quadratically and treated as a common nuisance parameter.
Theoretical uncertainties of main processes ($t\bar{t}V$ and VV) in each signal region are typically 30-35%. A flat 50% uncertainty is taken for the other processes (Rare), including cross-section, MC modelling

and PDF uncertainties. All variations from different SM processes are summed up in quadrature and treated as a single nuisance parameter.

6.5.2 Experimental uncertainties

In addition to the theoretical uncertainties, all experimental uncertainties on prompt processes are considered: luminosity, object reconstruction, trigger and pile-up reweighting. The uncertainties included in the statistical interpretation of the results are:

- **E-gamma scale/resolution:** uncertainties included to take into account imprecise measurement of E_T scale and resolution after the electron/photon energy calibration process [110]. The original set of 67 NP is reduced to one, since it simplifies the analysis without affecting the results. These uncertainties are negligible (<1% in all signal regions).
- **Electron efficiency:** uncertainties associated to electron efficiency, reconstruction and identification scale factors. Small contribution in signal regions (1-3%).
- **Muon scale/resolution:** as for electrons, uncertainties to assess inaccuracies of muons momentum scale and resolution corrections ($< 1\%$).
- **Muon efficiency:** similar to electrons, uncertainties associated to muon reconstruction, identification and isolation scale factors. Small contribution in signal regions (1-3%).
- **Jet energy scale/resolution:** uncertainties of the jet energy scale are estimated by varying the scale up and down by $\pm 1\sigma$ for each nuisance parameter and scaling each individual jet energy accordingly. Uncertainties on jet flavour, pile-up corrections, and η-dependence are included in the total 80 independent NP [71]. A four parameter reduced set is considered for this analysis. JES uncertainties on the normalisation range in 5-15%, while JER uncertainty is 1-3% in signal regions.
- **Flavour tagging:** Variations of the b-, c-, and light-jet efficiency scale factors are applied in jet p_{T} and η bins considering 6 different nuisance parameters. Uncertainties on flavour tagging scale factors are usually smaller than 10% and below 1% in b-jet vetoed signal regions.
- **Jet vertex tagger:** variations are applied to jets scale factors to cover pile-up dependency and differences rising from different MC generators. Uncertainties on JVT are negligible in all signal regions ($< 1\%$).
- $E_{\mathrm{T}}^{\mathrm{miss}}$ **hard/soft term:** imprecise calibrations of hard objects affect the calculated $E_{\mathrm{T}}^{\mathrm{miss}}$ value. Uncertainties associated to hard objects are propagated to $E_{\mathrm{T}}^{\mathrm{miss}}$ estimation and variations are derived. Soft term uncertainties reach up to 5% in signal regions.
- **Luminosity:** uncertainties estimated from calibration of the luminosity scale using beam-separation scans [86]: a total error of 3.2% is applied.
- **Trigger:** differences between data and MC in trigger efficiencies are corrected and evaluated for all triggers ($< 1\%$). For multi-object triggers and trigger combinations, the total uncertainty is computed from the individual uncertainties for each trigger.
- **Pile-up reweighting:** similarly, differences between simulation and data are corrected for the $< \mu >$ value: rescaled to cover full difference between applying and not-applying the nominal correction. The pile-up uncertainty due to reweighting is below 1% in all signal regions.

6.5.3 Data-driven methods uncertainties

The systematic uncertainties on the FNP estimation with the matrix method are evaluated separately for the real and fake rate[4].

The main source of systematic uncertainty in the real efficiency computation is the choice of the Z window mass range in the definition of the control region. By varying the considered mass range, different efficiencies are measured. In order to take into account this effect two extra mass ranges are considered: $75 < m_{\ell\ell} < 105$ GeV and $85 < m_{\ell\ell} < 95$ GeV. The efficiencies then are extracted and compared for each bin with respect to the nominal value, the largest difference is taken as systematic uncertainty for the corresponding p_{T}-η bin.

Other source of systematic uncertainties originate from varying the trigger strategy of the analysis and differences in the kinematics between control region and signal region (extrapolation to busy environment).

The fake rate is affected by two different kind of systematic uncertainties: the ones which are correlated between the different p_{T} and η bins and the uncorrelated one. In the first case, a source of systematic uncertainty is the contribution of the events with real leptons in the fake-enriched control region used to extract the efficiencies. To evaluate this, the expected yields from the prompt leptons in the CR (which is used in the fake lepton efficiency equation) is variated by 30% in both directions to obtain the variations in order to cover for the luminosity and cross-section uncertainties.

In the second case possible differences of the fake composition in the control region depending on the different kinematic cuts applied are taken into account. Alternative control regions are designed to estimate this variation. The overall uncertainties of the fake/non-prompt leptons in the total background estimates are between 18 and 21%, depending on the signal region.

Similarly, the charge-flip uncertainty is associated to the variation of the Z mass window from which the charge-flip rates are obtained. The range of mass window and side-band for background subtraction are varied by ± 5 GeV from the nominal values. For each (p_{T}, η) bin, the highest variation from nominal value is taken as uncertainty in that specific bin. Nevertheless, the dominant uncertainty is due to the high statistical error in the $Z \to ee$ data sample for same-sign events. The overall error of the charge-flip process ranges from 1 to 8 % in signal regions.

6.5.4 Uncertainties in signal regions

Figure 6.9 summarises the contributions of the different sources of systematic uncertainty on the total SM background predictions in the signal regions. The uncertainties amount to 25-45% of the total background depending on the signal region, dominated by the detector background uncertainties or the theory uncertainties.

[4] Systematic uncertainties resulting from the measurement of the ε_P and ε_F parameters, and their extrapolation to the signal regions, are propagated to uncertainties on the event weight through standard first-order approximations. The different sources of uncertainties are tracked separately so that correlations of uncertainties across different events can be accounted for correctly. The resulting set of uncertainties on the cumulated event weights are then added in quadrature to form the systematic uncertainty on the predicted fake lepton background yield. The corresponding statistical uncertainty is taken as the RMS of the event weights.

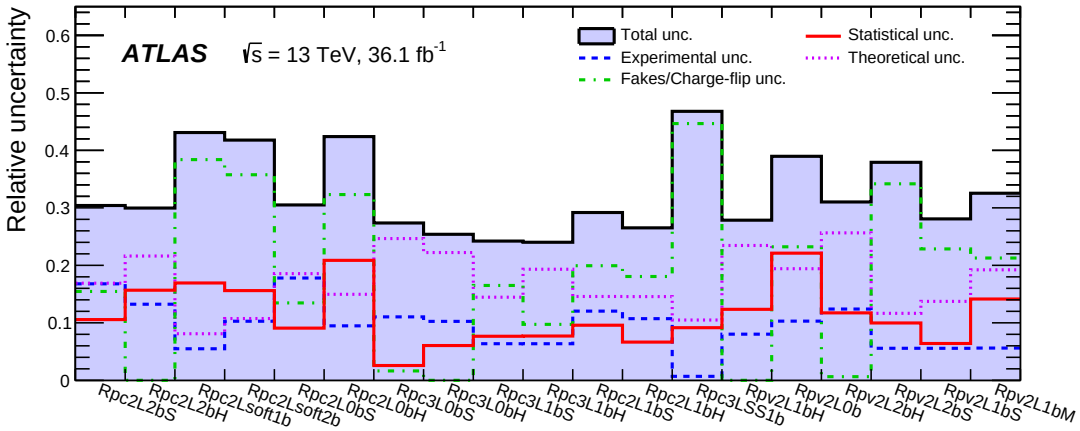

Figure 6.9: Relative uncertainties on the total background yield estimation in each signal region [105].

6.6 Background validation

Once all sources of background have been estimated, it is crucial to check the reliability of the results obtained. The validity of data-driven methods is evaluated comparing distributions of several kinematic variables in data and background prediction. Requirements on $E_{\mathrm{T}}^{\mathrm{miss}}$, jet multiplicity and b-jet multiplicity are loosen to guarantee a small signal contamination.

Figure 6.10 shows kinematic distributions after requiring at least two jets ($p_{\mathrm{T}} > 40$ GeV) and $E_{\mathrm{T}}^{\mathrm{miss}} > 50$ GeV, as well as at least two same-sign leptons ((a), (b), (c)) or three leptons (d). All distributions show a good agreement between data and background prediction apart from some deviation at high m_{eff}. This region is however dominated by diboson production, and will not be affected by the FNP and charge-flip estimate.

Estimation from MC simulation of main prompt background is validated in 5 dedicated Validation Regions (VR): $t\bar{t}W$, $t\bar{t}Z$, WZ4j, WZ5j and $W^{\pm}W^{\pm}jj$. Kinematic cuts are optimised to obtain the highest purity in the background composition and the lowest signal contamination. All VRs are additionally vetoing all events belonging to any SRs to ensure orthogonality with it. Table 6.6 summarises the kinematic selection. The obtained purity goes from 35% up to 65%, while signal contamination of models near the limit of exclusion is 20% in $t\bar{t}W$ and below 5% in all other VRs. Table 6.7 shows observed yields in these validation regions, compared with the background predictions. The agreement is good in all VRs.

Validation Region name	$N_{\mathrm{lepton}}^{\mathrm{signal}}$	$N_{\mathrm{b\text{-}jets}}$	N_{jets}	$p_{\mathrm{T,jet}}$ [GeV]	$E_{\mathrm{T}}^{\mathrm{miss}}$ [GeV]	m_{eff} [GeV]	Other
$t\bar{t}W$	=2SS	≥ 1	$\geq 4(e^{\pm}e^{\pm},e^{\pm},\mu^{\pm})$ $\geq 3(\mu^{\pm}\mu^{\pm})$	>40 >25	>45	>550	$p_T(l_2) > 40$ GeV $\sum p_T^{\text{b-jet}} / \sum p_T^{\text{jet}} > 0.25$
$t\bar{t}Z$	≥ 3 ≥ 1 SFOS pair	≥ 1	≥ 3	>35	-	>450	81<m_{SFOS}<101 GeV
WZ4j	= 3	= 0	≥ 4	> 25	-	>450	$E_{\mathrm{T}}^{\mathrm{miss}}/\sum p_T^l < 0.7$
WZ5j	= 3	= 0	≥ 5	> 25	-	>450	$E_{\mathrm{T}}^{\mathrm{miss}}/\sum p_T^l < 0.7$
$W^{\pm}W^{\pm}jj$	= 2 SS	= 0	≥ 2	> 50	> 55	> 650	veto 81 < $m_{e^{\pm}e^{\pm}}$ < 101 GeV $p_T^{l_2} > 30$ GeV $\Delta R_\eta(l_{1,2}, j) > 0.7$ $\Delta R_\eta(l_1, l_2) > 1.3$

Table 6.6: Summary of the event selection in the validation regions. In all VRs, events belonging to SRs are vetoed to avoid any signal contamination. In $t\bar{t}W$ VR, the requirement on the number of jets varies depending on the leptonic flavour.

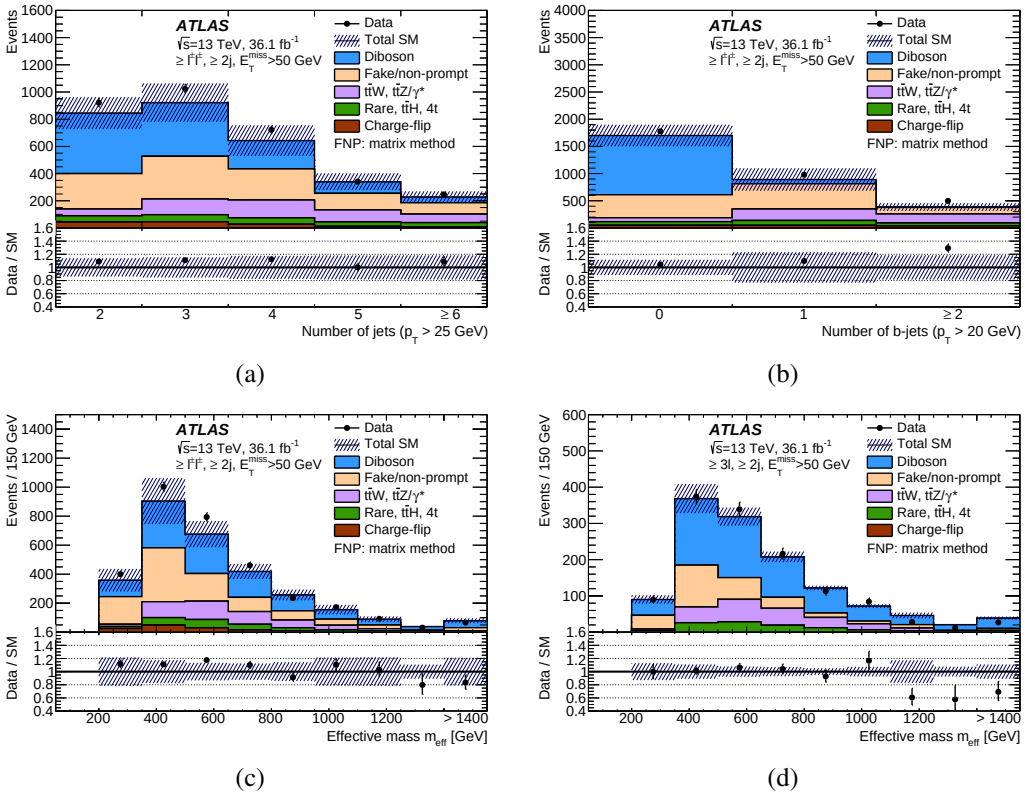

Figure 6.10: Distributions of the number of jets (a), of b-tagged jets (b) and the effective mass ((c), (d)). The statistical uncertainties in the background prediction are included in the uncertainty band, as well as the full systematic uncertainties for backgrounds with fake or non-prompt leptons, or charge-flip. In all figures, the last bin contains the overflow [105].

6.7 Statistical interpretation

6.7.1 Fit and p-values

Once the analysis strategy is defined and the event selection has been performed, it is of general interest to analyse specific distribution of variables among the candidate event samples. The goal is to compare distributions from data and theory and to extract physical quantities of interests via a fit to the data distribution:

- **Define the hypothesis:** theoretical function $y(x, \underline{\theta})$, with x as set of variables and $\underline{\theta}$ as set of parameters.
- **Define the test statistics *t*:** variable with a known probability density function (pdf). If the experiment is performed many times, the distribution of extracted t values will follow the defined pdf (if the hypothesis is correct).
- **Evaluate experimental results:** parameters $\underline{\theta}$ are adjusted to obtain the best agreement between data and theory. Then t is evaluated from data (t^*) and compared with the pdf. If t^* is in a region of high probability, then the hypothesis is likely to be correct; while if it belongs to a region with very low probability, it might be possible to exclude the hypothesis.

Validation regions	$t\bar{t}W$	$t\bar{t}Z$	WZ4j	WZ5j	$W^{\pm}W^{\pm}jj$
$t\bar{t}Z/\gamma^*$	6.2±0.9	123±17	17.8±3.5	10.1±2.3	1.06±0.22
$t\bar{t}W$	19.0±2.9	1.71±0.27	1.30±0.32	0.45±0.14	4.1±0.8
$t\bar{t}H$	5.8±1.2	3.6±1.8	1.8±0.6	0.96±0.34	0.69±0.14
$t\bar{t}t\bar{t}$	1.02±0.22	0.27±0.14	0.04±0.02	0.03±0.02	0.03±0.02
$W^{\pm}W^{\pm}$	0.5±0.4	-	-	-	26±14
WZ	1.4±0.8	29±17	200±110	70±40	27±14
ZZ	0.04±0.03	5.5±3.1	22±12	9±5	0.53±0.30
Rare	2.2±0.5	26±13	7.3±2.1	3.0±1.0	1.8±0.5
Fake/non-prompt leptons	18±16	22±14	49±31	17±12	13±10
Charge-flip	3.4±0.5	-	-	-	1.74±0.22
Total SM background	57±16	212±35	300±130	110±50	77±31
Observed	71	209	257	106	99
Ratio Obs./Exp.	1.25	0.99	0.86	0.96	1.29

Table 6.7: The number of observed data and expected background events in the validation regions. Background categories shown as a "-" denote that they cannot contribute to a given region (e.g. charge flips in 3-lepton regions) or that their estimates is lower than 0.01 events. The displayed yields include all sources of statistical and systematic uncertainties, except for the theoretical uncertainties which only affect the inclusive production cross-sections.

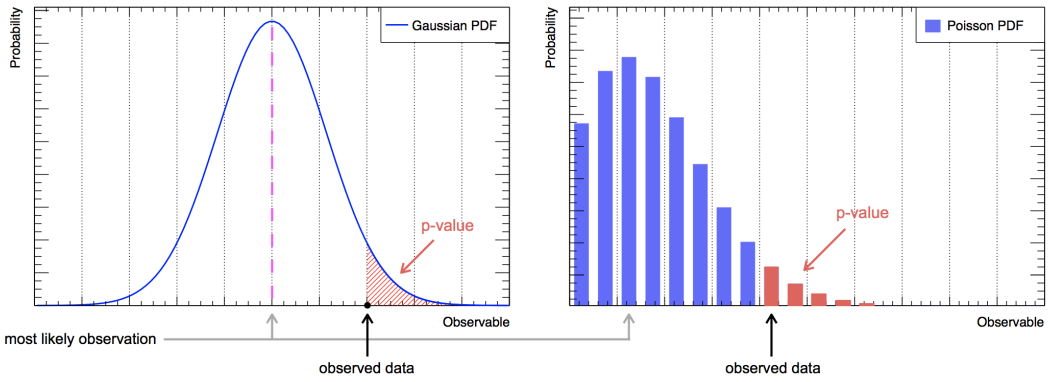

Figure 6.11: Examples for a p-value computation with a Gaussian (left) and Poisson (right) PDF. The p-value is given by the red area limited by the observed result.

In the context of a BSM analysis, the goal is to test the "SM-only" hypothesis set as null-hypothesis. Supposing to have a known pdf of the test statistics for the given hypothesis H_0. Once the fit is performed and t^* is obtained, it is possible to evaluate the validity of the null-hypothesis. The 'p-value' p_0 gives the probability that, if H_0 is true, the result of the experiment will fluctuate as much or more than t^* and is defined as:

$$p_0 = \int_{t^*}^{\infty} f(t|H_0)dt. \tag{6.9}$$

In other words, if the experiment is repeated and H_0 is true, p_0 is the fraction of times that $t > t^*$. Figure 6.11 shows two examples with a Gaussian (left) and a Poisson pdf (right). If the red area is small, the hypothesis is wrong or there was an anomalous large fluctuation.

The process described above is a simplification of the computation done in the analysis. The PDFs have to describe the observed number of events and constrain the nuisance parameters, parameters to be accounted in the test statistics but not of immediate interest. Additionally, correlations among different NP and NP correlating across different source of background have to be considered. This is done with a set of Gaussian PDFs (description of NP) convoluted with a Poisson PDF (observed events).

6.7.2 CL_S method

In all ATLAS analyses a modified frequentist approach is used to set upper and lower limits in new physics searches: the CL_S method. The number of expected events y, after applying the analysis selection, is defined as:

$$y = \mu s + b \tag{6.10}$$

where b is the number of events expected from SM processes (background), s is the number of events produced by the searched phenomenon (signal) and μ is the signal strength.
If μ=1, the signal has the rate predicted by theory, while μ=0 corresponds to an absence of new physics. The signal strength is defined as:

$$\mu = \frac{\sigma}{\sigma_{th}} \tag{6.11}$$

where σ_{th} is the cross-section predicted by the new theory and σ is the observed cross-section.
After defining a proper likelihood for the type of analysis, a test statistics q_μ can be defined as:

$$q_\mu = -2\ln\frac{L(\mu, \hat{\hat{\underline{\theta}}})}{L(\hat{\mu}, \underline{\hat{\theta}})} \tag{6.12}$$

where $\hat{\mu}$ and $\underline{\hat{\theta}}$ are the best values of the parameters obtained when maximising L; while $\hat{\hat{\underline{\theta}}}$ are the values of the NP when maximising L at fixed μ. The defined test statistics is called *profile likelihood ratio* since the NPs are profiled in order to maximise the likelihood when setting the parameter of interest.
Since it is a likelihood-ratio approach, the *Neyman-Person lemma* [111] ensures that the *likelihood ratio* is the most powerful test-statistics to reject a null-hypothesis.

Discovery
If a significant excess of data over the background is observed, a new discovery can be claimed if the null hypothesis H_0 is rejected. A test on the background-only hypothesis is done using the test statistics q_0 (setting $\mu = 0$):

$$q_0 = -2\ln\frac{L(0, \hat{\hat{\underline{\theta}}})}{L(\mu, \underline{\hat{\theta}})} \tag{6.13}$$

The p-value is simply defined as:

$$p_0 = \int_{q_0^{obs}}^{\infty} f(q_0|0)dq_0 \tag{6.14}$$

where q_0^{obs} is the value of q_0 observed with data.
If p_0 is below the defined limit, the hypothesis is rejected and a discovery has been made. The convention typically used in high-energy physics experiments is to declare an excess (evidence) at 3σ and a discovery when reaching 5σ.

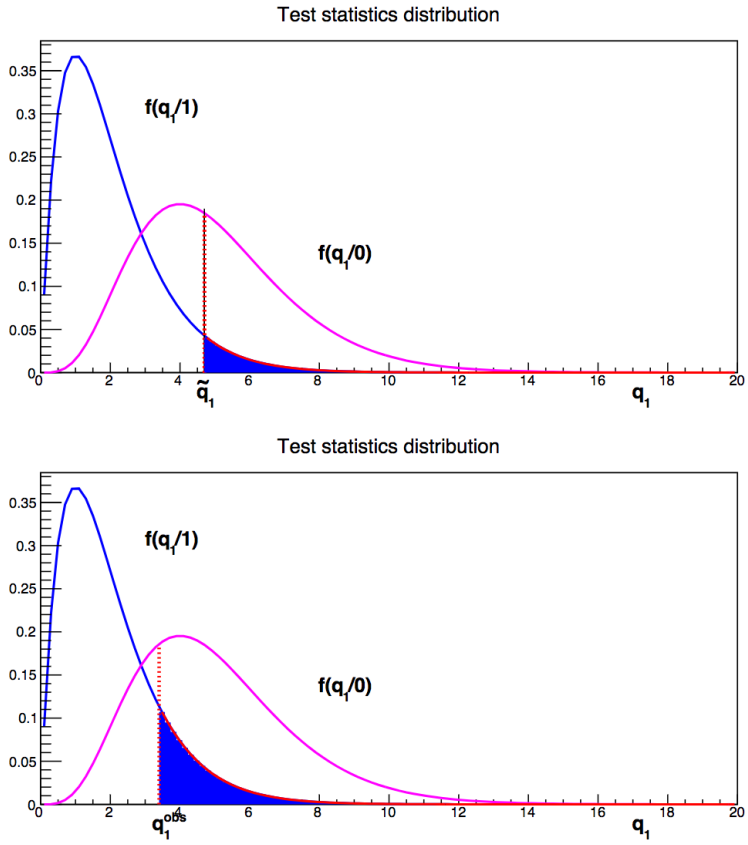

Figure 6.12: Example of q_1 distributions in the two hypotheses, namely μ = 1 and μ= 0. The separation between the two distributions indicate the capability to discriminate the two hypotheses.

Signal exclusion

Equation 6.12 can be used to exclude a given theory model. If μ=1, meaning that signal is expected, the test statistics becomes:

$$q_1 = -2\ln\frac{L(1,\hat{\hat{\theta}})}{L(\hat{\mu},\hat{\theta})} \tag{6.15}$$

The lower q_1, the more compatible are data and the proposed theory model, and in opposite the less compatible with a background-only expectation. In order to determine the discriminating power between searched model and background, two pdfs are defined: $f(q_1|0)$ evaluated from MC samples of pure background ($\mu = 0$) and $f(q_1|1)$ from MC samples generated with $\mu = 1$. Figure 6.12 shows an example of q_1 distribution in the two hypotheses.

The sensitivity of experiments is evaluated by taking the median of $f(q_1|0) \equiv \tilde{q}_1$ as the average expected result of a background-only experiment. The median is used to define the expected confidence level:

$$CL_{s+b}^{exp} = \int_{\tilde{q}_1}^{\infty} f(q_1|1)dq_1 \tag{6.16}$$

where CL_{s+b}^{exp} is the blue area in Figure 6.12 (top) and it represents the median confidence level with which the signal is excluded. Once the data have been collected, the value q_1^{obs} will define the observed confidence level:

$$CL_{s+b}^{obs} = \int_{\tilde{q}_1^{obs}}^{\infty} f(q_1|1)dq_1. \tag{6.17}$$

If it is below 5%, the signal model is excluded at 95% confidence level (CL).

The method explained is not protected from possible "under-fluctuations" of the background, which would lead to a wrong exclusion of a signal model. ATLAS analyses use the CL_s approach to avoid this problem, using a slightly different definition of confidence level:

$$CL_s = \frac{CL_{s+b}}{CL_b} \tag{6.18}$$

where CL_b is defined as:

$$CL_b = \int_{\tilde{q}_1^{obs}}^{\infty} f(q_1|0)dq_1 \tag{6.19}$$

CL_s is always larger than CL_{s+b} and allows to be more conservative and to protect the results from background fluctuations.

Upper limit

Similarly, upper limits on the signal strength may be obtained. In equation 6.12, q_μ is a function of the signal strength μ with a minimum at $\mu = \hat{\mu}$. To define an upper limit on the signal strength, the value μ^* is defined as the value of μ for which CL_S is equal to 1-α, where α is the required confidence level. A scan of μ is performed (when μ is increasing, CL_S is decreasing), until the value μ^* is found. Model-independent upper limits may be computed for an arbitrary signal model, allowing theorists to test their models in the defined SRs.

The signal strength μ is treated as a free parameter and the model independent upper limit is defined on the number of expected signal events in the considered SR. The number of signal events are then normalised to the integrated luminosity $\mathscr{L}_{int}$ and can be interpreted as upper limits on the visible signal cross-section σ_{vis}, defined as:

$$\sigma_{vis}^{obs(exp)} = \sigma_{prod} \times A \times \varepsilon = \frac{N_{BSM}^{obs(exp)}}{\mathscr{L}_{int}}, \tag{6.20}$$

where σ_{prod} is the signal production cross-section, A is the detector acceptance and ε the reconstruction efficiency.

The statistical interpretation of the results of SS3L analysis have been computed with the *HistFitter* software framework [112].

6.8 Results in signal regions

The observed event yields for data and the expected SM background are shown in Figure 6.13 and are summarised in Table 6.8 for all signal regions, including statistical and systematic uncertainties.

Figure 6.14 shows the relative contribution of all rare processes for each signal region. Triboson production is dominant when b-jets are vetoed, while tWZ and $t\bar{t}WW$ are mostly contributing when at least one b-jet is required.

Since no significant deviation from SM background is observed, upper limits on BSM production and model-dependent exclusion limits are computed. Confidence intervals are defined with a CL_S method at 95% confidence level. A profile-likelihood-ratio test is used, where the likelihood is constructed as the product of a Poisson pdf and a Gaussian distribution (as described above). The hypothesis tests are computed individually for each signal region.

Table 6.9 shows model-independent upper limits at 95% C.L. on the number of observed (expected) BSM events in the signal regions: $S_{obs}^{95}(S_{exp}^{95})$. The limits are also normalised to the integrated luminosity and expressed in limits on the visible signal cross-sections $\sigma_{\text{vis}}^{\text{obs}}$ ($\sigma_{\text{vis}}^{\text{exp}}$). The computation is done

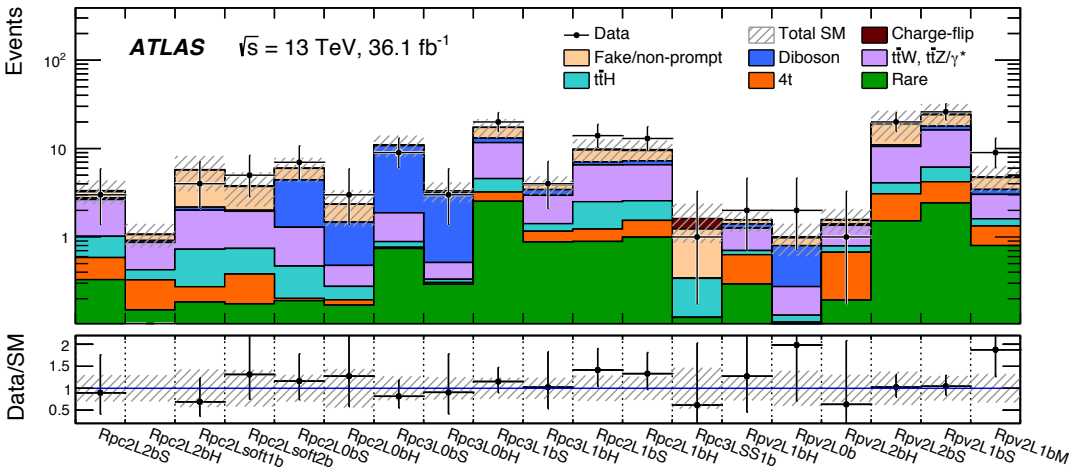

Figure 6.13: Observed and expected event yields in the signal regions for an integrated luminosity of 36.1 fb^{-1}. The bottom panel shows the ratio between data and the SM prediction. The uncertainty bands include all experimental and theoretical systematic uncertainties as well as the statistical errors [105].

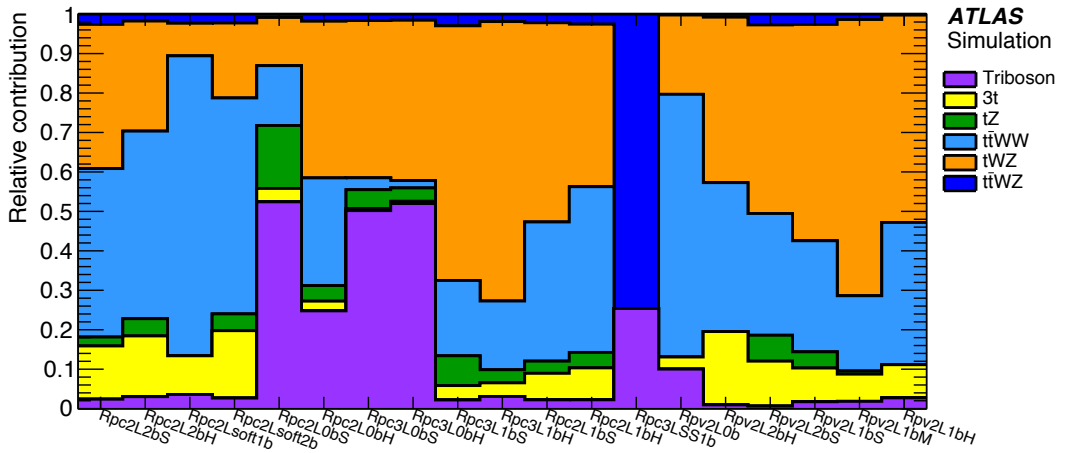

Figure 6.14: Relative contribution in each signal region from the processes in the category labelled as rare ($t\bar{t}WW$, $t\bar{t}WZ$, $t\bar{t}WZ$, tZ, tWZ, $t\bar{t}t$, WH, ZH and triboson production) [105].

with the method explained above using 10^4 pseudo-experiments to derive observed and expected upper limits at 95% CL. For all the considered SUSY signal benchmark scenarios, exclusion limits at 95% CL with pseudo-experiments are set on the SUSY particles masses.

Figure 6.15 shows the exclusion limits for the main RPC models, all other limits are shown in appendix A. Exclusion limits are shown in a two-dimensional plane with the sparticles masses as variables. The expected limit, computed considering MC simulation, is shown with a $\pm 1\sigma$ yellow band contour, which includes all statistical and systematic uncertainties, while the observed limit is shown with a solid red line along with the up and down variation due to the signal theory uncertainty as red dotted lines. The grey numbers show the upper limits on the signal cross-section (in fb) for a specific mass point.

As mentioned previously, two different SRs have been defined[5] to target each signal benchmark.

[5]Four different SRs for the gluino pair production with stop-mediated decay to gain sensitivity in the region of the phase space with production of off-shell top quarks.

Signal region	Rpc2L2bS	Rpc2L2bH	Rpc2Lsoft1b	Rpc2Lsoft2b	Rpc2L0bS	Rpc2L0bH
Observed events	3	0	4	5	7	3
Total background	3.3±1.0	1.80±0.32	5.8±2.5	3.8±1.6	6.0±1.8	2.4±1.0
Fake/non-prompt leptons	0.5±0.6	0.15±0.15	3.5±2.4	1.7±1.5	1.6±1.0	0.9±0.9
Charge-flip	0.10±0.01	0.02±0.01	0.08±0.02	0.08±0.02	0.05±0.01	0.01±0.01
$t\bar{t}$+W/Z	1.6±0.4	0.44±0.14	1.3±0.4	.21±0.33	0.82±0.31	0.20±0.10
Diboson	0.10±0.10	.04±0.02	0.17±0.09	0.05±0.03	3.1±1.4	1.0±0.5
$t\bar{t}$+H	0.43±0.25	0.10±0.06	0.45±0.24	0.36±0.21	0.27±0.15	.08±0.07
$t\bar{t}t\bar{t}$ (4-top)	0.26±0.13	0.18 ±0.09	0.09±0.05	0.21±0.11	0.01±0.01	0.02±0.02
Rare	0.33±0.18	0.15±0.09	.18±0.10	0.17±0.10	±0.19±0.11	0.17±0.10
p-value	0.71	.91	0.69	0.30	0.36	0.35
Significance	-	-	-	0.5σ	0.4σ	0.4σ

Signal region	Rpc3L0S	Rpc3L0bH	Rpc3L1bS	Rpc3L1bH	Rpc2L1bS	Rpc2L1bH	Rpc3LSS1b
Observed events	9	3	20	4	14	13	1
Total background	11.0±3.0	3.3±0.8	17±4	3.9±0.9	9.8±2.9	9.8±2.6	1.6±0.8
Fake/non-prompt leptons	0.23±0.23	0.15±0.15	4.2±3.1	0.5±0.5	2.5±2.2	2.3±1.9	0.9±0.7
Charge-flip	-	-	-	-	0.25±0.04	0.25±0.05	0.39±0.08
$t\bar{t}$+W/Z	0.98±0.25	0.18±0.08	7.1±1.1	1.54±0.28	4.0±1.0	4.0±0.9	-
Diboson	8.9±2.9	2.6±0.8	1.4±0.5	0.48±0.17	0.5±0.3	0.7±0.3	-
$t\bar{t}$+H	0.12±0.08	0.03±0.02	1.4±0.7	0.25±0.14	1.3±0.7	1.0±0.6	0.22±0.12
$t\bar{t}t\bar{t}$ (4-top)	0.02±0.01	0.01±0.01	0.7±0.4	0.28±0.15	0.34±0.17	0.54±0.28	-
Rare	0.7±0.4	0.29±0.16	2.5±1.3	0.9±0.5	0.9±0.5	1.0±0.6	0.12±0.07
p-value	0.72	0.85	0.32	0.46	0.17	0.21	0.56
Significance	-	-	0.5σ	0.1σ	1.0σ	0.8σ	-

Signal region	Rpv2L1bH	Rpv2L0b	Rpv2L2bH	Rpv2L2bS	Rpv2L1bS	Rpv2L1bM
Observed events	2	2	1	20	26	9
Total background	1.6±0.4	1.0±0.4	1.6±0.5	19±7	25±7	4.8±1.6
Fake/non-prompt leptons	0.15±0.15	0.18±0.31	0.15±0.15	8±7	6±6	1.3±1.2
Charge-flip	0.02±0.01	0.03±0.02	0.03±0.01	0.46±0.08	0.74±0.12	0.10±0.02
$t\bar{t}$+W/Z	0.56±0.14	0.14±0.08	0.56±0.15	6.5±1.3	10.1±1.7	1.4±0.5
Diboson	0.14±0.06	0.52±0.21	0.04±0.02	0.42±0.16	1.7±0.6	0.42±0.15
$t\bar{t}$+H	0.07±0.05	0.02±0.02	0.12±0.07	1.0±0.5	1.9±1.0	0.28±0.15
$t\bar{t}t\bar{t}$ (4-top)	0.34±0.17	0.01±0.01	0.48±0.24	1.6±0.8	1.8±0.9	0.53±0.27
Rare	0.29±0.17	0.10±0.06	0.19±0.13	1.5±0.8	2.4±1.2	0.8±0.4
p-value	0.33	0.19	0.55	0.48	0.44	0.07
Significance	0.4σ	0.9σ	-	0.1σ	0.2σ	1.5σ

Table 6.8: Observed and expected numbers of events in the signal regions for an integrated luminosity of 36.1 fb^{-1}. Background categories shown as "-" do not contribute to a region. The respective p-values and significances are also stated. Significances indicated as "-" correspond to regions with more expected than observed events ($p_0 > 0.5$).

The final exclusion limit is computed by taking the SRs with the best expected exclusion power. Figure 6.16 shows which SRs have been considered, per each signal point, in the four main considered RPC models.

Exclusion limits for direct production of right-handed down squarks with RPV decays, NUHM2 model and $\tilde{t}_1\tilde{t}_1^*$, which leads to a signature with three leptons with the same electric charge, are shown as a function of one free parameter. Figure 6.17 shows the observed and expected upper limit on the production cross-section times branching ratio ($\sigma_{\text{prod}} \times \text{BR}$) in pb.

Signal region	S^{96}_{obs}	S^{95}_{exp}	σ^{obs}_{vis} [fb]	σ^{exp}_{vis} [fb]
Rpc2L2bS	5.5	$5.6^{+2.2}_{-1.5}$	0.15	$0.16^{+0.06}_{-0.04}$
Rpc2L2bH	3.6	$3.9^{+1.4}_{-0.4}$	0.10	$0.11^{+0.04}_{-0.01}$
Rpc2Lsoft1b	6.3	$7.1^{+2.5}_{-1.5}$	0.17	$0.20^{+0.07}_{-0.04}$
Rpc2Lsoft2b	7.7	$6.2^{+2.6}_{-1.5}$	0.21	$0.17^{+0.07}_{-0.04}$
Rpc2L0bS	8.3	$7.5^{+2.6}_{-1.8}$	0.23	$0.20^{+0.07}_{-0.05}$
Rpc2L0bH	6.1	$5.3^{+2.1}_{-1.3}$	0.17	$0.16^{+0.06}_{-0.04}$
Rpc3L0bS	8.3	$9.3^{+3.1}_{-2.3}$	0.23	$0.26^{+0.09}_{-0.06}$
Rpc3L0bH	5.4	$5.5^{+2.2}_{-1.5}$	0.15	$0.16^{+0.06}_{-0.04}$
Rpc3L1bS	14.7	$12.6^{+5.1}_{-3.4}$	0.41	$0.35^{+0.14}_{-0.10}$
Rpc3L1bH	6.1	$5.9^{+2.2}_{-1.8}$	0.17	$0.16^{+0.06}_{-0.05}$
Rpc2L1bS	13.7	$10.0^{+3.7}_{-1.6}$	0.38	$0.28^{+0.10}_{-0.05}$
Rpc2L1bH	12.4	$9.7^{+3.4}_{-2.6}$	0.34	$0.27^{+0.09}_{-0.07}$
Rpc3LSS1b	3.9	$4.0^{+1.8}_{-0.3}$	0.11	$0.11^{+0.05}_{-0.01}$
Rpv2L1bH	4.8	$4.1^{+1.9}_{-0.4}$	0.13	$0.11^{+0.05}_{-0.01}$
Rpv2L0b	5.2	$4.0^{+1.7}_{-0.3}$	0.14	$0.11^{+0.05}_{-0.01}$
Rpv2L2bH	3.9	$4.1^{+1.8}_{-0.4}$	0.11	$0.11^{+0.05}_{-0.01}$
Rpv2L2bS	17.5	$16.8^{+5.2}_{-4.2}$	0.48	$0.47^{+0.14}_{-0.12}$
Rpv2L1bS	18.1	$17.2^{+5.9}_{-4.2}$	0.50	$0.48^{+0.16}_{-0.12}$
Rpv2L1bM	11.4	$7.3^{+2.5}_{-1.8}$	0.31	$0.20^{+0.07}_{-0.05}$

Table 6.9: Observed and expected model-independent upper limits on the number of BSM events (N_{BSM}) and on the visible signal cross-sections (σ_{vis}) for the 2016 signal regions.

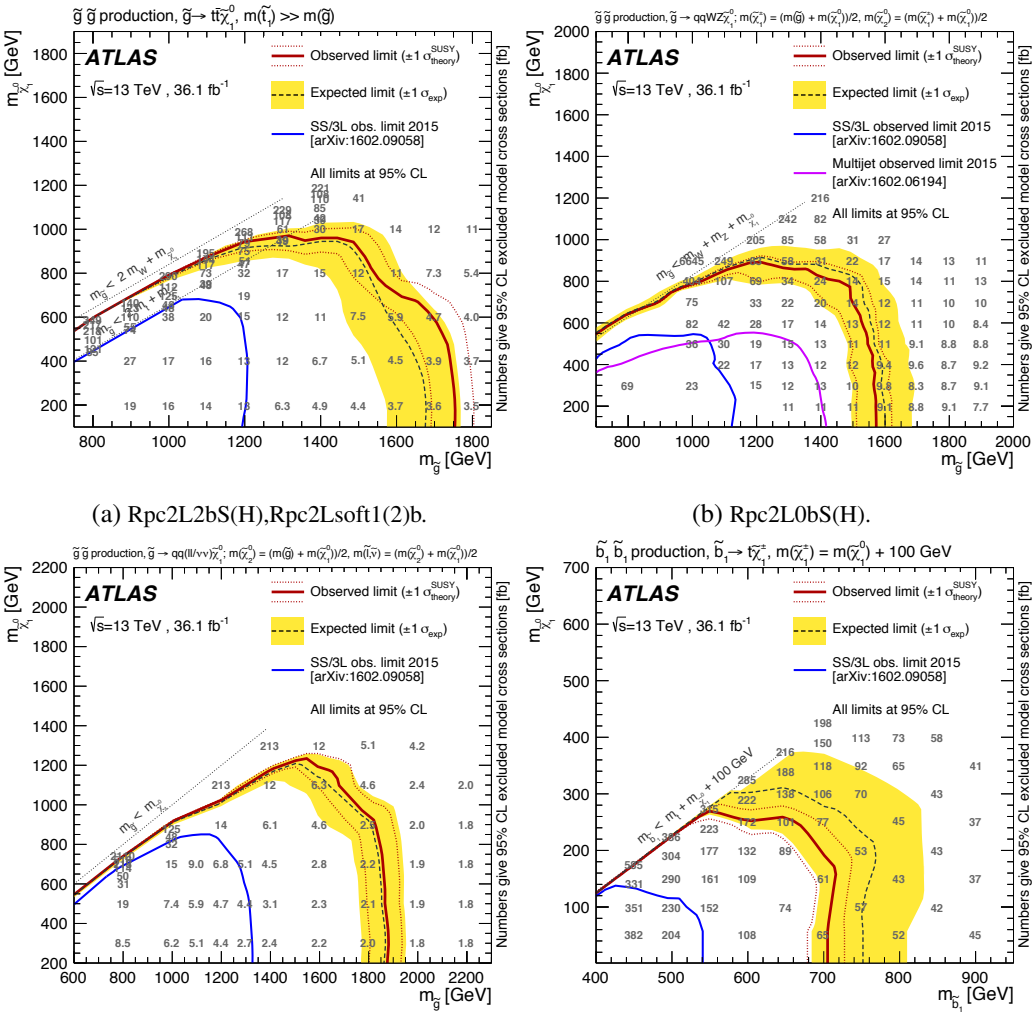

(a) Rpc2L2bS(H),Rpc2Lsoft1(2)b.

(b) Rpc2L0bS(H).

(c) Rpc3L0bS(H).

(d) Rpc2L1bS(H).

Figure 6.15: Observed and expected exclusion limits on superpartner masses in the context of the four main RPC SUSY scenarios for 36.1 fb^{-1}. All limits are computed at 95% CL. The dotted lines around the observed limit illustrate the change in the observed limit as the nominal signal cross-section is scaled up and down by the theoretical uncertainty. The contours of the band around the expected limit are the $\pm 1\sigma$ results including all uncertainties except the theoretical ones on the signal cross-section. The diagonal lines indicate the kinematic limit for the decays in each specified scenario and results are compared with the observed limits obtained by previous ATLAS searches [113, 114]. The SRs used to obtain the combined limit for each scenario are specified in the subtitles [105].

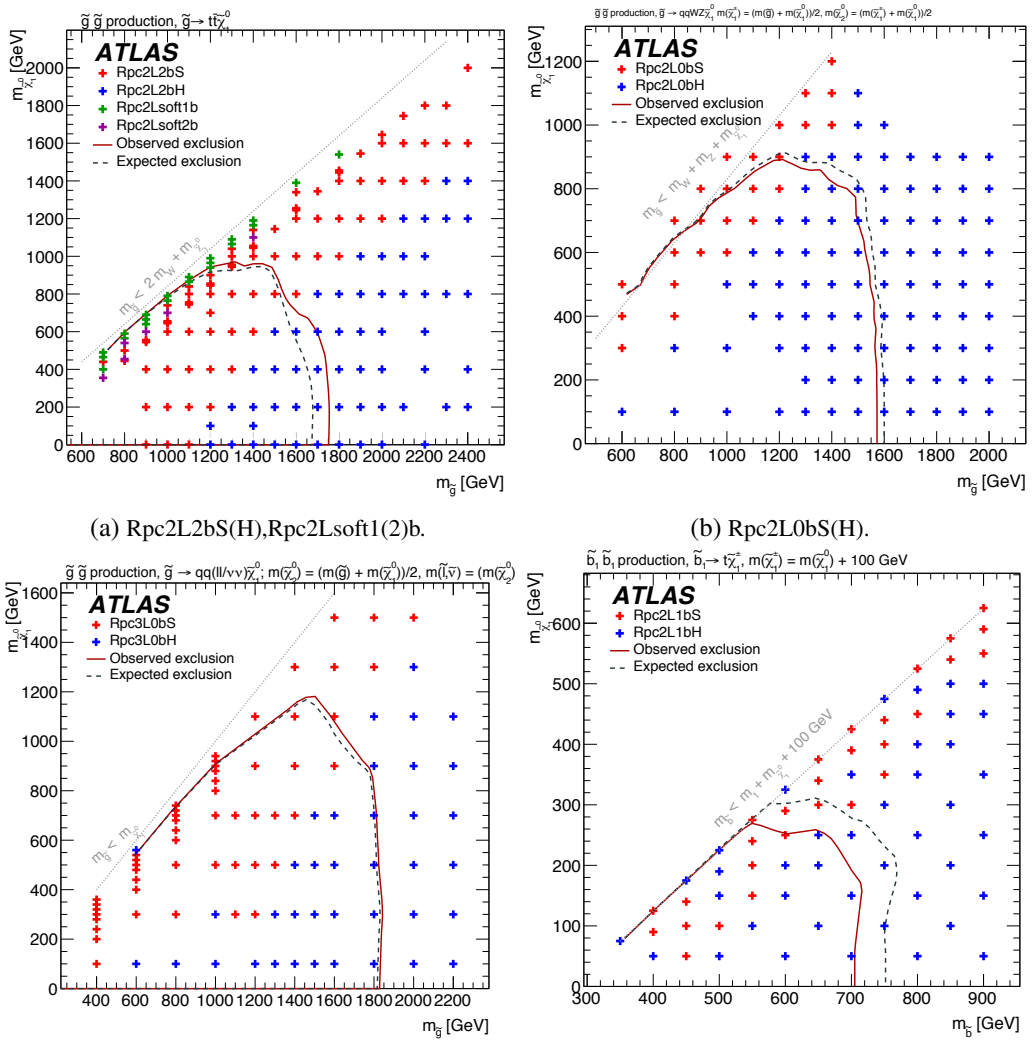

(a) Rpc2L2bS(H),Rpc2Lsoft1(2)b.

(b) Rpc2L0bS(H).

(c) Rpc3L0bS(H).

(d) Rpc2L1bS(H).

Figure 6.16: The best expected signal region per signal grid point. The SRs chosen for the individual signal points are indicated in different colours. These configurations are then used to set the final combined exclusion limits. The expected (dashed grey line) and observed (solid red line) exclusion limits are also shown. The diagonal lines indicate the kinematic limit for the decays in each specified scenario [105].

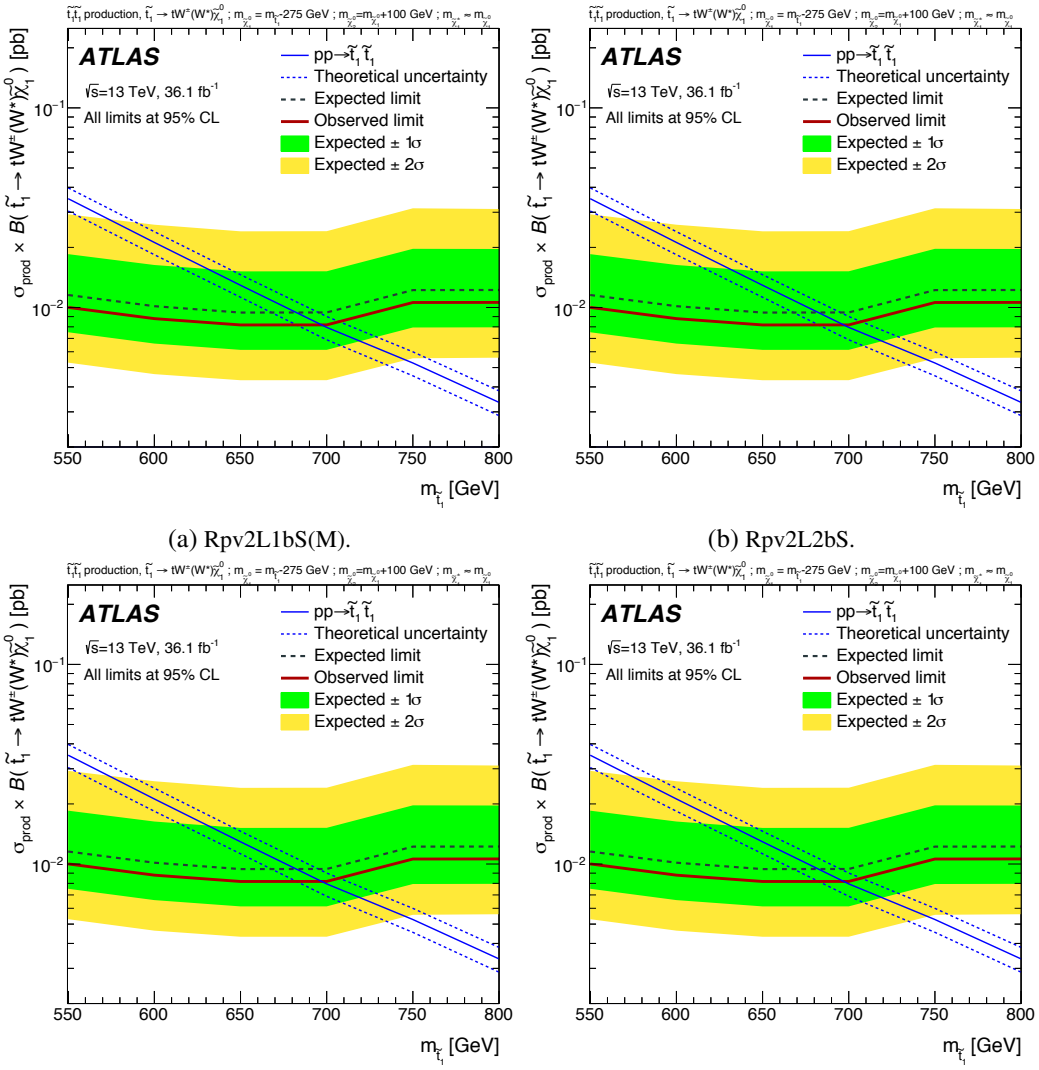

(a) Rpv2L1bS(M).

(b) Rpv2L2bS.

(c) Rpc3LSS1b.

(d) Rpc2L2bH.

Figure 6.17: Observed and expected upper limits on $\sigma_{\text{prod}} \times \text{BR}$ (in pb). The contours of the band around the expected limit are the $\pm 1\sigma$ (green) and $\pm 2\sigma$ (yellow) results including all uncertainties except the theoretical ones on the signal cross-section. The blue and red line show the theoretical expectation for the considered signal model, in Fig. (a) and (b) two different values of gluino are considered. The nominal signal cross-section is scaled up and down by the theoretical uncertainty (dashed blue and red lines). The SRs used to obtain the combined limit for each scenario are specified in the subtitles [105].

Chapter 7

Electroweak SUSY production

7.1 SUSY at electroweak scale

The ATLAS collaboration has placed stringent limits on the masses of gluino and squarks for several SUSY scenarios. Figure 7.1 shows a summary of the exclusion limits obtained with the complete set of SUSY analyses.
A SUSY model solves the hierarchy problem only if $m_{\tilde{g}}$ and $m_{\tilde{q}}$ are smaller than 1-2 TeV, unless the mass scale of the sparticles that only interact weakly (sleptons, gauginos, charginos and neutralinos) are decoupled from the mass of squarks and gluinos (same condition for the third generation squarks). It is therefore of great interest to perform similar searches for electroweakly produced SUSY particles. Since the particles do not interact via strong interaction, the cross-section is significantly lower than in the strong production searches. Moreover, leptons need an intermediate SM gauge boson to couple to the partons in the colliding beam protons, in contrast with gauginos which couple directly to the quark inside the protons, leading to a strong suppression in the production rate.
Figure 7.2 shows the production cross-section of SUSY particles as a function of the mass. The charginos and neutralinos have a production rate smaller by a factor 100 than strongly produced sparticles at the same mass scale[1]. Searches for electroweak SUSY are characterised also by a lower number of jets, softer objects and significantly lower $E_{\mathrm{T}}^{\mathrm{miss}}$ in the final state.

7.2 Analysis strategy

The analysis described in this thesis is a search for electroweak pair production of a chargino and a neutralino. The LSP is the lightest neutralino and all charginos $\tilde{\chi}_i^{\pm}$ (i=1,2) and neutralinos $\tilde{\chi}_j^0$ (j=1,2,3,4) are a mixture of higgsinos, binos and winos.
The naturalness condition [117, 118] suggests that the lightest charginos and neutralinos (also called electroweakinos) have masses at the electroweak scale (few hundreds GeV). If sleptons are heavier than electroweakinos, a $\tilde{\chi}_1^{\pm}$and $\tilde{\chi}_2^0$ production may be considered. In the two branches of the decay chain, the chargino decays to $\tilde{\chi}_1^0$ and a W boson ($\tilde{\chi}_1^{\pm}\rightarrow\tilde{\chi}_1^0 W^{\pm}$); while $\tilde{\chi}_2^0$ decays to the LSP and the lightest MSSM Higgs boson (SM-like) or a Z boson ($\tilde{\chi}_2^0\rightarrow\tilde{\chi}_1^0 \mathrm{Z}/h$) [119, 120, 121] .
If $\Delta m(\tilde{\chi}_2^0, \tilde{\chi}_1^0) > m_h = 125$ GeV and the higgsinos are heavier than the winos, the decay via a Higgs

[1] For this reason historically strong SUSY searches can be already performed with smaller dataset, while electroweak SUSY searches need a sufficient amount of data collected.

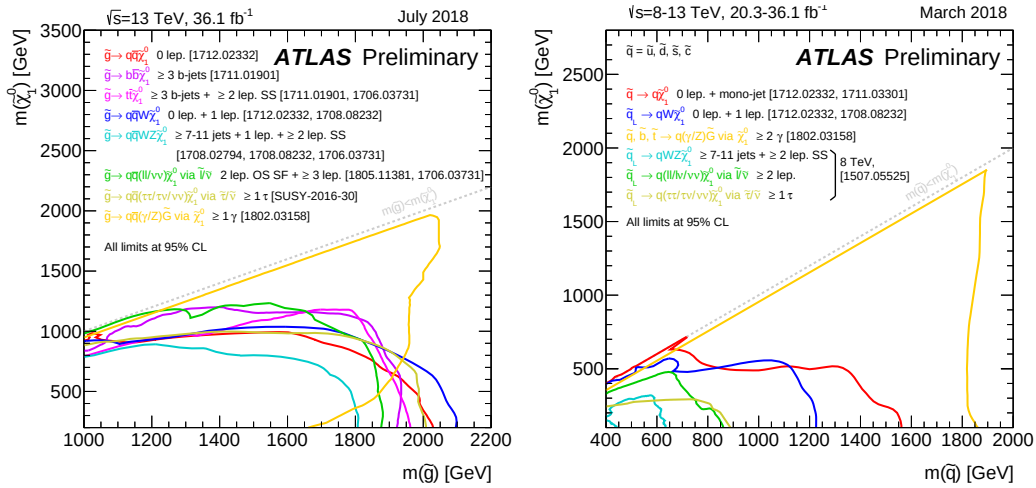

Figure 7.1: Exclusion limits at 95% CL based on 8 and 13 TeV data in the (gluino, lightest neutralino) (left) and (squark, lightest neutralino) (right) mass plane for different simplified models featuring the decay of squarks/gluinos to the lightest supersymmetric particle (lightest neutralino or gravitino) either directly or through a cascade chain featuring other SUSY particles with intermediate masses. For each line, the gluino and squark decay mode is reported in the legend and it is assumed to proceed with 100% branching ratio. Some limits depend on additional assumptions on the mass of the intermediate states, as described in the references provided in the plot [115].

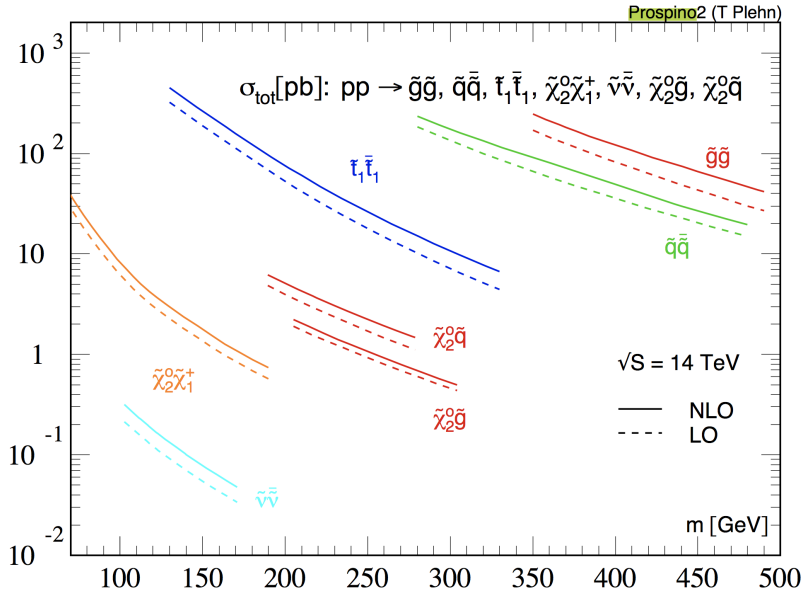

Figure 7.2: LHC production cross-sections for supersymmetric particles at $\sqrt{s}$=14 TeV. All cross-sections are shown as a function of the average final-state mass [116].

boson is dominant. The composition of the lightest chargino and next-to-lightest neutralino is wino-like and the two particles are nearly mass degenerate, while the lightest neutralino is assumed to be bino-like.

The hadronic and leptonic decay of the W boson are considered in combination with three different Higgs decay modes: a pair of b-quarks, a pair of photons, a pair of W/Z boson or τ leptons (where at least one of the $W/Z/\tau$ decays leptonically). The search is therefore split into five separate channels, depending on the W and h decay mode: $0\ell 1b\bar{b}$ (full hadronic), $1\ell 1b\bar{b}$, $1\ell\gamma\gamma$ (diphoton), $\ell^{\pm}\ell^{\pm}$ (same sign) and 3ℓ [126]. Figure 7.3 shows the diagrams of the considered signal scenarios.

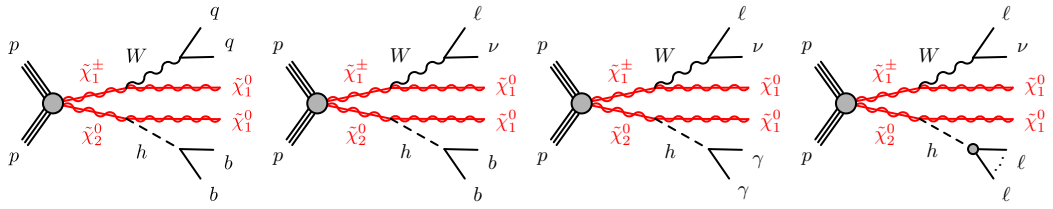

Figure 7.3: Diagrams illustrating the signal scenarios considered for the pair production of chargino and next-to-lightest neutralino targeted by the hadronic ($0l1b\bar{b}$) (a) and $1l1b\bar{b}$ (b), $1l\gamma\gamma$ (diphoton) (c), $l^{\pm}l^{\pm}$, $3l$ leptonic (d) channel selections. In (a) and (b) the Higgs boson decays to two b-quarks. In (c), the two photon channel is shown with $h \to \gamma\gamma$. In (d), the multilepton visible final state of the Higgs boson is shown [126].

The author contributed to the multileptonic channels (same-sign and 3ℓ) with the fake lepton background estimation and estimation of theoretical uncertainties.
The same sign channel has many similarities with the strong production SS3L analysis described in the previous chapter. From the phenomenological point of view, the difference is given only by the absence of b-jets in the final state and a lower number of expected jets.
The estimation of the prompt and charge flip background is identical with the strong SS3L analysis, except for differences in the choice of the Monte Carlo generators for some processes. While the non-prompt/fake lepton background is estimated only with the dynamic matrix method (no combination with the MC template method). The general flow of the analysis is the same as presented in the previous chapter, therefore many logical steps will not be repeated.

7.2.1 Object definitions

The object definition is similar to the one presented in 6.1.3, along with the overlap removal procedure. Jets, b-tagged jets and $E_{\mathrm{T}}^{\mathrm{miss}}$ do not have any difference in the definition.
Electrons and muons have a slightly different selection, due to the need to keep a good synchronisation among the different channels (in particular 3ℓ).
Electrons: Electrons with $p_{\mathrm{T}} > 10$ GeV and $|\eta| < 2.47$ and satisfying *LooseAndBLayerLH* likelihood based electron identification are considered as preselected (also called baseline) electrons. The region between barrel and end-cap EM calorimeters ($1.37 < |\eta| < 1.52$) is not vetoed. Signal electrons must satisfy the *Medium* likelihood based electron identification and have $p_T > 25$ GeV. The *GradientLoose* isolation working point is not optimal to reject non-prompt/fake leptons, but it was the optimal choice among the channels including leptons. The BDT to reduce the charge-flip contribution [101] introduced in 6.1.3 is also applied.
Muons: Muons with $p_{\mathrm{T}} > 10$ GeV and $|\eta| < 2.4$ and satisfying *Medium* identification requirement are considered as preselected muons. Signal muons are also required to pass the *GradientLoose* isolation requirements and additionally the cuts on the impact parameter ($|d_0/\sigma_{d_0}| < 3$ and $|z_0 \cdot \sin(\theta)| < 0.5$ mm). Table 7.1 summarises the selection criteria for electrons and muons.
Jets: Table 7.2 summarises the selection criteria for jets and b-tagged jets.

	Baseline electrons	**Baseline muons**
Acceptance	p_{T}> 10 GeV, $\lvert\eta^{\mathrm{clust}}\rvert < 2.47$	$p_{\mathrm{T}} > 10$ GeV, $\lvert\eta\rvert < 2.4$
Quality WP	*LooseAndBLayerLH*	*Medium*
l-jet isolation	ΔR(e,jet) > 0.4	ΔR(μ,jet) > 0.4
Impact parameter	$\lvert d_0/\sigma(d_0)\rvert < 5.0$	
	Signal electrons	**Signal muons**
Acceptance	p_{T}> 25 GeV	$p_{\mathrm{T}} > 25$ GeV
Quality WP	*LLHMedium*	*Medium*
Isolation WP	*GradientLoose*	*GradientLoose*
Impact parameter	$\lvert z_0 \cdot \sin(\theta)\rvert < 0.5$ mm $\lvert d_0/\sigma(d_0)\rvert < 5.0$	$\lvert z_0 \cdot \sin(\theta)\rvert < 0.5$ mm $\lvert d_0/\sigma(d_0)\rvert < 3.0$

Table 7.1: Summary of the selection criteria for electron (left) and muons (right).

	Jets
Collection	AntiKt4EMTopo
Acceptance	$p_{\mathrm{T}} > 20$ GeV, $\lvert\eta\rvert < 2.8$
Jet vertex tagger	JVT>0.64 for jets with $p_{\mathrm{T}} < 60$ GeV, $\lvert\eta\rvert < 2.4$ (after OR)
	***b*-jets**
Acceptance	$p_{\mathrm{T}} > 20$ GeV, $\lvert\eta\rvert < 2.5$
Identification	MV2c10 at 70% OP (85% OP for OR)

Table 7.2: Summary of the selection criteria for jets (top) and b-tagged jets (bottom).

7.2.2 Analysis inputs and event selection

The dataset and simulated background and signal processes are described in Section 6.1.2.
While the irreducible background processes samples are shown in Table 7.3. Comparing with the Monte Carlo samples used in the equivalent strong analysis, there are some differences due to harmonisation with other channels.

Trigger strategy: The trigger strategy is slightly different from the strong analysis. Events are selected when firing a single lepton trigger or a dilepton trigger.
The single lepton trigger have both low and high p_{T} thresholds which vary from 24 to 120 GeV for electrons and from 26 to 140 GeV for muons. While dilepton triggers consider all three possible lepton flavour combinations:

- electron-electron: $p_{\mathrm{T}}^{\mathrm{el}}$>12 GeV for 2015 data and $p_{\mathrm{T}}^{\mathrm{el}}$>17 GeV for 2016 data;
- electron-muon: $p_{\mathrm{T}}^{\mathrm{el}}$>17 GeV and p_{T}^{μ}>14 GeV;
- muon-muon: p_{T}^{μ}>8 GeV for the subleading muon and p_{T}^{μ}>12 (22) GeV for the leading muon for 2015 (2016) data.

The p_{T} requirement on the signal lepton of 25 GeV ensures an high efficiency of the triggers.

7.3 Signal regions

The selection of the signal regions is based on a wide set of kinematic variables and the requirement of exactly two signal leptons with same electric charge. In addition to the conditions on jet multiplicity, $E_{\mathrm{T}}^{\mathrm{miss}}$ and m_{eff}, a set of variables attempting to reconstruct the masses of particles involved in the decay are used. The discriminant variables used in this analysis are:

- $m_{\mathrm{T}}^{\mathrm{max}}$: transverse mass of the W boson. It is defined as $m_{\mathrm{T}} = \sqrt{2p_{\mathrm{T}}^{\ell}E_{\mathrm{T}}^{\mathrm{miss}}(1-\cos\Delta\phi)}$, where $\Delta\phi$ is the azimuthal angle between the considered lepton and the missing transverse momentum. The mass is computed with the leading lepton or the subleading lepton, the highest value among the two cases is taken.

- $m_{\ell j(j)}$: invariant mass of the highest p_{T} jet (when requiring exactly one jet) or of the dijet system with the closest lepton (testing all the di-jet pairs), where the measure of distance is $\Delta R = \sqrt{(\Delta\Phi)^2 + (\Delta\eta\ )^2}$. It attempts to reconstruct the mass of the Higgs boson. In the first order approximation, the kinematic endpoint carries model independent information about the mass difference between the primary and the secondary supersymmetric particles.

- "Stransverse mass" m_{T2} : this variable is closely related to m_{T}, and it has a kinematic endpoint which is directly related to the mass difference between the primary and the secondary supersymmetric particles in the decay chain. It is defined by:

$$m_{T2} = \min_{q_{\mathrm{T}}} \left[\max \left(m_{\mathrm{T}}(\mathbf{p}_{\mathrm{T}}^{1}, \mathbf{q}_{\mathrm{T}}), m_{\mathrm{T}}(\mathbf{p}_{\mathrm{T}}^{2}, \mathbf{p}_{\mathrm{T}}^{\mathrm{miss}} - \mathbf{q}_{\mathrm{T}}) \right) \right], \tag{7.1}$$

  where $\mathbf{q}_{\mathrm{T}}$ is the transverse vector that minimises the larger of the two transverse masses m_{T} and, in this case, $(\mathbf{p}_{\mathrm{T}}^{1}, \mathbf{p}_{\mathrm{T}}^{2})$ are the momenta of the detected leptons [122, 123].

The analysis optimisation has been performed by scanning different set of cuts to find the best combination of signal efficiency and background suppression. The expected sensitivity was estimated with a flat 30% systematic error on the background prediction added in quadrature to the MC statistical error. The significance Z_n was computed with the RooStats framework [124] and defined in terms of one-sided Gaussian standard deviations.

Process	Generator + fragmentation/hadronization	Tune	PDF set	Cross-section order
Diboson WW, WZ, ZZ	Sherpa-2.2.1	Default	NNPDF3.0NNLO	NLO
$t\bar{t}+X$ $t\bar{t}W/Z$ 4 tops	MadGraph-2.2.2 + Pythia-8.186	A14	NNPDF2.3	NLO
$t\bar{t}h$	MadGraph5_aMC@NLO-2.2.1 + Herwig++-2.7.1	UEEE5 [97]	CT10	NLO
Wh, Zh	Pythia-8.186	A14	NNPDF2.3	LO

Table 7.3: List of generators used for the simulation of the different SM processes considered in the analysis.

Starting from the signal regions used in the Run 1 analysis [125], the optimisation was based on two regions orthogonal in the jet multiplicity. However, the splitting into electron-electron, muon-muon and electron-muon channels was dropped due to a lower exclusion power. A b-jet veto is applied *a priori* since the considered signal model does not contain the production of a b-jet. In the optimisation process, the prompt lepton and charge-flip background are estimated using MC simulation. The fake lepton background is extracted from data with the dynamic matrix method to have a more reliable estimation of the dominant background processes.
Table 7.4 shows the kinematic cuts chosen for the definition of the two SRs. The same-sign lepton fulfil the signal lepton criteria.

	N_{jets}	N_{b-jets}	$\Delta\eta_{\ell\ell}$	E_T^{miss}	m_T^{max}	m_{eff}	$m_{\ell j(j)}$	m_{T2}
SRjet1	= 1	= 0	≤ 1.5	≥ 100 GeV	≥ 140 GeV	≥ 260 GeV	< 180 GeV	≥ 80 GeV
SRjet23	= 2,3	= 0	-	≥ 100 GeV	≥ 120 GeV	≥ 240 GeV	< 130 GeV	≥ 70 GeV

Table 7.4: Summary of the kinematic cuts defining the two signal regions of the SS channel.

7.4 Background estimation

As mentioned above, the methods used to estimate the background yields in the SRs are the same as in the strong SS3L analysis (Section 6). The prompt SM background is estimated with the MC samples listed in Table 7.3. The charge-flip contribution is determined using the likelihood technique described in Section 6.4.5.

7.4.1 Non-prompt/fake lepton background

The sources of the fake lepton background and the dynamic matrix method are described in Section 6.4.2.
In order to determine this background, it is essential to measure the baseline to signal efficiencies of both real and fake leptons. In addition, all possible sources of systematic uncertainties need to be estimated and included in the matrix method computation.

Real lepton efficiency

The real lepton efficiency is the probability that a preselected real lepton satisfies the signal lepton criteria. It is measured with the tag and probe method using $Z \to \ell\ell$ events, as a function of p_T and η for both electrons and muons. Events with at least two baseline lepton candidates are selected. One of the two lepton candidates, the 'tag' lepton, is required to have a transverse momentum $p_T > 25$ GeV and pass the signal lepton requirements. The 'probe' lepton, which is used for the real efficiency measurement, is required to pass the baseline lepton requirements and has to carry opposite charge and same flavour with respect to the corresponding tag lepton. Moreover, the invariant mass of the two leptons has to be close to the Z boson mass ($80 < m_{ee/\mu\mu} < 100$ GeV), in order to guarantee a high purity data sample of opposite-sign same-flavour leptons, and to match the single lepton or dilepton triggers. All possible tag-and-probe combinations are considered in an event (including permutation of the tag and probe leptons), to avoid any bias and increase the dataset.

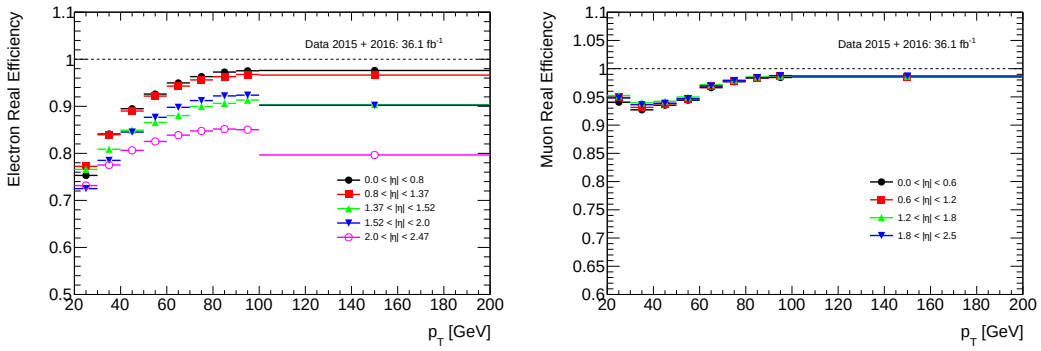

(a) Electrons (b) Muons

Figure 7.4: Baseline to signal efficiencies as a function of p_{T} for real electrons (a) and muons (b), measured in 2015+2016 data. The p_{T} distributions are shown for different $|\eta|$ bins, as indicated in the figure legend. The $|\eta|$ binning used in the electron case corresponds to the geometry of the electromagnetic calorimeter. For muons a homogeneous $|\eta|$ binning is considered. The last p_{T} bin is not inclusive. The error bars corresponds only to the statistical uncertainties.

The real lepton efficiency is obtained by computing the ratio between the number of probe leptons passing the signal requirements (N_{signal}) and the number of probe leptons passing the baseline requirements (N_{baseline}) as shown in Equation 7.2:

$$\varepsilon_{\mathrm{real}} = \frac{N_{\mathrm{signal}}}{N_{\mathrm{baseline}}}. \tag{7.2}$$

The measured real lepton efficiencies as a function of lepton p_{T} are shown in Fig 7.4. In the electron case, the efficiency deteriorates in the crack region $1.37 < |\eta| < 1.52$ and in the forward region due to the reconstruction efficiency drop.

Data to MC comparisons

The real lepton efficiencies computed using the Z tag and probe method in data are compared to those extracted with simulated $Z \to \ell\ell$ MC processes (SHERPA). Figure 7.5 shows the electron and the muon real efficiencies as a function of p_{T} and $|\eta|$ measured in data and in simulated $Z \to ee$ and $Z \to \mu\mu$ events, respectively. The associated uncertainties correspond to the statistical uncertainties only. A reasonable data to MC agreement is observed for both leptons, a difference below 2% is always observed.

An additional comparison is done in the p_{T} and $|\eta|$ bins used to extract the efficiencies, as shown in Figure 7.6 and Figure 7.7. For both electrons and muons the agreement is good. Few differences in particular bins are observed but all are below 4%.

Systematic uncertainties

One of the main source of systematic uncertainty is the choice of the Z window mass range in the definition of the control region used for real lepton efficiency determination. By varying the considered mass range, different efficiencies are measured. In order to take into account this effect, two additional mass ranges are considered: $75 < m_{\ell\ell} < 105\,\mathrm{GeV}$ and $85 < m_{\ell\ell} < 95\,\mathrm{GeV}$. The efficiencies are extracted and compared for each bin with respect to the nominal value. Then the largest difference is taken as systematic error for the specific p_{T}-η bin and symmetrised.

Table 7.5 and Table 7.6 show the uncertainties for the electron and muon cases, respectively.

The highest systematic uncertainties are affecting the low p_{T} bins.

	$0. < \|\eta\| < 0.8$	$0.8 < \|\eta\| < 1.37$	$1.37 < \|\eta\| < 1.52$	$1.52 < \|\eta\| < 2.01$
$25 < p_T < 35$ GeV	2.02%	2.79%	2.73%	3.51%
$35 < p_T < 45$ GeV	0.97%	1.63%	1.99%	2.18%
$45 < p_T < 55$ GeV	0.23%	0.36%	0.60%	0.54%
$55 < p_T < 65$ GeV	0.16%	0.21%	0.81%	0.31%
$65 < p_T < 75$ GeV	0.13%	0.15%	0.56%	0.22%
$75 < p_T < 85$ GeV	0.06%	0.12%	0.37%	0.08%
$85 < p_T < 95$ GeV	0.14%	0.12%	0.67%	0.16%
$95 < p_T < 200$ GeV	0.09%	0.15%	0.56%	0.26%

Table 7.5: The relative Z window mass cut systematic uncertainties in percentage on the real electron efficiencies.

	$0. < \|\eta\| < 0.6$	$0.6 < \|\eta\| < 1.2$	$1.2 < \|\eta\| < 1.8$	$1.8 < \|\eta\| < 2.5$
$25 < p_T < 35$ GeV	0.30%	0.27%	0.29%	0.35%
$35 < p_T < 45$ GeV	0.20%	0.25%	0.32%	0.39%
$45 < p_T < 55$ GeV	0.08%	0.07%	0.10%	0.12%
$55 < p_T < 65$ GeV	0.10%	0.10%	0.13%	0.11%
$65 < p_T < 75$ GeV	0.09%	0.10%	0.10%	0.12%
$75 < p_T < 85$ GeV	0.10%	0.09%	0.11%	0.05%
$85 < p_T < 95$ GeV	0.11%	0.11%	0.17%	0.14%
$95 < p_T < 200$ GeV	0.14%	0.11%	0.14%	0.10%

Table 7.6: The relative Z window mass cut systematic uncertainties in percentage on the real muon efficiencies.

In addition, the following systematic uncertainties were investigated:

- Background contamination: the Z background can contaminate the data and should be subtracted in the computation. Though, this effect is significant for $p_{\mathrm{T}} < 20$ GeV, so it is not been considered in this analysis;
- Trigger bias: a possible different trigger strategy of the analysis can be a source of systematic uncertainty. Different trigger strategies are considered and the difference with respect to the nominal one is taken as systematic uncertainty;
- Extrapolation to busy environments: the real lepton efficiency is calculated in a region of the phase space which is different from the one of the signal region and also the kinematic characteristics of the event can be significantly different and alterate the efficiency. To cover this difference, an uncertainty can be assigned by comparing efficiencies in simulated $Z \to ll$ and SUSY signal samples.

however, the effects listed above have been found to be negligible compared to the Z window mass systematic and are not included in the final systematic uncertainty.

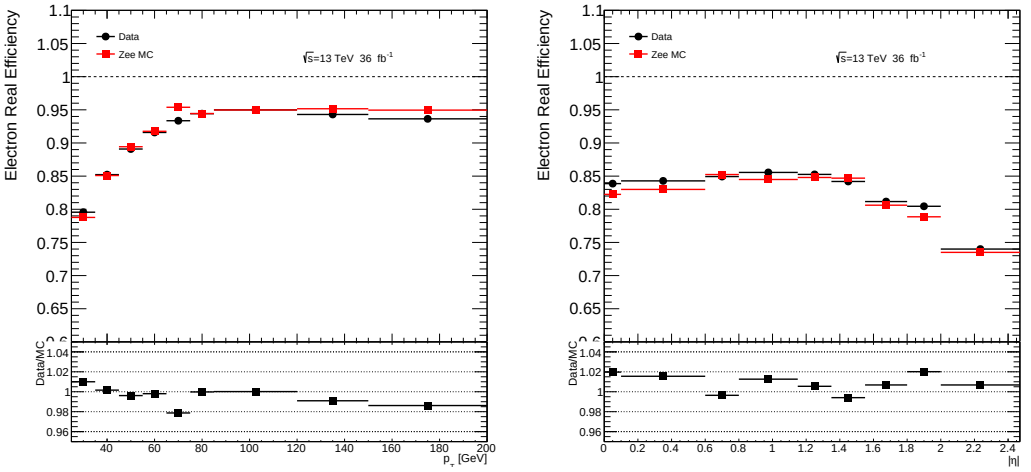

(a) Electron p_{T}

(b) Electron η

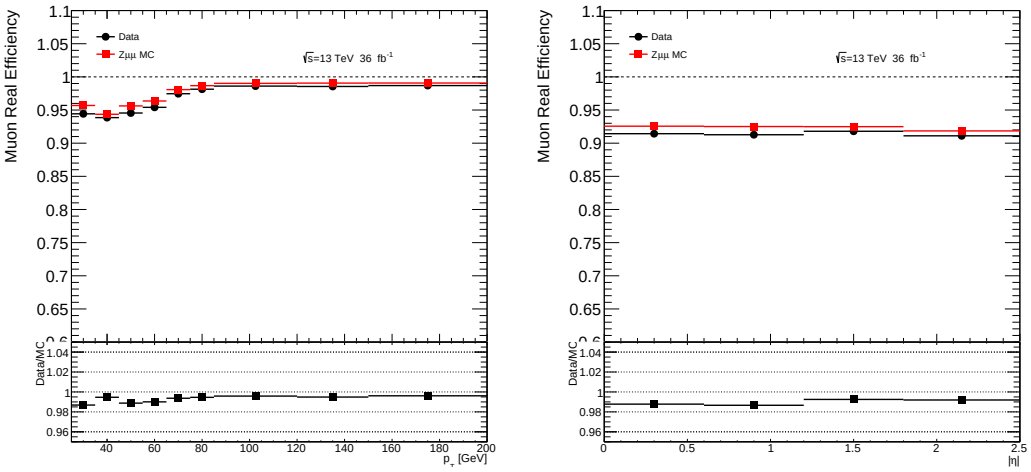

(c) Muon p_{T}

(d) Muon η

Figure 7.5: The real lepton efficiencies as a function of p_{T} and $|\eta|$ measured in data and MC using the Z tag and probe method. The plots in the top row correspond to the real electron efficiencies and the plots in the bottom row correspond to the real muon efficiencies. The 2015 + 2016 data are denoted by the black dots and the pile-up reweighted $Z \to \ell\ell$ MC by the red squares. The uncertainties shown in the plots are corresponding to the statistical uncertainties only.

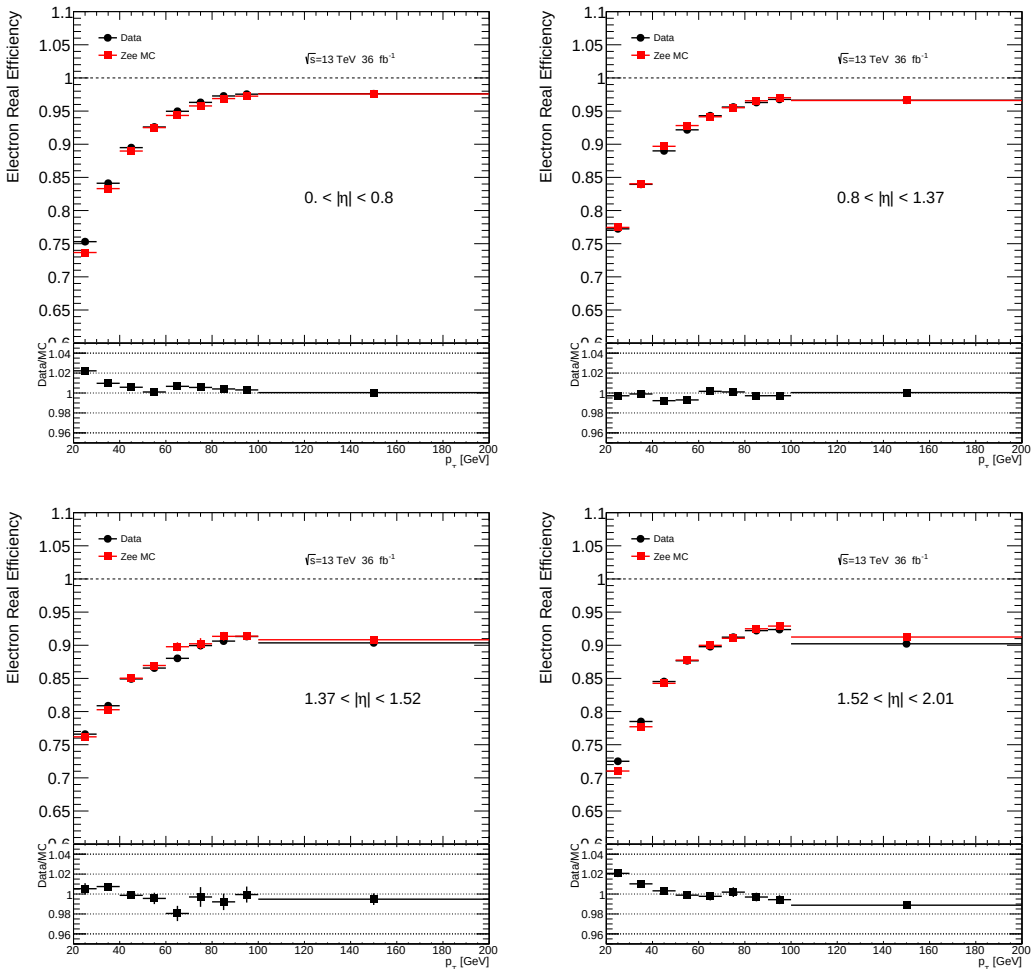

Figure 7.6: The real electron efficiencies as a function of p_{T}, in the 4 different η bins measured in data and MC simulation using the Z tag and probe method. The 2015 + 2016 data are denoted by the black dots and the pile-up reweighted $Z \to ee$ MC by the red squares. The uncertainties shown in the plots are corresponding to the statistical uncertainties only.

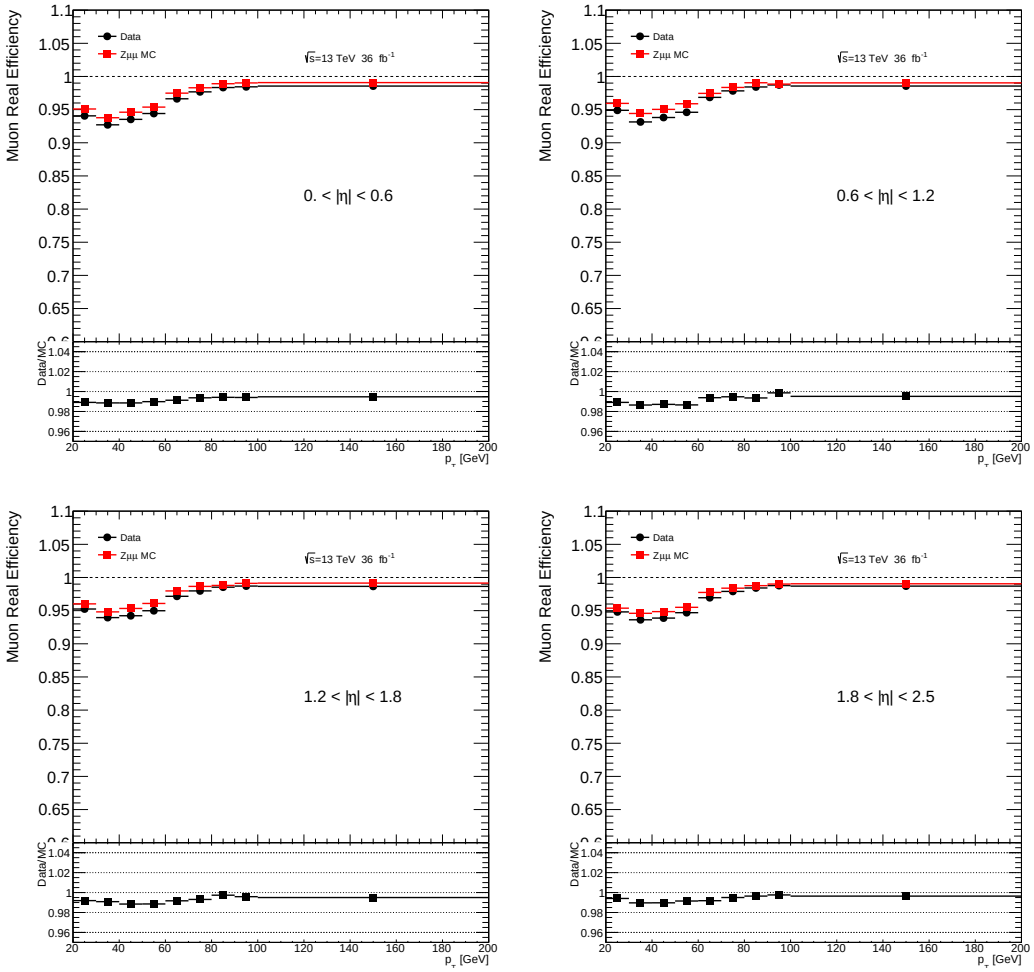

Figure 7.7: The real muon efficiencies as a function of p_{T}, in the 4 different η bins measured in data and MC simulation using the Z tag and probe method. The 2015 + 2016 data are denoted by the black dots and the pile-up reqeighted $Z \to \mu\mu$ MC by the red squares. The uncertainties shown in the plots are corresponding to the statistical uncertainties only.

Fake lepton efficiency

Muons

The fake lepton efficiency is the probability that a fake preselected lepton satisfies the signal lepton criteria. It is measured in a sample enriched in fake leptons, triggered events with two same sign baseline muons and at least one b-tagged jet are selected.

The muon firing the trigger does not have to be the leading muon in order to increase the statistics and to avoid any bias. One of the muons in the event (referred to as 'tag') is required to satisfy the signal requirements (tight), have $p_{\mathrm{T}} > 40$ GeV, and be trigger-matched. The measurement is then performed on the other lepton ('probe'), likely to be the fake lepton of the pair, which has to be a baseline lepton (loose) with $p_{\mathrm{T}} > 20$ GeV.

Furthermore, the composition of the source of the fake muons selected in this CR is studied with the truth MC information.

In Figure 7.8 is shown the origin of the probe muon, when passing the loose (left) and the tight (right) criteria. The main source of fake leptons is from semi-leptonic heavy-flavour decay.

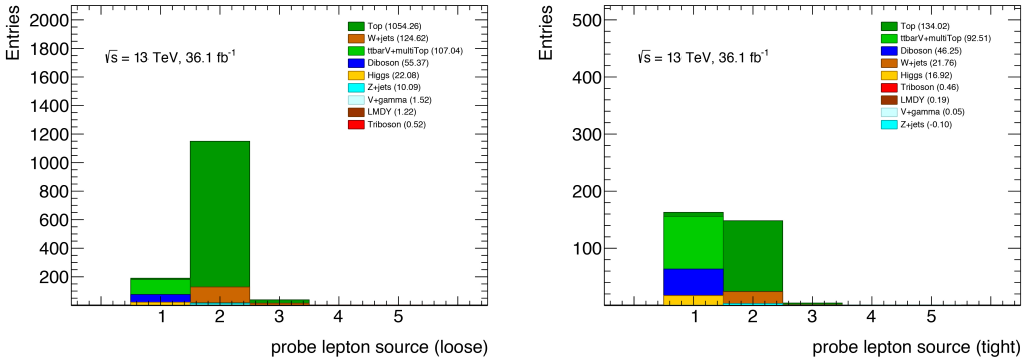

Figure 7.8: Composition of the source of the probe muon when passing the loose (left) and the tight (right) criteria in the control region defined to calculate the baseline to signal efficiency for fake muons. Where the possible options are denoted on the x-axis: prompt lepton (1), heavy-flavour (2), light-flavour (3), photon conversion (4) and charge-flipped lepton (5). In the legend are shown in brackets the yields from each background category.

Electrons

The measurement of the baseline to signal efficiency for fake electrons is done by selecting triggered events with a baseline electron-muon couple with same sign and at least one b-tagged jet, the muon firing the trigger does not have to be the leading lepton which allows to increase the statistics and to avoid possible bias. The muon in the event is in this case the tag lepton and is required to satisfy signal requirements, with $p_{\mathrm{T}} > 40$ GeV, and be trigger-matched. The measurement may then be performed on the electron (the probe lepton in this case), which has to be a baseline electron with $p_{\mathrm{T}} > 20$ GeV. The composition of the source of the fake electrons selected in the CR is studied with the truth MC information. The origin of the probe electron is shown in Figure 7.9, when passing the loose (left) and the tight (right) criteria. In this case the photon conversion, the charge-flip and electron from heavy flavour decays are the main sources.

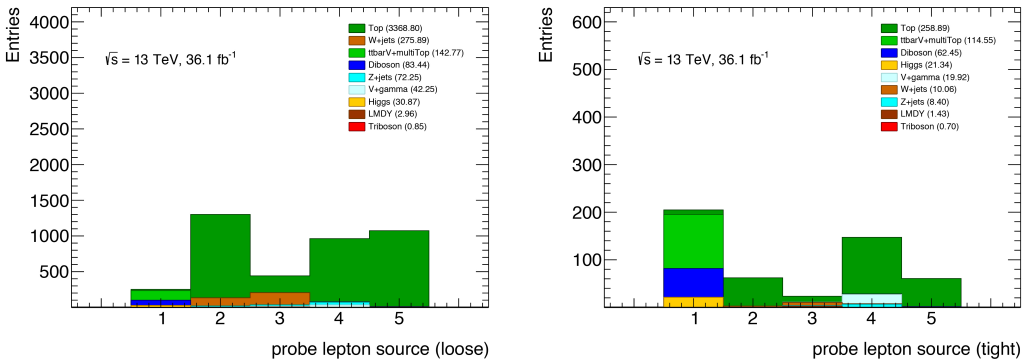

Figure 7.9: Composition of the source of the probe electron when passing the loose (left) and the tight (right) criteria in the control region defined to calculate the baseline to signal efficiency for fake electrons. Where the possible options are denoted on the x-axis: prompt lepton (1), heavy-flavour (2), light-flavour (3), photon conversion (4) and charge-flipped lepton (5). In the legend are shown in brackets the yields from each background category.

The efficiencies are extracted from the control region using equation 7.3 and are parametrised in p_{T} (4 bins) and η (3 bins) for both electrons and muons:

$$\varepsilon_{\text{fake}} = \frac{N^{\text{data}}_{\text{signal}} - N^{\text{prompt bkg}}_{\text{signal}}}{N^{\text{data}}_{\text{baseline}} - N^{\text{prompt bkg}}_{\text{baseline}}} \tag{7.3}$$

Fake composition in SRs

The composition of the fakes in the SR is shown in Figure 7.10 for the leading lepton (top) and subleading lepton (bottom) for SRjet1 (left) and SRjet23 (right). Differences are observed with respect to the composition in the CR. These differences will be covered by applying a systematic uncertainty. Other fake CR definitions have been tested, with a fake composition closer to the one in the SRs. Though the fake rate obtained with the alternative CR was leading to a worst agreement with data when validating the background. Therefore it was decided to keep the CR selection despite the differences observed.

Systematic uncertainties of the fake lepton efficiency

Two different kinds of systematic uncertainties have to be considered: the one affecting the measurement that are correlated between the different p_{T} and $|\eta|$ bins and the uncorrelated one.

In the first case, a source of systematic error is the contribution of the events with real leptons in the fake-enriched control region used to extract the efficiencies. To evaluate that, the expected yields from the prompt leptons in the CR (which is used in the fake lepton efficiency equation) is variated by 30% in both directions to obtain the variations. This is done to cover the luminosity and cross-section uncertainties.

While in the second case possible difference of the fake composition in the control region, depending on the different kinematic cuts applied, are taken into account. To cover this difference, several control region definitions are considered and the one leading to the highest variation is chosen.

Table 7.7 reports the kinematic cuts of the control region considered for the electron and the muon case, the variations used to estimate the systematic uncertainty are also shown.

In Figure 7.11 the composition of these CR is shown.

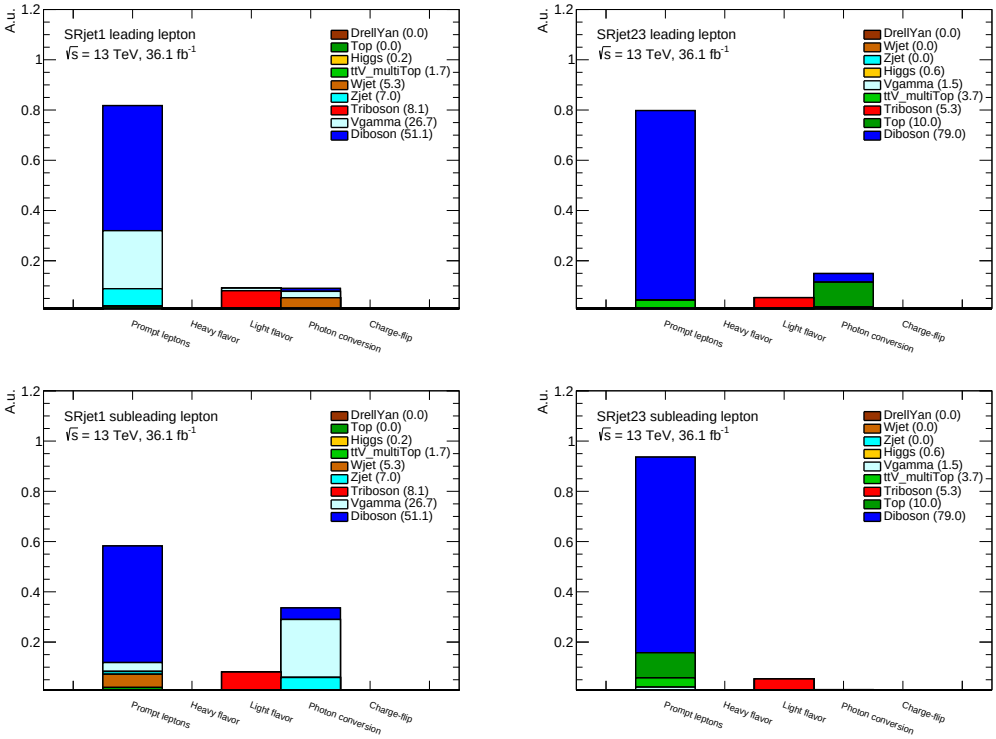

Figure 7.10: Composition of the fakes in SRjet1 (left) and SRjet23 (right) for the leading lepton (top) and sub-leading lepton (bottom) with no lepton flavour splitting. The number in brackets show the contribution in percentage of the total SR yields.

Control region	CRel1	CRel2	CRmu1	CRmu2
N_{jets}	≥ 1	≥ 1	≥ 1	≥ 2
Lepton couple flavour	$e\mu$	$e\mu$	$\mu\mu$	$\mu\mu$
Leading lepton p_{T} [GeV]	≥ 40	≥ 40	≥ 40	≥ 40
Sub-leading lepton p_{T} [GeV]	≥ 20	≥ 20	≥ 20	≥ 20
$N_{b-\text{jets}}$	≥ 1	≥ 0	≥ 1	≥ 0

Table 7.7: Fake-enriched CR definition. CRel1 and CRmu1 are used to extract the fake lepton efficiencies, while CRel2 and CRmu2 give the variations used to estimate the systematic error.

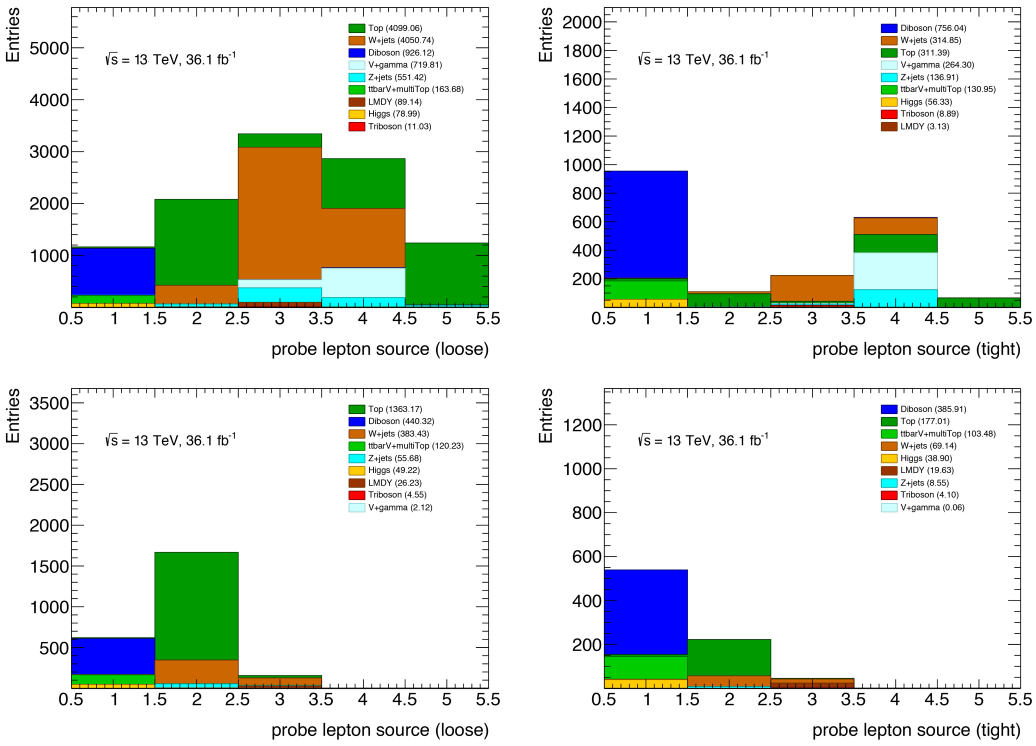

Figure 7.11: Composition of the source of the probe electron (top) and muon (bottom) when passing the loose (left) and the tight (right) criteria in the control region defined to calculate the systematic uncertainty on the fake lepton efficiency. Where the possible options are: prompt lepton (1), heavy-flavour (2), light-flavour (3), photon conversion (4) and charge-flipped lepton (5). In the legend are shown in brackets the yields from each background category.

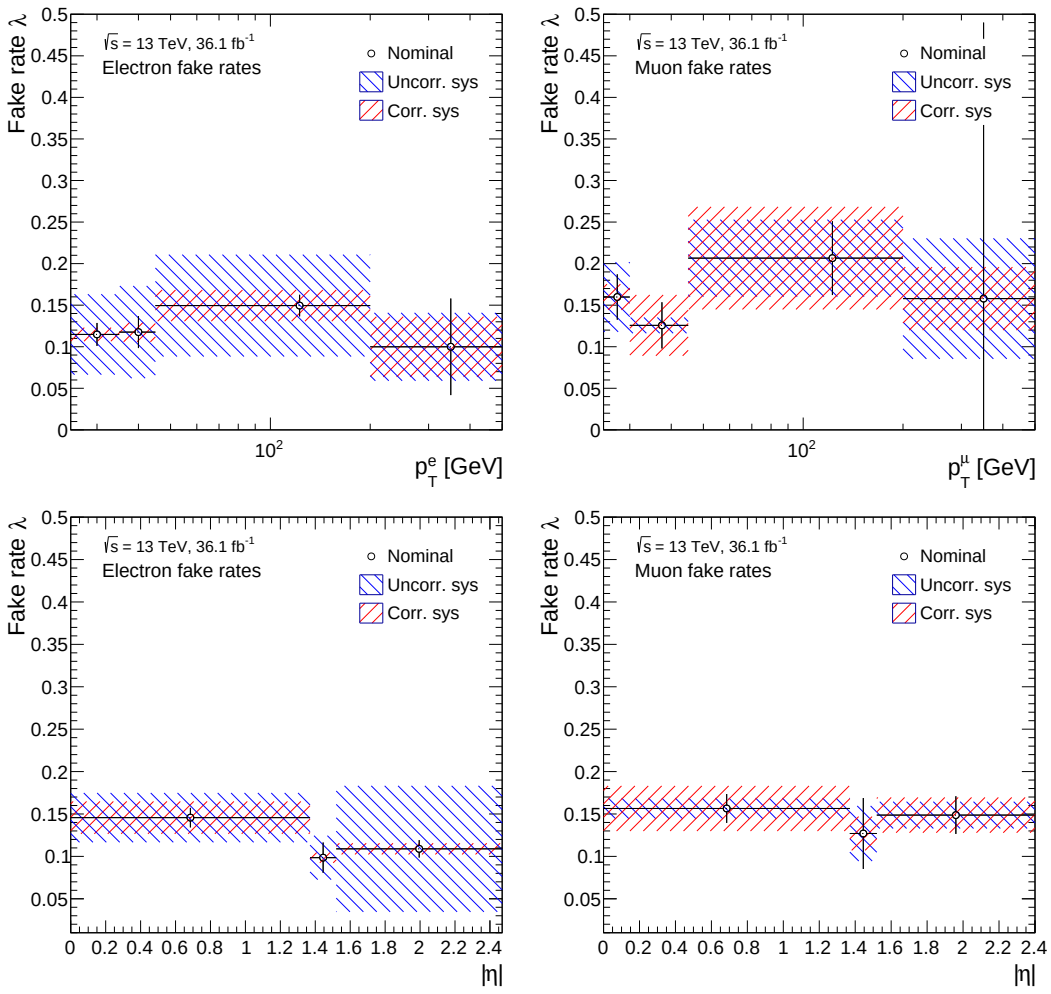

Figure 7.12: Fake lepton efficiencies as a function of p_{T} (top) and η (bottom) for fake electrons (left) and muons (right), measured in 2015+2016 data. The systematic uncertainty is shown for both correlated (red) and uncorrelated (blue) sources.

	ee channel	$\mu\mu$ channel	eμ channel
Fakes	65.8% (710.3)	23.8% (85.7)	49.4% (576.4)
Charge-flip	10.3% (111.6)	0.0% (0.0)	1.1% (13.6)
WZ	17.4% (188.5)	54.0% (194.5)	36.2% (422.0)
ZZ	0.7% (1.6)	0.5% (1.8)	0.3% (3.5)
WW	3.9% (42.3)	13.8% (50.0)	7.9% (92.4)
Rare	1.5% (16.9)	4.5% (16.3)	2.0% (23.5)
ttV	0.6% (8.0)	2.4% (8.8)	1.5% (17.3)
Total SM	1079$\pm$132	357.1 $\pm$ 25.3	1149 $\pm$ 165
Data	936	360	1166

Table 7.8: Relative background composition of the fakes validation region for each background category. In brackets the yields are shown.

Fake lepton rate

The fake lepton rate are presented in Figure 7.12 for both electrons and muons. The results show a rather flat fake rate in p_{T} up to 200 GeV, while at high p_{T} the rate decreases as expected (typically fake leptons have low p_{T}). This effect can be easily seen in the electron case, while for the muon the statistics in the last bin is too low. In the η parametrisation no particular dependency is observed for muons, while for electrons there is a drop in the forward region. Electron fake rate is mainly affected by uncorrelated systematic uncertainty, while muon fake rate has a higher contribution from the correlated systematic uncertainty.

The charge-flip background is not always negligible in the electron case depending on the phase space of the CR, and it could be necessary to subtract the contribution for both signal and baseline leptons. Here the charge-flip contribution in this CR is 2%, so no extra correction is applied.

Validation of the fake background estimation

In order to validate the fake lepton background estimation, the data and MC distributions are compared for several kinematic variables. The validation region (VR) consists of events with exactly two same-sign baseline leptons passing also signal criteria, a b-jet veto and at least one signal jet. An extra Z veto cut is applied ($|m_Z - m_{ll}| >$10 GeV) to reduce the Z+jets contribution and have a region dominated by fake lepton background. Finally, a $E_{\mathrm{T}}^{\mathrm{miss}}$ cut at 30 GeV is required since it is the lowest cut on $E_{\mathrm{T}}^{\mathrm{miss}}$ among all the SR of the SS and 3L analyses.

All distributions have been split by flavour into ee, $\mu\mu$ and eμ. In Table 7.8 the background composition in this region is shown. The purity reached is 66% in the electron channel, 49% in the electron-muon channel and 24% in the muon channel.

The agreement is good as it can be seen in Figure 7.13, 7.14 and 7.15. The p_{T} distribution of the leading lepton, m_{eff}, $E_{\mathrm{T}}^{\mathrm{miss}}$ and $m_{\mathrm{T}}^{\mathrm{max}}$ are shown. Since this validation region overlaps with the signal regions defined, the signal contamination has been checked (Figure 7.16) and it is below 2%.

Fake yields and systematic uncertainties

In Table 7.9 the final fake yields in all signal regions and validation regions are shown, along with the statistical uncertainties and the systematic uncertainties split into correlated and uncorrelated sources. All regions are dominated by the uncorrelated systematic uncertainty. The total uncertainty on the fake lepton estimation varies from 65% to 85% in SR and VR and it is the dominant uncertainty of the analysis.

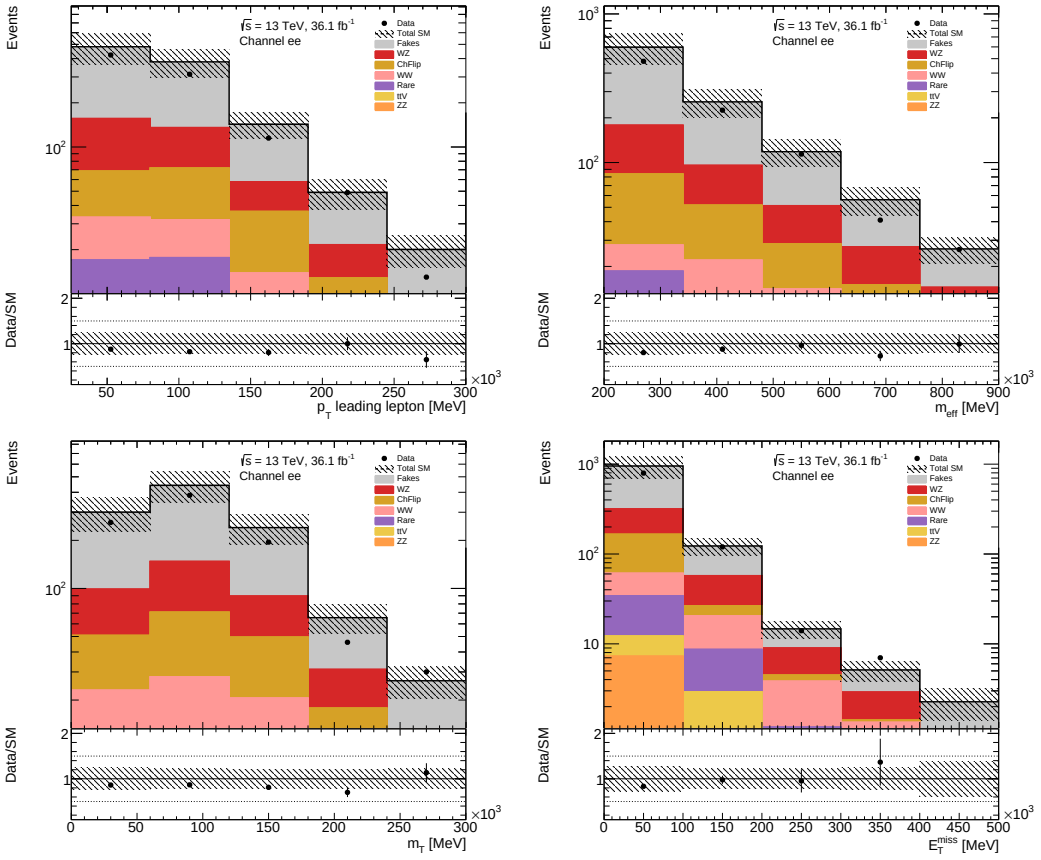

Figure 7.13: Distribution of the leading lepton p_{T}, m_{eff}, $m_{\mathrm{T}}^{\mathrm{max}}$ and $E_{\mathrm{T}}^{\mathrm{miss}}$ in the electron-electron channel. The ratio between data and SM is shown in the bottom panel of figures. The error bars include statistical uncertainties and all the systematic uncertainties except the theoretical uncertainties.

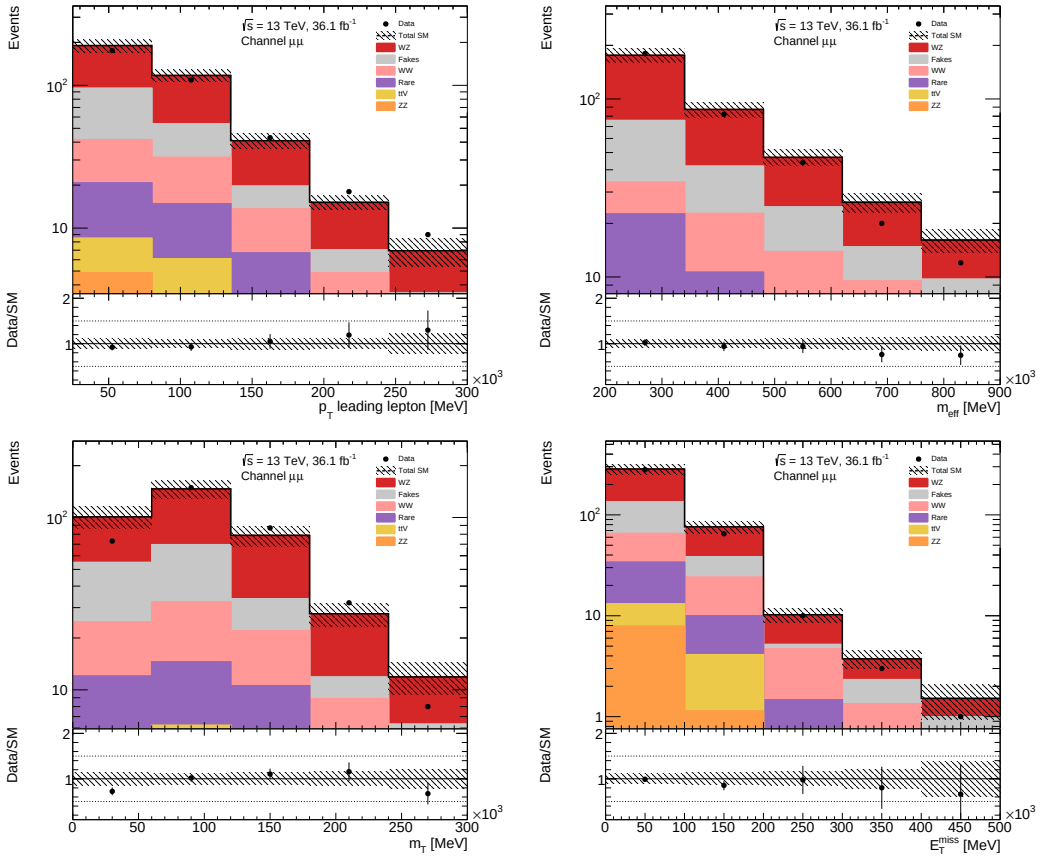

Figure 7.14: Distribution of the leading lepton p_{T}, m_{eff}, $m_{\mathrm{T}}^{\mathrm{max}}$ and $E_{\mathrm{T}}^{\mathrm{miss}}$ in the muon-muon channel. The ratio between data and SM is shown in the bottom panel of figures. The error bars include statistical uncertainties and all the systematic uncertainties except the theoretical uncertainties.

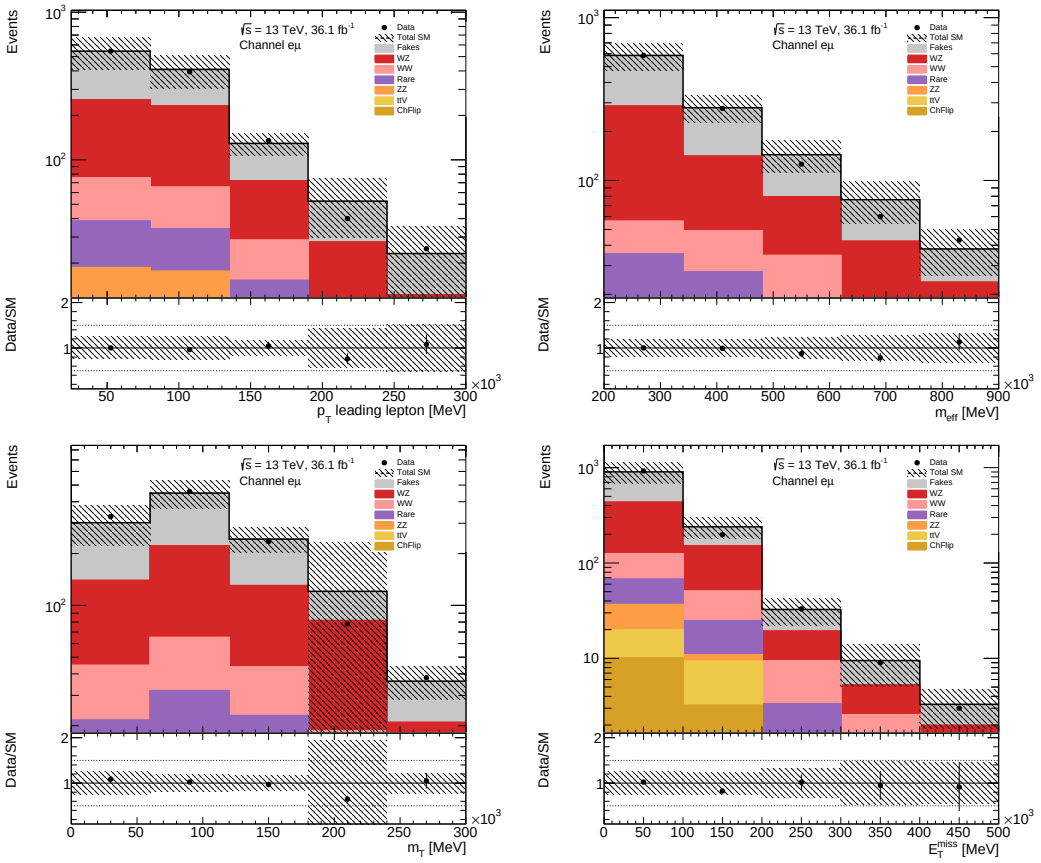

Figure 7.15: Distribution of the leading lepton p_{T}, m_{eff}, $m_{\mathrm{T}}^{\mathrm{max}}$ and $E_{\mathrm{T}}^{\mathrm{miss}}$ in the electron-muon channel. The ratio between data and SM is shown in the bottom panel of figures. The error bars include statistical uncertainties and all the systematic uncertainties except the theoretical uncertainties.

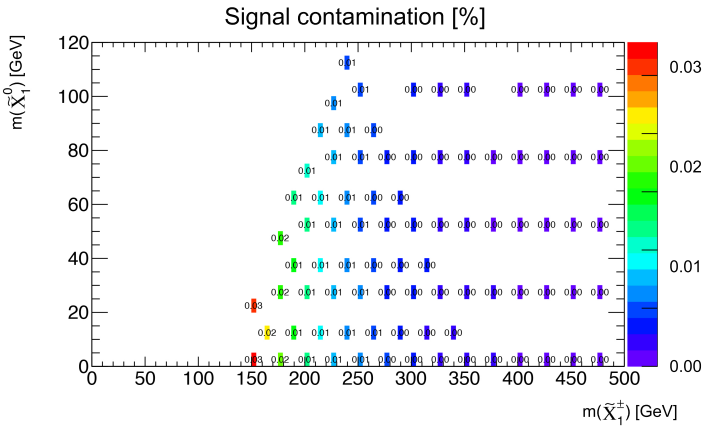

Figure 7.16: Signal contamination in the fake lepton VR.

	Fake yields	Statistical error	Syst. uncorrelated	Syst. correlated
SRjet1	3.29	±0.82	±1.79	±0.72
SRjet23	1.76	±0.71	±1.12	±0.64
VRjet1	8.02	±1.39	±5.20	±2.58
VRjet23	20.08	±2.02	±12.82	±4.45

Table 7.9: Non-prompt lepton background yields in VRs and SRs. Statistical uncertainties are reported, along with systematic uncertainty divided into correlated and uncorrelated.

7.5 Validation of SM background

The strategy to define the VRs is different compared to the SS3L strong analysis. In the latter, the five different VRs were designed to have the purest composition for each targeted SM background process. In this analysis, two VRs have been defined orthogonal to each of the SRs, but very close in the phase space. Moreover, the kinematic cuts are adjusted to reduce the signal contamination.

As shown in Table 7.10, VRjet1 has been obtained by inverting the $E_{\mathrm{T}}^{\mathrm{miss}}$ cut and adding a lower cut to define a [70-100] GeV range. This lower cut has been optimised until the background composition in this validation region was similar to the one of the SRjet1. The cut on m_{lj} has been inverted to reduce signal contamination and relaxed in order to increase statistics. The cuts on m_{eff} and m_{T2} have been removed in order to increase the statistics. The signal contamination for this validation region is lower than 12%.

The VRjet23 has been obtained by inverting the $m_{\mathrm{T}}^{\mathrm{max}}$ cut and adding a lower cut to define a [65-120] GeV range. This lower cut has been optimised until the background composition in this validation region was similar to the one of the SRjet23. The cut on $m_{\ell jj}$ has been inverted to reduce signal contamination, while the cut on m_{T2} has been removed in order to increase statistics. The signal contamination for this validation region is lower than 8%.

Table 7.10 shows the VRs selection, the cuts which differ from the SRs are marked in red.

The agreement between the observed and expected number of events is good, as shown in the Table 7.11. Figure 7.17 shows also the good agreement in the shape for $m_{\ell j(j)}$ in VRjet1 and m_{eff} in VRjet23.

Cut	VRjet1	VRjet23
N_{jets}	1	$[2,3]$
Leading lepton p_T [GeV]	>25	>25
Sub-leading lepton p_T [GeV]	>25	>25
$\lvert\Delta\eta_{\ell\ell}\rvert$	<1.5	–
E_T^{miss} [GeV]	$[70,100]$	>100
m_{eff} [GeV]	–	>240
$m_{\mathrm{T}}^{\mathrm{max}}$ [GeV]	>140	$[65,120]$
$m_{\ell j(j)}$ [GeV]	>130	>130
m_{T2} [GeV]	–	–

Table 7.10: Definition of the validation regions. The values in red represent the changes with respect to the cuts in the signal region.

	VRjet1	VRjet23
Observed events	17	54
exp. SM	16.84 ± 6.06	55.62 ± 14.41
Ratio (Obs./Exp.)	1.01	0.97
Fake lepton (DD)	8.02 ± 5.97	20.08 ± 13.72
WZ events	4.91 ± 0.83	19.33 ± 4.16
Rare events	0.78 ± 0.33	2.47 ± 0.43
ttV events	0.04 ± 0.01	0.96 ± 0.14
WW events	0.80 ± 0.12	10.48 ± 0.78
ZZ events	0.30 ± 0.06	0.25 ± 0.08
Charge-flip events (DD)	2.00 ± 0.26	2.07 ± 0.17

Table 7.11: Yields in the validation regions. Only the statistical error is included for the MC expectation. Fake/non-prompt lepton and charge-flip lepton backgrounds are estimated with data-driven methods (DD).

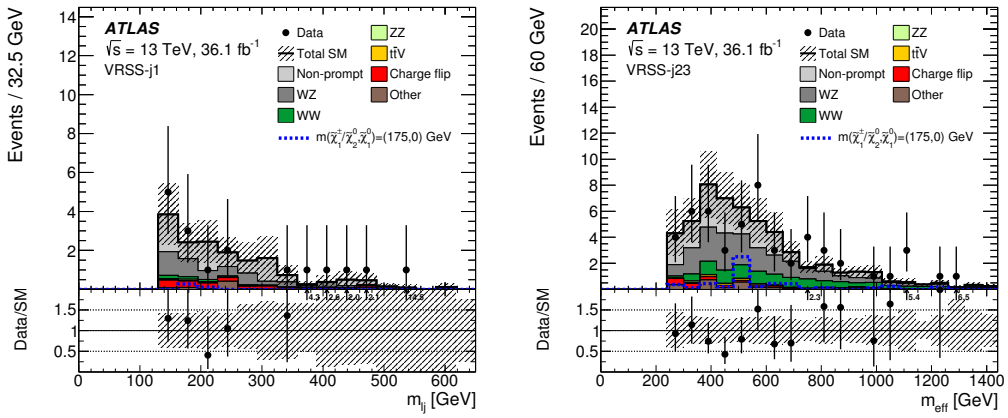

Figure 7.17: Distribution of $m_{\ell j(j)}$ in VRjet1 region and m_{eff} distribution in VRjet23 region. The statistical uncertainties in the background prediction are included in the uncertainty band, as well as the full systematic uncertainties for backgrounds with fake or non-prompt leptons, or charge-flip [126].

7.6 Results

Table 7.12 shows the expected yields in the signal regions and the observed number of data events; these numbers correspond to the yields after performing a background-only fit. No significant excess over the SM background expectation is observed. As mentioned before, the uncertainty on the fake lepton estimation is dominant, with a 30% uncertainty on the total expected yield. More details on the systematic uncertainties and SR yields after model dependent fit are shown in Appendix C.

Figure 7.18 shows the m_{T2} and $m_{\ell j(j)}$ distributions for SRjet1, and $E_{\text{T}}^{\text{miss}}$ and m_{T2} distributions for SRjet23. Since no excess is observed, a simultaneous model dependent fit on SRjet1 and SRjet23 is performed to derive exclusion limits. The resulting exclusion limit is presented in Figure 7.19. The observed exclusion obtained by the SS channel excludes $\tilde{\chi}_1^{\pm}/\tilde{\chi}_2^0$masses up to 240 GeV and $\tilde{\chi}_1^0$up to 40 GeV for the considered model. Nevertheless, the wide error band (yellow), due to the high systematic uncertainty caused by the fake lepton estimation, covers completely the region of the phase space excluded.

	SRjet1	SRjet23	VRjet1	VRjet23
Observed events	2	8	17	54
exp. SM events	6.74 ± 2.17	5.33 ± 1.59	16.84 ± 6.06	55.62 ± 14.41
Fakes events	3.30 ± 2.10	1.76 ± 1.47	8.02 ± 5.97	20.08 ± 13.72
MC exp. WZ events	2.18 ± 0.42	1.85 ± 0.52	4.91 ± 0.83	19.33 ± 4.16
MC exp. Rare events	0.44 ± 0.13	0.73 ± 0.17	0.78 ± 0.33	2.47 ± 0.43
MC exp. ttV events	0.12 ± 0.04	0.14 ± 0.04	0.04 ± 0.01	0.96 ± 0.14
MC exp. WW events	0.17 ± 0.03	0.51 ± 0.07	0.80 ± 0.12	10.48 ± 0.78
MC exp. ZZ events	0.06 ± 0.02	0.07 ± 0.02	0.30 ± 0.06	0.25 ± 0.08
Charge-flip events	0.47 ± 0.07	0.27 ± 0.03	2.00 ± 0.26	2.07 ± 0.17

Table 7.12: Yields in the various signal and validation regions

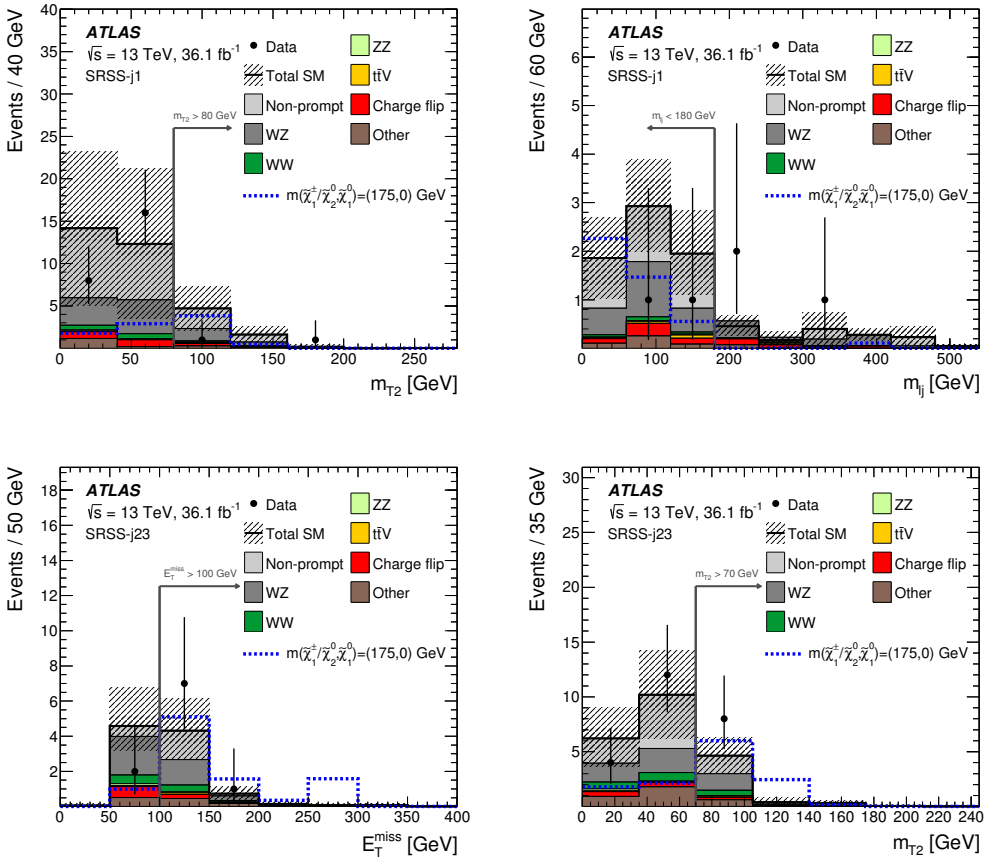

Figure 7.18: The m_{T2} and $m_{\ell j(j)}$ distributions in SRjet1 region (top) and $E_{\mathrm{T}}^{\mathrm{miss}}$ and m_{T2} distributions in SRjet23 region (bottom). The statistical uncertainties in the SM background prediction are included in the uncertainty band, as well as the full systematic uncertainties for backgrounds with fake or non-prompt leptons, or charge-flip [126].

In Table 7.13 are shown the results of the model independent upper limits calculation, as explained in Section 6.7.2.

A summary of the exclusion limits of all channels mentioned in Section 7.2 is shown in Figure 7.20. The $\ell^{\pm}\ell^{\pm}$ channel is mainly sensitive at low $m(\tilde{\chi}_1^{\pm}/\tilde{\chi}_2^0)$ and it slightly improves the observed exclusion for models with small mass difference between $\tilde{\chi}_1^{\pm}/\tilde{\chi}_2^0$ and $\tilde{\chi}_1^0$.

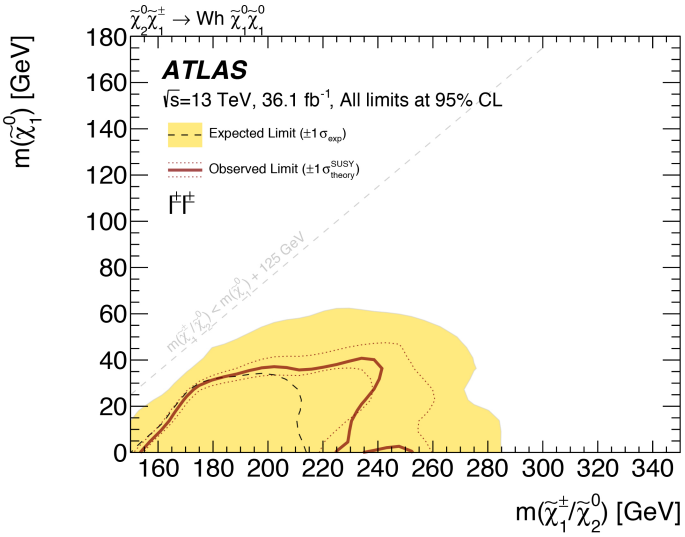

Figure 7.19: Exclusion limits for electroweak pair production of a chargino and a neutralino. The chargino $\tilde{\chi}_1^{\pm}$ decays to the lightest neutralino and a W boson while the neutralino $\tilde{\chi}_2^0$ decays to the lightest neutralino $\tilde{\chi}_1^0$ and a Standard Model like 125 GeV Higgs boson. The combined SRjet1 and SRjet23 limits, calculated with the data driven fake and charge flip estimation [126].

	σ_{vis} [fb]	S^{95}_{obs}	S^{95}_{exp}	p_0-value
SRjet1	0.12	4.2	$6.1^{+2.7}_{-1.5}$	0.50
SRjet23	0.27	9.9	$6.6^{+3.4}_{-1.1}$	0.17

Table 7.13: From left to right: model independent 95% CL upper limits on the visible cross section (σ_{vis}), the observed (S^{95}_{obs}) and the expected (S^{95}_{exp}) 95% CL upper limits on the number of signal events, and the discovery p-value (p_0, truncated at 0.5 in case the observed event yields are below the SM expectation) [126].

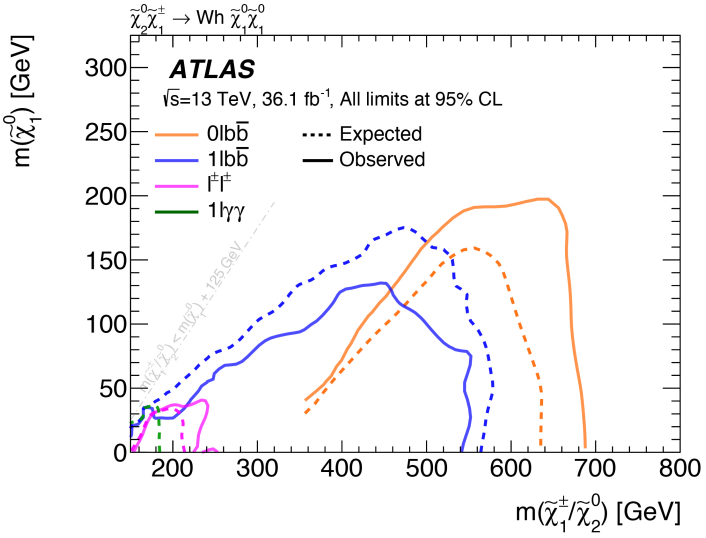

Figure 7.20: Comparison of the expected and observed exclusion limits for each analysis channel. Only the expected exclusion is shown for the $1l\gamma\gamma$ channel since the observed exclusion does not appear due to the excess observed [126].

Chapter 8

Higgsino at high luminosity LHC

The results of the SUSY searches in Run-II with 36.1 fb^{-1} do not show any signs of New Physics. An important step is to perform analyses with similar final states also with the full Run-II dataset which will reach 150 fb^{-1}, increasing significantly the sensitivity in many models.
However it is of utmost importance to start designing the future of ATLAS. Many studies are already on-going to provide important feedback for the construction of the future detector, in particular for the High Luminosity LHC (HL-LHC).
A final state with leptons and missing transverse momentum is important also in a pure natural MSSM model. The following chapter introduces the project of the HL-LHC and the prospect studies of the exclusion power for the natural mass range of a pure higgsino scenario.

8.1 High luminosity LHC

At the end of Run-II, LHC will have collected $\sim$ 150 fb^{-1} of data with peak of the instantaneous luminosity being $\sim 2\times10^{34}$cm^{-2}s^{-1}. The maximum average number of proton-proton interactions per bunch crossing (reached in 2018) is $<\mu>\sim 37$. During the second long shutdown (LS2) in 2019-2020, the injection chain will be improved and the instantaneous luminosity will be stable around $\sim 2\times10^{34}$cm^{-2}s^{-1} with $<\mu>\sim 60$. Moreover, the centre-of-mass energy will be increased up to 14 TeV. The total amount of data collected at the end of Run-III will be $\sim$ 300 fb^{-1}.
During LS3 in 2024-2026, the accelerator will be upgraded to the HL-LHC and it will achieve an instantaneous luminosity of $\sim 7\times10^{34}$cm^{-2}s^{-1}. The average number of interactions per bunch-crossing will strongly increase up to $<\mu>\sim 200$. The LHC is expect to deliver 3000 fb^{-1} at $\sqrt{s}$ =14 TeV. Figure 8.1 shows the timeline of the LHC and HL-LHC project for the upcoming years.
The increase of centre-of-mass energy and amount of data collected will allow to improve significantly the discovery potential and exclusion power of many analyses.
Also the ATLAS experiment will be upgraded to sustain the increasing particle flux at the of LHC:

- The ID will be extended to provide precise tracking of charged particles up to $|\eta|<4.0$. A 2T axial magnetic field will surrounded it. Pixel and Silicon-microstrip detectors will form the future ID;
- The LAr sampling calorimeters ($|\eta|<3.2$) and tile calorimeters ($|\eta|<1.7$) will not be replaced. In the endcap and forward regions, a new high-granularity forward calorimeters will cover the $3.1<|\eta|<4.9$ range;

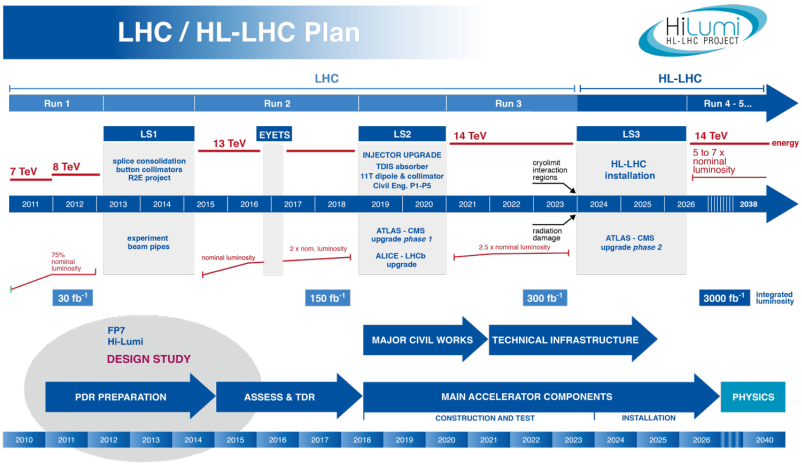

Figure 8.1: Schedule of the LHC and HL-LHC projects from 2010 to 2040 [127].

- The muon spectrometer will be upgraded by adding a very forward muon tagger;
- A two-level trigger will reduce the event rate to ∼10 kHz. In the case of leptonic triggers, the rate may be lowered to 2.2 kHz with a lepton p_{T} threshold set at $p_{\mathrm{T}} > 22$ GeV (electrons) or $p_{\mathrm{T}} > 20$ GeV (muons).

8.2 Theoretical motivation

The main motivation for a low-energy SUSY is given by the mass hierarchy problem. The observed characteristics of the Higgs boson and the non-discovery of SUSY particles leads to a strong exclusion in the parameter space of MSSM, where naturalness is satisfied.
The recent limits on gluino masses [115] indicate that SUSY lies at the TeV scale, meaning that fine-tuning is needed to stabilize the Higgs boson mass.
The naturalness condition in the MSSM can be summarised as [128]:

$$-\frac{m_Z^2}{2} = |\mu|^2 + m_{H_u}^2, \tag{8.1}$$

where m_{H_u} is the up-like supermultiplet introduced by the MSSM (Section 3.1.2).
If superpartners are too heavy, fine-tuning is needed to obtain the symmetry breaking at the electroweak scale. Therefore, μ and m_{H_u} must be in the range 100-200 GeV to satisfy the naturalness condition.
Since μ drives the higgsino masses, it should not be too heavy, while stops and gluinos, which enter in the first and second loop corrections, can be heavier. All other superpartner masses, including binos and winos (M_1, M_2), can reach the TeV scale.
In the considered scenario, the three lightest electroweakinos ($\tilde{\chi}_1^0, \tilde{\chi}_1^{\pm}, \tilde{\chi}_2^0$) are dominated by the higgsino component and are almost mass degenerate. The mass difference is determined by mixing and M_1, M_2 values, it lies in a range between 100 MeV and 10 GeV.
Searches for nearly degenerate higgsinos are very challenging, since the products of the decay chain have low transverse momentum. Final states with a jet (or Z boson or photon) from initial state radiation (ISR) help to improve the acceptance of these searches, which are affected by small signal rates

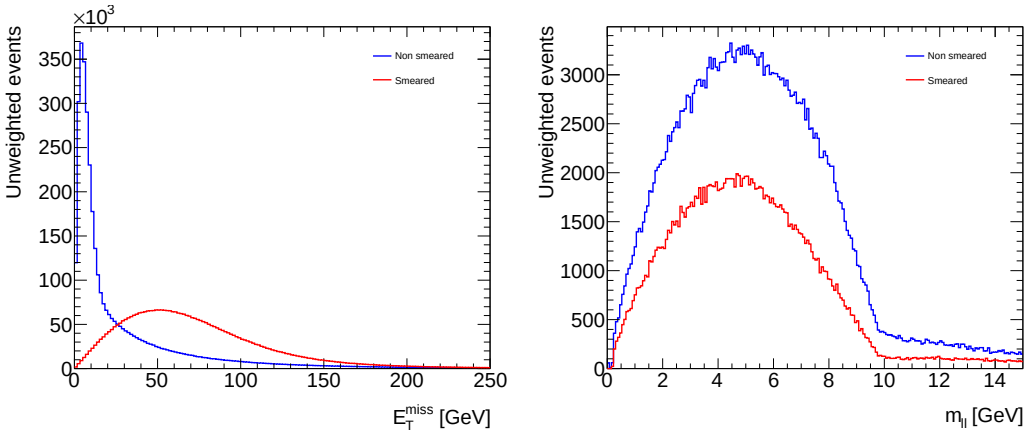

Figure 8.2: Distribution of $E_{\mathrm{T}}^{\mathrm{miss}}$ (left) and $m_{\ell\ell}$ (right) for a signal sample ($\Delta m = 10$ GeV) without any smearing (blue) and considering smearing (red).

and statistical limitations.
In compressed higgsino scenarios, a final state with ISR jet and two same flavour opposite sign (SFOS) leptons allows to reach a good sensitivity.
During Run-II, ATLAS has published a result which exploits this final state [129]. The following study takes strong inspiration from this analysis.

8.3 Analysis strategy

The strategy and selection of the analysis are strongly inspired by the search conducted in Run-II with 36.1 fb^{-1}.
The SRs are designed to reduce the background contribution, which originate mainly from WW and $Z \to \tau\tau$ for prompt leptons. Also W+jets and $t\bar{t}$ contribute significantly, especially at lower dilepton invariant masses, with fake/non-prompt leptons.
Unlike electrons, muon reconstruction and fake rates are not expected to grow dramatically with the increased pile-up conditions, thus states with two low-p_{T} reconstructed muons are considered. The following section describes the MC samples generated for the main background processes and signal, the discriminating variables and the final selection.

8.3.1 Monte Carlo samples

The MC samples used in this analysis have been generated at 14 TeV of pp collision energy, with equivalent luminosities of at least 3000 fb^{-1}. Detector effects are taken into account by applying energy smearing, efficiencies and fake rates to truth level quantities, following parameterisations based on detector performance studies with GEANT taking into account the upgraded detector in high luminosity conditions. The smearing properly models jets and $E_{\mathrm{T}}^{\mathrm{miss}}$, while leptons suffer of some mis-modelling. Figure 8.2 shows the effect of smearing on $E_{\mathrm{T}}^{\mathrm{miss}}$ and $m_{\ell\ell}$ dsitributions for a signal sample with $\Delta m = 10$ GeV.

The W+jets, WW and $Z \to \tau\tau$ processes are generated using MADGRAPH5_AMC@NLO V2.2.3 interfaced to PYTHIA8.186 with the A14 tune for the modelling of the parton showers (PS), hadronisation and underlying events. The samples are filtered requiring one jet with $p_{\mathrm{T}} > 100$ GeV and forcing the W decay into muon.
The top quark pair production is simulated using POWHEG interfaced to PYTHIA8.186, and normalised to approximate next-to-next-to-leading-order calculations.
The higgsino pair production includes $\tilde{\chi}_2^0\tilde{\chi}_1^0$, $\tilde{\chi}_2^0\tilde{\chi}_1^\pm$, $\tilde{\chi}_1^\pm\tilde{\chi}_1^\mp$ production modes. The masses of $\tilde{\chi}_2^0$ and $\tilde{\chi}_1^0$ are varied, while the masses of the charginos are set to $m(\tilde{\chi}_1^\pm) = \frac{1}{2}[m(\tilde{\chi}_2^0) + m(\tilde{\chi}_1^0)]$.
The signal samples are generated with different mass splitting, varying from 1 GeV to 50 GeV. The larger mass splittings require some mixing with binos and winos states. However, in this simplified model, the calculated cross-sections assume electroweakino mixing matrices corresponding to pure higgsino scenarios.
The signal events were generated with up to two extra partons in the matrix element using MG5_AMC@NLO V2.3.3 at LO interfaced to PYTHIA 8.186 for parton showering and hadronisation.
The NNPDF23LO PDF set was used. The electroweakino decays are then produced with MADSPIN [130], requiring to produce at least two muons in the final state and including those from decays of τ-leptons.
The branching ratios for $\tilde{\chi}_2^0 \to Z^*\tilde{\chi}_1^0$ and $\tilde{\chi}_1^\pm \to W^*\tilde{\chi}_1^0$ were fixed to 100%. The $Z^* \to \ell^+\ell^-$ and $W^* \to \ell\nu$ branching ratios depend on the mass splittings and were computed using SUSY-HIT [131].

8.3.2 Event selection and Signal region

The reconstruction of physics objects are performed at truth-level with parameterised detector functions. Jets are reconstructed with the anti-k_t algorithm with a radius parameter of 0.4 and selected with $|\eta| < 2.8$. Jets are tagged as originating from b-decays (b-tagged) using a parameterisation in p_{T} and $|\eta|$ modelling the performances of the MV2c10 b-tagging algorithm, as introduced in Section 5.3.
Muons are selected with $p_{\mathrm{T}} > 3$ GeV and $|\eta| < 2.5$. Fake or non-prompt muons are rejected by applying a *FixedCutTightTrackOnly* isolation criteria, introduced in Section 5.2. The magnitude of $E_{\mathrm{T}}^{\mathrm{miss}}$ is calculated at truth level as the vectorial sum of the momenta of neutral weakly-interacting particles (neutrinos and neutralinos) and then smeared to simulate the detector response, with a function parameterised in the average number of interactions per bunch crossing $< \mu >$ and the scalar sum of energy in the calorimeter ΣE_{T}.
As mentioned before, the mass difference between electroweakinos ($\tilde{\chi}_1^\pm, \tilde{\chi}_2^0$) and the LSP ($\tilde{\chi}_1^0$) is rather small. Therefore, the W and Z bosons are produced highly off-shell and consequently the leptons in the final state are very soft. Due to this, the cut on the lepton p_{T} has to be strongly reduced[1] to 3 GeV.
Figure 8.3 shows the Feynman diagrams of the considered signal models. The SFOS lepton couple is either produced by Z^* or by two W^* decaying leptonically.
Since no b-jets are expected, a veto is applied to reject $t\bar{t}$ and single top background.
The leading jet is required to have $p_{\mathrm{T}} > 100$ GeV to select ISR jets, while the ideal cut on $E_{\mathrm{T}}^{\mathrm{miss}}$ is studied to understand whether a low requirement[2] enhances the sensitivity and to provide feedback for the HL-LHC trigger preparation.

[1] Typically SUSY analyses select signal leptons with $p_{\mathrm{T}} > 20 - 25$ GeV.
[2] In Run-II, $E_{\mathrm{T}}^{\mathrm{miss}}$ triggers start to be efficient around 200-250 GeV depending on the trigger threshold.

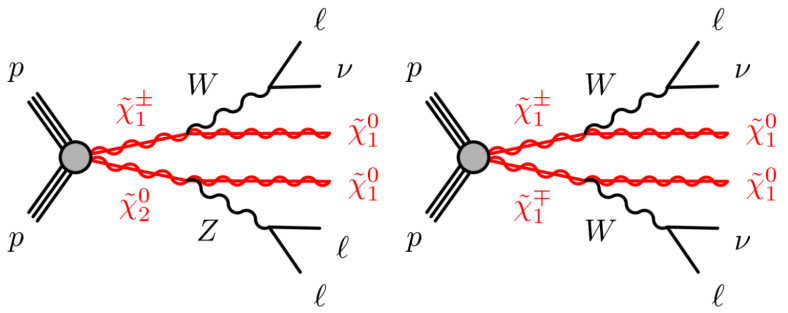

Figure 8.3: Diagrams depicting the pair production of $\tilde{\chi}_1^{\pm}\tilde{\chi}_2^0$ and $\tilde{\chi}_1^{\pm}\tilde{\chi}_1^{\mp}$ with decays into leptonically decaying off-shell W and Z bosons and $\tilde{\chi}_1^0$.

Additional cuts are applied on the following variables:

- $\Delta\phi(E_{\mathrm{T}}^{\mathrm{miss}},\mathrm{jet}_1)$: since it is required to have the LSP particles recoiling against the ISR jet, a lower cut is applied to the azimuthal separation between $E_{\mathrm{T}}^{\mathrm{miss}}$ and the leading jet;
- $m_{\tau\tau}$: it approximately reconstructs the invariant mass of leptonically decaying τ from a Z boson decay. The variable is defined as $\mathrm{sign}(m_{\tau\tau}^2)\sqrt{|m_{\tau\tau}^2|}$, where $m_{\tau\tau}^2 = 2p_{l_1}\cdot p_{l_2}(1+\xi_1)(1+\xi_2)$. The parameters ξ_1 and ξ_2 are determined by solving $\mathbf{p}_{\mathrm{T}}^{\mathrm{miss}} = \xi_1\mathbf{p}_{\mathrm{T}}^{\ell_1} + \xi_2\mathbf{p}_{\mathrm{T}}^{\ell_2}$, where $\mathbf{p}_{\mathrm{T}}^{\ell_1,\ell_2}$ are the lepton four-momenta. As shown in Figure 8.4, the distribution peaks at the Z pole mass for $Z\rightarrow\tau\tau$ while the signal has a rather flat distribution. Unfortunately the smearing affects significantly the distribution, leading to a more broad Z mass peak; as a consequence the efficiency of the cut is reduced compared to Run-II and the contribution to the final background is more significant.
- $E_{\mathrm{T}}^{\mathrm{miss}}/H_{\mathrm{T}}^{\mathrm{lep}}$: the scalar sum of leptonic momenta is expected to be smaller for SUSY compressed models. Therefore, $E_{\mathrm{T}}^{\mathrm{miss}}/H_{\mathrm{T}}^{\mathrm{lep}}$ is a powerful discriminant. The lower limit required is defined with an event-by-event reconstruction: $E_{\mathrm{T}}^{\mathrm{miss}}/H_{\mathrm{T}}^{\mathrm{lep}} > \max[5, 15-2m_{\ell\ell}/(1\ \mathrm{GeV})]$. The dependency on $m_{\ell\ell}$ connects directly to the Δm, as mentioned above.
- $\Delta R_{\ell\ell}$: a lower limit is applied to the separation of the two leptons to suppresses lepton pairs originating from photon conversions (nearly collinear) or muons producing pairs of tracks with shared hits;
- $m_{\ell\ell}$: the dilepton invariant mass is required to be outside of the [3.0-3.2] GeV range to exclude the J/ψ resonance. Furthermore, the $m_{\ell\ell}$ distribution of the considered signal models has a kinematic endpoint given by $\Delta m(\tilde{\chi}_2^0,\tilde{\chi}_1^0)$. Figure 8.5 shows dilepton invariant mass distribution obtained from simulation [132]. The SRs are therefore binned in $m_{\ell\ell}$ to exploit this characteristic.

Taking inspiration from the Run-II analysis, the SR definition is shown in Table 8.1. The choice of the cuts of lepton p_T and $E_{\mathrm{T}}^{\mathrm{miss}}$ are important, since it provides useful information for the design of future triggers and performance of the detector.
The lepton momentum it is lowered down to 3 GeV, which allows to be more sensitive to smaller mass splitting as shown in Figure 8.6. The expected exclusion significance, computed with the RooStats framework and defined in terms of one-sided Gaussian standard deviations, as a function of different p_{T} lepton cuts is shown for different Δm and with a flat 30% systematic uncertainty. A clear trend towards low lepton p_{T} is observed, especially for Δm=2,4 GeV where the significance grows at 3 GeV.

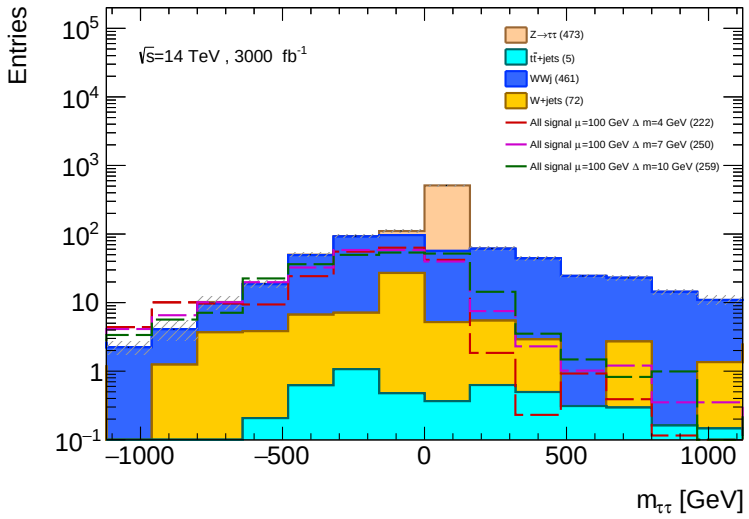

Figure 8.4: Distribution of $m_{\tau\tau}$ for background and signal processes. The events are preselected applying a b-jet veto and $E_{\mathrm{T}}^{\mathrm{miss}}$>400 GeV.

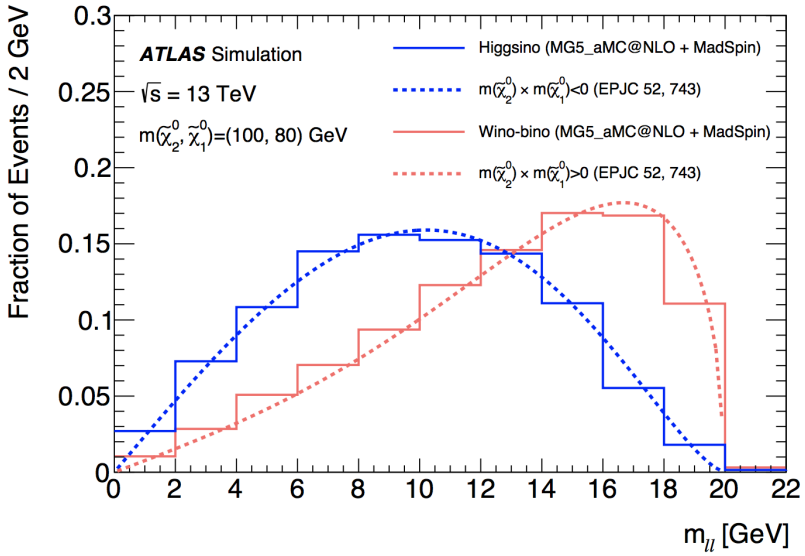

Figure 8.5: Dilepton invariant mass ($m_{\ell\ell}$) for higgsino and wino-bino simplified models. The endpoint of the $m_{\ell\ell}$ distribution is determined by the difference between the masses of the $\tilde{\chi}_2^0$ and $\tilde{\chi}_1^0$. The results from simulation (solid) are compared with an analytic calculation of the expected lineshape (dashed), where the product of the signed mass eigenvalues (m($\tilde{\chi}_1^0$)×m($\tilde{\chi}_2^0$)) is negative for higgsino and positive for wino-bino scenarios [129].

The fake lepton rate increases at low p_{T}, the Monte Carlo simulation gives a reliable result when comparing with data-driven yields obtained in Run-II.

A similar scan has been performed on $E_{\mathrm{T}}^{\mathrm{miss}}$. Trigger threshold are around 200 GeV and for such soft LSP in the final state it is reasonable to expect a low $E_{\mathrm{T}}^{\mathrm{miss}}$. Therefore is important to study whether a lower $E_{\mathrm{T}}^{\mathrm{miss}}$ cut would allow to increase the sensitivity.

Figure 8.7 shows the expected significance as a function of the $E_{\mathrm{T}}^{\mathrm{miss}}$ cut. The sensitivity is shown for different μ values and Δm=7 GeV, considering the [3,5] GeV $m_{\ell\ell}$ bin where the signal is expected to peak, and it requires to have at least 3 raw events in the total background estimation. Surprisingly the scan shows that at higher $E_{\mathrm{T}}^{\mathrm{miss}}$ values the significance rises, reaching a plateau at 400 GeV.

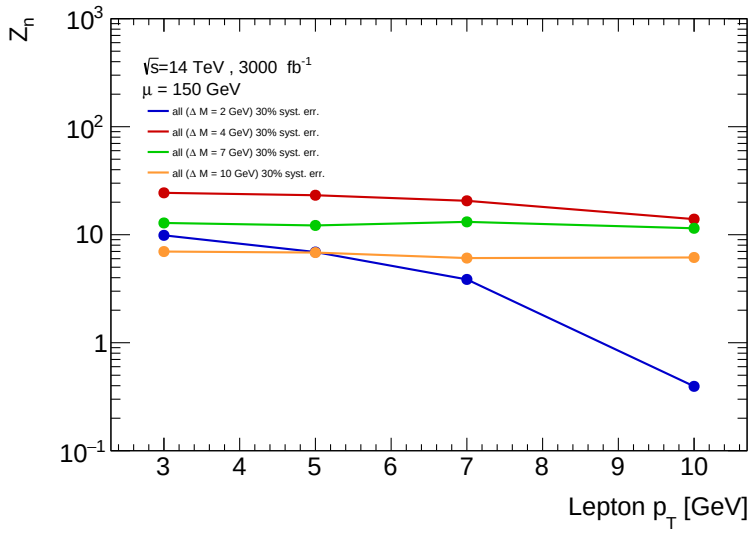

Figure 8.6: Scan of the significance as a function of the lepton p_T cut. The signal considered is at μ=100 GeV and for different Δm values. The solid line shows the significance with a 30% flat uncertainty.

This is caused by the ISR jet, which boosts significantly the LSP particles and therefore causes an higher E_T^{miss} in the final state.

8.4 Results

Table 8.2 shows the background yields at each step of the selection of the SR. The fake leptons background (W+jets) is the dominant one, also $Z \to \tau\tau$ and W+jets processes contribute significantly. The $t\bar{t}$+jets background is strongly suppressed due to the two lepton requirement and the b-tagged jet veto, while the $m_{\tau\tau}$ veto is highly efficient to reject the Z background.
Figure 8.8 shows the distribution of E_T^{miss}, E_T^{miss}/H_T and leading lepton p_T with SR selection applied except the shown variable.
The SR is further binned in $m_{\ell\ell}$ to exploit the dependence of the peak from the mass splitting. Subsequently a shape fit is performed with the HISTFITTER framework to estimate the exclusion power of

Variable	Requirement
Number of leptons	=2
Leading lepton $p_T^{\ell_1}$	> 3 GeV
Subleading lepton $p_T^{\ell_2}$	> 3 GeV
$\Delta R_{\ell\ell}$	> 0.05
$m_{\ell\ell}$	$\in$ [1,60] GeV excluding [3.0,3.2] GeV
E_T^{miss}	> 400 GeV
Number of jets	$\geq$ 1
Leading jet p_T	> 100 GeV
$\Delta\phi(j_1, E_T^{miss})$	> 2.0
Number of b-tagged jets	=0
$m_{\tau\tau}$	<0 or > 160 GeV
E_T^{miss}/H_T^{lep}	> max(5,15-2$\frac{m_{\ell\ell}}{\text{GeV}}$)
Binned in	$m_{\ell\ell}$

Table 8.1: Summary of the kinematic cuts of the signal region.

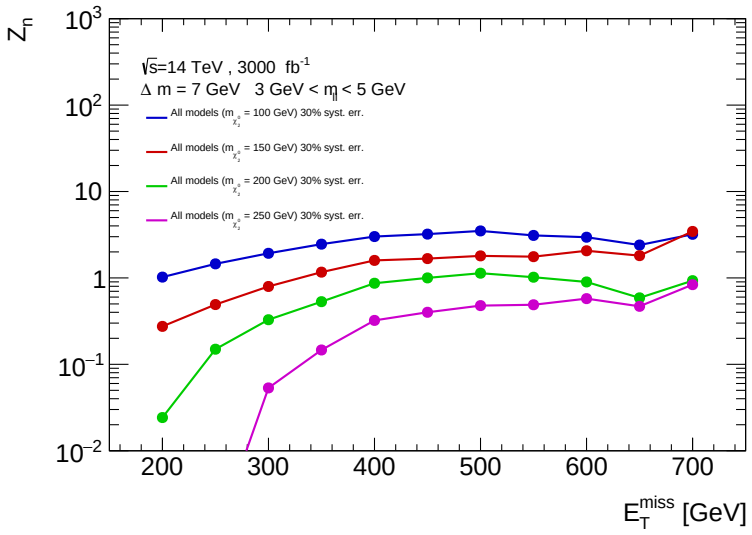

Figure 8.7: Scan of the significance as a function of the E_T^{miss}cut. The signal considered is at Δm=7 GeV and $m_{\tilde{\chi}_2^0}$=100,150,200,250 GeV. The significance is estimated considering only the $m_{\ell\ell}$ bin [3,5] GeV. The solid line shows the significance with a 30% flat uncertainty.

this analysis with 3000 fb^{-1}. A 30% flat systematic uncertainty is added in quadrature to the statistical uncertainty of the Monte Carlo samples, no shape uncertainty is taken into account.

Figure 8.8 shows the distribution of the first four bins of the SR. The signal is super-imposed on the background distribution. The signal shown is the sum of the yields obtained with the three different types of production processes: $\tilde{\chi}_2^0\tilde{\chi}_1^0$, $\tilde{\chi}_2^0\tilde{\chi}_1^\pm$and $\tilde{\chi}_1^\pm\tilde{\chi}_1^\mp$. It is interesting to notice that the signal model peaks in the bin which includes Δm/2, as example a signal point with Δm=4 GeV peaks in the first $m_{\ell\ell}$ bin ([1,3] GeV). The shape fit enhances significantly the exclusion limit, exploiting this characteristic of the considered model.

The background and signal yields in each bin are shown in table 8.3. It is again important to notice that the highest contribution of the considered signal point is in the bin corresponding to half of the mass splitting.

In Figure 8.9 is shown the projected exclusion limit in $m(\tilde{\chi}_1^\pm)$ - Δm parameter plane at 3000 fb^1 for the chosen SR, after performing a shape fit over the $m_{\ell\ell}$ bins.

The result can be compared with the Run-II limit at 36.1 fb^{-1} in Figure 8.10. The exclusion limit is strongly improved in the chargino mass from 150 GeV to 300 GeV thanks to the significantly higher statistics and the increase in centre-of-mass energy. The lower p_T cut on the leptons allows to reach a smaller mass splitting.

Cut	$Z \to \tau\tau$	$t\bar{t}$+jets	WW+jets	W+jets
$E_T^{miss} > 400$ GeV	765.0 ±14.2	504.7 ±1.1	2447.9 ±16.0	160829.4 ±440.7
$N_{lep} = 2$	505.5 ±11.5	17.2 ±0.2	1305.9 ±11.7	101.4 ±11.1
$N_{b-jet} = 0$	473.5 ±11.2	5.9 ±0.1	513.0 ±7.3	85.7 ±10.2
p_T(jet)>100 GeV	473.5 ±11.2	3.0 ±0.1	316.3 ±5.8	82.1 ±10.0
$\|\Delta\Phi(\text{jet},E_T^{miss})\| > 2$	471.9 ±11.1	2.2 ±0.1	142.7 ±3.9	39.8 ±6.9
$m_{\tau\tau}$ veto	18.2 ±2.1	2.1 ±0.1	138.8 ±3.8	39.8 ±6.9
$m_{\ell\ell} < 60$ GeV	18.2 ±2.1	0.6 ±0.0	23.3 ±1.6	29.0 ±5.9
E_T^{miss}/H_T cut	7.2 ±1.4	0.4 ±0.0	14.9 ±1.3	20.5 ±5.0
$0.05 < \Delta R_{ll} < 2$	7.0 ±1.3	0.2 ±0.0	6.9 ±0.9	8.5 ±3.2

Table 8.2: Yields breakdown of the background processes, weighted events are normalised to a luminosity of 3000 fb^{-1}.

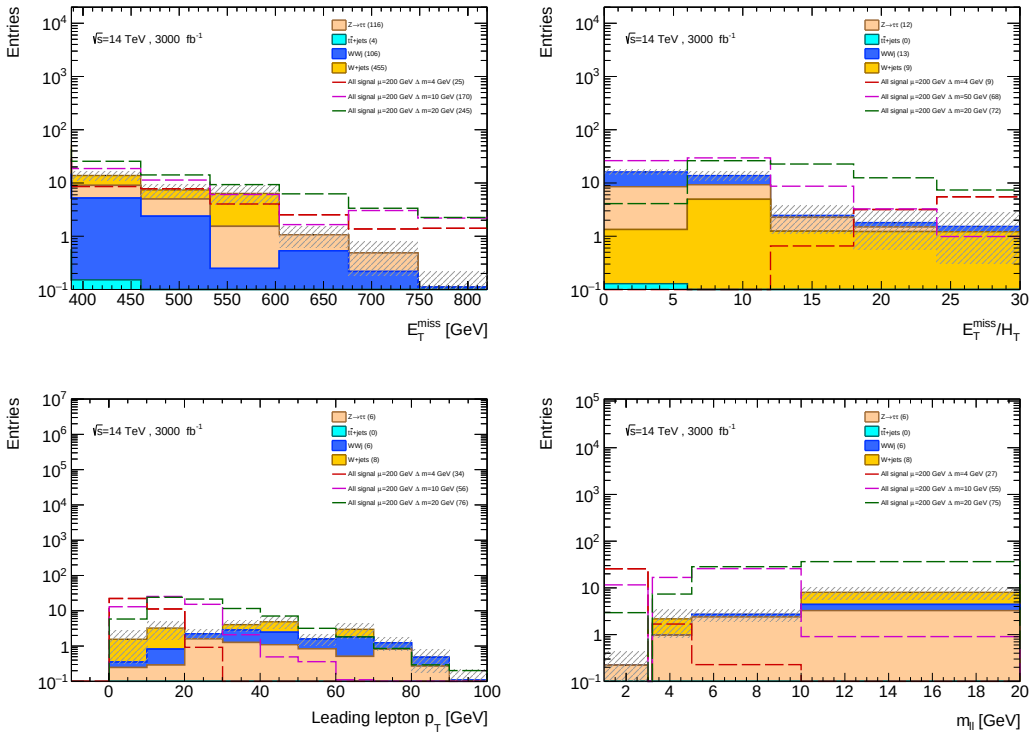

Figure 8.8: Distribution of $E_{\mathrm{T}}^{\mathrm{miss}}$ (top left), $E_{\mathrm{T}}^{\mathrm{miss}}/H_{\mathrm{T}}$ (top righ), leading lepton p_{T} (bottom left) and first four bins of the dilepton invariant mass, after applying the SR selection except the selection on the variable shown. The signal with μ=100 GeV and Δm=4,7,10 GeV are super-imposed and include all possible production modes. The signal samples with μ=100 GeV and Δm=4,7,10 GeV are super-imposed. In brackets are shown the expected yields at 3000 fb^{-1}. The [3.0,3.2] $m_{\ell\ell}$ range is vetoed to veto the J/Ψ contribution.

Therefore it would be important to perform this analysis at HL-LHC, to test even further a pure higgsino scenario of the MSSM.

The mass splitting below 1 GeV are hardly reachable by this kind of analysis, since the leptons would be too soft. For very small Δm, the disappearing track analysis is able to exclude a wide area of the phase space [133]. The region in between these two analyses (0.1-1 GeV), the leptons are too soft to be detected and decay length is too short to exploit a disappearing tracks analysis. This region could be explored including a photon from final state radiation (FSR) [134]. An eventual photon emitted by the chargino would tend to be collinear with it, and consequently with the transverse missing momentum. Therefore, exploiting angular distributions of FSR photon, ISR jet and $E_{\mathrm{T}}^{\mathrm{miss}}$ would allow to be sensitive to the intermediate range of Δm.

	[1,3] GeV	[3.2,5] GeV	[5,10] GeV	[10,20] GeV	[20,30] GeV	[30,40] GeV	[40,60] GeV
W+jets	0.00±0.00	1.21±1.21	0.0±0.0	3.62±0.92	2.42±1.71	0.0±0.0	1.21±1.21
WW+jets	0.00±0.00	0.00±0.00	0.32±0.18	1.16±0.35	1.47±0.39	1.47±0.39	2.52±0.51
$t\bar{t}$+jets	0.01±0.00	0.00±0.00	0.03±0.01	0.06±0.01	0.05±0.01	0.04±0.01	0.04±0.01
$Z \to \tau\tau$	0.22±0.22	0.97±0.49	2.35±0.79	3.21±0.93	0.00±0.00	0.00±0.00	0.00±0.00
Total bkg.	0.23±0.22	2.18±1.30	2.70±0.81	8.05±1.35	3.94±1.75	1.51±0.39	3.77±1.31
m($\tilde{\chi}_1^{\pm}/\tilde{\chi}_2^0$,$\tilde{\chi}_1^0$)							
(102,100) GeV	22.7±2.5	0.2±0.2	0.0±0.0	0.0±0.0	0.0±0.0	0.0±0.0	0.0±0.0
(104,100) GeV	107.8±6.1	9.0±1.9	10.4±0.2	0.5±0.4	0.0±0.0	0.0±0.0	0.0±0.0
(110,100) GeV	24.7±2.3	44.0±3.1	68.7±3.8	3.7±0.8	0.1±0.0	0.0±0.0	0.0±0.0
(120,100) GeV	7.9±1.6	14.0±2.4	47.8±4.0	63.8±4.8	1.4±0.5	0.4±0.3	0.0±0.0

Table 8.3: Expected MC background and signal yields for an integrated luminosity of 3000 fb^{-1} in the different $m_{\ell\ell}$ bins of the signal region.

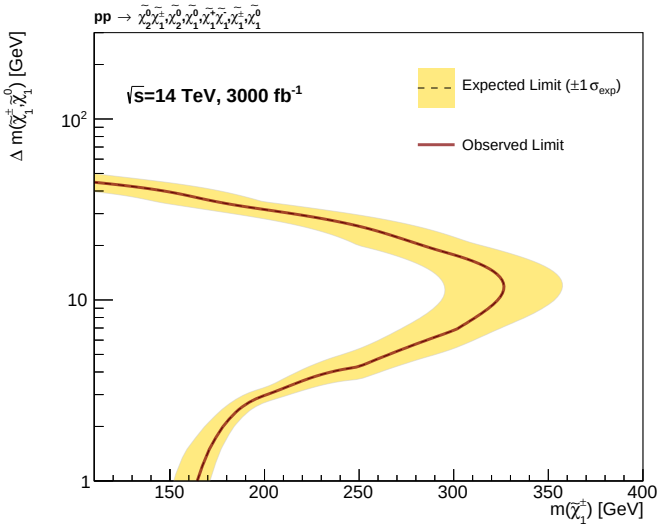

Figure 8.9: Exclusion limit at 3000 fb^{-1} for the higgsino searches with soft leptons.

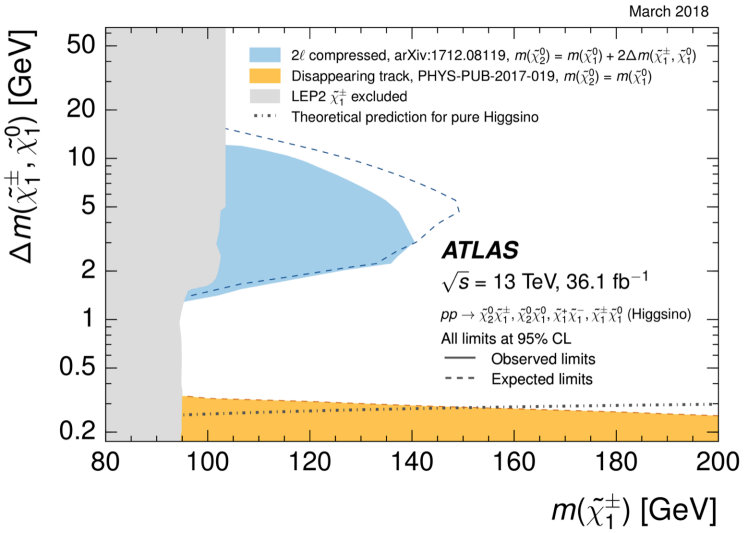

Figure 8.10: Exclusion limit at 36.1 fb^{-1} for the higgsino searches with soft leptons. In addition, the exclusion limit obtained by the disappearing tracks analysis is shown [129].

Chapter 9

Conclusions

The search for supersymmetric particles in final states with either two leptons with same electric charge or three leptons (SS3L), jets and missing transverse momentum is a powerful tool to explore scenarios with compressed mass spectra or R-parity violation. The analyses presented in this dissertation were performed with data collected in proton-proton collisions at a center-of-mass energy of $\sqrt{s} = 13$ TeV by the ATLAS detector in 2015 and 2016. No significant excess of data over the expected SM background has been observed. Therefore, the two analyses were able to set stringent exclusion limits on a wide range of SUSY models with particles produced via the strong or the electroweak interaction, and provide model-independent upper limits.

The results obtained in Run-1 and at the early stage of Run-2 (3.21 fb^{-1}) have been strongly improved in all scenarios. In the case of the strong production SS3L analysis several new signal models have been included in the final interpretation and dedicated signal regions have been designed. In addition, the fake/non-prompt lepton background estimation was improved combining statistically the dynamic matrix method and MC template method results, giving a more robust estimate. In the electroweak SS3L analysis, the first results obtained with Run-2 data were presented. The exclusion limits were strongly improved compared to Run-1, also thanks to a complete re-optimisation of the signal region definitions and the increase of center-of-mass energy and integrated luminosity.

For the R-parity conserving models, the limits on the masses of the gluinos and sbottoms are improved by up to 400 GeV compared to the earlier limits, thanks to the improvements in the signal region definitions as well as the increase in luminosity. In these models, the masses of gluinos below 1.75 TeV and bottom squarks below 700 GeV are excluded at 95% confidence level for a light $\tilde{\chi}_1^0$. The coverage of the compressed regions has been improved and LSP masses up to 1200 and 250 GeV can be excluded in the gluino and bottom squark pair production models, respectively. A completely new signal region targeting three leptons with the same electric charge was designed and allowed to exclude top-squark pair production up to 700 GeV when decaying to a top quark and a cascade of electroweakinos.

For the R-parity violating simplified models considering gluino pair production, gluino masses below 1.3 TeV are excluded, while models considering pair production of $\tilde{d}_R$ are excluded for down squark masses below 500 GeV.

The production rate of SUSY particles produced with the electroweak interaction is significantly lower than in the strong production searches. Therefore searches for electroweak pair production of SUSY particles are very challenging. Despite the difficulties, exclusion limits for the model considering the electroweak pair production of a chargino and a neutralino decaying via a W and a Higgs boson have been placed with the same-sign leptons analysis. A statistical combination of the two signal regions allows to be sensitive at low m($\tilde{\chi}_1^{\pm}/\tilde{\chi}_2^0$), covering the compressed region which is not excluded by

other channels. The same-sign channel excludes $\tilde{\chi}_1^0$masses up to 30 GeV for ($\tilde{\chi}_1^{\pm}$,$\tilde{\chi}_2^0$) masses in the range 150-240 GeV.

Since no sign of new physics has been observed at the LHC in this early Run-2, it is important to start planning future projects which will increase the center-of-mass energy at 14 TeV and the instantaneous luminosity, such as the High Luminosity LHC (HL-LHC). Since the SUSY searches performed so far in Run-2 excluded gluinos and squarks up to 1-2 TeV, the naturalness condition in the minimal supersymmetric model model (MSSM) suggests that the higgsino mass should lie at the electroweak scale. In this scenario, the electroweakinos ($\tilde{\chi}_1^{\pm}$,$\tilde{\chi}_2^0$,$\tilde{\chi}_1^0$) are nearly degenerate in mass, therefore searches are more challenging. In this thesis, a prospect study of the search for higgsino production with final state radiation jet and low p_{T} leptons at HL-LHC was presented. The increase of energy and integrated luminosity (3000 fb^{-1}) allows to improve by 150 GeV the exclusion on the $\tilde{\chi}_1^{\pm}$mass obtained by the Run-2 analysis at 36.1 fb^{-1}. Moreover, a lower p_{T} threshold for leptons has been used, which allows to explore lower mass splittings between $\tilde{\chi}_1^{\pm}$and $\tilde{\chi}_1^0$.

In conclusion, despite the absence of discovery of SUSY particles, the results obtained in the searches with the SS3L analyses are impressive. This kind of searches are able to access regions of the phase-space which are complementary to other analyses, such a compressed mass spectras and R-parity violating models. The efforts of ATLAS and other experiments in the SUSY hunt will continue and the searches with leptons, jets and missing transverse momentum will play a key role in the search for new physics with the ATLAS experiment.

Appendix A

Exclusion limits of SS3L strong analysis

In Figure A.1 are shown exclusion limits for the signal models 6.2a, 6.2b, 6.2c, 6.2d.

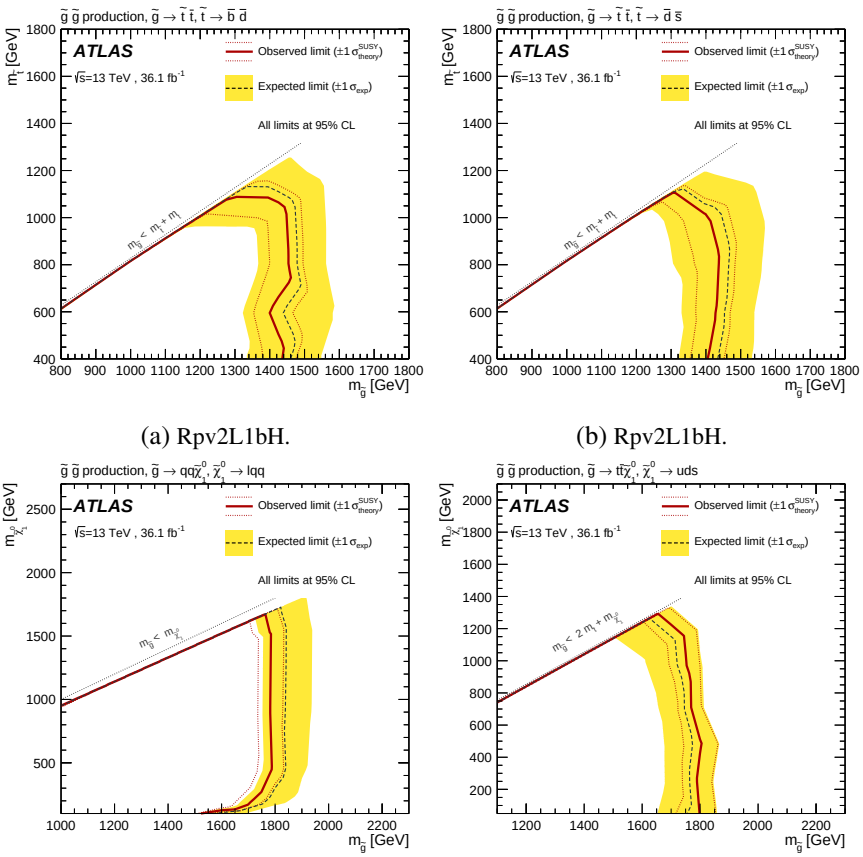

(a) Rpv2L1bH.

(b) Rpv2L1bH.

(c) Rpv2L0b.

(d) Rpv2L2bH.

Figure A.1: Observed and expected exclusion limits on the $\tilde{g}$ masses in the context of the RPV SUSY scenarios. The signal regions used to obtain the limits are (a)-(b) Rpv2L1bH, (c) Rpv2L0b, (d) Rpv2L2bH. All limits are computed at 95% CL. [105].

Appendix B

Details on statistical interpretation of strong SS3L analysis

A detailed breakdown of the dominant systematic uncertainties on the background estimation in each of the 2016 signal regions is provided in the tables B.1- B.19. The individual components of the uncertainties can be correlated and do not necessarily add up quadratically to the total uncertainty. The percentages show the size of the uncertainties relative to the total expected background. The largest components are usually theoretical uncertainties or uncertainties associated with the data-driven methods.

The 95% CL model-independent upper limits on the signal production cross-sections $\mathrm{UL}^{95}(\sigma_{\mathrm{prod}})$ (in fb) for each signal point of the considered models are stated in the Tables B.20- B.26.

Uncertainty of signal region	Rpc3LSS1b
Total background expectation	1.62
Statistical error ($\sqrt{N_{\mathrm{exp}}}$)	$\pm$1.27
Total background systematic	$\pm$0.76 [46.9%]
Fake lepton systematics	$\pm$0.72 [44.4%]
Theory uncertainty: Rare	$\pm$0.17 [10.5%]
MC statistics	$\pm$0.15 [9.3%]
Charge-flip systematics	$\pm$0.07 [4.3%]
Luminosity	$\pm$0.01 [0.6%]
Muon SF (sys.)	$\pm$0.01 [0.6%]
Electron identification SF	$\pm$0.01 [0.6%]

Table B.1: Breakdown of the dominant systematic uncertainties on the background estimation in signal region Rpc3LSS1b for an integrated luminosity of 36.1fb^{-1}. The individual uncertainties can be correlated and do not necessarily add up quadratically to the total uncertainty. The percentages show the size of the uncertainties relative to the total expected background.

Uncertainty of signal region	Rpc2L2bS
Total background expectation	3.35
Statistical error ($\sqrt{N_{\text{exp}}}$)	$\pm$1.83
Total background systematic	$\pm$1.02 [30.4%]
Fake lepton systematics	$\pm$0.52 [15.5%]
Theory uncertainty: Rare	$\pm$0.51 [15.2%]
Jet energy scale (NP-1)	$\pm$0.50 [14.9%]
MC statistics	$\pm$0.35 [10.4%]
Theory uncertainty: ttW/Z	$\pm$0.25 [7.5%]
b-jets SF	$\pm$0.19 [5.7%]
Luminosity	$\pm$0.09 [2.7%]
c-jets SF	$\pm$0.08 [2.4%]
Jet energy scale (NP-3)	$\pm$0.08 [2.4%]
Jet energy scale (NP-2)	$\pm$0.06 [1.8%]
Jet energy resolution	$\pm$0.06 [1.8%]
MET soft-term resolution 1	$\pm$0.06 [1.8%]
MET soft-term resolution 2	$\pm$0.04 [1.2%]
Jet vertex tagger	$\pm$0.04 [1.2%]
Theory uncertainty: diboson	$\pm$0.04 [1.2%]
MET soft-term scale	$\pm$0.03 [0.9%]
Muon SF (sys.)	$\pm$0.03 [0.9%]
EGamma resolution	$\pm$0.03 [0.9%]
Electron identification SF	$\pm$0.03 [0.9%]
EGamma scale	$\pm$0.01 [0.3%]
Electron isolation SF	$\pm$0.01 [0.3%]
Muon (ID reconstruction)	$\pm$0.01 [0.3%]
Flavor tagging 1	$\pm$0.01 [0.3%]
Light-jets SF	$\pm$0.01 [0.3%]
Electron reconstruction SF	$\pm$0.01 [0.3%]
Muon SF (stat.)	$\pm$0.01 [0.3%]
Muon (MS reconstruction)	$\pm$0.01 [0.3%]
Flavor tagging 2	$\pm$0.01 [0.3%]

Table B.2: Breakdown of the dominant systematic uncertainties on the background estimation in signal region Rpc2L2bS for an integrated luminosity of 36.1fb^{-1}. The individual uncertainties can be correlated and do not necessarily add up quadratically to the total uncertainty. The percentages show the size of the uncertainties relative to the total expected background.

Uncertainty of signal region	Rpc2L2bH
Total background expectation	1.08
Statistical error ($\sqrt{N_{\text{exp}}}$)	$\pm$1.04
Total background systematic	$\pm$0.32 [29.6%]
Theory uncertainty: Rare	$\pm$0.21 [19.4%]
MC statistics	$\pm$0.17 [15.7%]
Jet energy scale (NP-1)	$\pm$0.11 [10.2%]
Theory uncertainty: ttW/Z	$\pm$0.10 [9.3%]
b-jets SF	$\pm$0.06 [5.6%]
Jet energy scale (NP-2)	$\pm$0.04 [3.7%]
Jet energy scale (NP-3)	$\pm$0.04 [3.7%]
Luminosity	$\pm$0.03 [2.8%]
Jet energy resolution	$\pm$0.03 [2.8%]
c-jets SF	$\pm$0.02 [1.9%]
Jet η-intercalibration	$\pm$0.02 [1.9%]
Electron identification SF	$\pm$0.02 [1.9%]
Theory uncertainty: diboson	$\pm$0.01 [0.9%]
Muon SF (sys.)	$\pm$0.01 [0.9%]
MET soft-term resolution 1	$\pm$0.01 [0.9%]
MET soft-term resolution 2	$\pm$0.01 [0.9%]
Jet vertex tagger	$\pm$0.01 [0.9%]
Flavor tagging 1	$\pm$0.01 [0.9%]
Electron isolation SF	$\pm$0.01 [0.9%]

Table B.3: Breakdown of the dominant systematic uncertainties on the background estimation in signal region Rpc2L2bH for an integrated luminosity of 36.1fb^{-1}. The individual uncertainties can be correlated and do not necessarily add up quadratically to the total uncertainty. The percentages show the size of the uncertainties relative to the total expected background.

Uncertainty of signal region	Rpc2Lsoft1b
Total background expectation	5.78
Statistical error ($\sqrt{N_{\text{exp}}}$)	±2.40
Total background systematic	±2.49 [43.1%]
Fake lepton systematics	±2.22 [38.4%]
MC statistics	±0.98 [17.0%]
Theory uncertainty: Rare	±0.36 [6.2%]
Jet energy scale (NP-1)	±0.30 [5.2%]
Theory uncertainty: ttW/Z	±0.29 [5.0%]
Luminosity	±0.07 [1.2%]
Theory uncertainty: diboson	±0.06 [1.0%]
Jet energy scale (NP-3)	±0.06 [1.0%]
MET soft-term resolution 1	±0.04 [0.7%]
Jet energy scale (NP-2)	±0.04 [0.7%]
Jet energy resolution	±0.03 [0.5%]
b-jets SF	±0.03 [0.5%]
Jet vertex tagger	±0.03 [0.5%]
Electron identification SF	±0.03 [0.5%]
c-jets SF	±0.03 [0.5%]
MET soft-term scale	±0.02 [0.3%]
Light-jets SF	±0.02 [0.3%]
Charge-flip systematics	±0.02 [0.3%]
Muon SF (sys.)	±0.02 [0.3%]
Electron reconstruction SF	±0.01 [0.2%]
Jet η-intercalibration	±0.01 [0.2%]
MET soft-term resolution 2	±0.01 [0.2%]
Muon (ID reconstruction)	±0.01 [0.2%]
Muon SF (stat.)	±0.01 [0.2%]

Table B.4: Breakdown of the dominant systematic uncertainties on the background estimation in signal region Rpc2Lsoft1b for an integrated luminosity of 36.1fb^{-1}. The individual uncertainties can be correlated and do not necessarily add up quadratically to the total uncertainty. The percentages show the size of the uncertainties relative to the total expected background.

Uncertainty of signal region	Rpc2Lsoft2b
Total background expectation	3.80
Statistical error ($\sqrt{N_{\text{exp}}}$)	$\pm$1.95
Total background systematic	$\pm$1.59 [41.8%]
Fake lepton systematics	$\pm$1.36 [35.8%]
MC statistics	$\pm$0.59 [15.5%]
Theory uncertainty: Rare	$\pm$0.37 [9.7%]
Jet energy scale (NP-1)	$\pm$0.35 [9.2%]
Theory uncertainty: ttW/Z	$\pm$0.17 [4.5%]
b-jets SF	$\pm$0.13 [3.4%]
c-jets SF	$\pm$0.07 [1.8%]
Luminosity	$\pm$0.06 [1.6%]
Jet energy scale (NP-3)	$\pm$0.06 [1.6%]
MET soft-term resolution 2	$\pm$0.04 [1.1%]
Jet energy scale (NP-2)	$\pm$0.04 [1.1%]
MET soft-term scale	$\pm$0.03 [0.8%]
Jet energy resolution	$\pm$0.03 [0.8%]
Jet vertex tagger	$\pm$0.03 [0.8%]
MET soft-term resolution 1	$\pm$0.02 [0.5%]
Charge-flip systematics	$\pm$0.02 [0.5%]
Theory uncertainty: diboson	$\pm$0.02 [0.5%]
Muon SF (sys.)	$\pm$0.02 [0.5%]
Electron identification SF	$\pm$0.01 [0.3%]
Muon (MS reconstruction)	$\pm$0.01 [0.3%]
EGamma scale	$\pm$0.01 [0.3%]
EGamma resolution	$\pm$0.01 [0.3%]
Jet η-intercalibration	$\pm$0.01 [0.3%]
Electron reconstruction SF	$\pm$0.01 [0.3%]
Light-jets SF	$\pm$0.01 [0.3%]

Table B.5: Breakdown of the dominant systematic uncertainties on the background estimation in signal region Rpc2Lsoft2b for an integrated luminosity of 36.1fb^{-1}. The individual uncertainties can be correlated and do not necessarily add up quadratically to the total uncertainty. The percentages show the size of the uncertainties relative to the total expected background.

Uncertainty of signal region	Rpc2L0bS
Total background expectation	6.02
Statistical error ($\sqrt{N_{\text{exp}}}$)	±2.45
Total background systematic	±1.84 [30.6%]
Theory uncertainty: diboson	±1.06 [17.6%]
Jet energy scale (NP-1)	±1.01 [16.8%]
Fake lepton systematics	±0.81 [13.5%]
MC statistics	±0.55 [9.1%]
Theory uncertainty: ttW/Z	±0.24 [4.0%]
Theory uncertainty: Rare	±0.23 [3.8%]
Jet energy scale (NP-3)	±0.19 [3.2%]
b-jets SF	±0.18 [3.0%]
Jet energy scale (NP-2)	±0.15 [2.5%]
Luminosity	±0.14 [2.3%]
Jet energy resolution	±0.13 [2.2%]
c-jets SF	±0.09 [1.5%]
Jet vertex tagger	±0.06 [1.0%]
Muon SF (sys.)	±0.05 [0.8%]
Light-jets SF	±0.04 [0.7%]
Electron identification SF	±0.04 [0.7%]
Jet η-intercalibration	±0.04 [0.7%]
MET soft-term scale	±0.03 [0.5%]
MET soft-term resolution 1	±0.02 [0.3%]
Electron isolation SF	±0.02 [0.3%]
Electron reconstruction SF	±0.01 [0.2%]
Muon SF (stat.)	±0.01 [0.2%]
MET soft-term resolution 2	±0.01 [0.2%]
Charge-flip systematics	±0.01 [0.2%]
EGamma resolution	±0.01 [0.2%]
Electron charge-ID SF	±0.01 [0.2%]
Muon isolation SF (sys.)	±0.01 [0.2%]
Muon TTVA (stat.)	±0.01 [0.2%]
Muon scale	±0.01 [0.2%]
Flavor tagging 1	±0.01 [0.2%]
Pile-up reweighting	±0.01 [0.2%]
Muon (MS reconstruction)	±0.01 [0.2%]

Table B.6: Breakdown of the dominant systematic uncertainties on the background estimation in signal region Rpc2L0bS for an integrated luminosity of 36.1fb^{-1}. The individual uncertainties can be correlated and do not necessarily add up quadratically to the total uncertainty. The percentages show the size of the uncertainties relative to the total expected background.

Uncertainty of signal region	Rpc2L0bH
Total background expectation	2.35
Statistical error ($\sqrt{N_{\text{exp}}}$)	$\pm$1.53
Total background systematic	$\pm$1.00 [42.6%]
Fake lepton systematics	$\pm$0.76 [32.3%]
MC statistics	$\pm$0.49 [20.9%]
Theory uncertainty: diboson	$\pm$0.32 [13.6%]
Jet energy scale (NP-1)	$\pm$0.19 [8.1%]
Theory uncertainty: Rare	$\pm$0.14 [6.0%]
Jet energy resolution	$\pm$0.08 [3.4%]
b-jets SF	$\pm$0.06 [2.6%]
Theory uncertainty: ttW/Z	$\pm$0.06 [2.6%]
Luminosity	$\pm$0.05 [2.1%]
c-jets SF	$\pm$0.04 [1.7%]
Jet energy scale (NP-3)	$\pm$0.03 [1.3%]
Jet energy scale (NP-2)	$\pm$0.03 [1.3%]
Muon SF (sys.)	$\pm$0.02 [0.9%]
Jet vertex tagger	$\pm$0.01 [0.4%]
Light-jets SF	$\pm$0.01 [0.4%]
Electron identification SF	$\pm$0.01 [0.4%]
MET soft-term resolution 1	$\pm$0.01 [0.4%]
Electron isolation SF	$\pm$0.01 [0.4%]
Jet η-intercalibration	$\pm$0.01 [0.4%]
Flavor tagging 1	$\pm$0.01 [0.4%]

Table B.7: Breakdown of the dominant systematic uncertainties on the background estimation in signal region Rpc2L0bH for an integrated luminosity of 36.1fb^{-1}. The individual uncertainties can be correlated and do not necessarily add up quadratically to the total uncertainty. The percentages show the size of the uncertainties relative to the total expected background.

Uncertainty of signal region	Rpc3L0bS
Total background expectation	11.02
Statistical error ($\sqrt{N_{\text{exp}}}$)	±3.32
Total background systematic	±3.02 [27.4%]
Theory uncertainty: diboson	±2.68 [24.3%]
Jet energy scale (NP-1)	±1.04 [9.4%]
Theory uncertainty: Rare	±0.44 [4.0%]
Jet energy resolution	±0.37 [3.4%]
Luminosity	±0.35 [3.2%]
MC statistics	±0.28 [2.5%]
b-jets SF	±0.21 [1.9%]
c-jets SF	±0.20 [1.8%]
Jet energy scale (NP-3)	±0.20 [1.8%]
Jet energy scale (NP-2)	±0.20 [1.8%]
Muon SF (sys.)	±0.18 [1.6%]
Fake lepton systematics	±0.18 [1.6%]
Electron identification SF	±0.17 [1.5%]
Theory uncertainty: ttW/Z	±0.16 [1.5%]
Jet vertex tagger	±0.09 [0.8%]
Electron isolation SF	±0.09 [0.8%]
MET soft-term resolution 2	±0.08 [0.7%]
Light-jets SF	±0.08 [0.7%]
Jet η-intercalibration	±0.05 [0.5%]
Electron reconstruction SF	±0.04 [0.4%]
Flavor tagging 1	±0.04 [0.4%]
Muon SF (stat.)	±0.04 [0.4%]
Muon isolation SF (sys.)	±0.03 [0.3%]
Electron charge-ID SF	±0.03 [0.3%]
MET soft-term resolution 1	±0.03 [0.3%]
Pile-up reweighting	±0.03 [0.3%]
Muon (MS reconstruction)	±0.02 [0.2%]
Muon TTVA (stat.)	±0.02 [0.2%]
EGamma scale	±0.02 [0.2%]
Muon TTVA (sys.)	±0.02 [0.2%]
Muon isolation SF (stat.)	±0.02 [0.2%]
MET soft-term scale	±0.01 [0.1%]

Table B.8: Breakdown of the dominant systematic uncertainties on the background estimation in signal region Rpc3L0bS for an integrated luminosity of 36.1fb^{-1}. The individual uncertainties can be correlated and do not necessarily add up quadratically to the total uncertainty. The percentages show the size of the uncertainties relative to the total expected background.

Uncertainty of signal region	Rpc3L0bH
Total background expectation	3.31
Statistical error ($\sqrt{N_{\text{exp}}}$)	$\pm$1.82
Total background systematic	$\pm$0.84 [25.4%]
Theory uncertainty: diboson	$\pm$0.71 [21.5%]
Jet energy scale (NP-1)	$\pm$0.27 [8.2%]
MC statistics	$\pm$0.20 [6.0%]
Theory uncertainty: Rare	$\pm$0.17 [5.1%]
Jet energy scale (NP-2)	$\pm$0.10 [3.0%]
Luminosity	$\pm$0.10 [3.0%]
Jet energy resolution	$\pm$0.08 [2.4%]
c-jets SF	$\pm$0.07 [2.1%]
Jet energy scale (NP-3)	$\pm$0.07 [2.1%]
Muon SF (sys.)	$\pm$0.07 [2.1%]
Theory uncertainty: ttW/Z	$\pm$0.06 [1.8%]
Electron identification SF	$\pm$0.06 [1.8%]
b-jets SF	$\pm$0.06 [1.8%]
Electron isolation SF	$\pm$0.04 [1.2%]
Jet vertex tagger	$\pm$0.03 [0.9%]
Light-jets SF	$\pm$0.03 [0.9%]
Flavor tagging 1	$\pm$0.02 [0.6%]
MET soft-term resolution 1	$\pm$0.01 [0.3%]
MET soft-term resolution 2	$\pm$0.01 [0.3%]
Muon isolation SF (sys.)	$\pm$0.01 [0.3%]
Muon SF (stat.)	$\pm$0.01 [0.3%]
Electron reconstruction SF	$\pm$0.01 [0.3%]
Electron charge-ID SF	$\pm$0.01 [0.3%]
Pile-up reweighting	$\pm$0.01 [0.3%]
Muon (ID reconstruction)	$\pm$0.01 [0.3%]
Muon (MS reconstruction)	$\pm$0.01 [0.3%]
MET soft-term scale	$\pm$0.01 [0.3%]
Muon TTVA (stat.)	$\pm$0.01 [0.3%]
Jet η-intercalibration	$\pm$0.01 [0.3%]
Muon TTVA (sys.)	$\pm$0.01 [0.3%]

Table B.9: Breakdown of the dominant systematic uncertainties on the background estimation in signal region Rpc3L0bH for an integrated luminosity of 36.1fb^{-1}. The individual uncertainties can be correlated and do not necessarily add up quadratically to the total uncertainty. The percentages show the size of the uncertainties relative to the total expected background.

Uncertainty of signal region	Rpc3L1bS
Total background expectation	17.33
Statistical error ($\sqrt{N_{\text{exp}}}$)	±4.16
Total background systematic	±4.20 [24.2%]
Fake lepton systematics	±2.86 [16.5%]
Theory uncertainty: Rare	±2.29 [13.2%]
MC statistics	±1.33 [7.7%]
Jet energy scale (NP-1)	±0.93 [5.4%]
Theory uncertainty: ttW/Z	±0.92 [5.3%]
Theory uncertainty: diboson	±0.45 [2.6%]
Luminosity	±0.42 [2.4%]
c-jets SF	±0.29 [1.7%]
Electron identification SF	±0.26 [1.5%]
b-jets SF	±0.25 [1.4%]
Muon SF (sys.)	±0.21 [1.2%]
Jet energy scale (NP-3)	±0.17 [1.0%]
Jet energy scale (NP-2)	±0.14 [0.8%]
Jet vertex tagger	±0.12 [0.7%]
Electron isolation SF	±0.11 [0.6%]
Jet η-intercalibration	±0.08 [0.5%]
MET soft-term resolution 2	±0.06 [0.3%]
Light-jets SF	±0.05 [0.3%]
Electron reconstruction SF	±0.05 [0.3%]
Muon SF (stat.)	±0.04 [0.2%]
Jet energy resolution	±0.04 [0.2%]
EGamma scale	±0.03 [0.2%]
Muon isolation SF (sys.)	±0.03 [0.2%]
MET soft-term scale	±0.03 [0.2%]
Electron charge-ID SF	±0.03 [0.2%]
Pile-up reweighting	±0.03 [0.2%]
Muon TTVA (stat.)	±0.03 [0.2%]
Muon TTVA (sys.)	±0.02 [0.1%]
Muon isolation SF (stat.)	±0.02 [0.1%]
EGamma resolution	±0.01 [0.1%]
Muon (MS reconstruction)	±0.01 [0.1%]
Flavor tagging 2	±0.01 [0.1%]
Muon low-p_{T}(sys.)	±0.01 [0.1%]

Table B.10: Breakdown of the dominant systematic uncertainties on the background estimation in signal region Rpc3L1bS for an integrated luminosity of 36.1fb^{-1}. The individual uncertainties can be correlated and do not necessarily add up quadratically to the total uncertainty. The percentages show the size of the uncertainties relative to the total expected background.

Uncertainty of signal region	Rpc3L1bH
Total background expectation	3.90
Statistical error ($\sqrt{N_{\text{exp}}}$)	$\pm$1.97
Total background systematic	$\pm$0.94 [24.1%]
Theory uncertainty: Rare	$\pm$0.71 [18.2%]
Fake lepton systematics	$\pm$0.38 [9.7%]
MC statistics	$\pm$0.30 [7.7%]
Theory uncertainty: ttW/Z	$\pm$0.22 [5.6%]
Jet energy scale (NP-1)	$\pm$0.16 [4.1%]
Theory uncertainty: diboson	$\pm$0.15 [3.8%]
Luminosity	$\pm$0.11 [2.8%]
c-jets SF	$\pm$0.09 [2.3%]
Jet energy resolution	$\pm$0.08 [2.1%]
Electron identification SF	$\pm$0.08 [2.1%]
Muon SF (sys.)	$\pm$0.07 [1.8%]
b-jets SF	$\pm$0.05 [1.3%]
Electron isolation SF	$\pm$0.04 [1.0%]
Jet energy scale (NP-3)	$\pm$0.04 [1.0%]
Jet η-intercalibration	$\pm$0.04 [1.0%]
Light-jets SF	$\pm$0.03 [0.8%]
Jet vertex tagger	$\pm$0.03 [0.8%]
MET soft-term resolution 2	$\pm$0.02 [0.5%]
Electron reconstruction SF	$\pm$0.01 [0.3%]
MET soft-term resolution 1	$\pm$0.01 [0.3%]
MET soft-term scale	$\pm$0.01 [0.3%]
Muon SF (stat.)	$\pm$0.01 [0.3%]
Muon isolation SF (sys.)	$\pm$0.01 [0.3%]
Pile-up reweighting	$\pm$0.01 [0.3%]
Electron charge-ID SF	$\pm$0.01 [0.3%]
Jet energy scale (NP-2)	$\pm$0.01 [0.3%]
Flavor tagging 1	$\pm$0.01 [0.3%]
EGamma scale	$\pm$0.01 [0.3%]
Muon TTVA (stat.)	$\pm$0.01 [0.3%]
Muon TTVA (sys.)	$\pm$0.01 [0.3%]

Table B.11: Breakdown of the dominant systematic uncertainties on the background estimation in signal region Rpc3L1bH for an integrated luminosity of 36.1fb^{-1}. The individual uncertainties can be correlated and do not necessarily add up quadratically to the total uncertainty. The percentages show the size of the uncertainties relative to the total expected background.

Uncertainty of signal region	Rpc2L1bS
Total background expectation	9.88
Statistical error ($\sqrt{N_{\text{exp}}}$)	±3.14
Total background systematic	±2.89 [29.3%]
Fake lepton systematics	±1.97 [19.9%]
Theory uncertainty: Rare	±1.25 [12.7%]
Jet energy scale (NP-1)	±1.14 [11.5%]
MC statistics	±0.95 [9.6%]
Theory uncertainty: ttW/Z	±0.69 [7.0%]
Luminosity	±0.23 [2.3%]
Theory uncertainty: diboson	±0.18 [1.8%]
Jet energy scale (NP-3)	±0.15 [1.5%]
Jet energy scale (NP-2)	±0.14 [1.4%]
MET soft-term resolution 2	±0.12 [1.2%]
b-jets SF	±0.11 [1.1%]
Jet energy resolution	±0.10 [1.0%]
Jet vertex tagger	±0.10 [1.0%]
MET soft-term scale	±0.09 [0.9%]
MET soft-term resolution 1	±0.08 [0.8%]
c-jets SF	±0.07 [0.7%]
Muon SF (sys.)	±0.07 [0.7%]
Electron identification SF	±0.05 [0.5%]
Charge-flip systematics	±0.04 [0.4%]
Muon (ID reconstruction)	±0.03 [0.3%]
EGamma scale	±0.02 [0.2%]
Electron isolation SF	±0.02 [0.2%]
Electron reconstruction SF	±0.02 [0.2%]
Muon SF (stat.)	±0.02 [0.2%]
Jet η-intercalibration	±0.02 [0.2%]
EGamma resolution	±0.02 [0.2%]
Flavor tagging 2	±0.01 [0.1%]
Electron charge-ID SF	±0.01 [0.1%]
Light-jets SF	±0.01 [0.1%]
Muon scale	±0.01 [0.1%]
Muon isolation SF (sys.)	±0.01 [0.1%]
Muon TTVA (stat.)	±0.01 [0.1%]
Pile-up reweighting	±0.01 [0.1%]

Table B.12: Breakdown of the dominant systematic uncertainties on the background estimation in signal region Rpc2L1bS for an integrated luminosity of 36.1fb^{-1}. The individual uncertainties can be correlated and do not necessarily add up quadratically to the total uncertainty. The percentages show the size of the uncertainties relative to the total expected background.

Uncertainty of signal region	Rpc2L1bH
Total background expectation	9.75
Statistical error ($\sqrt{N_{\text{exp}}}$)	$\pm$3.12
Total background systematic	$\pm$2.59 [26.6%]
Fake lepton systematics	$\pm$1.76 [18.1%]
Theory uncertainty: Rare	$\pm$1.28 [13.1%]
Jet energy scale (NP-1)	$\pm$0.98 [10.1%]
MC statistics	$\pm$0.65 [6.7%]
Theory uncertainty: ttW/Z	$\pm$0.56 [5.7%]
Theory uncertainty: diboson	$\pm$0.24 [2.5%]
Luminosity	$\pm$0.23 [2.4%]
Jet energy scale (NP-2)	$\pm$0.19 [1.9%]
Jet energy scale (NP-3)	$\pm$0.19 [1.9%]
b-jets SF	$\pm$0.11 [1.1%]
Jet energy resolution	$\pm$0.11 [1.1%]
Jet vertex tagger	$\pm$0.09 [0.9%]
Muon SF (sys.)	$\pm$0.08 [0.8%]
Electron identification SF	$\pm$0.08 [0.8%]
c-jets SF	$\pm$0.07 [0.7%]
MET soft-term scale	$\pm$0.07 [0.7%]
MET soft-term resolution 2	$\pm$0.06 [0.6%]
MET soft-term resolution 1	$\pm$0.05 [0.5%]
Jet η-intercalibration	$\pm$0.05 [0.5%]
Charge-flip systematics	$\pm$0.04 [0.4%]
Electron isolation SF	$\pm$0.03 [0.3%]
Light-jets SF	$\pm$0.03 [0.3%]
Muon SF (stat.)	$\pm$0.02 [0.2%]
Muon (ID reconstruction)	$\pm$0.02 [0.2%]
Electron reconstruction SF	$\pm$0.02 [0.2%]
Electron charge-ID SF	$\pm$0.01 [0.1%]
Flavor tagging 2	$\pm$0.01 [0.1%]
Muon isolation SF (sys.)	$\pm$0.01 [0.1%]
Pile-up reweighting	$\pm$0.01 [0.1%]
EGamma resolution	$\pm$0.01 [0.1%]
Muon TTVA (stat.)	$\pm$0.01 [0.1%]
Muon (MS reconstruction)	$\pm$0.01 [0.1%]
Muon TTVA (sys.)	$\pm$0.01 [0.1%]

Table B.13: Breakdown of the dominant systematic uncertainties on the background estimation in signal region Rpc2L1bH for an integrated luminosity of 36.1fb^{-1}. The individual uncertainties can be correlated and do not necessarily add up quadratically to the total uncertainty. The percentages show the size of the uncertainties relative to the total expected background.

Uncertainty of signal region	Rpv2L1bH
Total background expectation	1.57
Statistical error ($\sqrt{N_{\text{exp}}}$)	$\pm$1.25
Total background systematic	$\pm$0.44 [28.0%]
Theory uncertainty: Rare	$\pm$0.35 [22.3%]
MC statistics	$\pm$0.19 [12.1%]
Jet energy scale (NP-1)	$\pm$0.10 [6.4%]
Theory uncertainty: ttW/Z	$\pm$0.10 [6.4%]
Theory uncertainty: diboson	$\pm$0.05 [3.2%]
Luminosity	$\pm$0.04 [2.5%]
c-jets SF	$\pm$0.04 [2.5%]
Electron identification SF	$\pm$0.04 [2.5%]
Jet energy scale (NP-2)	$\pm$0.03 [1.9%]
Jet energy scale (NP-3)	$\pm$0.02 [1.3%]
Muon SF (sys.)	$\pm$0.02 [1.3%]
Electron isolation SF	$\pm$0.02 [1.3%]
MET soft-term resolution 1	$\pm$0.02 [1.3%]
Jet η-intercalibration	$\pm$0.01 [0.6%]
Jet vertex tagger	$\pm$0.01 [0.6%]
Jet energy resolution	$\pm$0.01 [0.6%]
b-jets SF	$\pm$0.01 [0.6%]
MET soft-term resolution 2	$\pm$0.01 [0.6%]
EGamma scale	$\pm$0.01 [0.6%]
Light-jets SF	$\pm$0.01 [0.6%]

Table B.14: Breakdown of the dominant systematic uncertainties on the background estimation in signal region Rpv2L1bH for an integrated luminosity of 36.1fb^{-1}. The individual uncertainties can be correlated and do not necessarily add up quadratically to the total uncertainty. The percentages show the size of the uncertainties relative to the total expected background.

Uncertainty of signal region	Rpv2L0b
Total background expectation	1.01
Statistical error ($\sqrt{N_{\text{exp}}}$)	$\pm$1.00
Total background systematic	$\pm$0.39 [38.6%]
Fake lepton systematics	$\pm$0.23 [22.8%]
MC statistics	$\pm$0.22 [21.8%]
Theory uncertainty: diboson	$\pm$0.18 [17.8%]
Jet energy scale (NP-1)	$\pm$0.08 [7.9%]
Theory uncertainty: Rare	$\pm$0.07 [6.9%]
Theory uncertainty: ttW/Z	$\pm$0.05 [5.0%]
b-jets SF	$\pm$0.04 [4.0%]
Luminosity	$\pm$0.03 [3.0%]
Jet energy scale (NP-2)	$\pm$0.02 [2.0%]
Jet energy scale (NP-3)	$\pm$0.02 [2.0%]
c-jets SF	$\pm$0.02 [2.0%]
Jet energy resolution	$\pm$0.02 [2.0%]
Muon SF (sys.)	$\pm$0.01 [1.0%]
Flavor tagging 1	$\pm$0.01 [1.0%]
Light-jets SF	$\pm$0.01 [1.0%]
Jet vertex tagger	$\pm$0.01 [1.0%]
Jet η-intercalibration	$\pm$0.01 [1.0%]
Electron isolation SF	$\pm$0.01 [1.0%]
Electron identification SF	$\pm$0.01 [1.0%]

Table B.15: Breakdown of the dominant systematic uncertainties on the background estimation in signal region Rpv2L0b for an integrated luminosity of 36.1fb^{-1}. The individual uncertainties can be correlated and do not necessarily add up quadratically to the total uncertainty. The percentages show the size of the uncertainties relative to the total expected background.

Uncertainty of signal region	Rpv2L2bH
Total background expectation	1.58
Statistical error ($\sqrt{N_{\text{exp}}}$)	$\pm$1.26
Total background systematic	$\pm$0.49 [31.0%]
Theory uncertainty: Rare	$\pm$0.40 [25.3%]
MC statistics	$\pm$0.19 [12.0%]
Jet energy scale (NP-1)	$\pm$0.13 [8.2%]
c-jets SF	$\pm$0.10 [6.3%]
Theory uncertainty: ttW/Z	$\pm$0.09 [5.7%]
b-jets SF	$\pm$0.06 [3.8%]
Jet energy resolution	$\pm$0.05 [3.2%]
Jet energy scale (NP-3)	$\pm$0.05 [3.2%]
Luminosity	$\pm$0.04 [2.5%]
Jet energy scale (NP-2)	$\pm$0.04 [2.5%]
Jet η-intercalibration	$\pm$0.03 [1.9%]
Electron identification SF	$\pm$0.03 [1.9%]
Flavor tagging 1	$\pm$0.02 [1.3%]
Muon SF (sys.)	$\pm$0.02 [1.3%]
Theory uncertainty: diboson	$\pm$0.02 [1.3%]
Jet vertex tagger	$\pm$0.02 [1.3%]
Electron isolation SF	$\pm$0.01 [0.6%]
Charge-flip systematics	$\pm$0.01 [0.6%]
Flavor tagging 2	$\pm$0.01 [0.6%]
Light-jets SF	$\pm$0.01 [0.6%]
EGamma resolution	$\pm$0.01 [0.6%]

Table B.16: Breakdown of the dominant systematic uncertainties on the background estimation in signal region Rpv2L2bH for an integrated luminosity of 36.1fb^{-1}. The individual uncertainties can be correlated and do not necessarily add up quadratically to the total uncertainty. The percentages show the size of the uncertainties relative to the total expected background.

Uncertainty of signal region	Rpv2L2bS
Total background expectation	19.49
Statistical error ($\sqrt{N_{\text{exp}}}$)	±4.41
Total background systematic	±7.39 [37.9%]
Fake lepton systematics	±6.66 [34.2%]
Theory uncertainty: Rare	±2.04 [10.5%]
MC statistics	±1.94 [10.0%]
Theory uncertainty: ttW/Z	±0.98 [5.0%]
b-jets SF	±0.70 [3.6%]
Jet energy scale (NP-1)	±0.60 [3.1%]
c-jets SF	±0.37 [1.9%]
Luminosity	±0.35 [1.8%]
Electron identification SF	±0.25 [1.3%]
Jet energy scale (NP-2)	±0.18 [0.9%]
Muon SF (sys.)	±0.16 [0.8%]
Theory uncertainty: diboson	±0.13 [0.7%]
Flavor tagging 1	±0.13 [0.7%]
Jet energy scale (NP-3)	±0.12 [0.6%]
Electron isolation SF	±0.11 [0.6%]
Jet energy resolution	±0.11 [0.6%]
Jet vertex tagger	±0.10 [0.5%]
Light-jets SF	±0.07 [0.4%]
Charge-flip systematics	±0.07 [0.4%]
Jet η-intercalibration	±0.06 [0.3%]
MET soft-term resolution 1	±0.05 [0.3%]
MET soft-term resolution 2	±0.04 [0.2%]
MET soft-term scale	±0.03 [0.2%]
EGamma scale	±0.03 [0.2%]
Electron reconstruction SF	±0.03 [0.2%]
Muon SF (stat.)	±0.03 [0.2%]
Electron charge-ID SF	±0.03 [0.2%]
Muon isolation SF (sys.)	±0.02 [0.1%]
Pile-up reweighting	±0.02 [0.1%]
Muon (MS reconstruction)	±0.02 [0.1%]
Muon TTVA (stat.)	±0.02 [0.1%]
Muon TTVA (sys.)	±0.01 [0.1%]
Trigger SF	±0.01 [0.1%]
Muon isolation SF (stat.)	±0.01 [0.1%]

Table B.17: Breakdown of the dominant systematic uncertainties on the background estimation in signal region Rpv2L2bS for an integrated luminosity of 36.1fb^{-1}. The individual uncertainties can be correlated and do not necessarily add up quadratically to the total uncertainty. The percentages show the size of the uncertainties relative to the total expected background.

Uncertainty of signal region	Rpv2L1bS
Total background expectation	24.86
Statistical error ($\sqrt{N_{\text{exp}}}$)	±4.99
Total background systematic	±6.98 [28.1%]
Fake lepton systematics	±5.68 [22.8%]
Theory uncertainty: Rare	±3.07 [12.3%]
MC statistics	±1.59 [6.4%]
Theory uncertainty: ttW/Z	±1.41 [5.7%]
Jet energy scale (NP-1)	±1.14 [4.6%]
Luminosity	±0.57 [2.3%]
Theory uncertainty: diboson	±0.50 [2.0%]
c-jets SF	±0.38 [1.5%]
Electron identification SF	±0.37 [1.5%]
Muon SF (sys.)	±0.27 [1.1%]
b-jets SF	±0.26 [1.0%]
Jet energy scale (NP-2)	±0.25 [1.0%]
Jet energy scale (NP-3)	±0.20 [0.8%]
Electron isolation SF	±0.17 [0.7%]
Jet vertex tagger	±0.15 [0.6%]
Charge-flip systematics	±0.11 [0.4%]
Jet η-intercalibration	±0.11 [0.4%]
Light-jets SF	±0.11 [0.4%]
MET soft-term resolution 2	±0.08 [0.3%]
MET soft-term resolution 1	±0.05 [0.2%]
Electron reconstruction SF	±0.05 [0.2%]
Muon SF (stat.)	±0.05 [0.2%]
Electron charge-ID SF	±0.04 [0.2%]
EGamma scale	±0.04 [0.2%]
Flavor tagging 1	±0.04 [0.2%]
Muon isolation SF (sys.)	±0.04 [0.2%]
Pile-up reweighting	±0.04 [0.2%]
MET soft-term scale	±0.03 [0.1%]
Muon TTVA (stat.)	±0.03 [0.1%]
Muon TTVA (sys.)	±0.02 [0.1%]
Jet energy resolution	±0.02 [0.1%]
Trigger SF	±0.02 [0.1%]
Muon (ID reconstruction)	±0.02 [0.1%]
Muon (MS reconstruction)	±0.02 [0.1%]

Table B.18: Breakdown of the dominant systematic uncertainties on the background estimation in signal region Rpv2L1bS for an integrated luminosity of 36.1fb^{-1}. The individual uncertainties can be correlated and do not necessarily add up quadratically to the total uncertainty. The percentages show the size of the uncertainties relative to the total expected background.

Uncertainty of signal region	Rpv2L1bM
Total background expectation	4.80
Statistical error ($\sqrt{N_{\text{exp}}}$)	$\pm$2.19
Total background systematic	$\pm$1.56 [32.5%]
Fake lepton systematics	$\pm$1.02 [21.3%]
Theory uncertainty: Rare	$\pm$0.80 [16.7%]
MC statistics	$\pm$0.68 [14.2%]
Theory uncertainty: ttW/Z	$\pm$0.43 [9.0%]
Jet energy scale (NP-1)	$\pm$0.19 [4.0%]
Theory uncertainty: diboson	$\pm$0.13 [2.7%]
Luminosity	$\pm$0.11 [2.3%]
Electron identification SF	$\pm$0.11 [2.3%]
Jet energy scale (NP-2)	$\pm$0.08 [1.7%]
c-jets SF	$\pm$0.07 [1.5%]
Muon SF (sys.)	$\pm$0.06 [1.3%]
b-jets SF	$\pm$0.05 [1.0%]
Electron isolation SF	$\pm$0.04 [0.8%]
Jet energy scale (NP-3)	$\pm$0.04 [0.8%]
Jet energy resolution	$\pm$0.03 [0.6%]
Jet vertex tagger	$\pm$0.03 [0.6%]
Jet η-intercalibration	$\pm$0.02 [0.4%]
Charge-flip systematics	$\pm$0.02 [0.4%]
MET soft-term resolution 1	$\pm$0.01 [0.2%]
EGamma scale	$\pm$0.01 [0.2%]
Light-jets SF	$\pm$0.01 [0.2%]
Muon (MS reconstruction)	$\pm$0.01 [0.2%]
Muon SF (stat.)	$\pm$0.01 [0.2%]
MET soft-term resolution 2	$\pm$0.01 [0.2%]
Electron reconstruction SF	$\pm$0.01 [0.2%]
MET soft-term scale	$\pm$0.01 [0.2%]
Muon isolation SF (sys.)	$\pm$0.01 [0.2%]
Electron charge-ID SF	$\pm$0.01 [0.2%]
Pile-up reweighting	$\pm$0.01 [0.2%]
Muon scale	$\pm$0.01 [0.2%]

Table B.19: Breakdown of the dominant systematic uncertainties on the background estimation in signal region Rpv2L1bM for an integrated luminosity of 36.1fb^{-1}. The individual uncertainties can be correlated and do not necessarily add up quadratically to the total uncertainty. The percentages show the size of the uncertainties relative to the total expected background.

Model $\tilde{g} \to t\bar{t}\tilde{\chi}_1^0$			
$(m_{\tilde{g}}, m_{\tilde{\chi}_1^0})$ [GeV]	$\mathrm{UL}^{95}(\sigma_{\mathrm{prod}})$ [fb]	$(m_{\tilde{g}}, m_{\tilde{\chi}_1^0})$ [GeV]	$\mathrm{UL}^{95}(\sigma_{\mathrm{prod}})$ [fb]
(700, 490)	449.2	(1600, 1245)	38.7
(1600, 1390)	365.4	(1300, 955)	38.6
(800, 590)	349.5	(1900, 1545)	38.5
(1000, 790)	289.6	(1000, 600)	38.1
(1200, 990)	268.5	(2000, 1645)	33.7
(700, 440)	237.7	(1200, 800)	31.9
(1300, 1090)	229.1	(1400, 1000)	29.8
(1400, 1190)	220.7	(2200, 1800)	28.7
(800, 540)	217.6	(1600, 1200)	27.7
(800, 565)	217.3	(2400, 2000)	27.5
(1100, 890)	194.9	(2000, 1600)	26.9
(1100, 865)	143.6	(900, 400)	26.9
(900, 665)	139.9	(1800, 1400)	25.9
(1600, 1340)	136.2	(1100, 600)	20.1
(700, 355)	125.3	(900, 1)	20.0
(1000, 700)	124.8	(1200, 700)	19.3
(900, 640)	123.3	(900, 200)	18.6
(800, 455)	120.7	(1000, 1)	17.4
(1100, 840)	117.1	(1300, 800)	17.3
(1300, 1040)	117.0	(1000, 400)	16.8
(1000, 740)	112.3	(1900, 1400)	16.7
(1200, 965)	111.3	(1500, 1000)	16.7
(1400, 1140)	110.4	(1700, 1200)	16.4
(900, 600)	109.8	(1100, 1)	16.3
(1300, 1065)	107.9	(2100, 1600)	15.9
(1400, 1165)	107.7	(1100, 400)	15.8
(800, 500)	100.6	(1000, 200)	15.7
(1800, 1540)	97.3	(2300, 1800)	15.0
(1400, 1100)	85.3	(1200, 600)	14.9
(800, 445)	85.2	(1400, 800)	14.5
(1200, 940)	78.6	(1100, 200)	14.5
(1200, 900)	75.3	(1600, 1000)	13.7
(900, 545)	74.2	(2200, 1600)	13.1
(1100, 800)	73.2	(1200, 200)	13.1
(1300, 1000)	60.6	(2000, 1400)	13.1
(900, 555)	55.3	(1800, 1200)	13.0
(1200, 855)	50.7	(1200, 400)	12.6
(1300, 945)	48.6	(1300, 600)	12.5
(1000, 645)	48.3	(1300, 400)	12.3
(1000, 655)	48.0	(1500, 800)	12.1
(1100, 745)	48.0	(1700, 1000)	11.5
(1600, 1255)	46.7	(1400, 600)	11.3
(1200, 845)	46.5	(2100, 1400)	11.3
(1400, 1055)	41.7	(1800, 1000)	10.9
(1800, 1445)	41.1	(1600, 800)	10.9
(1500, 1145)	41.0	(1900, 1200)	10.9
(2100, 1745)	40.7	(2300, 1600)	10.6
(1100, 755)	39.5	(2200, 1400)	10.6
(1400, 1045)	39.2	(2000, 1200)	10.4
(1700, 1345)	39.1	(2400, 1600)	10.2
(1800, 1455)	38.8	(2300, 1400)	7.2

Table B.20: The 95% CL_s upper limits on production cross-sections (in fb) obtained using the signal efficiency and acceptance specific to each point of the $\tilde{g} \to t\bar{t}\tilde{\chi}_1^0$ signal grid.

Model $\tilde{b}_1 \to t\tilde{\chi}_1^{\pm}$

$(m_{\tilde{b}_1}, m_{\tilde{\chi}_1^0})$ [GeV]	$\mathrm{UL}^{95}(\sigma_{\mathrm{prod}})$ [fb]	$(m_{\tilde{b}_1}, m_{\tilde{\chi}_1^0})$ [GeV]	$\mathrm{UL}^{95}(\sigma_{\mathrm{prod}})$ [fb]
(350, 75)	1661.1	(750, 300)	70.4
(400, 125)	787.2	(900, 500)	66.0
(400, 50)	597.7	(700, 50)	65.4
(450, 175)	584.6	(800, 350)	64.8
(400, 90)	576.8	(700, 150)	61.0
(500, 225)	385.6	(850, 400)	58.2
(450, 50)	382.0	(750, 100)	57.0
(450, 100)	350.7	(900, 450)	53.1
(450, 140)	331.2	(750, 200)	52.6
(550, 275)	314.9	(800, 50)	52.5
(500, 190)	303.9	(800, 250)	45.0
(500, 150)	290.0	(900, 50)	44.8
(600, 325)	285.0	(850, 300)	43.0
(500, 100)	229.9	(800, 150)	42.9
(550, 240)	222.7	(850, 200)	42.5
(600, 290)	222.1	(850, 100)	41.6
(650, 375)	216.0	(900, 350)	41.4
(500, 50)	204.3	(900, 150)	36.6
(700, 425)	197.6	(900, 250)	36.6
(650, 340)	187.8		
(550, 200)	177.0		
(600, 250)	172.4		
(800, 525)	164.9		
(550, 150)	160.9		
(900, 625)	152.3		
(550, 100)	151.9		
(750, 475)	150.8		
(700, 390)	150.0		
(850, 575)	145.3		
(650, 300)	138.0		
(800, 490)	134.6		
(600, 200)	132.0		
(750, 440)	122.9		
(700, 350)	118.5		
(750, 400)	112.5		
(850, 540)	111.4		
(600, 150)	109.4		
(800, 450)	108.6		
(600, 50)	108.0		
(900, 590)	107.3		
(700, 300)	106.1		
(650, 250)	101.0		
(900, 550)	93.9		
(850, 500)	93.3		
(750, 350)	91.7		
(650, 200)	89.1		
(700, 250)	76.9		
(850, 450)	75.0		
(650, 100)	74.4		
(800, 400)	72.6		

Table B.21: The 95% CL_s upper limits on production cross-sections (in fb) obtained using the signal efficiency and acceptance specific to each point of the $\tilde{b}_1 \to t\tilde{\chi}_1^{\pm}$ signal grid.

Model $\tilde{g} \to q\bar{q}l\bar{l}\tilde{\chi}_1^0$			
$(m_{\tilde{g}}, m_{\tilde{\chi}_1^0})$ [GeV]	$\mathrm{UL}^{95}(\sigma_{\mathrm{prod}})$ [fb]	$(m_{\tilde{g}}, m_{\tilde{\chi}_1^0})$ [GeV]	$\mathrm{UL}^{95}(\sigma_{\mathrm{prod}})$ [fb]
(800, 740)	2110.4	(1400, 300)	2.4
(800, 720)	516.3	(1400, 100)	2.4
(800, 700)	217.9	(2000, 1100)	2.4
(1400, 1300)	213.1	(2000, 1100)	2.4
(1200, 1100)	212.7	(1600, 500)	2.3
(400, 240)	161.8	(1600, 100)	2.3
(600, 480)	157.5	(1800, 700)	2.2
(1000, 880)	125.2	(1600, 300)	2.2
(400, 200)	121.0	(1800, 500)	2.1
(800, 680)	113.8	(1800, 100)	2.1
(600, 440)	65.0	(2000, 900)	2.0
(600, 400)	54.9	(2200, 1100)	2.0
(800, 640)	49.7	(1800, 300)	2.0
(1000, 840)	47.5	(2000, 100)	1.9
(600, 100)	43.4	(2000, 500)	1.9
(1000, 800)	31.7	(2000, 700)	1.9
(800, 600)	31.0	(2200, 700)	1.8
(600, 300)	23.7	(2200, 900)	1.8
(800, 500)	19.2	(2000, 300)	1.8
(1000, 700)	15.1	(2200, 300)	1.8
(1200, 900)	14.4	(2200, 500)	1.8
(1400, 1100)	12.4	(2200, 100)	1.7
(1600, 1300)	11.9		
(800, 100)	11.1		
(1800, 1500)	10.6		
(1100, 700)	9.0		
(800, 300)	8.5		
(1000, 500)	7.4		
(1200, 700)	6.8		
(1600, 1100)	6.3		
(1000, 300)	6.2		
(1400, 900)	6.1		
(1100, 500)	5.9		
(2000, 1500)	5.3		
(1300, 700)	5.1		
(1800, 1300)	5.1		
(1100, 300)	5.1		
(1200, 500)	4.7		
(1800, 1100)	4.6		
(1600, 900)	4.6		
(1400, 700)	4.5		
(1200, 300)	4.4		
(1300, 500)	4.4		
(2000, 1300)	4.2		
(1000, 100)	4.1		
(1400, 500)	3.1		
(1600, 700)	2.8		
(1200, 100)	2.7		
(1300, 300)	2.7		
(1300, 100)	2.6		

Table B.22: The 95% CL_s upper limits on production cross-sections (in fb) obtained using the signal efficiency and acceptance specific to each point of the $\tilde{g} \to q\bar{q}l\bar{l}\tilde{\chi}_1^0$ signal grid.

Model $\tilde{g} \to q\bar{q}^{'}WZ\tilde{\chi}_1^0$			
$(m_{\tilde{g}}, m_{\tilde{\chi}_1^0})$ [GeV]	$\mathrm{UL}^{95}(\sigma_{\mathrm{prod}})$ [fb]	$(m_{\tilde{g}}, m_{\tilde{\chi}_1^0})$ [GeV]	$\mathrm{UL}^{95}(\sigma_{\mathrm{prod}})$ [fb]
(1000, 900)	6645.4	(1300, 400)	13.5
(600, 400)	920.0	(1400, 300)	13.1
(1000, 800)	403.5	(1800, 900)	13.0
(600, 300)	253.4	(1400, 500)	12.9
(600, 100)	252.1	(1900, 800)	12.6
(1100, 900)	249.4	(1500, 600)	12.5
(1300, 1100)	241.8	(1300, 300)	12.0
(1400, 1200)	215.6	(1400, 400)	11.9
(1200, 1000)	205.3	(1300, 100)	11.9
(1100, 800)	106.8	(1600, 700)	11.6
(1300, 1000)	84.7	(1500, 400)	11.5
(1200, 900)	83.2	(1600, 600)	11.5
(1400, 1100)	82.2	(1700, 700)	11.5
(1000, 600)	82.2	(1600, 500)	11.4
(1000, 700)	74.5	(1300, 200)	11.4
(1200, 800)	69.0	(1900, 900)	11.1
(800, 300)	68.6	(1800, 800)	11.0
(1500, 1100)	57.7	(1400, 100)	10.9
(1400, 1000)	57.7	(1400, 200)	10.9
(1300, 900)	57.6	(1500, 500)	10.9
(1100, 600)	42.3	(1700, 600)	10.6
(800, 100)	37.1	(1500, 200)	10.5
(1000, 500)	35.5	(2000, 600)	10.5
(1300, 800)	34.1	(1500, 100)	10.4
(1200, 700)	33.4	(1800, 700)	10.3
(1400, 900)	31.1	(1800, 600)	10.3
(1500, 1000)	30.6	(1500, 300)	10.2
(1100, 500)	29.9	(1900, 700)	10.1
(1200, 600)	28.2	(1600, 300)	9.8
(1600, 1000)	26.5	(2000, 400)	9.8
(1400, 800)	24.1	(2000, 800)	9.6
(1000, 300)	22.9	(1700, 400)	9.6
(1300, 700)	21.9	(1900, 100)	9.6
(1100, 400)	21.6	(1600, 400)	9.4
(1500, 900)	21.6	(2000, 900)	9.2
(1400, 700)	19.5	(1900, 400)	9.2
(1000, 100)	19.0	(1900, 300)	9.1
(1200, 500)	19.0	(1700, 500)	9.1
(1200, 400)	17.4	(2000, 700)	9.1
(1300, 600)	17.4	(1600, 100)	9.1
(1600, 900)	17.4	(1800, 200)	9.1
(1600, 800)	14.9	(2000, 100)	8.9
(1200, 300)	14.6	(1800, 500)	8.8
(1300, 500)	14.6	(1700, 200)	8.8
(1500, 800)	14.4	(1700, 100)	8.8
(1500, 700)	14.3	(1900, 500)	8.8
(1200, 100)	14.2	(1800, 400)	8.7
(1400, 600)	14.1	(2000, 500)	8.7
(1700, 900)	13.7	(1800, 300)	8.7
(1700, 800)	13.7	(2000, 300)	8.5

Table B.23: The 95% CL_s upper limits on production cross-sections (in fb) obtained using the signal efficiency and acceptance specific to each point of the $\tilde{g} \to q\bar{q}^{'}WZ\tilde{\chi}_1^0$ signal grid.

Model $\tilde{g} \to q\bar{q}\tilde{\chi}_1^0, \tilde{\chi}_1^0 \to lq\bar{q}$	
$(m_{\tilde{g}}, m_{\tilde{\chi}_1^0})$ [GeV]	$\mathrm{UL}^{95}(\sigma_{\mathrm{prod}})$ [fb]
(2000, 50)	79.6
(1900, 50)	58.0
(1800, 50)	54.9
(1600, 50)	37.2
(1400, 50)	33.8
(1200, 50)	28.5
(1000, 50)	26.8
(1000, 100)	9.9
(1000, 125)	7.7
(1200, 120)	6.6
(1000, 950)	6.3
(1400, 140)	6.2
(1200, 150)	5.4
(1600, 160)	5.1
(1800, 180)	5.0
(1000, 250)	4.9
(1900, 190)	4.8
(1600, 200)	4.7
(1400, 175)	4.6
(1200, 1140)	4.6
(2000, 200)	4.5
(1000, 500)	4.4
(2200, 220)	4.4
(1800, 225)	4.2
(1000, 850)	4.1
(1900, 237)	4.0
(2000, 250)	3.8
(1600, 1520)	3.8
(1200, 300)	3.8
(1400, 1330)	3.6
(2200, 275)	3.6
(2200, 2090)	3.6
(1800, 1710)	3.4
(1400, 700)	3.3
(1400, 350)	3.3
(1900, 475)	3.2
(2200, 550)	3.2
(1900, 1805)	3.2
(1200, 1020)	3.2
(1600, 400)	3.2
(1800, 900)	3.1
(1200, 600)	3.1
(1800, 1530)	3.1
(1900, 950)	3.0
(2000, 500)	3.0
(1900, 1615)	3.0
(2200, 1100)	3.0
(1800, 450)	3.0
(1600, 800)	3.0
(1600, 1360)	2.9
(1400, 1190)	2.9

Table B.24: The 95% CL_s upper limits on production cross-sections (in fb) obtained using the signal efficiency and acceptance specific to each point of the RPV $\tilde{g} \to qq\tilde{\chi}_1^0, \tilde{\chi}_1^0 \to lqq$ signal grid

Model $\tilde{g} \to tt\tilde{\chi}_1^0, \tilde{\chi}_1^0 \to uds$	
$(m_{\tilde{g}}, m_{\tilde{\chi}_1^0})$ [GeV]	$\mathrm{UL}^{95}(\sigma_{\mathrm{prod}})$ [fb]
(1100, 740)	13.9
(1200, 840)	10.3
(1300, 940)	8.5
(1100, 375)	7.5
(1500, 1140)	7.3
(1400, 1040)	7.0
(1800, 1440)	6.3
(1700, 1340)	6.2
(1100, 10)	6.1
(1100, 50)	6.1
(1600, 1240)	6.1
(1200, 563)	5.8
(1200, 287)	5.0
(1200, 50)	5.0
(1300, 630)	4.8
(1400, 783)	4.7
(1200, 10)	4.4
(1300, 320)	4.2
(1600, 994)	4.1
(1500, 858)	4.1
(1300, 50)	3.9
(1800, 1202)	3.8
(1700, 1118)	3.7
(1300, 10)	3.7
(1800, 963)	3.6
(1800, 725)	3.5
(1400, 525)	3.5
(1500, 575)	3.5
(1600, 748)	3.4
(1700, 50)	3.3
(1400, 10)	3.3
(1500, 293)	3.3
(1600, 50)	3.2
(1400, 50)	3.1
(1400, 268)	3.1
(2000, 243)	3.0
(1500, 10)	3.0
(1800, 10)	3.0
(1700, 10)	3.0
(1700, 675)	3.0
(1800, 248)	3.0
(1600, 256)	2.9
(1600, 502)	2.9
(2000, 10)	2.9
(1600, 10)	2.9
(2000, 50)	2.8
(1800, 50)	2.8
(1700, 453)	2.8
(1700, 232)	2.8
(2000, 476)	2.7
(1800, 487)	2.7

Table B.25: The 95% CL_s upper limits on production cross-sections (in fb) obtained using the signal efficiency and acceptance specific to each point of the RPV $\tilde{g} \to tt\tilde{\chi}_1^0, \tilde{\chi}_1^0 \to uds$ signal grid.

Model $\tilde{g} \to tdb$	
$(m_{\tilde{g}}, m_{\tilde{\chi}_1^0})$ [GeV]	$\mathrm{UL}^{95}(\sigma_{\mathrm{prod}})$ [fb]
(800, 400)	344.8
(800, 600)	303.3
(1000, 800)	111.6
(1000, 600)	110.9
(1000, 400)	88.4
(1200, 1000)	66.5
(1200, 400)	41.1
(1200, 600)	34.6
(1400, 1200)	34.5
(1200, 800)	32.7
(1800, 1600)	31.0
(1600, 1400)	29.2
(1400, 600)	25.7
(1400, 400)	21.7
(1400, 1000)	20.6
(1400, 800)	20.0
(1600, 400)	19.7
(1600, 1200)	18.6
(1600, 800)	17.8
(1800, 400)	16.7
(1800, 1000)	16.6
(1800, 1200)	16.1
(1800, 1400)	15.5
(1800, 600)	15.5
(1600, 600)	15.1
(1800, 800)	13.4
(1600, 1000)	8.8
Model $\tilde{g} \to tds$	
(800, 600)	326.0
(1000, 800)	96.5
(1000, 600)	70.5
(1200, 1000)	48.5
(1200, 800)	47.0
(1400, 1200)	45.6
(1800, 1600)	41.0
(1200, 600)	39.4
(1600, 1400)	28.3
(1400, 1000)	24.3
(1400, 600)	22.4
(1400, 800)	21.8
(1800, 1400)	21.4
(1800, 400)	20.7
(1600, 600)	20.4
(1600, 400)	20.3
(1800, 1200)	19.6
(1600, 1200)	19.4
(1800, 800)	18.3
(1600, 800)	17.4
(1800, 1000)	17.3
(1600, 1000)	16.4
(1800, 600)	14.8

Table B.26: The 95% CL_s upper limits on production cross-sections (in fb) obtained using the signal efficiency and acceptance specific to each point of the RPV $\tilde{g} \to tdb$ (top) and $\tilde{g} \to tds$ (bottom) signal grid.

Appendix C

Fit results of WhSS analysis

The systematic uncertainties in the signal regions after the model-dependent fit are shown in Table C.1 and Table C.2. Table C.3 shows the expected yields from background and signal pre-fit and post-fit. Error only include the statistic error, except for Fakes which also include systematic errors.

Uncertainty of signal region	SRjet1
Total background expectation	4.54
Statistical error ($\sqrt{N_{\text{exp}}}$)	$\pm$2.13
Total background systematic	$\pm$1.52 [33.6%]
Fake lepton systematics	$\pm$1.64 [36.2%]
Signal strength	$\pm$0.56 [12.3%]
MC statistics	$\pm$0.37 [8.2%]
MET soft-term resolution	$\pm$0.29 [6.3%]
Theory uncertainty: diboson	$\pm$0.19 [4.1%]
Jet energy scale (NP-1)	$\pm$0.18 [4.0%]
Jet energy resolution	$\pm$0.09 [1.9%]
Jet η-intercalibration	$\pm$0.08 [1.7%]
Charge-flip	$\pm$0.07 [1.6%]
Muon SF (sys.)	$\pm$0.07 [1.6%]
Jet energy scale (NP-2)	$\pm$0.03 [0.6%]
c-jets SF	$\pm$0.02 [0.4%]
Jet energy scale (NP-3)	$\pm$0.02 [0.4%]
Electron identification SF	$\pm$0.02 [0.4%]
Theory uncertainty: Triboson	$\pm$0.01 [0.3%]
b-jets SF	$\pm$0.01 [0.3%]
Theory uncertainty: ttW/Z	$\pm$0.01 [0.3%]
Luminosity	$\pm$0.01 [0.3%]
Jet vertex tagger	$\pm$0.01 [0.2%]
Light-jets SF	$\pm$0.01 [0.2%]
Electron isolation SF	$\pm$0.01 [0.1%]

Table C.1: Breakdown of the dominant systematic uncertainties on the background estimation in signal region SRjet1 for an integrated luminosity of 36.1fb^{-1}. The individual uncertainties can be correlated and do not necessarily add up quadratically to the total uncertainty. The percentages show the size of the uncertainties relative to the total expected background.

Uncertainty of signal region	SRjet23
Total background expectation	6.35
Statistical error ($\sqrt{N_{\text{exp}}}$)	±2.52
Total background systematic	±1.34 [21.1%]
Fake lepton systematics	±1.46 [22.9%]
Signal strength	±1.17 [18.4%]
MC statistics	±0.51 [8.0%]
Theory uncertainty: diboson	±0.28 [4.4%]
MET soft-term resolution	±0.26 [4.1%]
Jet energy scale (NP-1)	±0.24 [3.7%]
b-jets SF	±0.10 [1.6%]
Muon SF (sys.)	±0.07 [1.0%]
Jet energy resolution	±0.07 [1.0%]
c-jets SF	±0.04 [0.7%]
Light-jets SF	±0.04 [0.6%]
Jet vertex tagger	±0.03 [0.5%]
Theory uncertainty: Triboson	±0.03 [0.5%]
Jet η-intercalibration	±0.02 [0.4%]
Charge-flip	±0.03 [0.4%]
Jet energy scale (NP-3)	±0.02 [0.3%]
Electron identification SF	±0.02 [0.3%]
Theory uncertainty: ttW/Z	±0.02 [0.3%]
Luminosity	±0.01 [0.1%]
Electron isolation SF	±0.01 [0.1%]

Table C.2: Breakdown of the dominant systematic uncertainties on the background estimation in signal region SRjet23 for an integrated luminosity of 36.1fb^{-1}. The individual uncertainties can be correlated and do not necessarily add up quadratically to the total uncertainty. The percentages show the size of the uncertainties relative to the total expected background.

	SRjet1	SRjet23
Observed events	2	8
Fitted bkg events	4.54 ± 1.52	6.35 ± 1.34
Fitted Fakes events	$0.93^{+1.54}_{-0.93}$	2.07 ± 1.46
Fitted WZ events	2.08 ± 0.38	1.93 ± 0.57
Fitted Rare events	0.43 ± 0.12	0.72 ± 0.18
Fitted ttV events	0.12 ± 0.04	0.14 ± 0.04
Fitted WW events	0.16 ± 0.02	0.53 ± 0.08
Fitted ZZ events	0.05 ± 0.02	0.07 ± 0.02
Fitted Charge-Flip events	0.47 ± 0.07	0.27 ± 0.03
Fitted m$(\tilde{\chi}_1^{\pm}, /\tilde{\chi}_2^0, \tilde{\chi}_1^0) = (175, 0)$ GeV events	$0.30^{+0.55}_{-0.30}$	$0.63^{+1.17}_{-0.63}$
MC exp. SM events	11.02 ± 2.32	13.93 ± 2.28
Fakes events	3.30 ± 2.10	1.76 ± 1.47
MC exp. WZ events	2.18 ± 0.38	1.85 ± 0.54
MC exp. Rare events	0.44 ± 0.12	0.73 ± 0.18
MC exp. ttV events	0.12 ± 0.04	0.14 ± 0.04
MC exp. WW events	0.17 ± 0.03	0.51 ± 0.08
MC exp. ZZ events	0.06 ± 0.02	0.07 ± 0.03
ChargeFlip events	0.47 ± 0.07	0.27 ± 0.03
MC exp. m$(\tilde{\chi}_1^{\pm}, /\tilde{\chi}_2^0, \tilde{\chi}_1^0) = (175, 0)$ GeV events	4.29 ± 0.73	8.60 ± 1.35

Table C.3: Background yields in the signal regions, with one example signal mass point.

Bibliography

[1] ATLAS Collaboration, *Observation of a new particle in the search for the Standard Model Higgs boson with the ATLAS detector at the LHC*, 2012, Phys. Lett. **B716** (2012) 1–29, arXiv:1207.7214 [hep-ex].

[2] CMS Collaboration, *Observation of a new boson at a mass of 125 GeV with the CMS experiment at the LHC*, 2012, Phys. Lett. **B716** (2012) 30–61, arXiv:1207.7235 [hep-ex].

[3] A. Purcell, *Go on a particle quest at the first CERN webfest. Le premier webfest du CERN se lance à la conquête des particules*, 2012, URL: https://cds.cern.ch/record/1473657.

[4] A. Pich, *The Standard model of electroweak interactions*, 2008, arXiv:0705.4264 [hep-ph], [1(2007)].

[5] C. Patrignani and P. D. Group, *Review of Particle Physics*, 2016, Chinese Physics C **40** (2016) 100001.

[6] D. Hanneke, S. Fogwell, and G. Gabrielse, *New Measurement of the Electron Magnetic Moment and the Fine Structure Constant*, 2008, Physical Review Letters **100** (2008) 120801, arXiv:0801.1134 [physics.atom-ph].

[7] E. Fermi, *Tentativo di una Teoria Dei Raggi β*, 2008, Il Nuovo Cimento (1924-1942) **11** (2008) 1.

[8] S. L. Glashow, *Partial-symmetries of weak interactions*, 1961, Nuclear Physics **22** (1961) 579 – 588.

[9] A. Salam, *Weak and Electromagnetic Interactions*, 1968, Conf. Proc. **C680519** (1968) 367–377.

[10] S. Weinberg, *A Model of Leptons*, 1967, Phys. Rev. Lett. **19** (1967) 1264–1266.

[11] C. N. Yang and R. L. Mills, *Conservation of Isotopic Spin and Isotopic Gauge Invariance*, 1954, Phys. Rev. **96** (1954) 191–195.

[12] A. J. MacFarlane, A. Sudbery, and P. H. Weisz, *On Gell-Mann's λ-matrices, d- and f-tensors, octets, and parametrizations of SU(3)*, 1968, Communications in Mathematical Physics **11** (1968) 77–90.

[13] P. W. Higgs, *Broken Symmetries and the Masses of Gauge Bosons*, 1964, Phys. Rev. Lett. **13** (1964) 508–509.

[14] F. Englert and R. Brout, *Broken Symmetry and the Mass of Gauge Vector Mesons*, 1964, Phys. Rev. Lett. **13** (1964) 321–323.

[15] CMS, W. de Boer, *The Discovery of the Higgs Boson with the CMS Detector and its Implications for Supersymmetry and Cosmology* in *Time and Matter 2013 (TAM2013) Venice, Italy*. 2013, . arXiv:1309.0721 [hep-ph].

[16] J. Goldstone, A. Salam, and S. Weinberg, *Broken Symmetries*, 1962, Phys. Rev. **127** (1962) 965–970.

[17] ATLAS and CMS Collaborations, *Combined Measurement of the Higgs Boson Mass in pp Collisions at $\sqrt{s} = 7$ and 8 TeV with the ATLAS and CMS Experiments*, 2015, Phys. Rev. Lett. **114** (2015) 191803, arXiv:1503.07589 [hep-ex].

[18] ATLAS Collaboration, *Measurement of the Higgs boson mass in the $H \to ZZ^* \to 4\ell$ and $H \to \gamma\gamma$ channels with $\sqrt{s} = 13$ TeV pp collisions using the ATLAS detector*, 2018, Phys. Lett. **B784** (2018) 345–366, arXiv:1806.00242 [hep-ex].

[19] Super-Kamiokande, Y. Fukuda et al., *Evidence for oscillation of atmospheric neutrinos*, 1998, Phys. Rev. Lett. **81** (1998) 1562–1567, arXiv:hep-ex/9807003 [hep-ex].

[20] Z. Maki, M. Nakagawa, and S. Sakata, *Remarks on the Unified Model of Elementary Particles*, 1962, Progress of Theoretical Physics **28** (1962) 870–880.

[21] F. Zwicky, *On the Masses of Nebulae and of Clusters of Nebulae*, 1937, Astrophysical Journal (1937) .

[22] NASA, *Detailed Dark Matter Map Yields Clues to Galaxy Cluster Growth.* URL: https://www.nasa.gov/mission_pages/hubble/science/dark-matter-map.html.

[23] J. R. Brownstein and J. W. Moffat, *The Bullet Cluster 1E0657-558 evidence shows Modified Gravity in the absence of Dark Matter*, 2007, Mon. Not. Roy. Astron. Soc. **382** (2007) 29–47, arXiv:astro-ph/0702146 [astro-ph].

[24] *Dark Energy, Dark Matter* NASA Science: Astrophysics. June 5, 2015. URL: https://science.nasa.gov/astrophysics/focus-areas/what-is-dark-energy.

[25] J. Wess and B. Zumino, *Supergauge transformations in four dimensions*, 1974, Nuclear Physics B **70** (1974) 39 – 50.

[26] A. Salam and J. Strathdee, *Super-symmetry and non-Abelian gauges*, 1974, Physics Letters B **51** (1974) 353 – 355.

[27] J. Wess and B. Zumino, *Supergauge invariant extension of quantum electrodynamics*, 1974, Nuclear Physics B **78** (1974) 1 – 13.

[28] S. Ferrara and B. Zumino, *Supergauge invariant Yang-Mills theories*, 1974, Nuclear Physics B **79** (1974) 413 – 421.

[29] S James Gates, Jr, *Sticking with SUSY.* URL: http://live.iop-pp01.agh.sleek.net/2014/09/25/sticking-with-susy/.

[30] R. Haag, J. T. Lopuszanski, and M. Sohnius, *All possible generators of supersymmetries of the S-matrix*, 1975, Nuclear Physics B **88** (1975) 257 – 274.

[31] S. Dimopoulos and H. Georgi, *Softly broken supersymmetry and SU(5)*, 1981, Nuclear Physics B **193** (1981) 150 – 162.

[32] N. Craig, *The State of Supersymmetry after Run I of the LHC* in *Beyond the Standard Model after the first run of the LHC Arcetri, Florence, Italy, May 20-July 12, 2013*. 2013, . arXiv:1309.0528 [hep-ph].

[33] L. Evans and P. Bryant, *LHC Machine*, 2008, JINST **3** (2008) S08001.

[34] ATLAS Collaboration, *Luminosity Public Results for Run-2,* URL: https://twiki.cern.ch/twiki/bin/view/AtlasPublic/LuminosityPublicResultsRun2.

[35] ATLAS Collaboration, *The ATLAS Experiment at the CERN Large Hadron Collider*, 2008, JINST **3** (2008) S08003.

[36] Assamagan, Ketevi A and Di Ciaccio, A and Goldfarb, S. and Laporte, J. F. and Lellouch, D. and Rimoldi, A. and Virchaux, M., *A Hierarchical Software Identifier Scheme for the ATLAS Muon Spectrometer,* URL: http://inspirehep.net/record/1194854.

[37] ATLAS Collaboration, *ATLAS magnet system: Technical Design Report, 1*, CERN, Geneva, 1997, URL: https://cds.cern.ch/record/338080.

[38] ATLAS Collaboration, *ATLAS inner detector: Technical design report. Vol. 1*, 1997, CERN-LHCC-97-16, (1997), URL: https://cds.cern.ch/record/331063.

[39] ATLAS Collaboration, *ATLAS inner detector: Technical design report. Vol. 2*, 1997, CERN-LHCC-97-17 (1997), URL: https://cds.cern.ch/record/331064.

[40] ATLAS Collaboration, K. Potamianos, *The upgraded Pixel detector and the commissioning of the Inner Detector tracking of the ATLAS experiment for Run-2 at the Large Hadron Collider*, 2015, arXiv:1608.07850 [physics.ins-det].

[41] ATLAS Collaboration, M. Capeans, G. Darbo, K. Einsweiller, M. Elsing, T. Flick, M. Garcia-Sciveres, C. Gemme, H. Pernegger, O. Rohne, and R. Vuillermet, *ATLAS Insertable B-Layer Technical Design Report* Tech. Rep. CERN-LHCC-2010-013. ATLAS-TDR-19, 2010, . URL: https://cds.cern.ch/record/1291633.

[42] ATLAS, A. Airapetian et al., *ATLAS calorimeter performance Technical Design Report*, 1996, CERN-LHCC-96-40 (1996), URL: https://cds.cern.ch/record/331059.

[43] W. Lampl et al., *Calorimeter Clustering Algorithms: Description and Performance*, ATL-LARG-PUB-2008-002, 2008, URL: http://inspirehep.net/record/807147.

[44] ATLAS Collaboration, *ATLAS muon spectrometer: Technical design report*, CERN, Geneva, 1997, URL: https://cds.cern.ch/record/331068.

[45] ATLAS Collaboration, *Standalone vertex finding in the ATLAS muon spectrometer*, 2014, Journal of Instrumentation **9** (2014) P02001, URL: http://stacks.iop.org/1748-0221/9/i=02/a=P02001.

[46] ATLAS Collaboration, *2015 start-up trigger menu and initial performance assessment of the ATLAS trigger using Run-2 data* Tech. Rep. ATL-DAQ-PUB-2016-001, CERN, Geneva, 2016, . URL: https://cds.cern.ch/record/2136007.

[47] ATLAS Collaboration, *Performance of the ATLAS Trigger System in 2015*, 2017, Eur. Phys. J. **C77** (2017) 317, arXiv:1611.09661 [hep-ex].

[48] V. N. Gribov and L. N. Lipatov, *Deep inelastic ep scattering in perturbation theory*, 1972, Sov. J. Nucl. Phys. **15** (1972) 438, Yad. Fiz.15,781(1972).

[49] Y. L. Dokshitzer, *Calculation of the Structure Functions for Deep Inelastic Scattering and e^+ e^- Annihilation by Perturbation Theory in Quantum Chromodynamics.*, 1977, Sov. Phys. JETP **46** (1977) 641–653, [Zh. Eksp. Teor. Fiz.73,1216(1977)].

[50] G. Altarelli and G. Parisi, *Asymptotic Freedom in Parton Language*, 1977, Nucl. Phys. **B126** (1977) 298–318.

[51] S. Dulat, T.-J. Hou, J. Gao, M. Guzzi, J. Huston, P. Nadolsky, J. Pumplin, C. Schmidt, D. Stump, and C. P. Yuan, *New parton distribution functions from a global analysis of quantum chromodynamics*, 2016, Phys. Rev. **D93** (2016) 033006, arXiv:1506.07443 [hep-ph].

[52] A. D. Martin, W. J. Stirling, R. S. Thorne, and G. Watt, *Parton distributions for the LHC*, 2009, Eur. Phys. J. **C63** (2009) 189–285, arXiv:0901.0002 [hep-ph].

[53] NNPDF, R. D. Ball et al., *Parton distributions for the LHC Run II*, 2015, JHEP **04** (2015) 040, arXiv:1410.8849 [hep-ph].

[54] M. R. Whalley, D. Bourilkov, and R. C. Group, *The Les Houches accord PDFs (LHAPDF) and LHAGLUE*, 2005, arXiv:hep-ph/0508110 [hep-ph].

[55] S. Höche, *Introduction to parton-shower event generators*, 2015, arXiv:1411.4085 [hep-ph].

[56] D. Amati and G. Veneziano, *Preconfinement as a property of perturbative QCD*, 1979, Physics Letters B **83** (1979) 87 – 92.

[57] B. Andersson, G. Gustafson, G. Ingelman, and T. Sjöstrand, *Parton fragmentation and string dynamics*, 1983, Physics Reports **97** (1983) 31 – 145.

[58] T. Sjostrand, S. Mrenna, and P. Z. Skands, *A Brief Introduction to PYTHIA 8.1*, 2008, Comput. Phys. Commun. **178** (2008) 852–867, arXiv:0710.3820 [hep-ph].

[59] S. Platzer and S. Gieseke, *Dipole Showers and Automated NLO Matching in Herwig++*, 2012, Eur. Phys. J. **C72** (2012) 2187, arXiv:1109.6256 [hep-ph].

[60] T. Gleisberg, S. Hoeche, F. Krauss, M. Schonherr, S. Schumann, F. Siegert, and J. Winter, *Event generation with SHERPA 1.1*, 2009, JHEP **02** (2009) 007, arXiv:0811.4622 [hep-ph].

[61] D. J. Lange, *The EvtGen particle decay simulation package*, 2001, Nucl. Instrum. Meth. **A462** (2001) 152.

[62] R. Field, *The Underlying Event in Hadronic Collisions*, 2012, Annual Review of Nuclear and Particle Science **62** (2012) 453–483, https://doi.org/10.1146/annurev-nucl-102711-095030.

[63] S. Agostinelli et al., *Geant4 - a simulation toolkit*, 2003, Nucl. Instrum. Meth. **506** (2003) 250 – 303.

[64] The ATLAS Collaboration, *The ATLAS Simulation Infrastructure*, 2010, The European Physical Journal C **70** (2010) 823–874.

[65] ATLAS Collaboration, *Electron identification efficiency measured with $Z \to ee$ events using 2016 data,* URL: https://atlas.web.cern.ch/Atlas/GROUPS/PHYSICS/PLOTS/EGAM-2016-002/index.html.

[66] ATLAS Collaboration, *Topological cell clustering in the ATLAS calorimeters and its performance in LHC Run 1*, 2017, Eur. Phys. J. **C77** (2017) 490, arXiv:1603.02934 [hep-ex].

[67] ATLAS Collaboration, *Electron efficiency measurements with the ATLAS detector using the 2015 LHC proton-proton collision data,* tech. rep., CERN, 2016, . URL: http://inspirehep.net/record/1467063.

[68] T. Cornelissen, M. Elsing, S. Fleischmann, W. Liebig, E. Moyse, and A. Salzburger, *Concepts, Design and Implementation of the ATLAS New Tracking (NEWT),* Tech. Rep. ATL-SOFT-PUB-2007-007. ATL-COM-SOFT-2007-002, CERN, Geneva, 2007, . URL: https://cds.cern.ch/record/1020106.

[69] ATLAS Collaboration, *Muon reconstruction performance of the ATLAS detector in proton-proton collision data at $\sqrt{s}$ =13 TeV*, 2016, Eur. Phys. J. **C76** (2016) 292, arXiv:1603.05598 [hep-ex].

[70] M. Cacciari, G. P. Salam, and G. Soyez, *The Anti-k(t) jet clustering algorithm*, 2008, JHEP **04** (2008) 063, arXiv:0802.1189 [hep-ph].

[71] ATLAS Collaboration, *Jet energy scale measurements and their systematic uncertainties in proton-proton collisions at $\sqrt{s} = 13$ TeV with the ATLAS detector*, 2017, Phys. Rev. **D96** (2017) 072002, arXiv:1703.09665 [hep-ex].

[72] ATLAS Collaboration, *Jet Calibration and Systematic Uncertainties for Jets Reconstructed in the ATLAS Detector at $\sqrt{s} = 13$ TeV,* Tech. Rep. ATL-PHYS-PUB-2015-015, CERN, Geneva, 2015, . URL: https://cds.cern.ch/record/2037613.

[73] ATLAS collaboration, *Tagging and suppression of pileup jets*, 2014, URL: https://cds.cern.ch/record/1700870.

[74] ATLAS Collaboration, *JVT Public Plots for ICHEP 2016,* URL: https://atlas.web.cern.ch/Atlas/GROUPS/PHYSICS/PLOTS/JETM-2016-011/.

[75] ATLAS Collaboration, *Expected performance of the ATLAS b-tagging algorithms in Run-2* Tech. Rep. ATL-PHYS-PUB-2015-022, CERN, Geneva, 2015, . URL: https://cds.cern.ch/record/2037697.

[76] ATLAS Collaboration, *Missing transverse energy performance and systematic uncertainties using the full 2015 dataset* URL: http://atlas.web.cern.ch/Atlas/GROUPS/PHYSICS/PLOTS/JETM-2016-003/.

[77] ATLAS collaboration, *Search for supersymmetry with two same-sign leptons or three leptons using 13.2 fb^{-1} of $\sqrt{s} = 13$ TeV pp collision data collected by the ATLAS detector* ATLAS-CONF-2016-037 , URL: http://inspirehep.net/record/1479668.

[78] P. Huang, A. Ismail, I. Low, and C. E. M. Wagner, *Same-Sign Dilepton Excesses and Light Top Squarks*, 2015, Phys. Rev. **D92** (2015) 075035, arXiv:1507.01601 [hep-ph].

[79] H. Baer, V. Barger, P. Huang, D. Mickelson, A. Mustafayev, W. Sreethawong, and X. Tata, *Radiatively-driven natural supersymmetry at the LHC*, 2013, JHEP **12** (2013) 013, arXiv:1310.4858 [hep-ph], [Erratum: JHEP06,053(2015)].

[80] H. Baer, V. Barger, P. Huang, D. Mickelson, A. Mustafayev, W. Sreethawong, and X. Tata, *Same sign diboson signature from supersymmetry models with light higgsinos at the LHC*, 2013, Phys. Rev. Lett. **110** (2013) 151801, arXiv:1302.5816 [hep-ph].

[81] H. Baer, V. Barger, M. Savoy, and X. Tata, *Multichannel assault on natural supersymmetry at the high luminosity LHC*, 2016, Phys. Rev. **D94** (2016) 035025, arXiv:1604.07438 [hep-ph].

[82] E. Nikolidakis and C. Smith, *Minimal Flavor Violation, Seesaw, and R-parity*, 2008, Phys. Rev. **D77** (2008) 015021, arXiv:0710.3129 [hep-ph].

[83] C. Csaki, Y. Grossman, and B. Heidenreich, *MFV SUSY: A Natural Theory for R-Parity Violation*, 2012, Phys. Rev. **D85** (2012) 095009, arXiv:1111.1239 [hep-ph].

[84] G. Durieux and C. Smith, *The same-sign top signature of R-parity violation*, 2013, JHEP **10** (2013) 068, arXiv:1307.1355 [hep-ph].

[85] J. Berger, M. Perelstein, M. Saelim, and P. Tanedo, *The Same-Sign Dilepton Signature of RPV/MFV SUSY*, 2013, JHEP **04** (2013) 077, arXiv:1302.2146 [hep-ph].

[86] ATLAS Collaboration, *Luminosity determination in pp collisions at $\sqrt{s}$ = 8 TeV using the ATLAS detector at the LHC*, 2016, Eur. Phys. J. **C76** (2016) 653, arXiv:1608.03953 [hep-ex].

[87] J. Alwall, R. Frederix, S. Frixione, V. Hirschi, F. Maltoni, O. Mattelaer, H. S. Shao, T. Stelzer, P. Torrielli, and M. Zaro, *The automated computation of tree-level and next-to-leading order differential cross sections, and their matching to parton shower simulations*, 2014, JHEP **07** (2014) 079, arXiv:1405.0301 [hep-ph].

[88] R. D. Ball et al., *Parton distributions with LHC data*, 2013, Nucl. Phys. **B867** (2013) 244–289, arXiv:1207.1303 [hep-ph].

[89] ATLAS Collaboration, *ATLAS Run 1 Pythia8 tunes,* Tech. Rep. ATL-PHYS-PUB-2014-021, CERN, 2014, . URL: https://cds.cern.ch/record/1966419.

[90] G. Corcella, I. G. Knowles, G. Marchesini, S. Moretti, K. Odagiri, P. Richardson, M. H. Seymour, and B. R. Webber, *HERWIG 6: An Event generator for hadron emission reactions with interfering gluons (including supersymmetric processes)*, 2001, JHEP **01** (2001) 010, arXiv:hep-ph/0011363 [hep-ph].

[91] A. Kulesza and L. Motyka, *Threshold resummation for squark-antisquark and gluino-pair production at the LHC*, 2009, Phys. Rev. Lett. **102** (2009) 111802, arXiv:0807.2405 [hep-ph].

[92] A. Kulesza and L. Motyka, *Soft gluon resummation for the production of gluino-gluino and squark-antisquark pairs at the LHC*, 2009, Phys. Rev. D **80** (2009) 095004.

[93] W. Beenakker, S. Brensing, M. Kramer, A. Kulesza, E. Laenen, and I. Niessen, *Soft-gluon resummation for squark and gluino hadroproduction*, 2009, JHEP **12** (2009) 041, arXiv:0909.4418 [hep-ph].

[94] W. Beenakker, S. Brensing, M. n. Kramer, A. Kulesza, E. Laenen, L. Motyka, and I. Niessen, *Squark and Gluino Hadroproduction*, 2011, Int. J. Mod. Phys. **A26** (2011) 2637–2664, arXiv:1105.1110 [hep-ph].

[95] M. Kramer, A. Kulesza, R. van der Leeuw, M. Mangano, S. Padhi, T. Plehn, and X. Portell, *Supersymmetry production cross sections in pp collisions at* $\sqrt{s} = 7$ *TeV*, 2012, arXiv:1206.2892 [hep-ph].

[96] J. Pumplin, D. R. Stump, J. Huston, H. L. Lai, P. M. Nadolsky, and W. K. Tung, *New generation of parton distributions with uncertainties from global QCD analysis*, 2002, JHEP **07** (2002) 012, arXiv:hep-ph/0201195 [hep-ph].

[97] S. Gieseke, C. Rohr, and A. Siodmok, *Colour reconnections in Herwig++*, 2012, Eur. Phys. J. **C72** (2012) 2225, arXiv:1206.0041 [hep-ph].

[98] H.-L. Lai, M. Guzzi, J. Huston, Z. Li, P. M. Nadolsky, J. Pumplin, and C. P. Yuan, *New parton distributions for collider physics*, 2010, Phys. Rev. **D82** (2010) 074024, arXiv:1007.2241 [hep-ph].

[99] ATLAS Collaboration. LHC SUSY Cross Section Working Group. URL: https://twiki.cern.ch/twiki/bin/view/LHCPhysics/SUSYCrossSections.

[100] ATLAS Collaboration, *Optimisation of the ATLAS b-tagging performance for the 2016 LHC Run* Tech. Rep. ATL-PHYS-PUB-2016-012, CERN, Geneva, 2016, . URL: https://cds.cern.ch/record/2160731.

[101] ATLAS Collaboration, *Electron efficiency measurements with the ATLAS detector using 2012 LHC proton-proton collision data*, 2017, Eur. Phys. J. **C77** (2017) 195, arXiv:1612.01456 [hep-ex].

[102] ATLAS Collaboration, *Performance of missing transverse momentum reconstruction for the ATLAS detector in the first proton-proton collisions at at* $\sqrt{s}$*= 13 TeV* Tech. Rep. ATL-PHYS-PUB-2015-027, CERN, Geneva, 2015, . URL: https://cds.cern.ch/record/2037904.

[103] ATLAS Collaboration, *Expected performance of missing transverse momentum reconstruction for the ATLAS detector at* $\sqrt{s} = 13$ *TeV* Tech. Rep. ATL-PHYS-PUB-2015-023, CERN, Geneva, 2015, . URL: https://cds.cern.ch/record/2037700.

[104] R. D. Cousins, K. E. Hymes, and J. Tucker, *Frequentist evaluation of intervals estimated for a binomial parameter and for the ratio of Poisson means*, 2010, Nuclear Instruments and Methods in Physics Research A **612** (2010) 388–398, arXiv:0905.3831 [physics.data-an].

[105] ATLAS Collaboration, *Search for supersymmetry in final states with two same-sign or three leptons and jets using 36* fb^{-1} *of* $\sqrt{s} = 13$ *TeV pp collision data with the ATLAS detector*, 2017, JHEP **09** (2017) 084, arXiv:1706.03731 [hep-ex].

[106] ATLAS Collaboration, *Search for supersymmetry at* $\sqrt{s}$*=8 TeV in final states with jets and two same-sign leptons or three leptons with the ATLAS detector*, 2014, JHEP **06** (2014) 035, arXiv:1404.2500 [hep-ex].

[107] ATLAS Collaboration, *Multi-Boson Simulation for 13 TeV ATLAS Analyses,* Tech. Rep. ATL-PHYS-PUB-2016-002, CERN, Geneva, 2016, . URL: https://cds.cern.ch/record/2119986.

[108] LHC Higgs Cross Section Working Group, D. de Florian et al., *Handbook of LHC Higgs Cross Sections: 4. Deciphering the Nature of the Higgs Sector*, 2016, arXiv:1610.07922 [hep-ph].

[109] A. Buckley, J. Ferrando, S. Lloyd, K. Nordström, B. Page, M. Rüfenacht, M. Schönherr, and G. Watt, *LHAPDF6: parton density access in the LHC precision era*, 2015, Eur. Phys. J. **C75** (2015) 132, arXiv:1412.7420 [hep-ph].

[110] ATLAS Collaboration, *Electron and photon energy calibration with the ATLAS detector using data collected in 2015 at* $\sqrt{s} = 13$ TeV Tech. Rep. ATL-PHYS-PUB-2016-015, CERN, Geneva, 2016, . URL: https://cds.cern.ch/record/2203514.

[111] J. Neyman, E. S. Pearson , *IX. On the problem of the most efficient tests of statistical hypotheses*, 1933, Philosophical Transactions of the Royal Society of London A **231** (1933) 289–337.

[112] M. Baak, G. J. Besjes, D. Côte, A. Koutsman, J. Lorenz, and D. Short, *HistFitter software framework for statistical data analysis*, 2015, Eur. Phys. J. **C75** (2015) 153, arXiv:1410.1280 [hep-ex].

[113] ATLAS Collaboration, *Search for supersymmetry at* $\sqrt{s} = 13$ *TeV in final states with jets and two same-sign leptons or three leptons with the ATLAS detector*, 2016, Eur. Phys. J. **C76** (2016) 259, arXiv:1602.09058 [hep-ex].

[114] ATLAS Collaboration, *Search for new phenomena in final states with large jet multiplicities and missing transverse momentum with ATLAS using* $\sqrt{s} = 13$ *TeV proton-proton collisions*, 2016, Phys. Lett. **B757** (2016) 334–355, arXiv:1602.06194 [hep-ex].

[115] ATLAS Collaboration, *Summary plots from the ATLAS Supersymmetry physics group.* URL: https://atlas.web.cern.ch/Atlas/GROUPS/PHYSICS/CombinedSummaryPlots/SUSY/.

[116] W. Beenakker, R. Hopker, M. Spira, and P. M. Zerwas, *Squark and gluino production at hadron colliders*, 1997, Nucl. Phys. **B492** (1997) 51–103, arXiv:hep-ph/9610490 [hep-ph].

[117] R. Barbieri and G. Giudice, *Upper bounds on supersymmetric particle masses*, 1988, Nuclear Physics B **306** (1988) 63 – 76.

[118] B. de Carlos and J. A. Casas, *One loop analysis of the electroweak breaking in supersymmetric models and the fine tuning problem*, 1993, Phys. Lett. **B309** (1993) 320–328, arXiv:hep-ph/9303291 [hep-ph].

[119] G. R. Farrar and P. Fayet, *Phenomenology of the production, decay, and detection of new hadronic states associated with supersymmetry*, 1978, Physics Letters B **76** (1978) 575 – 579.

[120] P. Fayet, *Supersymmetry and weak, electromagnetic and strong interactions*, 1976, Physics Letters B **64** (1976) 159 – 162.

[121] P. Fayet, *Spontaneously broken supersymmetric theories of weak, electromagnetic and strong interactions*, 1977, Physics Letters B **69** (1977) 489 – 494.

[122] A. Barr, C. Lester, and P. Stephens, *m(T2): The Truth behind the glamour*, 2003, J. Phys. **G29** (2003) 2343–2363, arXiv:hep-ph/0304226 [hep-ph].

[123] C. G. Lester and D. J. Summers, *Measuring masses of semiinvisibly decaying particles pair produced at hadron colliders*, 1999, Phys. Lett. **B463** (1999) 99–103, arXiv:hep-ph/9906349 [hep-ph].

[124] G. Schott, *RooStats for Searches*, 2011, arXiv:1203.1547 [physics.data-an].

[125] ATLAS Collaboration, *Search for direct pair production of a chargino and a neutralino decaying to the 125 GeV Higgs boson in $\sqrt{s} = 8$ TeV pp collisions with the ATLAS detector*, 2015, Eur. Phys. J. **C75** (2015) 208, arXiv:1501.07110 [hep-ex].

[126] ATLAS, M. Aaboud et al., *Search for chargino and neutralino production in final states with a Higgs boson and missing transverse momentum at $\sqrt{s} = 13$ TeV with the ATLAS detector*, 2018, Submitted to: Phys. Rev. (2018), arXiv:1812.09432 [hep-ex].

[127] HL-LHC Project, *Industry Relations and Procurement Website for the HL-LHC project* URL: https://project-hl-lhc-industry.web.cern.ch/content/project-schedule,.

[128] M. Papucci, J. T. Ruderman, and A. Weiler, *Natural SUSY endures*, 2012, Journal of High Energy Physics **2012** (2012) 35.

[129] ATLAS Collaboration, *Search for electroweak production of supersymmetric states in scenarios with compressed mass spectra at $\sqrt{s} = 13$ TeV with the ATLAS detector*, 2018, Phys. Rev. **D97** (2018) 052010, arXiv:1712.08119 [hep-ex].

[130] P. Artoisenet, R. Frederix, O. Mattelaer, and R. Rietkerk, *Automatic spin-entangled decays of heavy resonances in Monte Carlo simulations*, 2013, JHEP **03** (2013) 015, arXiv:1212.3460 [hep-ph].

[131] A. Djouadi, M. M. Muhlleitner, and M. Spira, *Decays of supersymmetric particles: The Program SUSY-HIT (SUspect-SdecaY-Hdecay-InTerface)*, 2007, Acta Phys. Polon. **B38** (2007) 635–644, arXiv:hep-ph/0609292 [hep-ph].

[132] U. De Sanctis, T. Lari, S. Montesano, and C. Troncon, *Perspectives for the detection and measurement of supersymmetry in the focus point region of mSUGRA models with the ATLAS detector at LHC*, 2007, The European Physical Journal C **52** (2007) 743–758.

[133] ATLAS Collaboration, *Search for long-lived charginos based on a disappearing-track signature in pp collisions at $\sqrt{s} = 13$ TeV with the ATLAS detector* Tech. Rep. ATLAS-CONF-2017-017, CERN, Geneva, 2017, . URL: https://cds.cern.ch/record/2258131.

[134] A. Ismail, E. Izaguirre, and B. Shuve, *Illuminating New Electroweak States at Hadron Colliders*, 2016, Phys. Rev. **D94** (2016) 015001, arXiv:1605.00658 [hep-ph].

List of Figures

List of Tables

Appendix D

List of publications

Most of the material presented in this thesis is based on work performed within the ATLAS Collaboration. Thus, it is typically created from the contributions of many people and cannot be attributed to a single person. The figures and plots containing an ATLAS or ATLAS Preliminary label were created in the context of ATLAS papers or conference notes. The publications with a significant contribution from the author of this thesis and the details about these contributions are indicated in this section. All plots without dedicated ATLAS or ATLAS Preliminary labels are private work done by the author of this thesis.

- *Search for supersymmetry at $\sqrt{s} = 13$ TeV in final states with jets and two same-sign leptons or three leptons with the ATLAS detector* [113]:
  Studies about event selection and optimization of signal regions (lepton p_{T} requirements and flavor selection). Implementation of the analysis in the HISTFITTER framework. Statistical interpretations of the results and production of SUSY exclusion plots and systematic tables.

- *Search for supersymmetry with two same-sign leptons or three leptons using 13.2 fb^{-1} of $\sqrt{s} = 13$ TeV pp collision data collected by the ATLAS detector* [77]:
  Implementation of the analysis in the HISTFITTER framework. Statistical interpretations of the results and production of SUSY exclusion plots and systematic tables.

- *Search for supersymmetry in final states with two same-sign or three leptons and jets using 36 fb^{-1} of $\sqrt{s}$ = 13 TeV pp collision data with the ATLAS detector* [105]:
  Study of feasibility of multi-bin fit. Production of signal region summary plots and tables. Statistical interpretations of the results and production of SUSY exclusion plots with HISTFITTER.

- *Search for chargino and neutralino production in final states with a Higgs boson and missing transverse momentum at $\sqrt{s}$ = 13 TeV with the ATLAS detector* [126]:
  Production of input trees with experimental systematic uncertainties. Estimation of the fake lepton background with the dynamic matrix method and measurement of the real lepton efficiency and fake lepton efficiency. Validation of the fake lepton background estimation. Estimation of the theoretical uncertainties of prompt SM background. All items are related to the same-sign channel.

Appendix E

Acknowledgments

First of all, I would like to thank my advisors *Prof. Gregor Herten* and *Prof. Ulrich Landgraf* for giving me the opportunity to spend my PhD years in Freiburg and for the constant supervision and support.
Then I would like to thank the people who shared with me the joys and pains of the PhD: *Fabio*, for being a great office and analysis mate and for teaching me many things. *Manfredi*, for visiting the best Bed and Breakfast in town and for introducing me into the best parts of Freiburg. *Thor*, for pushing me to do sports and learn German and for all the incredible help. *Vroni*, for leading me into the caffeine tunnel and for all the conferences adventures! I was lucky to find friends and not simple colleagues.
I would also like to thank all the other people from Herten's group: *Manuel, Patrick, Martina, Andrea, Valerio, Bernhard and Jürgen*, and of course *Andrea* and *Zuzana* who had the patience to review many times my thesis.
During my years in Freiburg, I was also lucky to meet so many great friends (the famous Savona group), in particular: *Stefano*, sei stato il primo ad accogliermi a Friburgo, mi mancheranno le nostre lunghe chiacchierate mentre giochiamo alla PS. *Valentina*, grazie per tutte le volte che mi hai accolto a casa come se fossi in famiglia (e per tutti i pranzi e cene!). *Ric* and *Maria*, la vostra allegria e bontà contagiosa mi mancherà. *Sunga*, thanks for standing all my annoying jokes and for the great moments we shared. *Danny*, I will wait for you to go to watch a Sampdoria match together. *Simona* detta *Sgargiul*, so che hai avuto tanta pazienza a sopportarmi, ma ci vedremo presto a Ginevra e non la scamperai! *Scurcino*, purtroppo sei stato poco tempo, ma che cene e feste! *Tazietto*, grazie per le mille risate e per esserci stato nei momenti che contavano. *Giulia* detta *Scody*, non pensavo che un soprannome cosi brutto potesse diventare così famoso (sarà sempre il mio orgoglio!), ma anche grazie a quello è nata un'amicizia incredibile!
Many thanks also to: *Pablo, Sara, Michele, Vlad, Olha* and *Michi*.
A special thank also to the people of the SS/3L team, in particular to *Otilia*, *Julien*, *Ximo*, *Jeanette* and *Alberto* who taught me so much about particle physics and data analysis. I would also like to thank my analysis-mates: *Othmane, Yang, Fab* and *Dani*. Last but not least, a big thank to my greek friends *Stathis* and *Christos*.
Molti mesi del mio dottorato li ho spesi a Ginevra, dove ho ritrovato amicizie che non si erano mai perse (e che mai lo faranno): *Giuliano*. grazie per avermi aiutato a trovare casa, ospitato, dato da mangiare, sostenuto, etc. insomma hai solo fatto il tuo dovere di fratello. *Giulia* detta *Sfettu*, potrei dire una santa, ma anche una spalla perfetta per ogni serata e un nuovo tassello perfetto. *Ari* e *Dani*, penso che ci sia una sola parola che possa riassumere tutto: Friends! *Capriots*, perchè per ogni mangiata, bevuta, viaggio, avventura lui ci sarà sempre! *Bea*, per essere mia amica nonostante mi abbia

psicanalizzato più volte. *Gizza*, tu sei il fratello lontano con cui spero riusciremo a ricongiungerci un giorno, giuro che ora mi leggo tutti i tuoi messaggi degli ultimi 3 anni!
Un grazie glitterato a *Andrea* e *Serena*, gli stampini non mentono e infatti finiamo il dottorato nello stesso momento!
Un grazie enorme anche a tutti i cernioti e non con cui ho condiviso momenti bellissimi a Ginevra: *Betto, Camilla, Fefe, Grazia, SilviaBiondi, Adele, Marco, Alessandra, Phelipe, Frankie, Serena, Chicco, Francesco, Veronica, Livia, Attilio, Valerio, Francesco, Annalisa, Elia, Graziana, Martina, Ciro, Franz.*
E tra le tante persone di Ginevra, voglio ringraziare soprattutto *Bibi*, per avermi tirato su di morale con le sue battute brutte nei momenti difficili, per aver avuto la pazienza di sopportarmi e anche di correggermi l'inglese, per essere sè stessa e darmi tanta gioia, ti amo!
Infine voglio ringraziare i miei genitori, per tutto quello che mi hanno sempre dato e insegnato in questi anni. Sono giunto alla conclusione dei miei studi e credo che vedere il loro sorriso alla fine di questo lungo percorso sia la soddisfazione più grande per me (e spero per loro!), vi voglio bene.